Design and Syntheses of Liquid Crystalline Perylene derivatives as Materials for Organic Electronics

A Thesis Submitted in Partial Fulfillment of the

Requirements for the Degree of

Doctor of Philosophy

at

IIT Guwahati

by

Paresh Kumar Behera

Roll No. 176122019

Department of Chemistry

Indian Institute of Technology Guwahati

Guwahati-781039, Assam

India

July 2023

"Success consists of going from failure to failure without loss of enthusiasm".

Winston Churchill

"Simplicity of all things is the hardest to be copy".

Richard Steele

Dedicated to

My Esteemed Mentor……

DECLARATION

I do hereby declare that the research work embodied in this thesis entitled "***Design and Syntheses of Liquid Crystalline Perylene derivatives as Materials for Organic Electronics***" has been carried out by me under the supervision of **Prof. A. S. Achalkumar** in the Department of Chemistry, Indian Institute of Technology Guwahati, Assam - 781039, India.

In keeping with the general practice of reporting scientific observations, due acknowledgements have been made wherever the work described is based on the findings of other investigators.

IIT Guwahati
July, 2023

Paresh Kumar Behera
Roll No. 176122019

Prof. A. S. Achalkumar, FRSC
Professor
Department of Chemistry
Indian Institute of Technology Guwahati
Guwahati – 781039, Assam, India
Phone: +91-361-258-2329
Fax: +91-361-258-2349
E-mail: achalkumar@iitg.ac.in
achalkumar78@gmail.com

CERTIFICATE

This is to certify that the research work presented in this thesis entitled "***Design and Syntheses of Liquid Crystalline Perylene derivatives as Materials for Organic Electronics***" is an authentic record of the results obtained from the research work carried out by **Mr. Paresh Kumar Behera (Roll No. 176122019)** under my supervision in the Department of Chemistry, Indian Institute of Technology Guwahati, India. This work is original and has not been submitted elsewhere for a degree or award.

IIT Guwahati — Prof. A. S. Achalkumar

July, 2023 — Thesis Supervisor

ACKNOWLEDGEMENTS

Throughout the process of accomplishing my thesis, the culmination of years of expertise and the transformation of ideas into wisdom, I encountered numerous obstacles that ultimately led to a triumphant achievement. During my research journey spanning more than five years, I have received immense support and assistance from a multitude of individuals. It is with deep gratitude that I express my heartfelt appreciation to these individuals for their generosity, elegance, attentiveness, motivation, and backing.

With utmost gratitude, I begin by extending my sincere thanks to my supervisor, Prof. Ammathnadu Sudhakar Achalkumar, whose expert guidance, inspiration, and innovative scientific ideas have been instrumental in shaping the scope of this thesis. His unwavering support has allowed me the freedom to explore my creativity and delve into research questions that have intrigued me. Countless hours spent in fruitful discussions about science and ideas have enriched my understanding and propelled this work forward. Without his patience and mentorship, completing this endeavor would have been an arduous task. Whenever I faced uncertainty or hesitated to venture into uncharted territories, his constant encouragement and unwavering scientific spirit provided the necessary push to achieve my objectives. Undoubtedly, selecting him as my supervisor has proven to be one of the most rewarding decisions of my academic journey.

In addition to my supervisor, I would like to extend my deepest gratitude and heartfelt appreciation to my esteemed doctoral committee members, namely Prof. Anil Kumar Saikia, Prof. Bhubaneswar Mondal, and Dr. Krishna Pada Bhabak. Their periodic evaluation of my work, invaluable suggestions, unwavering support, and constant encouragement have played a crucial role in my academic journey. I am truly grateful for their contributions. Furthermore, I would like to express my sincere thanks to Dr. Prasenjit Sarkar and Dr. Chandan Mukherjee for generously providing me access to their electrochemical workstation for analysis. I am also indebted to Dr. Upendra Kumar Pandey and Ms. Kajal Yadav from the Shiv Nadar University, who have assisted me in conductivity measurements. Additionally, I would like to acknowledge the contributions of Dr. Mangeyram Nagar and Prof. Jwo-Huei Jou from the National Tsing Hua University, who have also aided me in OLED device fabrication. Lastly, I would like to express my gratitude to Dr. D. S. Shankar Rao and Dr. S. K. Prasad from CeNS, Bangalore, for their guidance and support during

the X-ray Diffraction analysis. I am truly thankful to all of them for their invaluable contributions and support.

I would like to acknowledge Central Instruments Facility, IIT Guwahati for providing me the analytical facilities required during my research work. I wish to express my sincere gratitude to Indian Institute of Technology Guwahati for nurturing our research career and for all the facilities and financial support that was made available to me.

It would have been impossible for me to continue my five years stay of Ph. D research without the help and support of my batchmates; I am greatly indebted to them. I express my deep sense of gratitude to all my lab members (present and past) Dr. Ravindra Kumar Gupta, Dr. Vinod Kumar Vishwakarma, Dr. Hemant Kumar Singh, Dr. Balaram Pradhan, Dr. Priyanka Kanth, Dr. Rahul Uttam, Mr. Sibasankar Pradhan, Mr. Mrinmoy Roy, Mr. Rahul Ahmed, Mr. Nandan Kumar, Ms. Neichoi Lhouvum, Mr. Dharmendra Adak, Mr, Sarwar Parvez and Mr. Nihal Khatiwada, for their help, scientific conversations and also maintaining a pleasant working environment throughout my Ph.D. tenure. Of course, I would like to thank almighty to fulfill my PhD carrier with bunch of beloved senior friends and batch mates for being with me all the time starting from the beginning of my research career and for their help and guidance.

Finally, my Ph.D. would not have been completed without the eternal love, care, bless, support, patience, non-refundable sacrifices and encouragement of my parents and all family members. They encouraged me to pay attention to the world around me and to wonder why and how things work. Of course, everything will go invalid if I forget the blessings of almighty god without whom nothing will function and I pray him for his blessings.

Paresh Kumar Behera

Some of the findings of this thesis have been communicated / published in international journals as given below:

1. **P. K. Behera**, M. R. Nagar, R. K. Gupta, S. Pradhan, D. S. S. Rao, J. H. Jou, and A. S. Achalkumar, Highly stable deep red-to-NIR OLEDs with an external-quantum efficiency of 4.9% from room temperature nanostructured columnar fluids based on heteroatom *bay*-annulated perylene bisimides, ***J. Mater. Chem. C,* 2022**, *10*, 18351-18365.

2. **P. K. Behera**, K. Yadav, D. S. Shankar Rao, U. K. Pandey, and A. S. Achalkumar, Ambipolar columnar self-assembled organic semiconductors based on heteroatom *bay*-annulated perylene bisimides, ***Chem. Asian J.* 2023**, e202300086. DOI: 10.1002/asia.202300086.

3. **P. K. Behera**, K. Yadav, D. S. S. Rao, U. K. Pandey, and A. S. Achalkumar, Solution processable swallow tail perylene bisimides exhibiting room temperature columnar phases and efficient ambipolar charge carrier mobility. (manuscript communicated).

4. **P. K. Behera**, K. Yadav, R. K. Gupta, D. S. S. Rao, U. K. Pandey, and A. S. Achalkumar, Highly soluble anti-Perylene-3,4:9,10-bis(benzimidazole)s stabilizing room temperature columnar Phase with ambipolar conductivity. ***Chem. Euro. J.*, 2023**, e202302187. DOI: 10.1002/chem.202302187.

Articles that are not included in this thesis:

1. **P. K. Behera**, K. Yadav, N. Kumar, R. K. Gupta, D.S. Shankar Rao, U. K. Pandey, and A. S. Achalkumar, First example of ambipolar Naphthalene diimide exhibiting room temperature columnar phase, ***Chem. Commun.*, 2023,**59, 6028-6031**.**

2. **P. K. Behera,** S. Rao, L. T. Popoola, S. A. Swamirayachar, S. Kodange, G. Prashanth**,** A. S., Achalkumar, Room temperature columnar liquid crystalline perylene bisimide as a novel corrosion resistant surface film for mild steel surface, ***Journal of Bio- and Tribo-Corrosion***. **2023**, *9 (18)*, 1-14.

3. **P. K. Behera**, K. Yadav, D. S. S. Rao, U. K. Pandey, and A. S. Achalkumar, self-assembled Naphthalene cis-bis(4,5-dialkoxybenzimidazole)s or cis-perinones exhibiting Room temperature Columnar phse and ambipolar conductivity. ***ACS Appl. Electron. Mater.*** 2023, DOI: 10.1021/acsaelm.3c01101.

4. B. N. Sunil, **P. K. Behera**, A. S. Achalkumar, G. Shanker and G. Hegde, Influence of inter- and intramolecular H-bonding on the mesomorphic and photoswitching behavior of (E)-4-((4-(hexyloxy)phenyl)diazenyl)-N-phenyl benzamides, **RSC Adv., 2020, 10, 20222-20230.**

5. **P. K. Behera**, F. R. Chen, M. Roy, P. Gautam, I. Siddiqui, D. S. Shankar Rao, J. H. Jou, and A. S. Achalkumar, A Columnar Self-Assembled N-Annulated Perylene Bisimide Exhibiting Room Temperature Liquid Crystallinity and Yellow-orange Electroluminescence (EQE > 7%). (manuscript communicated).

6. **P. K. Behera**, F. R. Chen, M. Roy, P. Gautam, I. Siddiqui, D. S. Shankar Rao, J. H. Jou, and A. S. Achalkumar, Highly Fluorescent Room Temperature Liquid Crystalline *S*-Annulated Swallow Tail Perylene Bisimide exhibiting Enhanced Electroluminescence (EQE > 11%). (manuscript communicated).

7. **P. K. Behera**, A. Patra, S. Kumar and A. S. Achalkumar, Liquid Crystalline Perylene diester imides as a new class of self-assembled organic semiconductors. (Communicated).

Papers presented in National/International conferences: (Oral/Poster)

1. Oral Presentation at a National Conference: Research and Industrial Conclave - Integration' 2023, IIT Guwahati, India, on May 14-16, 2023.
2. Poster Presentation at an International Conference: "Frontiers in Chemical Science" (FICS) IIT Guwahati, India, on December 02-04, 2022.
3. Poster Presentation at an International Webinar: Liquid Crystalline Materials: Chemistry, Physics, and Biological Applications (RPLCM), Assam University, Silchar, India, on October 04-05, 2021.
4. Poster Presentation at a National Conference: Research Conclave' 19, IIT Guwahati, India, on March 14-17, 2019.
5. Poster Presentation at a National Conference: "National Conference on Liquid Crystals" (NCLC), Chitkara University, India, 2019.
6. Poster Presentation at an International Conference: "Frontiers in Chemical Science" (FICS) IIT Guwahati, India, on December 06-08, 2018.

CONTENTS

List of abbreviations used in the text

anhyd	anhydrous
bs	broad singlet
Cr	crystal
Col	columnar
d	doublet
DCM	dichloro methane
dd	doublet of a doublet
equiv	equivalents
Et	ethyl
Et_3N	triethyl amine
EtOAc	ethyl acetate
g	gram
h	hour
Hz	hertz
HRMS	high resolution mass spectrometry
I	isotropic
IR	infrared
J	joules
J	coupling constant
K	kelvin
LC	liquid crystal
m	multiplet
m	meta
MHz	megahertz
min	minutes
mmol	milli mole(s)

n	normal
N	nematic
NMR	Nuclear magnetic resonance
p	para
q	quartet
R_f	retention factor
rt	room temperature
s	singlet
t	triplet
THF	tetrahydrofuran
TMS	tetramethyl silane
TLC	thin layer chromatography
UV	ultra violet
XRD	X-ray diffraction

GENERAL REMARKS

Commercially available chemicals were utilized without further purification, and standard procedures were followed to dry the solvents. Chromatography was conducted using either silica gel (60-120 mesh) or neutral aluminum oxide. For thin-layer chromatography, aluminum sheets pre-coated with silica gel were employed. IR spectra were acquired at room temperature using a Perkin Elmer IR spectrometer (PerkinElmer UATR TWO). The spectral positions are reported in wave number (cm^{-1}) units. NMR spectra were recorded using a 400MHz and 600 MHz Nuclear Magnetic Resonance (NMR) Spectrometer (Make: Bruker, Model: AVANCE III HD). Chemical shifts in ^{1}H NMR spectra were referenced to TMS as an internal standard and reported in ppm. Coupling constants were provided in Hz. Mass spectra were obtained using a MALDI-TOF mass spectrometer (Matrix Assisted Laser Desorption Ionization- Time of Flight, Make: BRUKER Model: AUTOFLEX SPEED) with α-Cyano-4-hydroxycinnamic acid as a matrix. The liquid crystalline behavior of the mesogenic compounds, including birefringence and fluidity, was investigated using a polarizing optical microscope (Nikon Eclipse LV100POL) equipped with a programmable hot stage (Mettler Toledo FP90). Observations were made with clean glass slides and coverslips. Differential scanning calorimetry (DSC) under a nitrogen atmosphere was used to determine transition temperatures and associated enthalpy changes. A Mettler Toledo DSC1 instrument was employed, and the peak temperatures corresponding to transitions obtained from DSC were consistent with the polarizing optical microscopic observations. The first heating and cooling cycles were conducted at a rate of 5 °C/min, and the transition temperatures were recorded. Variable temperature XRD studies were performed using samples filled in Lindemann capillaries. A high-resolution X-ray powder diffractometer (PANalytical X'Pert PRO) equipped with a high-resolution fast detector PIXCEL was used. The sample temperature was controlled using a Mettler hot stage/programmer (FP82HT/FP90). Thermogravimetric analysis (TGA) was carried out using a thermogravimetric analyzer (Mettler Toledo, model TG/SDTA 851 e) under a nitrogen flow at a heating rate of 10 °C/min. UV-Vis spectra were recorded using a Perkin-Elmer Lambda 750 UV/VIS/NIR spectrometer. Fluorescence emission in solution state was investigated using either a Horiba Fluoromax-4 fluorescence spectrophotometer or a Perkin Elmer LS 50B spectrometer. Cyclic Voltammetry (CV) studies were conducted using a Metrohm Autolab PGSTAT204 Electrochemical workstation with the assistance of NOVA software.

PREFACE

Liquid crystals are unique states of matter with an intermediate order and mobility, also known as mesophase. Molecules that exhibit liquid crystallinity are called mesogens. Liquid crystals have orientational and sometimes positional order, making them anisotropic fluids stabilized by anisotropic dispersion forces resulting from the association of anisotropic molecules. They have combined properties of both the liquid state and crystalline state on a molecular, supramolecular, and macroscopic level. They are sensitive to external stimuli such as temperature, pressure, light, electric field, and magnetic field. Liquid crystals can be classified based on the molar mass of the constituent molecules, the way the liquid crystalline phase was obtained, and the geometrical shape of the cores. Conventional LCs include calamitic and discotic LCs, while non-conventional LCs include a variety of mesogens like bananas, phasmidic, star-shaped, dendrimeric, oligomeric, and polymeric LCs.

Liquid crystals can exist in different mesophases, including nematic (N) and smectic (Sm) phases, which are stabilized by rod-like or calamitic molecules. Disc-like molecules exhibit nematic phases known as discotic nematic (N_d) and can also form columnar phases (Col) with different 2D lattices. Smectic LCs have the potential as charge carrier materials due to their layered structure and strong face-to-face π-π interaction. Columnar phases are further classified into different types based on the lattice in which the individual columns organize. These are such as columnar hexagonal (Col_h), columnar rectangular (Col_r), columnar oblique (Col_{ob}), columnar square (Col_{sq}), columnar plastic (Col_p), columnar lamellar (Col_L), and helical phase (H phase).

Liquid crystals (LCs) self-assemble into different mesophases based on their molecular subunits, and these mesophases have potential applications in various fields. Smectic LCs have a layered structure with strong π-π interactions, making them useful as charge carrier materials. Discotic LCs exhibit discotic nematic and columnar phases, which offer pathways for charge migration and self-organize into different 2D lattices. The columnar phase has inherent self-assembling and self-healing abilities, enhancing its physical properties and making it a cheaper alternative to inorganic semiconductors. Columnar LCs derived from electron-rich/poor derivatives are ideal for organic solar cells and molecular electronic devices. They also have potential applications in xerographic and laser printing, sensors, and organic light-emitting diodes due to their conductive and luminescent properties.

This thesis entitled '*Design and Synthesis of Liquid Crystalline Perylene Derivatives as Materials for Organic Electronics*' comprises of five chapters. It describes the synthetic pathway by a green method using a microwave reactor for new liquid crystalline organic materials. It also reports their characterization, studies related to their structure-property relationship, their charge carrier mobilities, and applications in OLEDs. All molecules exhibit room-temperature discotic columnar liquid crystalline behavior and have been utilized for various applications. A brief overview of the different chapters presented in this thesis is given below:

Chapter 1 is an introductory chapter on liquid crystals. It also includes literature reports on perylene-based discotic liquid crystals. DLCs are generally formed by the stacking of disc-like molecules with an intimate π-π overlap. Perylene, a rigid and highly conjugated aromatic system composed of five fused benzene rings, exhibits strong π-π interactions that facilitate self-organization into columnar structures and the formation of discotic liquid crystals. Intelligent molecular engineering can provide access to tune its photophysical properties and self-assembling behavior. This chapter also attempts to provide an overview of the advantages of the *bay*-annulated perylene derivatives over *bay*-substituted ones for their liquid crystalline self-assembly.

Chapter 2 addresses the synthesis and characterization of a series of electron-deficient perylene derivatives, substituted with 3,4,5-tridecyl phenyl moiety at the imide position (**PBI^{10}**, **PBI-N^{10}**, **PBI-S^{10}**, **PBI-Se^{10}**). Out of these, three derivatives were *bay* annulated with heteroatoms like *N, S,* and *Se* in the bay positions of the perylene core *via* the Cadogan reaction. These compounds were liquid crystalline at room temperature exhibiting a columnar hexagonal phase exclusively, except *S*-annulated PBI which exhibited a columnar oblique phase. These self-organizing organic semiconductors in one-dimensional (1D) columnar structures are unique by having better solubility, ease of purification, reproducibility, and ease of handling in comparison to polymers or single crystals. Detailed photophysical studies of these compounds show that they exhibit high molar extinction coefficients with wide absorption spectra covering most of the visible spectrum and bright red fluorescence, making them promising candidates for organic electronics. Further, they exhibited technologically important red electroluminescence. One of the solution-processed host-guest OLEDs (CBP as host at 1 wt.% **PBI-N^{10}**) exhibited a maximum EQE of 4.9%, a lifetime of 12.4 h with an initial brightness of 2900 cd/m^2 and a deep red/NIR emission.

These results indicated that these materials exhibit significant potential in the field of columnar liquid crystal-based deep red/NIR emitters.

Chapter 3 reports PBI and its heteroatom *bay*-annulated analogs bearing tri-*n*-decyloxyphenyl moieties. Compounds **PBI^{O10}**, **PBI-S^{O10}**, and **PBI-Se^{O10}** exhibited a columnar rectangular phase, whereas the *N*-annulated perylene bisimide **PBI-N^{O10}** exhibited a columnar oblique phase, down to room temperature with a wide thermal range. These compounds exhibited intense absorption spectra with high molar extinction coefficients. This is promising considering their application potential in organic solar cells, where there is a scope to widen their absorption range by structural modification. With low LUMO levels, they can also function as non-fullerene acceptors for organic solar cells which are also promising for providing higher stability in organic solar cells as compared to much-explored fullerenes. Considering the requirement of new n-type semiconductors capable of self-assembly, this class of compounds is exceptional and encouraging. These PBIs were tested for their charge carrier mobility by the space charge limited current (SCLC) method and found that they exhibit ambipolar conductivity. In general, PBIs derived from tri-*n*-alkyl anilines exhibit higher mobility values than the PBIs derived from tri-*n*-alkoxy anilines. The only exception is found in the hole mobility value of **PBI-N^{O10}** which is almost double that of the **PBI-N^{10}**. *S*-annulated PBI derived from tri-*n*-alkyl aniline (**PBI-S^{10}**) was the best among these compounds exhibiting the highest hole (8.39×10^{-3} cm^2/ V.s) and electron (1.51×10^{-2} cm^2/ V.s) mobility values, which could be due to the S···S, S···O σ-hole interactions, and better core-core interaction in the columnar phase.

From the literature survey, it is evident that most of the reported PBIs are known for n-type semiconducting behavior, while the present set of compounds is unique by showing ambipolar conductivity. The present molecular design to achieve ambipolar conductivity can be further improved by tuning the mesophase clearing temperatures, and type of the mesophase, and enhancing the surface alignment. Further exploration of these compounds as a non-fullerene acceptor for solar cells is currently being explored. In **Chapter 4** a swallowtail has been introduced to reduce the clearing point. This chapter provides a detailed investigation of perylene bisimide (**PBIST**) and its heteroatom annulated derivatives (**PBI-NST**, **PBI-SST**, and **PBI-SeST**) that possess high solubility, strong fluorescence and form columnar phases at room temperature. These modified PBIs with branched alkyl tails exhibit liquid crystalline behavior with low melting points.

The compounds **PBIST** and **PBI-NST** form a columnar oblique phase, while **PBI-SST** and **PBI-SeST** form a columnar hexagonal phase over a broad thermal range at room temperature. These PBIs exhibit strong absorption spectra with high molar extinction coefficients. All the compounds except **PBI-SeST** demonstrate strong fluorescence with high quantum yield values. These compounds are remarkable and promising for the development of new n-type semiconductors that can self-assemble. The PBIs' charge carrier mobility was evaluated using the space charge limited current (SCLC) method, and they were found to exhibit ambipolar conductivity. Previous studies have shown that most PBIs exhibit n-type semiconducting behavior, but this group of compounds is unique in that they demonstrate ambipolar conductivity. The current molecular design for achieving ambipolar conductivity could be further optimized by adjusting the mesophase clearing temperatures, mesophase types, and surface alignment.

In the preceding three chapters, all prepared PBIs possess a band gap of approximately 2.3 eV and an absorption range of up to 550 nm. Literature reports indicate that to enhance solar cell efficiency, the molecule should possess a low band gap and a wide absorption range covering the entire visible spectra up to 780nm. This can be achieved by extending the conjugation by coupling benzene1,2-diamine with commercially available perylene bis anhydride (PBA) to form perylene bis benzimidazoles (PBs). In earlier reports, we discovered solubility issues with these derivatives, resulting in inseparable syn and anti-mixtures. To address this problem, in **Chapter 5**, PBs have been synthesized by coupling 3,4-alkoxy benzene diamines with PBA and incorporated branched chains at the alkoxy position of the benzene diamine. This improves solubility and enables us to isolate these isomers. For the first time, *anti*-perylene-3,4:9,10-bis(benzimidazole) derivatives were isolated and characterized successfully. Interestingly, these compounds exhibit a wide absorption spectrum (400-800 nm) with a high extinction coefficient due to the expansion of the perylene core by benzimidazole rings. The incorporation of hetero-atoms and expanded aromatic skeleton lead to enhanced core-core interaction, higher clearing temperatures, observation of core-core peak in the XRD studies, elevated LUMO and HOMO levels, and reduced bandgap, making them ideal for organic solar cells. Additionally, these nitrogen-enriched polyaromatic heterocyclic cores form a unique class of ambipolar organic semiconductors that self-organize with balanced hole and electron mobility. These compounds exhibit high solution processability and stabilized the room-temperature columnar hexagonal phase over a wide thermal range.

Chapter 1

Introduction to Liquid Crystalline Perylene Derivatives

1.1. Introduction

Liquid crystals (LCs) research has made considerable strides in the knowledge of supramolecular self-assembling process and its implications in technology throughout the years. The development and commercialization of liquid crystal displays has energized the field and spurred the scientific community to seek out novel materials with intriguing properties.[1] It is crucial to comprehend the structure-property interrelations in LCs since it enables us to use scientific knowledge, which calls for an immensely interdisciplinary approach. This particular form of matter demonstrates a rare amalgamation of mobility and order, bridging the gap between liquids and solids, and displays a high sensitivity to various external stimuli including electrical fields, magnetic fields, temperature, light, and pressure. Depending on the chemical makeup of LCs they might be inorganic, organic or organometallic. Furthermore, LCs are widely categorized as thermotropic and lyotropic, depending on their types of phase changes induced by external forces. A thermotropic LC typically consists of two parts: a flexible chain or chains coupled to a hardcore by a variety of connecting groups. However, even the sort of connecting group between these two units affects how the LC self-assembly behaves. The categorization of LCs extends further into conventional and non-conventional types, primarily depending on how the stiff anisotropic core is shaped. Calamitic LCs (resembling rod shape) and discotic (resembling disc shape) LCs are considered as conventional LCs, while non-conventional LCs comprise a diverse range of mesogens that deviate from the traditional rod or disc shapes. Examples of non-conventional LCs include bent-cores (resembling bananas), hybrid structures combining rod and disc-like elements (referred to as polycatenars or phasmidic), star-shaped compounds, as well as dimeric, oligomeric, and polymeric mesogens. The molecules within LCs have the propensity to arrange themselves parallel to each other or undergo nano-phase segregation due to the presence of incompatible molecular components.[1] The self-assembly of LCs typically follows the principle of condensed soft matter association, which involves optimizing the interaction energy while considering the limitations imposed by excluded volume effects. By balancing these factors, the LCs achieve their characteristic arrangements and structures within the condensed soft matter framework. The promotion of LC self-assembly is additionally aided to varying degrees by additional secondary interactions such as dipolar, Van der Waals, quadrupolar, ionic interaction, π-π interactions, charge transfer, hydrogen bonding, and metal coordination. In calamitic liquid crystals (LCs), their alignment parallel to each other plays

a crucial role in stabilizing the nematic (N) phase. In this phase, the LC molecules exhibit positional order but lack orientational order. On the other hand, when calamitic LCs transition into the smectic (Sm) phase, they form layers with both positional and orientational order. Within the smectic phase, the SmA and SmC classifications depend on the degree of tilt exhibited by the LC molecules within the layers. The layered structure and strong aromatic overlap make Smectic LCs, particularly the SmA phase, a promising option for use as charge transport material. Discotic liquid crystals, on the other hand, stabilize either the columnar (Col) or the phase nematic phase depending on the orientation of their disc-shaped molecules. The N phase is maintained by the long-range orientational order of disc-like molecules, while the Col phase is maintained by the stacking of these molecules on top of each other. (Figure 1.1).

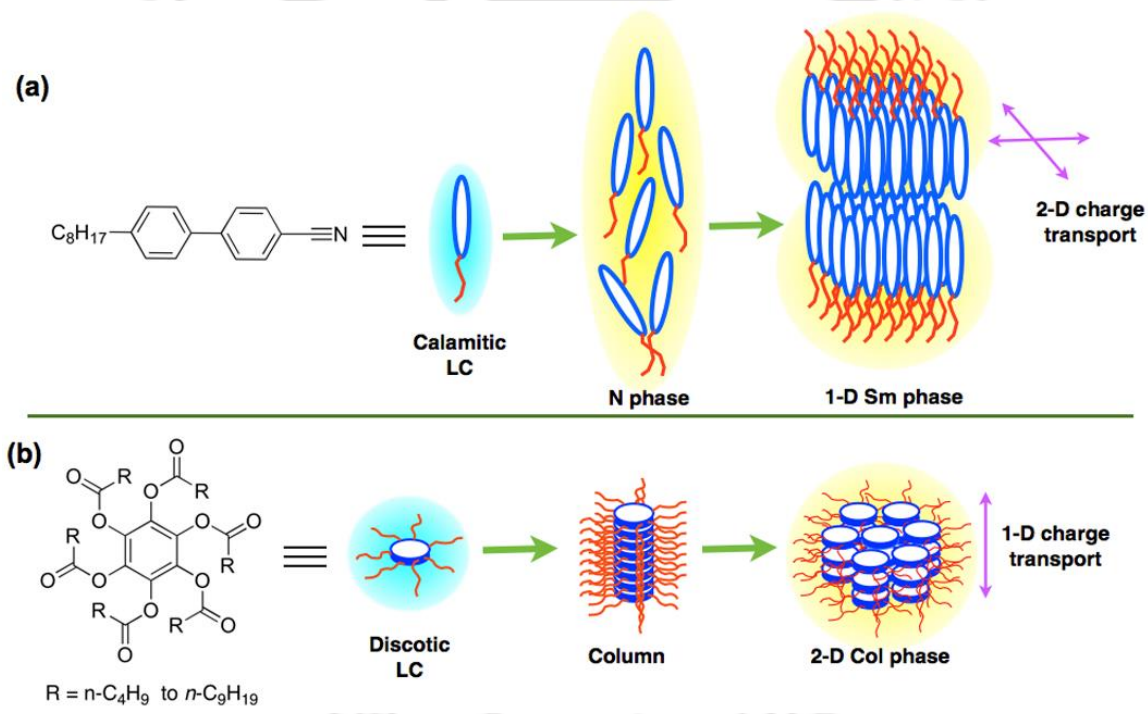

Figure 1.1. (a) Self-assembly of a typical rod-like molecule (8CB) to nematic (N) and smectic (Sm) phases; (b) a series of disc-like molecules (benzenehexa-*n*-alkanoates) to form the Col phase.

Two types of nematic phases can be formed in liquid crystals: the columnar nematic (N_C) phase, wherein numerous short columns are organized without forming a two-dimensional lattice structure, and the lateral nematic (N_L) phase, that involves the arrangement of various discotic aggregates with only orientational order. The columnar (Col) phase occurs when disc-like molecules are stacked vertically in a one-dimensional arrangement. Subsequently, these 1D

columns are then assembled into several 2D lattice patterns. The 2D symmetry of these lattices classifies the columnar phases into hexagonal (Col_h), oblique (Col_{ob}), rectangular (Col_r), and tetragonal or square (Col_{sq})columnar phases. In the lamellar columnar (Col_L) phase, the columns formed by disc-like molecules (DLCs) are structured in a layered arrangement. Within the columnar plastic (Col_p) phase, the discs enclosed within the columns have the ability to rotate around the axis of the column. Simultaneously, the molecules are free to rotate on their respective positions, but their lateral and longitudinal movements are constrained.[2] Due to their inherent self-assembling properties, columnar, smectic, and more recently nematic liquid crystals (LCs) have emerged as highly promising materials for organic semiconductors involved in charge transport. The remarkable characteristic of these liquid crystals (LCs) is their ability to form large-area films with high levels of order, free from any distinct domains. This property is highly desirable for their potential applications.[3,4] The main objective of this introductory chapter is to concentrate on LC perylene derivatives, particularly their annulated derivatives with various heteroatoms. The discussion is specifically dedicated to exploring this particular topic. It is worth mentioning that multiple scholarly reviews have already been published, delving into the self-assemblies of perylenes and their wide-ranging applications.[5]

1.2. Discotics in Organic Electronics: Application

Despite their potential to function as "molecular wires," columnar phases have not yet made a significant impact in organic electronics. The stacking of disc-like cores in columns, combined with the insulating sheath of flexible tails, creates an intimate overlap that allows them to behave as 1D-charge carriers. Currently, organic electronic devices including organic light-emitting diodes (OLEDs), organic thin film transistors (OTFTs), and organic photovoltaics (OPVs), employ organic single crystals with high-purity or polymers as operational layers. (Figure 1.2).

The high cost and difficulties in producing superior grade organic single crystals mostly make them impractical for widespread use, despite their excellent charge carrier mobility. Despite their potential as affordable substitutes, polymers have low solubility and batch-to-batch reliability. Additionally, the amorphous nature of polymers results in lower conductivity values in juxtaposition to single crystals. In contrast, Col LCs offer scalability, reproducibility, and solution-processability, but their conductivity is inferior to that of organic single crystals. However, this

particular problem can be addressed through achieving an intricately organized columnar phase, that can increase conductivity.[3]

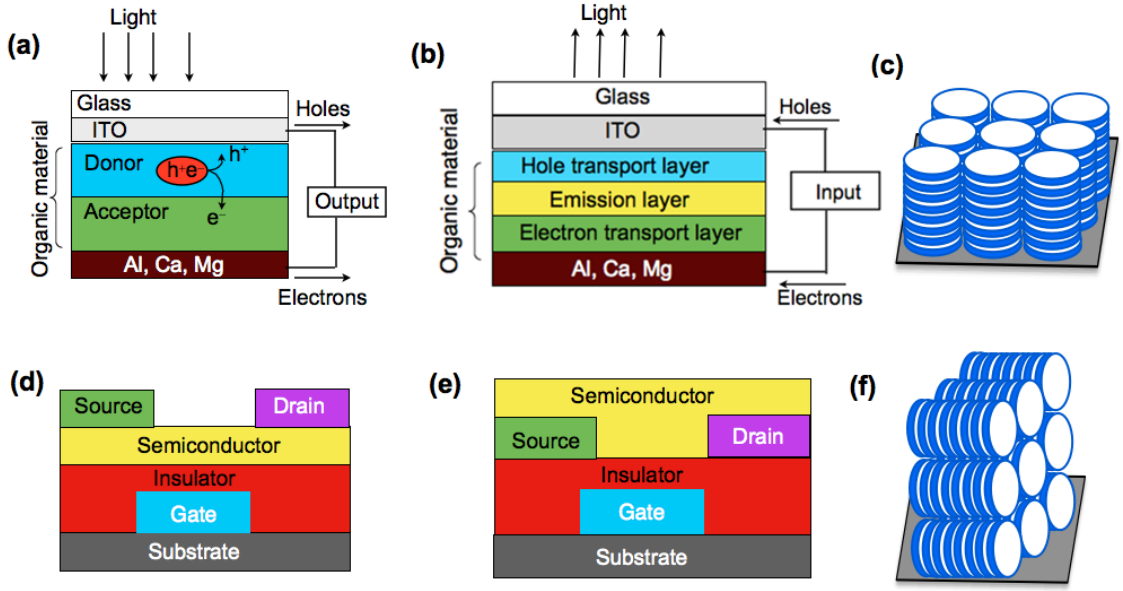

Figure 1.2. (a) Schematic showing the device structure of organic heterojunction solar cell; (b) organic light emitting diode; (c) homeotropic (face-on) alignment of columns; Schematic of the organic field effect transistor with (d) top-contact device, where the source and drain electrodes are deposited on an organic semiconducting layer; (e) bottom-contact device, where the organic semiconductor is deposited on to prefabricated source and drain electrodes; (f) homogeneous (edge-on) alignment of columns.

The configuration of OLEDs and OPVs are almost identical, with both employing organic semiconductor layers that are placed in between the two electrodes (as shown in Figure 1.2 a-b). The main difference between the two lies in how they function: in OSCs, excitons produced via absorbed light are separated into holes and electrons, which then migrate to their appropriate electrodes under the device's electric potential. Conversely, in OLEDs, a voltage applied across the electrodes causes the migration of holes and electrons that combine at the organic surface, releasing lights. Consequently, OSC molecules require an expansive spectrum of absorbance and a prominent exciton diffusion length, while OLED molecules necessitate an optimal conductivity and a reasonably high photoluminescence quantum yield (PLQY). Achieving optimal charge carrier mobility requires an ideal alignment of the columns in either a 'homeotropic' or 'face on' orientation (Figure 1.2c). On the other hand, in OFETs, the columns must be aligned in a "homogeneous" or "planar" manner between the drain and source electrodes (Figure 1.2d-f).[6] Therefore, initiatives have been taken to develop Columnar Liquid Crystals (Col LCs) that can

stabilize such required alignments. The majority of the Col LCs are created from electron-rich moieties and function as "p-type" semiconductors, such as triphenylene, pyrene, hexabenzocoronene, etc. However, there are fewer Col LCs originated from electron-deficient moieties that act as "n-type" semiconductors, such as hexaazatriphenylene, naphthalenebisimide, anthraquinone, etc. Having Col LCs that are n-type and tunable with optimal alignment features is vital for improving the performance of all these devices. Perylene-derived Col LCs can function as viable n-type materials, provided they undergo appropriate functionalization.

1.3. Perylene: a core with n-type semiconducting properties

Organic materials with high conjugation tend to have high crystallinity, which results in reduced solubility in organic solvents. As a consequence, it becomes arduous to manufacture superior quality thin films through solution processing methods. To address this issue, the general design template for discotic liquid crystals (DLCs) includes the inclusion of numerous alkyl chains on the outer edges. This enhances their processability, solubility, and facilitates purification through recrystallization and gravity-based column chromatography.[7] Furthermore, this promotes their columnar self-assembly and lowers their melting point. However, if an excess alkyl chains or hefty substituents are introduced, it can have an adverse effect on the self-assembling process and 1D-charge carrier mobility.

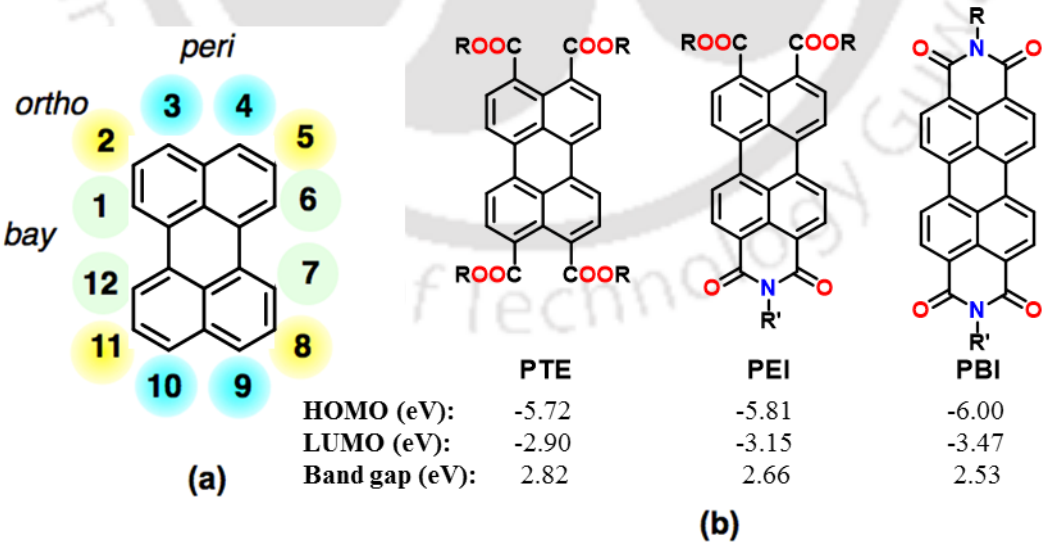

Figure 1.3. (a) Structure of perylene with possible options for substitution; (b) three classes of most commonly studied perylene derivatives for the application in liquid crystals and organic electronics (HOMO and LUMO frontier

molecular orbitals and band gaps of **PTE**, **PEI**, and **PBI** have been calculated from DFT method employing B3LYP/6-31G(d,p) functional for methyl derivatives).

Researchers have been intrigued by perylene derivatives for the past 20 years owing to their straightforward functionalization and promising potentials in organic electronics. These dye compounds possess a remarkable ability to absorb visible light, high quantum yield of photoluminescece, and a prolonged lifetime of fluorescence. Additionally, they possess exceptional stability when exposed to thermal and photochemical degradation.[5] This perylene moiety possess 12 positions which can be altered, offering a wide range of possibilities for modification. These positions can be divided into three sets: *bay* positions (1,6,7,12), *peri* positions (3,4,9,10), and *headland* positions (2,5,8,11), as illustrated in Figure 1.3a. Therefore, this perylene core offers numerous possibilities to customize the self-assembly and chemical structure, allowing for the adjustment of resulting properties.[8]

The classification of perylene-based LCs depending on the functional group linking the primary disc-shaped perylene moiety to the flexible exterior chains can be done into three primary categories (Figure 1.3b). Perylene tetra esters (PTEs) are the initial; followed by perylene ester-imides (PEIs) and perylene bisimides (PBIs) as the third class. Within these classes, additional modifications were made to these classes by expanding the primary perylene moiety either along the bay region or towards the long axis. Despite significant research efforts on exploring the charge migration properties of perylenes,[9] a comprehensive analysis that considers both molecular structure and self-assembly could reveal new possibilities for their potential applications. More than 200 perylene derivatives with liquid crystalline properties have been reported over the years, and research has been conducted on their potential use in the field of organic electronics. In the forthcoming sections, a concise introduction will be presented, shedding light on liquid crystalline perylene analogues and their possible implementation in the production of organic electronic devices.

1.3.1. Liquid crystalline perylene bisimides

1.3.1.1. Liquid crystalline perylene bisimides with alkyl chains

Within the domain of organic electronics, PBIs are recognized as a prominent class of acceptor materials with exceptional luminescent properties. They exhibit robust absorption

attributes and electron affinities that are comparable to those of fullerenes. Notably, among PBIs, dialkyl derivatives stand out with their remarkably low LUMO energy (-3.85 eV), granting them superior acceptor capabilities. This advantage holds true even when compared to other aromatic PBIs with comparable band gaps. This unique trait enables the potential of achieving charge separation at interfaces between electronically complementary aromatic PBIs. Despite being crystalline, PBI **2a** serves as a valuable benchmark and has found extensive application as an active n-type carrier in various organic electronic devices (see Figure 1.10).[10] The remarkable semiconducting characteristics of PBI **1a** were showcased by Kim and coworkers[11] through the annealing of the vapor-deposited polycrystalline film in its liquid-crystalline (LC) phase, attributed to its well-organised intermolecular structure. The elongation of the molecular chain, as observed in derivative **1b** and **1c**, resulted in decreased clearing temperatures.

The inclusion of symmetric alkyl chains in a swallowtail configuration resulted in lowered clearing temperatures for the compounds, albeit they exhibited a crystalline nature (**2b**-**2e**).[12, 13a-c, 14] It is worth noting that only compound **2c** demonstrated a monotropic Col_h phase.

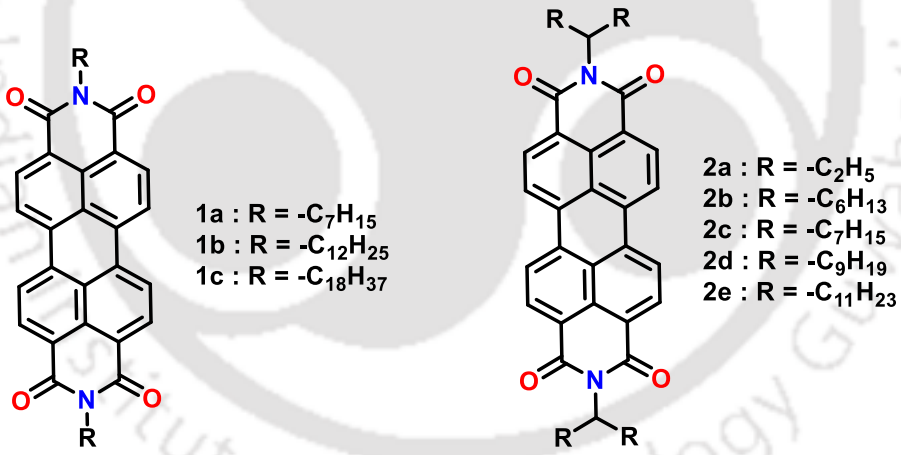

Figure 1.4. Structures of PBIs with alkyl chains.

By incorporating branched aliphatic chains as *N*-substituents, as observed in PBIs **3a** and **3b**, the clearing temperatures were brought down. Here compound **3a** possesses crystalline behavior, whereas compound **3b** remained in a liquid state.[13b] This demonstrates that the asymmetrical arrangement of alkyl chains, transitioning from swallowtails to 1-hexyl nonyl (**3a**) and 1-hexyl decyl (**3b**) effectively suppressed the isotropic temperature and mesomorphic behavior simultaneously.

In their study, Bock *et al.* sought to enhance the disc-like shape of PBIs by incorporating multiple racemic branches into the alkyl chains. They hypothesized that this modification would lead to an expansion in the volume of alkyl tails within the peripheral region. Compound **3c**, characterized by two distinct racemic centers in each alkyl chain and two alkyl chains in each molecule, would give rise to a combination of four diastereomeric pairs of enantiomers and two *meso* forms. While this modification did not impact the clearing temperature, it did lead to a reduction in melting point. As anticipated, PBI **3c**, featuring doubly racemic triple-tail alkyl chains, demonstrated the stabilization of an enantiotropic Col_h phase that spanned over a wide temperature range, including RT. Additionally, this compound also displayed favorable homeotropic alignment. The enhanced volume of alkyl chains surrounding the rigid core likely facilitated efficient space occupation and effective nanosegregation, contributing to these observed properties.[13b,15]

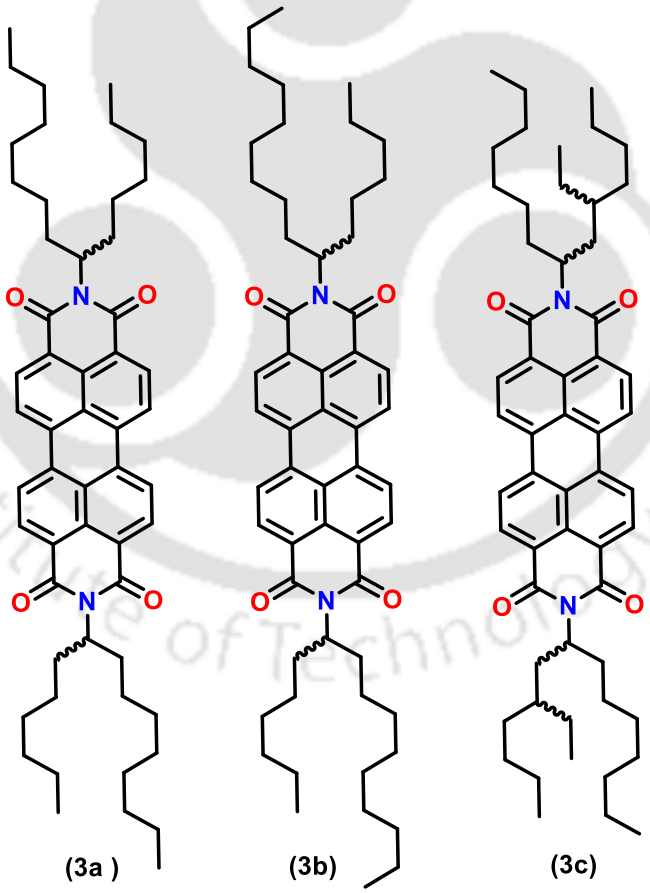

Figure 1.5. Structures of PBIs with racemic branched chains.

1.3.1.2. Liquid crystalline perylene bisimides with oligoethoxy chains

Initially, Cormier and colleagues documented several LC PBIs featuring linear (**4a**, **4b**) or branched (**4c**, **4d**) aliphatic oligoethoxy chains in 1997.[16] These compounds all displayed thermotropic LC phases as confirmed by POM and DSC analysis. PBI **4c**, in particular, exhibited a room temperature LC phase with a clearing point near around 55 ^{o}C. When the thin film was spin-coated and left undisturbed, it underwent slow crystallization over a period of 24 hours. Alternatively, upon rapid cooling, it solidified into an isotropic glassy state, which then underwent gradual crystallization. Notably, when the thin film was spin-coated onto untreated glass slides, it spontaneously arranged itself into elongated, ribbon-like crystals. The examination of emissions and absorptions yielded provided evidence that this inherent change was accompanied by a reduction in the disarray of energy within the coating, leading to a diminished number of locations that suppress excitons. The potential of these materials to repair defects and form a glassy state shows promise in the advancement of organic semiconductors. Likewise, researchers have examined various polyoxyethylene derivatives of PBIs in order to analyze their thermal characteristics using techniques such as POM and DSC.[17] The majority of these PBIs displayed a liquid crystal phase that spanned a broad range of temperatures. Notably, when it comes to PBI **4d**, which is a liquid crystal material at room temperature, its thin films demonstrated a remarkable ability to self-organize into a precisely organized crystalline phase, showcasing outstanding photophysical characteristics (Figure 1.6).

Thin polycrystalline films of LC PBI, **4a** exhibited cyclic voltammograms that provided clear indications of favorable interactions among the PBI molecules, suggesting their potential attractiveness. According to these interactions and spectroelectrochemical observations, the film undergoes two distinct structural rearrangements in order to accommodate the reduction to both the anionic and dianionic states. To determine the film's redox conductivity relative to electrochemical potential, interdigitated array electrodes were employed. Interestingly, the conductivity reached a semiconducting level prior to the emergence of the first discernible reduction wave. Remarkably, upon reducing the film by 1 equivalent of electrons, it exhibited a maximum conductivity of 0.044 S/cm, which contradicted the anticipated behavior of this state as a Mott insulator.[18]

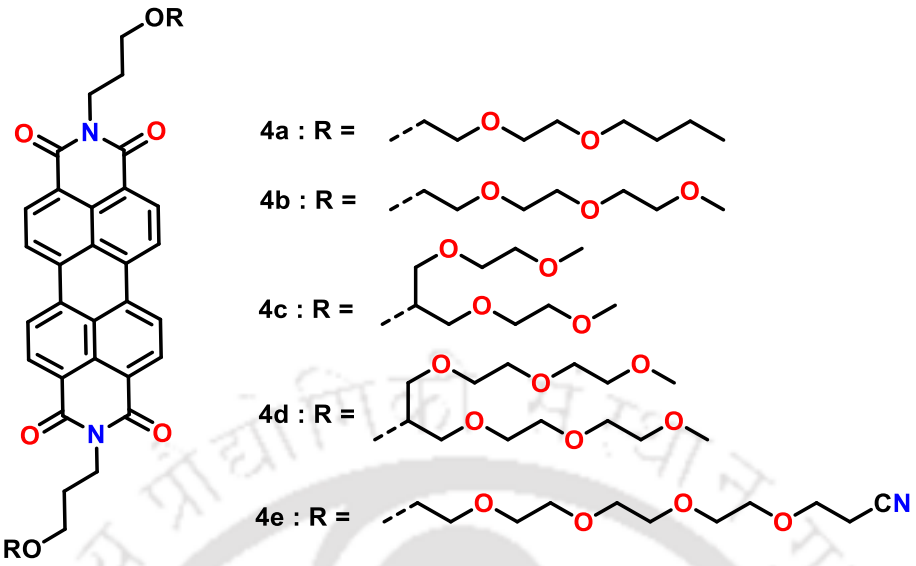

Figure 1.6. Structures of PBIs with oligoethoxy chains.

The thin film states of three distinct LC PBIs, namely **4a**,[16] **4d**[15-16], and **4e** were scrutinized for their physical and optical characteristics..[19] To produce these films, a range of techniques were employed, including Langmuir-Blodgett (LB) processes, thermal evaporation under vacuum, and spin coating. Glass slides, glass slides coated with highly oriented pyrolytic graphite (HOPG), and indium tin oxide (ITO) were among the substrates utilized for film deposition. XRD studies, fluorescence spectroscopy, UV-Vis, and POM, were conducted to characterize all the films. As shown in Figure 1.6, it was interestingly observed that modifications in the preparation methods/conditions or the use of different substrates have a substantial impact the characteristics of the produced thin films. Unlike many other materials that form thin films, these LC PBIs exhibit a remarkable self-organizing ability, facilitating their rapid attainment of a stable, low-energy configuration. This unique characteristic indicates their intrinsic inclination to self-assemble and align themselves in a remarkably precise manner. It's interesting to note that neither the substrate nor the deposition technique affects this ordering phenomena. The molecules exhibit a preference for adopting a J-type arrangement, employing attractive π-π interactions, where the axis of π-π stacking aligns parallel to the substrate. In the thin film state, the LC PBI (**4a**) molecules, specifically the perylene cores, exhibit an orientation relative to the substrate. Along the stacking axis, the molecules tilt at an approximate angle of 47 degrees, while perpendicular to this direction, they tilt at around 58 degrees. Similar structures were observed in the two other LC PBIs, namely 4d and 4e. To elucidate this pronounced preferred orientation, an investigation was proposed to

analyze the intermolecular steric and electronic interactions, as well as the interactions between the substrates and the molecules. For comparison, thin films of compound **4a** were also prepared using vacuum deposition, leading to the formation of highly ordered films, which can be attributed to the liquid crystalline properties of LC PBI **4a**.[18]

Swallowtail substituted symmetrical PBIs (**5a** and **5b**) with oligoethoxy chains made up of two and three ethyleneoxy units, respectively, were presented by Thelakkat and coworkers. These served to stabilize the Col_h phase. Compounds **5a** and **5b** showed a substantially wider enantiotropic thermal behavior than the symmetrical dialkyl swallowtail PBIs (**2d** [12] and **2e**, as illustrated in Figure 1.4). Furthermore, the oligo-ethylene glycol chain lengths had an impact on the isotropic temperature of PBIs. As anticipated, a comparatively lower clearing point was observed for PBI **5b,** owing to its lengthier oligoethoxy chains (consisting of three ethyleneoxy units in each branch). However, as seen in Figure 1.7, the enthalpy change related to the Col_h phase to isotropic transition remained essentially constant.[13]

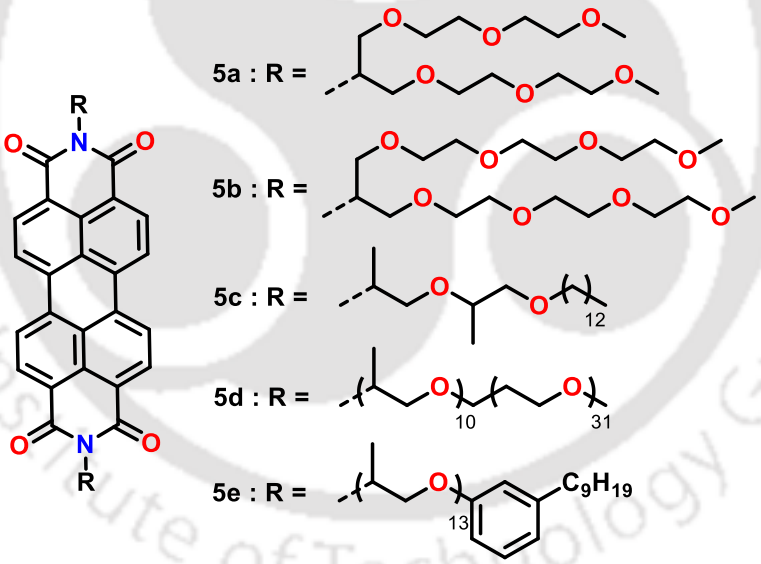

Figure 1.7. Structures of symmetrical PBIs with oligoethoxy chains.

Thermotropic PBIs (**5c**, **5d**, and **5e**) at room temperature (RT) that showed a variety of mesophases were the subject of a study by Bijak *et al.*[20] PBIs **5d** and **5e** showed a high relative photoluminescence quantum yield and numerous ethylene-oxy repeating units. With the exception of PBI **5c**, these PBIs' cyclic voltammogram examination identified one irreversible oxidation and two reversible reductions peak. Additionally, the electrochemical band gap of these compounds,

which ranged from 1.46 to 2.11 eV, was low. These PBIs are attractive materials for optoelectronic applications due to their narrow band gap, strong fluorescence, single RT mesophase structure, and superior processability. RT mesophases were generally stabilized and overall mesomorphic behavior was enhanced by the inclusion of oligoethoxy chains. However, a disadvantage of glycolic ether chains is their propensity to chelate with different cations, which could result in the PBIs becoming contaminated with ionic contaminants and complicate their use in electrical devices. (Figure 1.7).

1.3.1.3. Liquid crystalline perylene bisimides with silyloxy chains

Instead of using alkyl chains, PBIs incorporating oligosiloxy chains at the terminus were synthesized, as depicted in Figures 1.11 and 1.12. When symmetric PBIs with silyloxy chains were compared for their thermal behavior, it revealed that PBI **6a**, which contained two terminal chains, displayed a crystalline structure with a lamellar arrangement.[21] Similarly, the PBI with two cyclic silyloxy derivatives (**6f**) also displayed crystallinity. These results imply that the oligosilyloxy chains alone do not contribute enough thermal mobility to bring about a mesophase and reduce the transitioning temperatures. In contrast, symmetrical swallowtail-type PBIs (**6b-6e**) featuring silyloxy chains demonstrated a room temperature stabilized LC phases.[22] These LC phases offer greater flexibility and nanosegregation compared to alkyl chained swallow tailed PBIs (**2b-2e**), but remained as crystalline. The significantly broad ranges of mesophases displayed by PBIs incorporating oligosiloxane chains present an excellent opportunity to investigate their electron transport mechanisms.

In the LC phase, PBI **6b** demonstrated an exceptional electron mobility exceeding upto 10^{-3} $cm^2/V.s$. Additionally, a transition from Col_r - Col_h phase was also displayed by this compound, indicating a change in the orientation of the molecules.[23] As we moved from compound **6b** to **6c** and **6d**, the trimethylsilyl unit decreased while the length of the chains increased thanks to the hydrocarbon spacer, increasing the clearing point. Conversely, in the case of PBI **6b**, a drastic decrease in the clearing point to approximately 50 ^oC was observed as the length increased by adding a trimethylsilyloxy subunit. Regarding the swallowtail-type cyclotetrasiloxane derivatives, PBI **6f** and **6g** exhibited a crystalline nature, while a liquid crystalline behavior was noted for compounds **6h** and **6i** with an extended chain length. This difference may be attributed to the lessened constraint on the movement of cyclotetrasiloxane subunits at the chain endpoints.

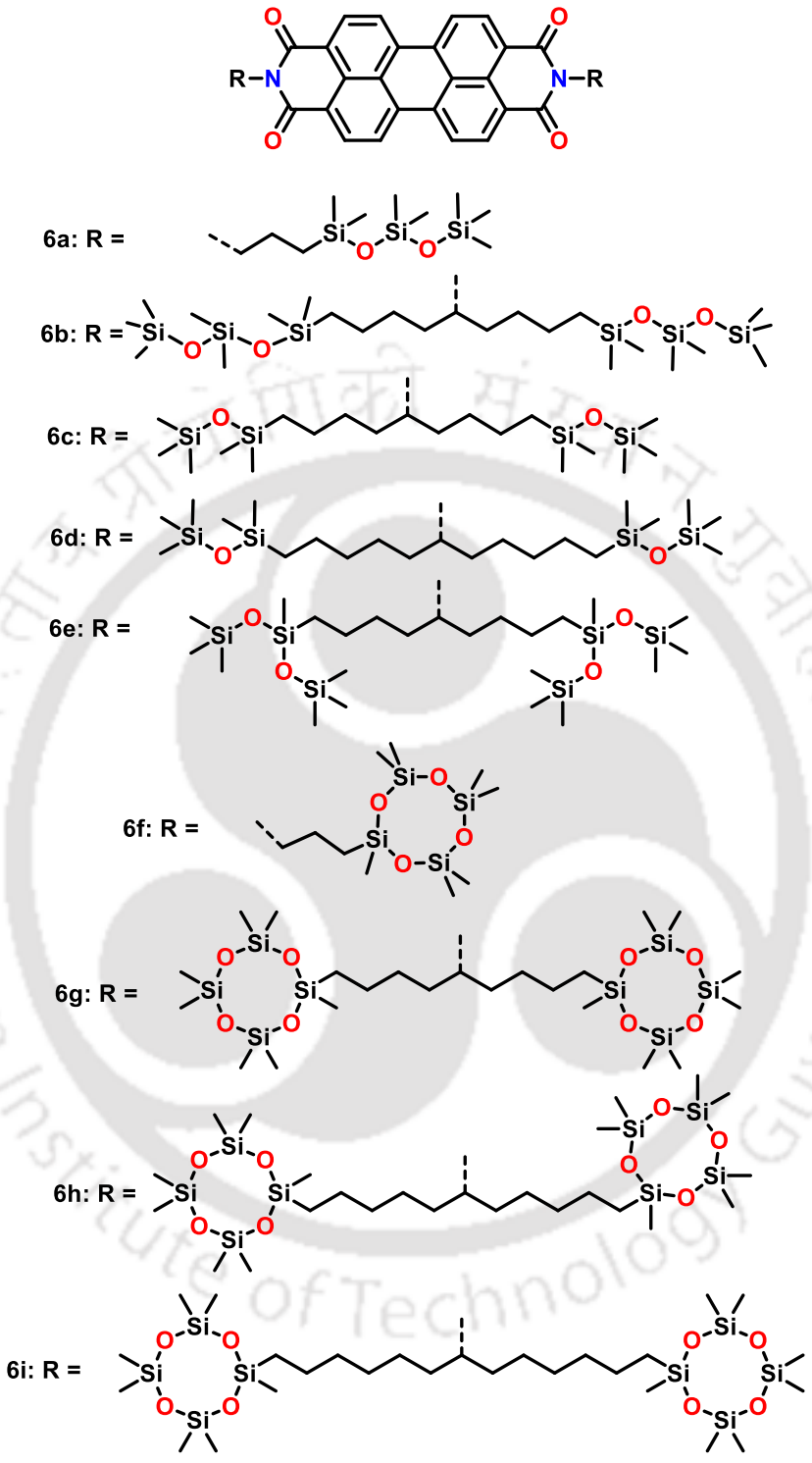

Figure 1.8. Structures of the symmetrical PBIs with silyloxy chains **6a-i**.

Compound **6h,** specifically, demonstrated a Col_r phase along with an impressive n-type mobility of 0.001 $cm^2/V.s$ at room temperature.[24] The prominent nanosegregation among the stiff

aromatic cores and the cyclotetrasiloxane rings serves as the primary stabilizing force for this columnar self-assembled phase. Additionally, the polymerization of the cyclotetrasiloxane segment opens up fascinating prospects for the realm of organic electronics.

1.3.1.4. Liquid crystalline perylene bisimides with aryl groups

As shown in Figure 1.9, Würthner *et al.* presented their findings on PBI **7b**, which is synthesized by condensation of perylene bis anhydride with 3,4,5-tridodecyloxy aniline. With an excellent thermal stability, this compound demonstrated a broad range of stability in the Col_h phase spanning RT to 373 ^oC.[25] Additionally, another PBI variant containing trialkyl phenyl groups (7a) displayed an extensive range of the Col_h phase, howbeit with a reduced clearing temperature that was reduced by approximately 70 ^oC.[26] Additionally, PBI **7c**, featuring chiral chains at periphery, displayed a well structued Col_h phase with helical arrangements of the molecules. Higher levels of order and increased charge-carrier mobility have been brought about by the presence of chiral peripheral chains in the Col phase. Consequently, this leads to an improvement in their conductivity within the Col phase.[27] The introduction of flexible chains instead of aromatic groups, such as carbazolyl and dialkyl fluorenyl groups, did not bring about mesomorphic behavior in the molecules due to their limited capacity for spacefilling.[28] However, a different outcome was observed when the 3,4,5-trialkoxy phenyl group was linked via a flexible -CH_2- linkage, as exemplified in PBI **8a**. In this case, the isotropic temperature decreased whilst preserving the mesomorphic behavior. Disorder in the Col_h phase, similar to that seen in **7a** and **7b**, was also observed. In the LC state, the measured conductivity, determined through steady-state space-charge limited current, yielded a value of 0.2 $cm^2/V.s$, while compound **8a** exhibited a higher mobility of 1.3 $cm^2/V.s$.[29] This surpasses the mobility value of amorphous silicon. In order to boost the mobility in these materials, it is possible to employ suitable alignment techniques and select electrodes with appropriate work functions to enhance charge injection.

In an investigation on dendronized PBIs, Percec and colleagues attached the 3,4,5-tridodecyloxyphenyl units to perylene dianhydrides, using spacers of varying lengths (shown in Figure 1.13).[30] In contrast to compound **7b,** these PBIs **8a-d** demonstrated the Col_h phase with a reduced clearing point. As the spacer length increased, the clearing points decreased. Compounds **8a** and **8b** demonstrated liquid crystalline nature at RT, while a crystalline characteristic was observed for compounds **8c** and **8d** at RT. These findings suggest that the PBI **7a** (without any

spacer), and compound **8b-8d** containing di, tri, and tetramethylene spacers underwent self-assembly into intricate helical columns produced from tetramers of PBI. Conversely, the self-assembly of dendronized PBI **8a,** with a single methylene spacer, led to the creation of helical columns comprising PBI dimers. At elevated temperatures, the helical columns formed by dendronized PBIs undergo self-organization to establish thermodynamically stable two-dimensional (2D) Col_h lattices, characterized by intracolumnar order. This self-assembly process occurs rapidly. Conversely, at lower temperatures, dendronized PBIs exhibit self-organization into thermodynamically stable three-dimensional (3D) columnar structures. For compounds **7a**, **8b-8d**, the self-organization results in a 3D columnar simple orthorhombic lattice, while compound **7b** forms a 3D columnar monoclinic lattice. The transition from the kinetic two-dimensional product to the closely related thermodynamically stable 3D lattices occurs through a remarkably slow self-assembly process. These studies provide evidence for the self-assembly of intricate helical columns formed by dimers and tetramers of dendronized PBIs. These structures persist in both two-dimensional (2D) and three-dimensional (3D) lattices within the solid state. Within the two-dimensional (2D) Col_h phase characterized by intracolumnar order, the dendronized PBI exhibits remarkable dynamics, enabling it to exit the columns and effectively heal structural defects. This self-healing mechanism is a unique feature of these dendritic structures. The observation of complex helical columnar arrays in both 2D and three-dimensional (3D) periodic arrangements is a pioneering discovery in the field of self-assembling dendritic structures. The racemic nature of these complex helical columns is worth noting. The elucidation of general self-assembly processes within these category of compounds can contribute to our understanding of charge carrier migration mechanisms. Moreover, it has the potential to enhance the design strategies for developing supramolecular electronic materials based on PBIs and other electron-deficient structures. These advancements are of utmost significance in the fabrication of organic solar cells and other organic electronic devices.

In general, previously documented PBIs have been found to primarily stabilize columnar or lamellar assemblies. However, Percec and colleagues demonstrated a remarkable discovery by showing that a suitably functionalized PBI (**8e**) can undergo self-assembly to form supramolecular spheres.[31] This particular PBI, modified at its imide groups with a second-generation dendron, exhibited self-assembly into supramolecular spheres that arranged themselves into a body-centered cubic (BCC) lattice. Upon functionalizing the imide groups of this PBI with a second-generation

dendron, it exhibited self-assembly behavior, forming supramolecular spheres. These spheres further organized themselves into a body-centered cubic (BCC) lattice, a phenomenon that is rarely observed in self-assembling dendrons but commonly seen in block copolymers (Figure 1.13b). Notably, at lower temperatures, these supramolecular spheres underwent assembly into a Col_h array, showcasing a rare transition from the Col_h phase to the cubic phase.

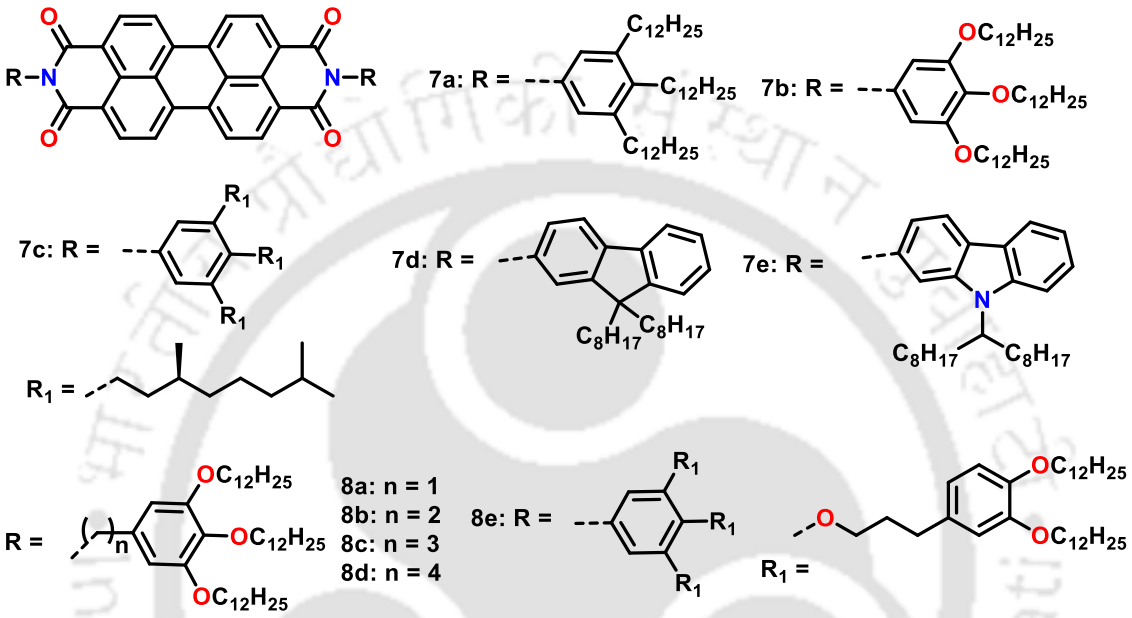

Figure 1.9. Structures of symmetrical **PBIs** with an aryl (**7a-7e**) and dendron substitution (**8a-8e**).

In their research, Asha and associates presented a collection of luminescent liquid crystalline (LC) PBI analogues featuring ester/amide linkages and had end-caps comprising phenyl, monododecyloxy phenyl, or tridodecyloxy phenyl substituents (depicted in Figure 1.10).[32] In polar organic solvents such as toluene, dichloromethane, and tetrahydrofuran (THF), the amide-functionalized collection of PBIs exhibited self-assembly into head-on or H-type aggregates, regardless of their end-capping. Conversely, within the ester series, only the molecule with a monododecyloxy phenyl end-cap displayed a propensity for self-organization into a typical J-type or slip-stacked aggregation, specifically in solvent toluene.

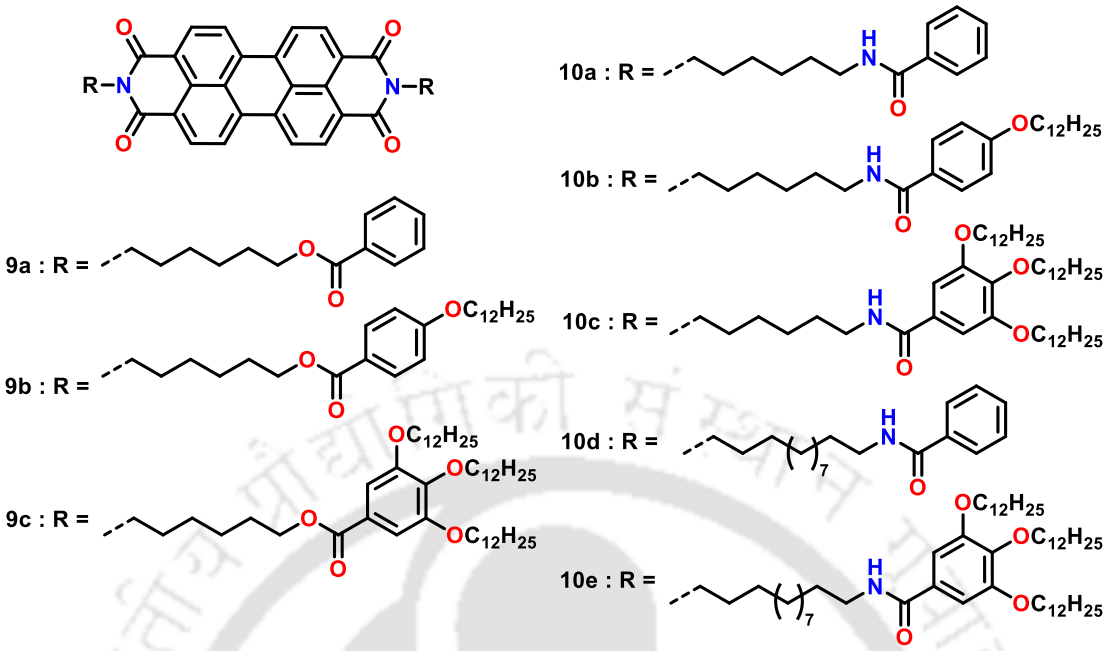

Figure 1.10. Structures of symmetrical **PBIs** with aryl groups connected with a long spacer (**9a-9c, 10a-10e**).

In general, it was seen that the luminescence was diminished when the trialkoxyphenyl group was coupled directly to the perylene moiety to produce PBIs. However, the researchers of the study proposed that joining them with spacers would not only preserve the liquid crystalline behaviour but also sustain photoluminescence in a condensed state. The amide and ester derivatives in this study can be categorized into three groups: (a) those lacking terminal substitutions, (b) those with monododecyloxy terminal substitutions, and (c) those with tridodecyloxy terminal substitutions. Taking the first scenario as an illustration and look at ester **9a** and amide **10a**. In the case of amide **10a**, both the melting and clearing points were observed to decrease compared to ester **9a**.

In contrast to **10a**, the isotropic point was reduced and the melting point was rose when the spacer length was increased from 6 to 12. This effect was shown in the amide **10d**. Contrarily, compound **10d**'s mesophase was solidified throughout the cooling cycle, forming a glassy state. The melting and clearing points of the tridodecyloxy analogue **9c** were lowered and it showed a room-temperature liquid crystal phase after the insertion of more flexible chains to the benzene end cap of the esters (**9b** and **9c**). This trend was not observed in the corresponding amide derivatives. Compound **10b** displayed higher melting and clearing points, whereas the

tridodecyloxy analogue **10c** demonstrated reduced temperatures for both. Nevertheless, increasing the spacer length to 12 (**10e**) resulted in higher melting and clearing points compared to **10c**, but lower than those of **10d**.

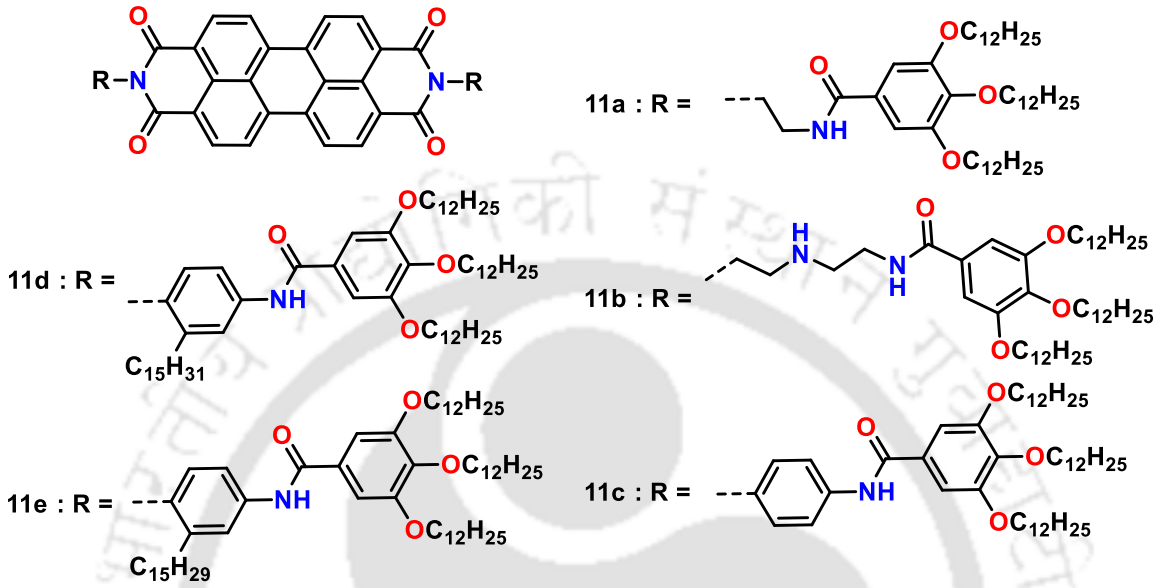

Figure 1.11. Structures and Graphical representation of the thermal behavior of symmetrical **PBIs** with aryl groups connected with different linking groups (**11a-e**).

Symmetrical PBIs, as described by Yang and colleagues, feature 3,4,5-tridodecyloxy benzoyl moieties linked by various spacers that contain amines at their ends (Figure 1.11). The symmetrical PBIs **11a** and **11b** showcased a RT columnar phase, characterized by soft-alkylene spacers containing amine units. Conversely, compound **11c**, featuring a rigid aromatic spacer, displayed a crystalline nature.[33] In a separate investigation conducted by Asha *et al.*, PBIs **11d** and **11e** were reported, wherein the connection between the 3,4,5-tridodecyloxy benzoyl moieties involved either cardanol or pentadecyl phenol (PDP).[34] Notably, PBI **11d**, distinguished by its saturated side chain, exhibited a heightened level of crystalline order. Compound **11d** demonstrated a plastic Col_h phase at low temperatures and a Col_h phase at high temperatures. On the other hand, compound **11e**, featuring an unsaturated side chain, displayed a Col_h phase that extended across a wide temperature range. It's interesting to note that these PBIs' capacity to form H-type aggregates was unaffected by the inclusion of the lengthy pentadecyl chain in the *ortho*-position to the imide bond. Notably, the aggregate type was unaffected but the aggregate length was drastically reduced when an alkyl chain bend was introduced via a cis-double bond.

1.3.2. Heteroatom *bay*-annulated perylene bisimides

Following Cornier's findings on LC PBIs,[16,17] numerous investigations on liquid crystals synthesized from aliphatic or aromatic amines that are based on perylene bisimides, were conducted. Various research groups have performed extensive studies to modify the physical properties of perylene derivatives. One such advantageous strategy for changing the photophysical properties of perylene derivatives is *bay*-substitution. However, due to the resulting twist, this substitution can have an adverse effect on molecular planarity. Consequently, the interaction between molecules becomes weaker, disrupting their self-assembly.[35] This disruption is undesirable because it affects the formation of organized structures. To overcome this challenge, significant research has been performed to maintain molecular planarity while modifying the physical properties of perylene derivatives. This was accomplished by expanding the aromatic moiety of perylene compounds either along the *bay*-region or in the long axis.[14] The aforementioned modifications were well-documented to induce a hypsochromic or a bathochromic shift in the absorption spectrum of the transformed compound.[14] In simpler terms, these alterations lead to a shift towards longer or shorter wavelengths in the absorbed light by the transformed compounds.

Incorporating heteroatom annulation into the aromatic moiety is an additional approach for modifying properties while preserving molecular planarity. Recently, the inclusion of chalcogen atoms has garnered significant attention in organic semiconductors.[36] Among chalcogen atoms, sulfur, and selenium have been extensively studied in organic semiconductors, while tellurium has received little attention. The stabilization of molecular self-assembly and the consequent enhancement of one-dimensional conductivity are notably facilitated by intermolecular interactions involving chalcogen atoms, specifically S···S and Se···Se interactions.[37,38,39] Additional findings have been made addressing the incorporation of nitrogen, a heteroatom, through annulation into the bay area of perylene analogues.[40] This also results in changed aromatic systems with enticing properties. Moreover, the inclusion of nitrogen into the molecular structure fosters enhanced hydrogen bonding with nearby molecules, potentially aiding in the process of self-assembly. Moreover, the alkyl substitution of nitrogen in the bay position through N-annulation offers the possibility to boost solubility and reduce the transition temperature.[41]

Noteworthy research conducted by Wang *et al.* has presented perylene derivatives annulated with nitrogen, sulfur, and selenium, demonstrating fascinating properties.[40] Sun and coworkers made an observation that the inclusion of sulfur into perylene (**12a**) results in remarkable solid-state packing owing to strong S···S interactions.[37] This unique packing arrangement was employed to fabricate field-effect transistors from single crystals derived from these compounds, exhibiting a high conductivity value of 0.8 cm^2/V.s. Tan *et al.* noticed the highest mobility value of 2.66 cm^2/V.s by *Se*-annulated perylene (**12b**).[38] The presence of shorter Se...Se contacts (3.49 Å) undoubtedly indicates that they are favorable for efficient carrier transport, thereby enhancing mobility. In a similar way, Jiang and colleagues demonstrated the fabrication of crystalline nanoribbon transistors using bis-*S*-annulated perylene (**13**), that displayed an improved conductivity value of 2.13 cm^2/V.s.[39] The inclusion of two sulfur atoms into the molecular structure of perylene achieved highly structured packing once again, primarily attributed to the presence of strong S···S interactions.

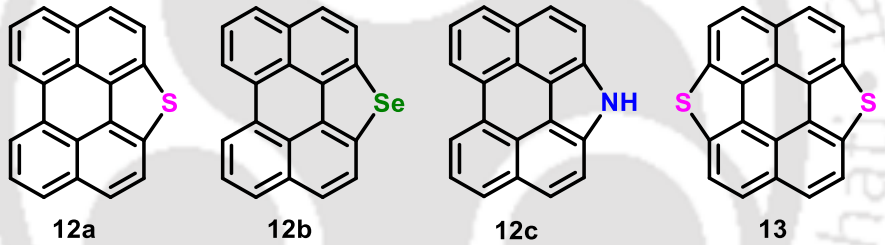

Figure 1.12. Structures of heteroatom annulated PBIs.

A perylene tetra ester compound with annulation of sulfur in both bay regions was reported by Mullen and colleagues. However, the liquid crystal behavior and photophysical characteristics of these compounds were not described in their communication.[42] Our prospect was that the inclusion of strong S···S interactions between the *S*-annulated perylenes, along with the incorporation of shape anisotropy, will enhance liquid crystal self-assembly. Our group also showed interest in the inclusion of chalcogens such as selenium and sulfur into the aromatic moieties to customize the self-assembly and electronic behavior. *S*-, *Se*- and *N*-annulated perylene tetra esters (**14a–e**, **15a–e**, **16a–e**) (Fig. 1.13) stabilizing liquid crystallinity have been reported.[43-46] All the bay-annulated perylene tetra esters (PTEs) with linear aliphatic chains (**14a–d**) were observed to form a well-organized Col_h phase with excellent homeotropic alignment except for **16d**. Their mesophase range gradually decreased as the alkyl chain length increased. At higher

temperatures, these compounds exhibited liquid crystalline behavior while at lower temperatures they were found to display non-liquid crystalline properties. However, the introduction of branched chains transformed these PTEs (**14e**, **15e**, **16e**) into room-temperature liquid crystalline materials.[46] In solution, *N*- and *S*-annulated PTEs emitted greenish and sky-blue emission, whereas spin-coated thin films emitted yellowish-orange and greenish yellow emission respectively. Consequently, PTE **14e** and **15e** were utilized as emitter layers in a host-guest OLED device, resulting in a greenish emission.[46] On the other hand, Se-annulated PTEs exhibited a weak green emission in solution and thin film states owing to the quenching effect caused by the heavy atom, selenium.[45]

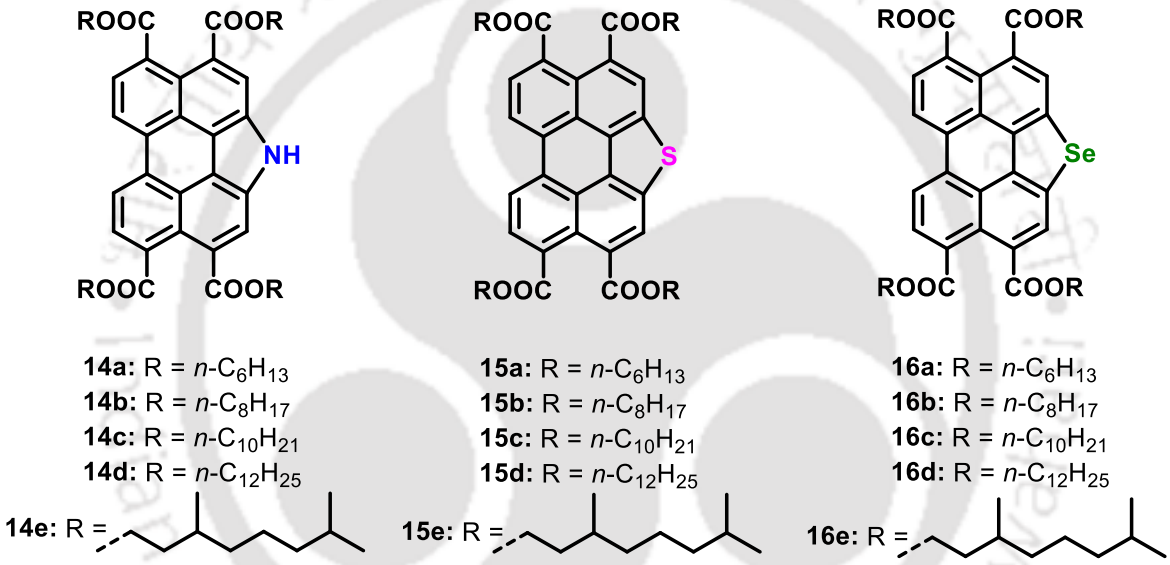

Figure 1.13. Structures of heteroatom annulated perylene tetra esters (PTEs).

In a recent study conducted by G. C. Welch *et al.*, they introduced an *N*-annulated perylene tetra butyl ester (**17**) as a potential material for alcohol-processed semiconducting films. When this compound (**17**) was utilized as the active material layer in an OFET device, fabricated by depositing it from a solution with 1-butanol as the solvent, it exhibited a p-type mobility of 0.39 × 10^{-4} $cm^2/V.s$.[47]

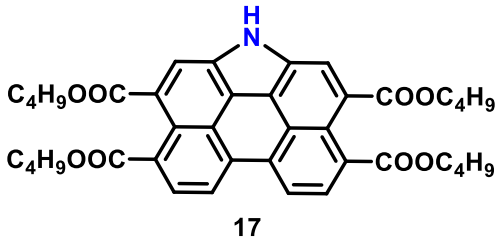

Figure 1.14. Structures of *N*-annulated PTE.

Another set of unsymmetrical perylene diester monoimides (PEIs) with S-, Se-, and *N*-annulation in the bay region (**18**, **19**, **20**) has also been reported by our research group (Fig. 1.15). Unfortunately, due to their unsymmetrical chemical structure, these molecules were found to be non-liquid crystalline. These PEIs, however, emitted white light when doped in polyvinyl carbazole and used as an emitter layer in a host-guest OLED system.[48,49]

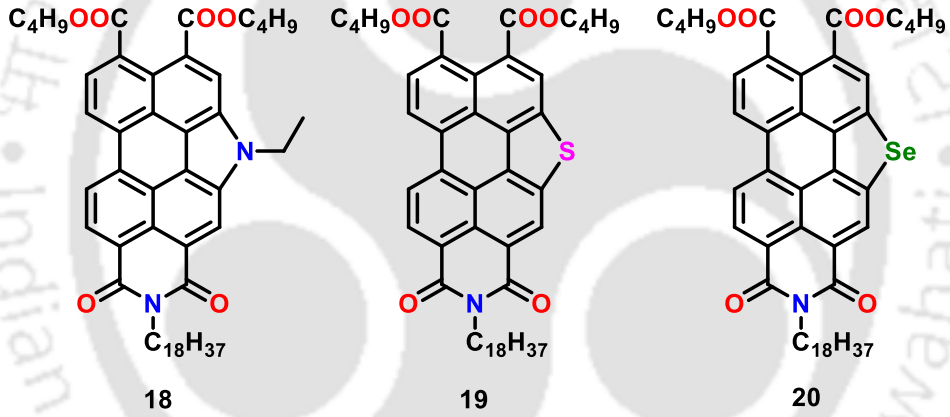

Figure 1.15. Structures of heteroatom annulated perylene ester imides (PEIs).

A variety of perylene bisimides (PBIs) (**21a**, **22a**, **23a**) with heteroatoms including S, Se, and N incorporated into the *bay* region were reported (Fig. 1.16).[50] At the imide position, these PBIs were functionalized with a 3,4,5-tri-dodecyloxy benzyl group. *N*- and *S*-annulated PBIs (**21a**, **22a**) displayed an ordered Col_h phase, whereas the *Se*-annulated PBI (**23a**) demonstrated both a high-temperature Col_h phase and a low-temperature Col_{ob} phase. These compounds displayed decreased melting and clearing temperatures, as well as enhanced solubility when compared to conventional PBI. The absorption spectrum of the *N*-annulated PBI was slightly redshifted, whereas the *S*- and *Se*-annulated PBIs showed a blue-shifted absorption spectra. In addition, *bay*-annulation resulted in a broadened band gap for the *S*- and *Se*-annulated PBIs.

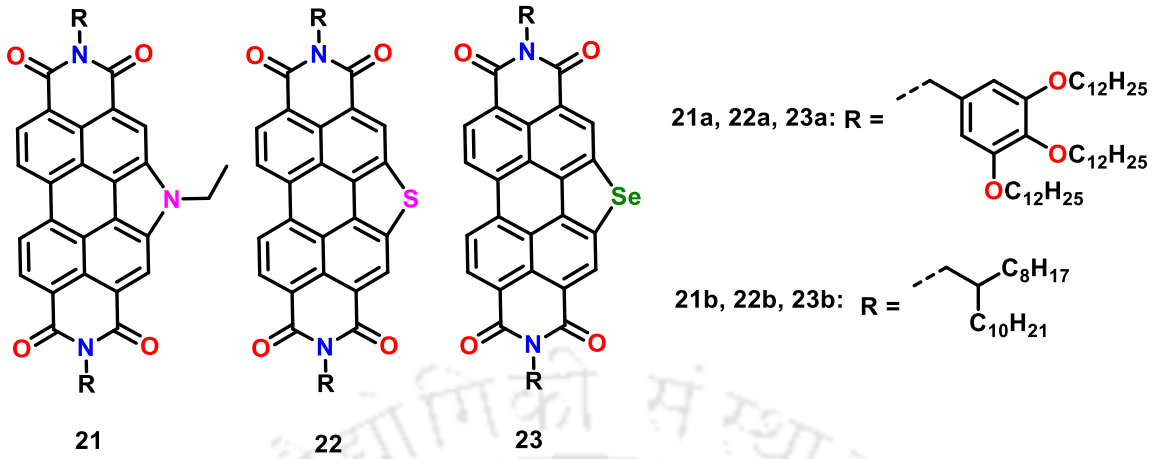

Figure 1.16. Structures of heteroatom annulated perylene bisimides (PBIs) with trialkoxy benzyl moiety and branched alkyl chains.

A separate set of bay-annulated PBIs (**21b**, **22b**, **23b**), with branched aliphatic 2-octyl-dodecyl chains at the imide positions, was also documented by our research group (Fig. 1.16).[51] This modification significantly improved their solubility, and all of the PBIs, with the exception of *Se*-annulated PBI (**23b**), displayed vibrant emission in both solutions and thin films. Despite not possessing liquid crystalline properties, the thin film XRD analysis revealed a lamellar arrangement in the film state. Consequently, these PBIs demonstrated excellent mobility values in OFET devices. Among them, the *S*-annulated derivative (**22b**) showcased the highest n-type mobility value of 0.0044 $cm^2/V.s$, while the *N*- and *Se*-annulated derivatives exhibited values of 0.0038 $cm^2/V.s$ and 0.0022 $cm^2/V.s$, respectively.

In a study conducted by Z. Wei *et al.*, an intriguing helicity inversion phenomenon was observed when chalcogen atoms (*S* and *Se*) were introduced into a perylene bisimide compound (**24**, **25**) that featured a chiral chain at the imide position. They postulated that chalcogen atoms play vital roles in modifying the helical aggregations of these perylene derivatives through their interactions governed by van der Waals forces. Furthermore, these chalcogenide-mediated supramolecular interactions were successfully translated into nanostructures, ultimately influencing the gas response properties of the devices.[52]

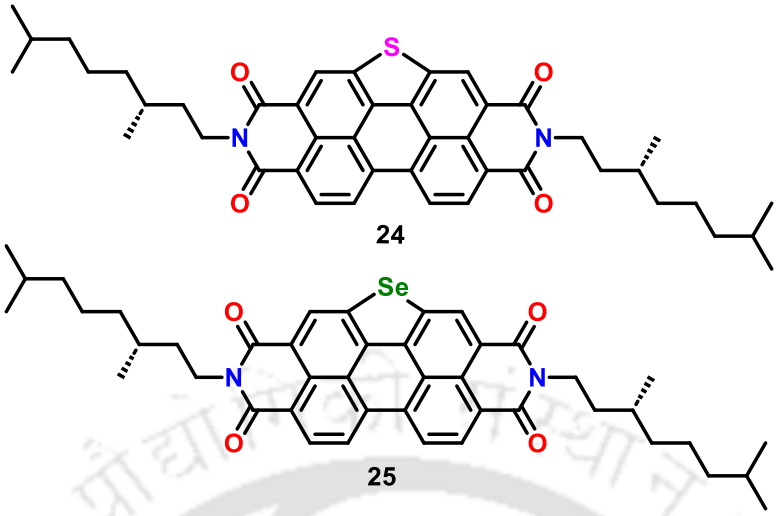

Figure 1.17. Structures of heteroatom annulated perylene bisimides (PBIs) with chiral alkyl chains.

J. Hua and coworkers successfully synthesized perylene bisimide (PBI) compounds with varying substituents (N, S, Se) at the bay position (**26**, **27**, **28**). Then, for the objective of photocatalytic H_2O_2 evolution, these PBIs were used to build heterojunctions with g-C_3N_4. When measured under visible light, the *Se*-PDI/g-C_3N_4 heterojunction produced H_2O_2 at the highest rate of all the PBIs, at 224.27 Mh^{-1}. This number exceeds the value of plain g-C_3N_4 by 10.1 times. The addition of substituents at the *bay*-region, that amplifies the differential in electron distribution between the several layers inside the heterojunction, is credited with the improved performance. Consequently, this disparity promotes the enhancement of the interfacial electric field, leading to the observed enhancement in H_2O_2 evolution.[53]

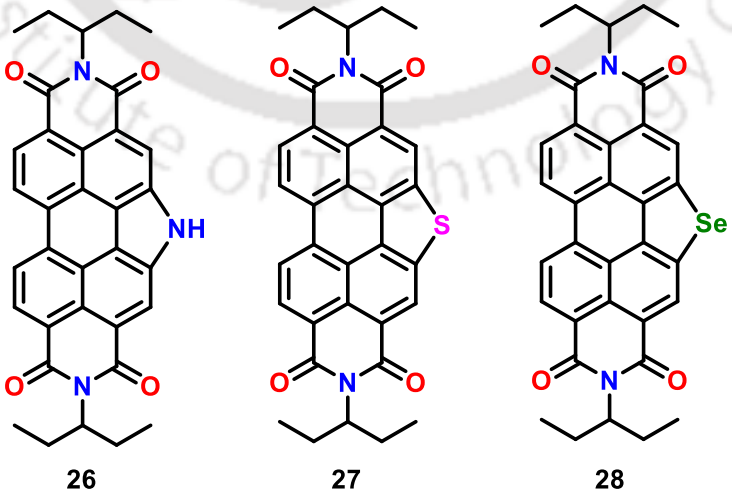

Figure 1.18. Structures of heteroatom annulated perylene bisimides (PBIs) for photocatalytic H_2O_2 evolution.

G. C. Welch and colleagues published a study on their findings on an *N*-annulated PBI (**29**) that was utilized as a non-fullerene acceptor in bulk heterojunction solar cells, yielding a PCE of 2.29%. In subsequent studies, they further explored the photophysical characteristics, self-assembly, and solubility features of several *N*-annulated PBIs. This was accomplished by attaching different functional groups such as amino, pyridine, iminopyridine, quaternary methyl ammonium, urea, and hexadecyl substituents to the pyrrolic *N*-position of the *N*-annulated PBI.[55] Additionally, they further explored the investigation of several dimers derived from *N*-annulated PDI, which were applied in OPVs and OLEDs.[56-59]

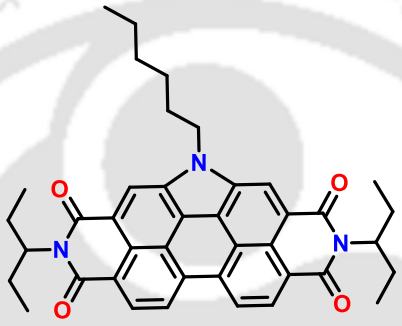

29

Figure 1.19. Structure of *N*-annulated perylene bisimide (PBI) utilized in solar cells.

Initially, Zhu *et al.* conducted the synthesis of a symmetrical bis-*S*-annulated PBI compound derived from tetrachloro-PBI (**30a**). This was accomplished via a one-step palladium-catalyzed reaction, incorporating a 2,6-diisopropyl phenyl group at the imide position. This molecule was annulated with two five-membered sulfur heterocycles at the bay region. The reaction employed $Bu_3SnSSnBu_3$ as the sulfur source, with $Pd(PPh_3)_4$ serving as the catalyst and toluene as the solvent.[60] Subsequently, Jiang *et al*. reported a similar bis-*S*-annulated PBI molecule (**30b**), featured with two polyhedral oligosilsesquioxane (POSS) nanoparticles at the imide position. The presence of hefty substituents in these molecules facilitated a distinct dimer packing arrangement. As a result, compound **30b** exhibited improved fluorescence properties in both solid and solution the state in juxtaposition to the reference compound, bis-*S*-annulated PBI, which lacked a pendant POSS cage.[61] using the aforementioned methodology, Zheng *et al*. synthesized a comparable bis-*S*-annulated PBI molecule (**30c**) featuring with two branched aliphatic chains at the imide position. They further substituted aryl groups at the *ortho*- position and utilized the modified compound in a solar cell.[62] Additionally, X. K. Ren *et al.* reported on a bis-*Se*-annulated

PBI derivative (**31**), equipped with POSS nanoparticles. Surprisingly, despite the discrete molecular packing observed in both solution and the crystalline state, its fluorescence was significantly quenched.[63]

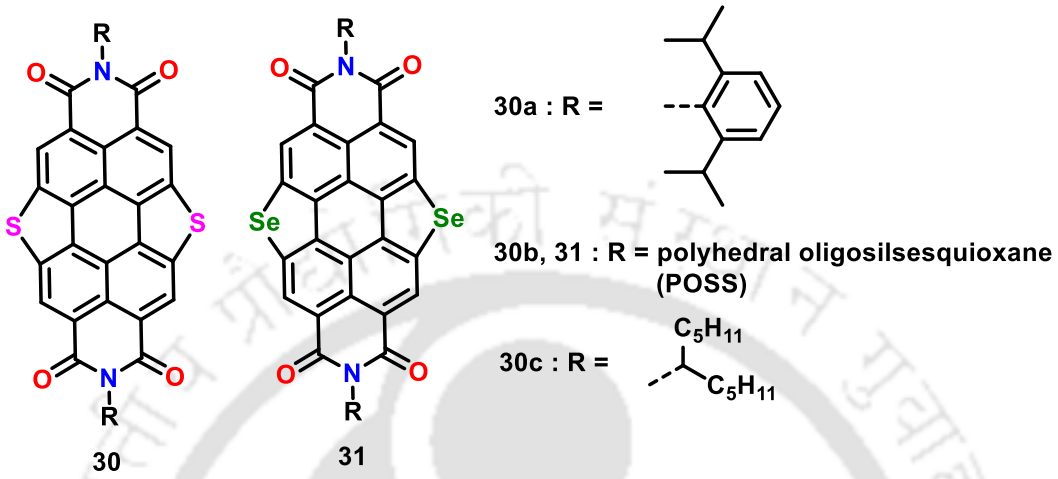

Figure 1.20. Structures of bis-chalcogen annulated perylene bisimides (PBIs).

Compound **32a**, an unsymmetrically core-enlarged PBI moiety, S-PBI-2S (**32a**), annulated with six- and five-membered sulphur heterocycles, was reported by Xiao and coworkers. Herein, the synthesis of compound **32a** was accomplished with an impressive yield by utilizing DMF and elemental sulfur (S_8), starting from the 1,7-dinitro-substituted PBI. Notably, this molecule exhibited a significant bathochromic shift in its absorbance up to 700 nm and possessed a low-lying LUMO level at -3.99 eV. Furthermore, it demonstrated a high n-type mobility of 4.8×10^{-3} $cm^2/V.s$ in a solution processed OFET device.[64]

Tang *et al.* presented a series of three newly synthesized perylene bisimides (PBI) that incorporated [1,2] dithiine and sulfur annulation onto the PBI core (**32b-d**), each having distinct branched alkyl chains. The compounds were prepared by conducting a sulfur-induced nucleophilic substitution reaction in NMP solvent, starting from the 1,6-/1,7-dinitro-substituted PBI. The incorporation of three sulfur atoms had a profound impact on the optical and electronic characteristics of the PBI molecules. They exhibited absorption spectra with a redshift compared to the parent PBI, owing to the presence of stronger electron-donating dithiano units. Interestingly, these molecules displayed a non-fluorescent green color in solution, in contrast to the fluorescent orange color observed for the parent PBI. Moreover, all these compounds demonstrated a narrow band gap of 1.8 eV. When incorporated into organic thin-film transistor (OTFT) devices, these

compounds demonstrated impressive electron mobility value of 0.008 $cm^2/V.s$ under ambient atmospheric conditions.[65]

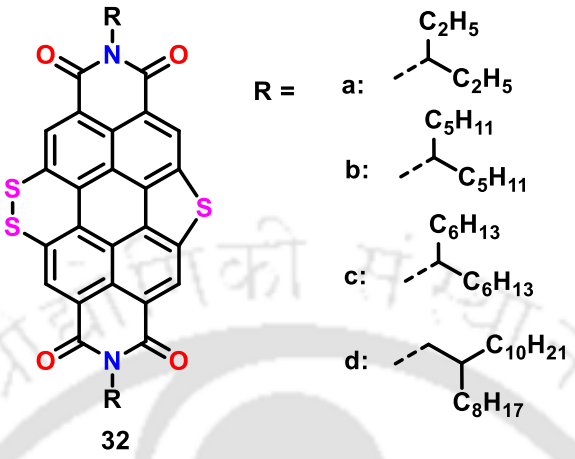

Figure 1.21. Structures of trisulphur annulated perylene bisimides (PBIs).

Gregg *et al.* documented the synthesis of a bis-dithiano perylene bisimide (**24**). In this study, they converted the 1,6-/1,7-dibromo-substituted PBI by utilizing an excess of potassium thioacetate in chloroform-methanol solvent. This transformation resulted in the formation of 1,6,7,12-tetrasulfur-annulated enlarged perylene ring systems. Compound **24** displayed the highest absorption wavelength at 680nm in solution and at 785 nm in a thin film state.[66]

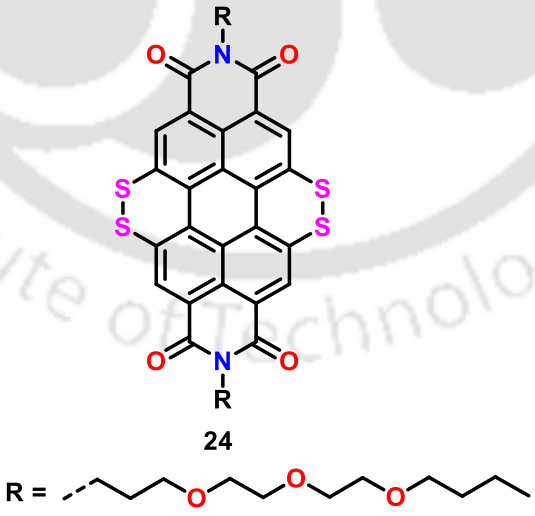

Figure 1.22. Structures of tetra Sulphur annulated Perylene bisimides (PBIs).

Z. Wang *et al.* incorporated a silicon (Si) atom into the bay regions of the PBI resulting in the formation of monosila- (**25**) and disilaperylene bisimides (**26**), which contained one or two

silole rings, respectively. These compounds were synthesized using a palladium-catalyzed Si−C bond formation strategy, starting from 1,6,7,12-tetra chlorinated PBI. These modified compounds exhibited significant bathochromic shifts in their absorption spectra and demonstrated excellent fluorescence quantum yields. Moreover, when utilized in OFET devices, they achieved an impressive n-type mobility of 0.30 cm^2/V.s, indicating their promising performance in electronic applications.[67]

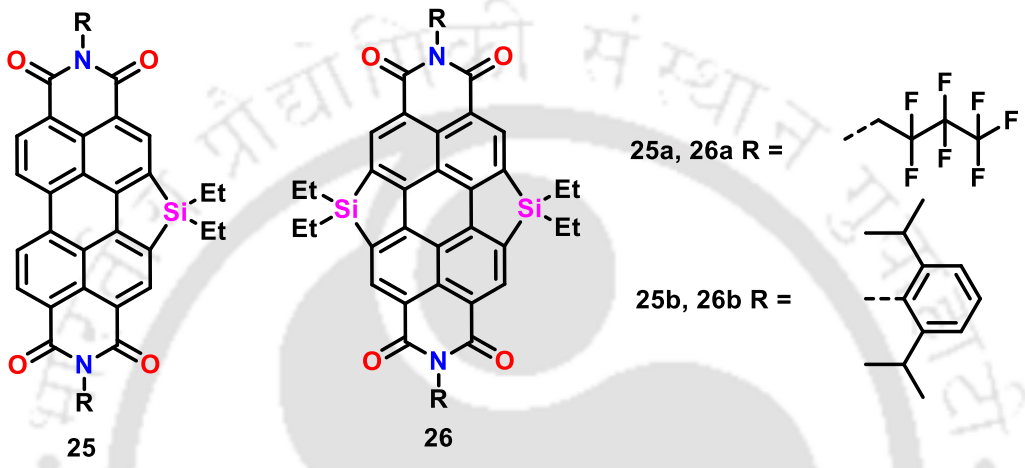

Figure 1.23. Structures of monosila- and disila-annulated perylene bisimides (PBIs).

1.3.3. π-extended Perylene Bis(benzimidazole) derivatives

In order to achieve an extended absorption spectrum spanning the visible to NIR (near-infrared) range along with low band gap and high thermal stabilities, the prospect of widening the π-system of perylene moieties was explored. This investigation led to the consideration of two elegant approaches. The first approach involved expanding the perylene moiety of PBIs to create quaterrylene or terrylene bisimides,[68] and The first approach focoused extending the π-system at the carboxyimide position to produce perylenebis(benzimidazole) analogues. In the subsequent approach, the synthesis of perylene bis(benzimidazoles) was accomplished by subjecting perylene dianhydride and 1,2-diamine to refluxing conditions in high-boiling solvents such as acetic acid, dimethyl naphthalene, imidazole, and quinoline with the aid of a Lewis acid.[69]

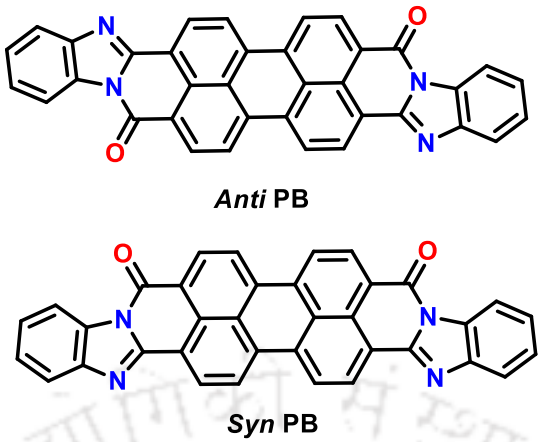

Figure 1.24. Structures of *anti*- and *syn*-Perylene bisbenzimidazole (PB).

With their remarkable photochemical and thermal stability, these perylene bis(benzimidazole)s hold significant promise as a crucial class of organic electronic materials. In 1985, C.W. Tang employed perylene bisbenzimidazoles (PBs) as an n-type substance in the first-ever organic thin film solar cell.[70] The device consisted of a two-layer thin-film structure composed of copper phthalocyanine and a perylene bisbenzimidazole. This breakthrough achieved a notable power conversion efficiency (PCE) of 0.95%. However, it is worth noting that the fabrication process necessitated the vacuum evaporation of the materials, marking a limitation of the approach. Subsequently, Forrest et al. made advancements in the device structure by introducing an exciton-blocking layer across the metal cathode and the photoactive organic layers.[71] Through the vacuum-deposition method, they successfully attained a PCE of 2.4%. This modification proved to be significant in improving the performance of the solar cell. Moreover, PBs were utilized by K. Murata and colleagues as electron acceptors in three-layer solar cells.[72] This implementation resulted in an impressive power conversion efficiency of 3.51%. Additionally, PBs were employed as electron transporters in p-i-n solar cells to expand the absorption spectrum of the active layer system, further enhancing their potential in photovoltaic applications.[73] Furthermore, S. R. Forrest and his colleagues investigated the electron mobility of PBs using the space charge limited current method, revealing a value of 2.4×10^{-6} $cm^2V^{-1}s^{-1}$.[74] This finding highlights the favourable electron transport characteristics of PBs. Expanding on the potential applications, P. Dhagat et al. prepared high-quality monolayers derived from PB and incorporated them into organic thin-film transistors (OTFTs).[75] Remarkably, these PB-based OTFTs exhibited an excellent electron mobility of 0.05 $cm^2V^{-1}s^{-1}$, further emphasizing the suitability of PBs for electronic device technologies.

PBs are characterized as low band gap materials with a notable feature of having a broad absorption band that spans from the UV-Vis to the near IR region. In a study conducted by N. Shimo et al., it was observed that PBs typically exist as a mixture of *anti*- and *syn*- isomers.[76] Upon separation, these isomers crystallize into distinct unit cells, with the *syn*-PB stabilizing in a monoclinic structure, and the *anti*-PB adopting a triclinic structure. This finding sheds light on the structural diversity and polymorphism exhibited by PBs, further contributing to their unique properties and potential applications. The literature clearly indicates that PBs emerged as promising materials even before their counterparts, perylene bisimides (PBIs).[5,77] However, over time, the interest in PBs has diminished, which can be attributed to several challenges. One significant challenge is the difficulty in achieving solution processability of PBs, hindering their practical application. Moreover, the structural modification of PB cores and the separation of isomers pose additional difficulties. When PBs undergo isomerization, two distinct isomers with different electronic properties are formed. Unfortunately, there is currently no efficient method to control the ratio of these isomers during synthesis. Consequently, the material properties of PBs heavily rely on the isomer ratio, making it challenging to achieve reproducibility in their performance. These factors collectively contribute to the reduced interest and limitations associated with PBs in comparison to PBIs.

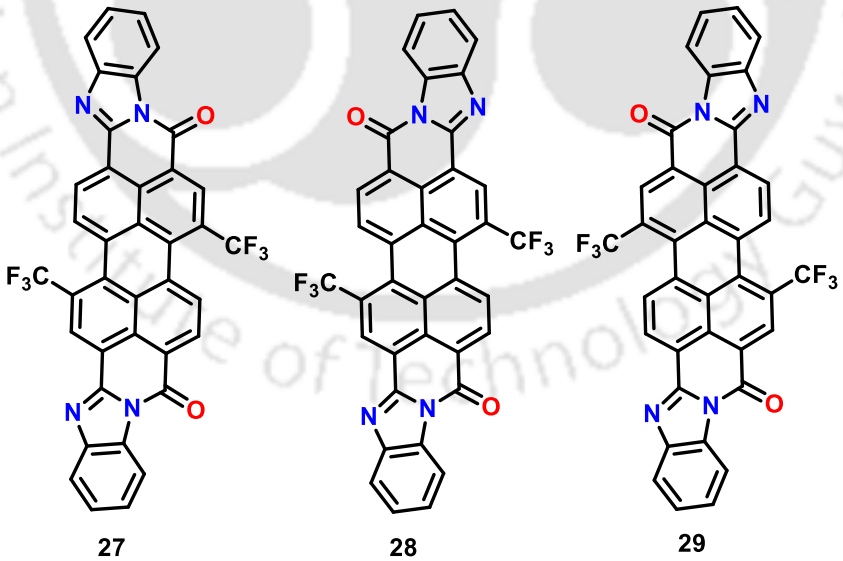

Figure 1.25. Structures of di *bay*-substituted Perylene bisbenzimidazole (PB).

A novel approach was employed by Qian *et al.* to effectively distinguish the isomers of PBs. They carried out trifluoromethylation at the bay-position, resulting in the isolation of three regioisomers

(**27**, **28**, **29**) with quantitative yields (Figure. 1.25). Despite the successful separation of these isomers, which exhibited distinct electronic properties, the process led to a loss of planarity in the aromatic core.[78]

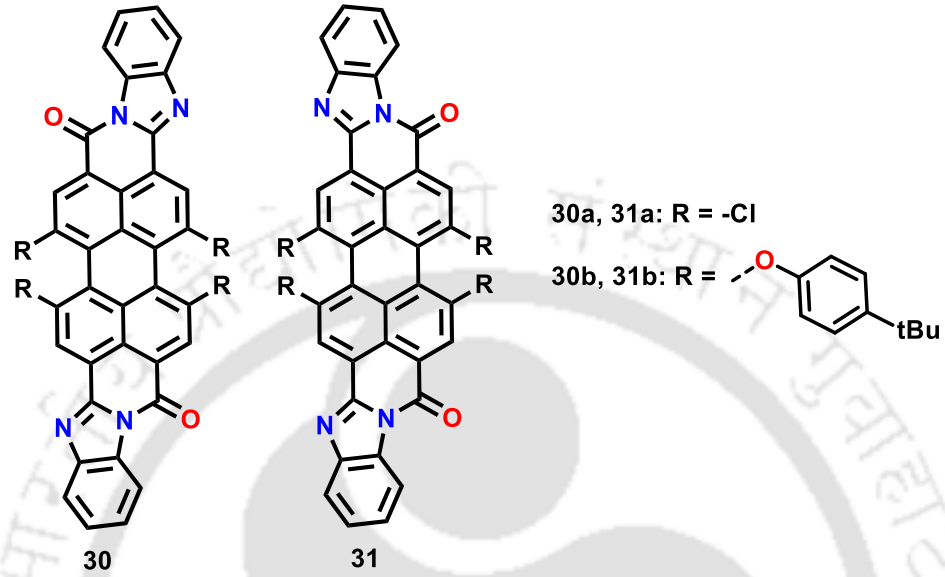

Figure 1.26. Structures of tetra *bay*-substituted Perylene bisbenzimidazoles (PB).

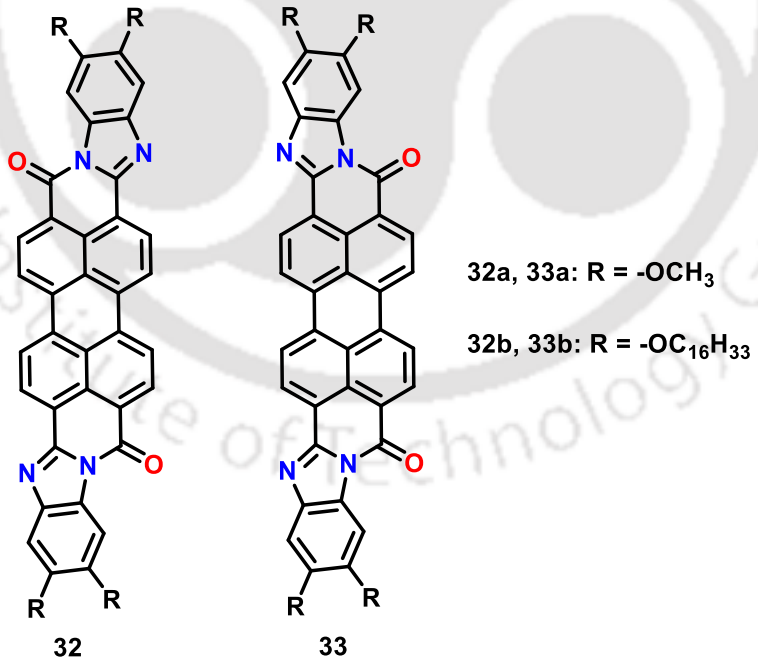

Figure 1.27. Structures of carboximide funtionalized perylene bisbenzimidazoles (PB).

Hudhomme and colleagues noticed that substituting the bay positions by chlorine atoms (**30a**, **31a**) or *tert*-butylphenoxy groups (**30b**, **31b**) did not lead to an enhancement the solubility of PBs in common organic solvents and the isomers were not separable (Figure. 1.26).[79] Then the inclusion of long aliphatic chains on the diamines used for the coupling with PBA (**32b**, **33b**) also did not improve the solubility of PBs in common organic solvents and the isomers remained inseparable (Figure. 1.27).[79]

Thelakkat and co-workers approached this problem by introducing unsymmetrical derivatives of perylene with an imide or diester unit at one end and a benzimidazole unit at the other end of the perylene core (Figure 1.28). These modifications allowed for the preservation of planarity while extending the π-conjugation system and tuning the optical properties of the materials. The derivative featured with an imide unit (**34**) exhibited a Col_{hd} phase (columnar hexagonal disordered phase) at high temperatures, transitioning to a columnar hexagonal plastic phase (Col_{hp}) at lower temperatures. The extended π-conjugation in these derivatives, compared to perylene bisimides (PBIs), led to a significant red-shift in absorption up to 650 nm. This extended absorption was attributed to the benzimidazole units, resulting in a reduced optical bandgap energy owing to the shift in the highest occupied molecular orbital (HOMO) value.[80]

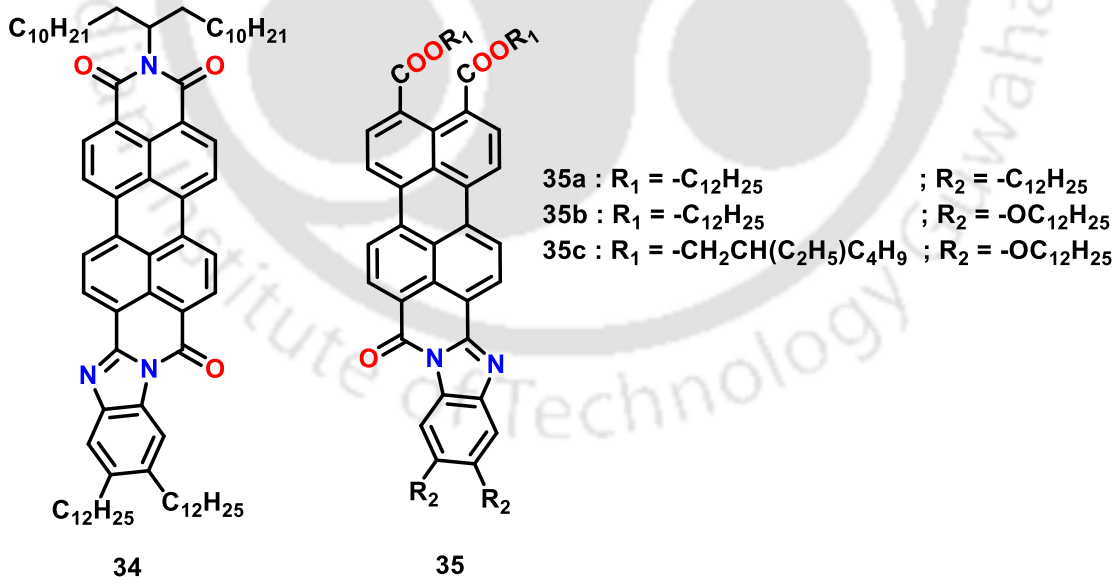

Figure 1.28. Structures of unsymmetrical perylene benzimidazoles (PB).

In a subsequent study, Thelakkat *et al.* replaced the imide unit of the perylene imide benzimidazole derivative with a diester unit while retaining the benzimidazole unit (**35**). Linear

and branched alkyl chains were attached to the ester units, and two alkoxy or alkyl chains were introduced at the benzimidazole moiety to enhance flexibility and solubility (Figure 1.29).[81] The resulting perylene diester benzimidazoles (PEBIs) exhibited extended absorption range, reaching up to 680 nm in the red region of the spectrum. This red-shift in absorption, approximately 130 nm longer compared to perylene bisimides (PBIs), was attributed to the extended π-conjugation facilitated by the presence of benzimidazole moieties.

The shift in absorption wavelength led to a reduction in the optical bandgap energy, primarily owing to the shift in the highest occupied molecular orbital (HOMO) value. All the PEBI dervatives showed self-organization into Col_h phases at higher temperatures, specifically under 250°C. Notably, compound **35b** and **35c** effectively maintained room temperature (RT) Col_h phases. Compound **35a** exhibited lamellar ordering, while compound **35b** displayed a columnar hexagonal plastic phase (Col_{hp}) at RT. These properties make the unsymmetrical perylene diester benzimidazoles an extremely intriguing class of n-type materials suitable for various applications in the field of organic electronics. Their extended absorption in the red region, enhanced self-organization into liquid crystalline phases, and the potential for room temperature stability contribute to their attractiveness for various optoelectronic applications.

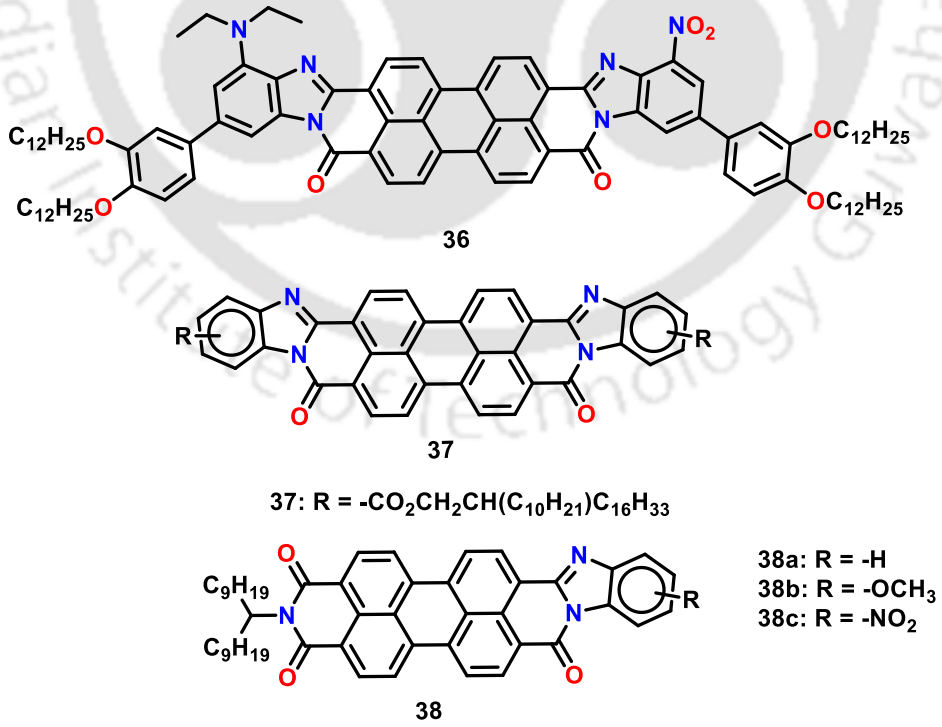

Figure 1.29. Structures of symmetrical and unsymmetrical perylene benzimidazoles (PB).

In the study conducted by P. Lazarev *et al.*, an unsymmetric perylene benzimidazole derivative (**36**) was reported.[82] Due to the unsymmetrical nature of the molecule, six regioisomers were formed. Although these regioisomers were not separated, the researchers utilized the mixture of isomers as a nonlinear dielectric material for energy storage in capacitors.

In another study by Do *et al.*, they reported on soluble perylene benzimidazole derivatives (**37**) that possessed symmetrical structures.[83] Additionally, they investigated asymmetric imide benzimidazoles in which the incorporation of electron-donating methoxy groups (**38b**) or electron-withdrawing nitro groups (**38c**) on the imidazole benzene unit allowed for the alteration of LUMO levels.

1.4. Conclusion and Perspective

Indeed, the exploration of perylene-based materials has expanded significantly in recent years, moving beyond their traditional use as dyes. By employing synthetic alterations and substitutions, perylene derivatives can be adjusted to achieve various chemical and physical characteristics, as well as facilitate their supramolecular self-organization. The manipulation of these compounds' properties relies on the ability to control their tunability. In the realm of this field, comprehending the connections between structure and properties becomes imperative due to the pivotal role that noncovalent interactions play in these mechanisms.

Liquid crystalline behavior in perylene derivatives has attracted considerable attention due to its potential applications in organic electronic devices. The ability to yield liquid crystalline self-assembly, even at room temperature, has been demonstrated in various derivatives, particularly perylene bisimides. However, there are other classes of perylene derivatives, including perylene tetra esters, perylene ester imides, core elongated derivatives and bay-extended derivatives, that remain less explored and offer untapped potential.

Incorporating heterocyclic units and functionalizing peripheral chains provide additional avenues for fine-tuning the self-assembly and electronic behavior of perylene analogues. By delving into these alterations, a vast array of possibilities emerges for manipulating the optoelectronic characteristics of perylene derivatives, thereby broadening their practical applications. Furthermore, studying the alignment of liquid crystalline perylene derivatives within device configurations is crucial for optimizing device performance. Understanding and controlling

the alignment of these materials concerning electrodes, as well as their interactions with other components within the device structure are key factors in achieving efficient charge transport and light emission.

Perylene bisimides (PBIs) have emerged as promising n-type semiconductors and potential as viable substitutes for fullerenes in organic photovoltaics. Their superior stability, optoelectronic properties, supramolecular self-assembly, and solution processability make them highly attractive for device applications. Ongoing research and development efforts aim to harness the advantages of PBIs and optimize their performance as electron acceptors in organic solar cells. Additional knowledge is necessary to comprehend perylene bisbenzimidazoles (PBs) due to their significant potential in organic electronics. Through appropriate structural design, it can be possible to isolate the *syn*- and *anti*-isomers of PBs, make them soluble, and facilitate their ordered self-assembly. Moreover, if these molecules could arrange themselves into columns of limitless length by stacking atop one another, it would result in one-dimensional (1D) charge carrier mobility along the columns. This advancement would reintroduce their viability for utilization in organic photovoltaics (OPVs) and organic field-effect transistors (OFETs). Collaboration between chemists and device scientists is vital to meet the specific requirements of various devices and drive the development of materials that can replace conventional inorganic semiconductors.

Incorporating liquid crystalline properties into perylene derivatives can further enhance their applicability in OLEDs and OFETs, improving their processability and performance. Interdisciplinary efforts combining chemical synthesis expertise with device engineering knowledge are key to achieving highly ordered self-assembled organic semiconductor materials. These materials should be solution-processable, cost-effective, and stable under ambient conditions. Advancements in this field have the potential to revolutionize the semiconductor industry by providing environmentally friendly and versatile alternatives to traditional inorganic semiconductors. Keeping this in mind the following chapters will discuss the molecular design of perylene derivatives to introduce liquid crystallinity, tune the photophysical properties and their application in organic electronic devices.

1.5. References

1. C. Tschierske, *Angew. Chem. Int. Ed.*, 2013, **52**, 8828-8878.
2. T. Wöhrle, I. Wurzbach, J. Kirres, A. Kostidou, N. Kapernaum, J. Litterscheidt, J. C. Haenle, P. Staffeld, A. Baro and F. Giesselmann, *Chem. Rev.*, 2015, **116**, 1139-1241.
3. Q. Li, *Self-organized organic semiconductors: from materials to device applications*, John Wiley & Sons, 2011.
4. a) M. Funahashi and J. I. Hanna, *Adv. Mater.*, 2005, **17**, 594-598; b) A. Van de Craats, J. Warman, A. Fechtenkötter, J. D. Brand, M. Harbison and K. Müllen, *Adv. Mater.*, 1999, **11**, 1469-1472; c) K. L. Woon, M. P. Aldred, P. Vlachos, G. H. Mehl, T. Stirner, S. M. Kelly and M. O'Neill, *Chem. Mater.*, 2006, **18**, 2311-2317.
5. a) F. Würthner, *Chem. Commun.*, 2004, 1564-1579; b) F. Würthner, C. R. Saha-Möller, B. Fimmel, S. Ogi, P. Leowanawat and D. Schmidt, *Chem. Rev.*, 2015, **116**, 962-1052.
6. a) J. Wu, W. Pisula and K. Müllen, *Chem. Rev.*, 2007, **107**, 718-747; b) R. J. Bushby and K. Kawata, *Liq. Cryst.*, 2011, **38**, 1415-1426.
7. M. J. Hollamby and T. Nakanishi, *J. Mater. Chem. C*, 2013, **1**, 6178-6183.
8. C. Li and H. Wonneberger, *Adv. Mater.*, 2012, **24**, 613-636.
9. a) V. Marcon, D. W. Breiby, W. Pisula, J. Dahl, J. Kirkpatrick, S. Patwardhan, F. Grozema and D. Andrienko, *J. Am. Chem. Soc.*, 2009, **131**, 11426-11432; b) N. Tasios, C. Grigoriadis, M. R. Hansen, H. Wonneberger, C. Li, H. W. Spiess, K. Müllen and G. Floudas, *J. Am. Chem. Soc.*, 2010, **132**, 7478-7487; c) E. Di Donato, R. P. Fornari, S. Di Motta, Y. Li, Z. Wang and F. Negri, *J. Phys. Chem. B*, 2010, **114**, 5327-5334.
10. M. G. Debije, Z. Chen, J. Piris, R. B. Neder, M. M. Watson, K. Müllen and F. Würthner, *J. Mater. Chem.*, 2005, **15**, 1270-1276.
11. J. Y. Kim, I. J. Chung, Y. C. Kim and J.-W. Yu, *Chem. Phys. Lett.*, 2004, **398**, 367-371.
12. K. Balakrishnan, A. Datar, T. Naddo, J. Huang, R. Oitker, M. Yen, J. Zhao and L. Zang, *J. Am. Chem. Soc.*, 2006, **128**, 7390-7398.
13. a) A. Wicklein, A. Lang, M. Muth and M. Thelakkat, *J. Am. Chem. Soc.*, 2009, **131**, 14442-14453; b) D. M. Pereira de Oliveira Santos, M. G. Belarmino Cabral, A. Bentaleb, R. Cristiano, H. Gallardo, F. Durola and H. Bock, *Chem. Eur. J.*, 2016, **22**, 7389-7393; c) J. A. Quintana, J. M. Villalvilla, A. de la Peña, J. L. Segura and M. A. Díaz-García, *J. Phys. Chem. C*, 2014, **118**, 26577-26583; d) N. Mizoshita, T. Tani and S. Inagaki, *Chem. Commun.*, 2012, **48**, 10772-10774.
14. F. Nolde, W. Pisula, S. Müller, C. Kohl and K. Müllen, *Chem. Mater.*, 2006, **18**, 3715-3725.
15. M. G. B. Cabral, D. M. Pereira de Oliveira Santos, A. Bentaleb, E. A. Hillard, R. Cristiano, H. Gallardo, F. Durola and H. Bock, *Chem. Eur. J.*, 2016, **22**, 8043-8047.
16. R. A. Cormier and B. A. Gregg, *J. Phys. Chem. B*, 1997, **101**, 11004-11006.
17. R. A. Cormier and B. A. Gregg, *Chem. Mater.*, 1998, **10**, 1309-1319.
18. B. A. Gregg and R. A. Cormier, *J. Phys. Chem. B*, 1998, **102**, 9952-9957.
19. S. G. Liu, G. Sui, R. A. Cormier, R. M. Leblanc and B. A. Gregg, *J. Phys. Chem. B*, 2002, **106**, 1307-1315.
20. K. Bijak, H. Janeczek, M. Grucela-Zajac and E. Schab-Balcerzak, *Opt. Mater.*, 2013, **35**, 1042-1050.
21. a) M. Funahashi and A. Sonoda, *Org. Electron.*, 2012, **13**, 1633-1640; b) M. Funahashi and A. Sonoda, *J. Mater. Chem.*, 2012, **22**, 25190-25197.
22. M. Funahashi, N. Takeuchi and A. Sonoda, *RSC Advances*, 2016, **6**, 18703-18710.

23. M. Funahashi and A. Sonoda, *Phys. Chem. Chem. Phys.*, 2014, **16**, 7754-7763.
24. a) M. Funahashi, M. Yamaoka, K. Takenami and A. Sonoda, *J. Mater. Chem. C*, 2013, **1**, 7872-7878; b) K. Takenami, S. Uemura and M. Funahashi, *RSC Advances*, 2016, **6**, 5474-5484.
25. F. Würthner, C. Thalacker, S. Diele and C. Tschierske, *Chem. Eur. J.*, 2001, **7**, 2245-2253.
26. Z. Chen, U. Baumeister, C. Tschierske and F. Würthner, *Chem. Eur. J.*, 2007, **13**, 450-465.
27. V. Dehm, Z. Chen, U. Baumeister, P. Prins, L. D. Siebbeles and F. Würthner, *Org. Lett.*, 2007, **9**, 1085-1088.
28. a) C. Lei, M. S. Al Khalifah, M. O'Neill, M. P. Aldred, S. P. Kitney, P. Vlachos and S. M. Kelly, 2008 *International Society for Optics and Photonics*; p 705214.; b) M. S. AlKhalifah, C. Lei, S. A. Myers, M. O'Neill, S. P. Kitney and S. M. Kelly, *Liq. Cryst.*, 2014, **41**, 402-417.
29. Z. An, J. Yu, S. C. Jones, S. Barlow, S. Yoo, B. Domercq, P. Prins, L. D. Siebbeles, B. Kippelen and S. Marder, *Adv. Mater.*, 2005, **17**, 2580-2583.
30. V. Percec, M. Peterca, T. Tadjiev, X. Zeng, G. Ungar, P. Leowanawat, E. Aqad, M. R. Imam, B. M. Rosen and U. Akbey, *J. Am. Chem. Soc.*, 2011, **133**, 12197-12219.
31. D. Sahoo, M. Peterca, E. Aqad, B. E. Partridge, P. A. Heiney, R. Graf, H. W. Spiess, X. Zeng and V. Percec, *J. Am. Chem. Soc.*, 2016, **138**, 14798-14807.
32. B. Jancy and S. Asha, *Chem. Mater.*, 2007, **20**, 169-181.
33. a) L. Meng, Q. Wu, F. Yang and H. Guo, *New J. Chem.*, 2015, **39**, 72-76; b) M. Zhu, H. Guo, F. Yang and Z. Wang, *Dyes Pigm.*, 2016, **133**, 387-394.
34. G. A. Bhavsar and S. Asha, *Chem. Eur. J.*, 2011, **17**, 12646-12658.
35. R. Schmidt, M. M. Ling, J. H. Oh, M. Winkler, M. Könemann, Z. Bao, F. Würthner, *Adv. Mater.* 2007, **19**, 3692−3695.
36. a) A. Patra, M. Bendikov, *J. Mater. Chem.*, 2010, 20, 422–433; b) J. Dhar, K. Swathi, D. P. Karothu, K. S. Narayan, S. Patil, *ACS Appl. Mater. Interfaces*, 2015, **7**, 670–681.
37. Y. Sun, L. Tan, S. Jiang, H. Qian, Z. Wang, D. Yan, C. Di, Y. Wang, W. Wu, G. Yu, S. Yan, C. Wang, W. Hu, Y. Liu, and D. Zhu, *J. Am. Chem. Soc.*, 2007, **129**, 7, 1882–1883.
38. L. Tan, W. Jiang, L. Jiang, S. Jiang, Z. Wang, S. Yan, W. Hu, *Appl. Phys. Lett.*, 2009, **94**, 153306.
39. W. Jiang, Y. Zhou, H. Geng, S. Jiang, S. Yan, W. Hu, Z. Wang, Z. Shuai, J. Pei, *J. Am. Chem. Soc.*, 2011, **133**, 1−3.
40. W. Jiang, H. Qian, Y. Li, and Z. Wang, *J. Org. Chem.*, 2008, **73**, 7369–7372.
41. (a) Y. Zhen, H. Qian, J. Xiang, J. Qu and Z. Wang, *Org. Lett.*, 2009, **11**, 3084–3087; (b) Y. Li and Z. Wang, *Org. Lett.*, 2009, **11**, 1385–1387; (c) H. Chen, C. He, G. Yu, Y. Zhao, J. Huang, M. Zhu, H. Liu, Y. Guo, Y. Li and Y. Liu, *J. Mater. Chem.*, 2012, **22**, 3696–3698.
42. Y. Zagranyarski, L. Chen, D. Jänsch, T. Gessner, C. Li, K. Müllen, *Org. Lett.*, 2014, **16**, 2814−2817.
43. R. K. Gupta, S. K. Pathak, B. Pradhan, D. S. S. Rao, S. K. Prasad, A. S. Achalkumar, *Soft Matter*, 2015, **11**, 3629–3636.
44. R. K. Gupta, B. Pradhan, S. K. Pathak, M. Gupta, S. K. Pal, A. S. Achalkumar, *Langmuir*, 2015, **31**, 8092–8100.
45. R. K. Gupta, S. K. Pathak, B. Pradhan, M. Gupta, S. K. Pal and A. S. Achalkumar, *ChemPhysChem*, 2016, **17**, 859–872.

46. R K. Gupta, D. Das, M. Gupta, S. K. Pal, P. K. Iyer and A. S. Achalkumar, *J. Mater. Chem. C*, 2017, **5**, 1767.
47. K. M Wolfe, M. Mooney, C. Crep, S. R. Gagné and G. C Welch, *Flex. Print. Electron.*,2022, **7**, 044007.
48. R. K. Gupta, D. Das, P. K. Iyer, and A. S. Achalkumar, *ChemistrySelect*, 2018, **3**, 5123 – 5129.
49. R. K. Gupta and A. S. Achalkumar, *J. Org. Chem.*, 2018, **83**, 6290−6300.
50. R. K. Gupta, D. S. S. Rao, S. K. Prasad, and A. S. Achalkumar, *Chem. Eur. J.*, 2018, **24**, 3566−3575.
51. R. K. Gupta, A. Dey, A. Singh, P. K. Iyer, and A. A. Sudhakar, *ACS Appl. Electron. Mater.* 2019, **1**, 1378−1386.
52. Q. Deng, E. Zhou, Y. Huang, W. Qing, H. Zhai, Z. Liu and Z. Wei, *Chem. Commun.*, 2019, **55**, 4379.
53. S. Feng, Y. P. Zhang, H. Xu, X. q. Gong, J. Hua, *J. Alloys and Compounds*, 2023, **938**,168500.
54. M. Nazari, E. Cieplechowicz, T. A. Welsh and G. C. Welch, *New J. Chem.*, 2019, **43**, 5187.
55. M. Martell, M. U. Ocheje, B. S. Gelfand, S. R. Gagne and G. C. Welch, *New J. Chem.*, 2021, **45**, 21001.
56. A. D. Hendsbee, J. P. Sun, W. K. Law, H. Yan, I. G. Hill, D. M. Spasyuk, and G. C. Welch, *Chem. Mater.*, 2016, **28**, 7098−7109.
57. M. Rahmati, S. V. Dayneko, M. Pahlevani, and G. C. Welch, *ACS Appl. Electron. Mater.*, 2020, **2**, 48−55.
58. L. Yang, A. D. Hendsbee, Q. Xue, S. He, C. R. D. Jager, G. Xie, G. C. Welch, and Z. Ding, *ACS Appl. Mater. Interfaces*, 2020, **12**, 51736−51743.
59. S. V. Dayneko, M. Rahmati, M. Pahlevani and G. C. Welch, *J. Mater. Chem. C*, 2020, **8**, 2314.
60. H. Qian, C. Liu, Z. Wang and D. Zhu, *Chem. Commun.*, 2006, 4587–4589.
61. H. J. Ben, X. K. Ren, B. Song, X. Li, Y. Feng, W. Jiang, E. Q. Chen, Z. Wang and S. Jiang, *J. Mater. Chem. C*, 2017, **5**, 2566—2576.
62. X. Li, H. Wang, J. A. Schneider, Z. Wei, W. Y. Lai, W. Huang, F. Wudl and Y. Zheng, *J. Mater. Chem. C*, 2017, **5**, 2781.
63. G. B. Huang, L. Shen, J. Liu, W. F. Zhou, K. Traskovskis, Y. L. Song, W. Jiang, Z. H. Wange and X. K. Ren, *Chem. Commun.*, 2020, **56**, 3123-3126.
64. L. Chen, P. Xia, T. Du, Y. Deng, and Y. Xiao, *Org. Lett.*, 2019, **21**, 5529−5532.
65. G. Li, D. Li, X. Liu, H. Xu, J. Zhang, S. Wang, Z. Liua and B. Tang, *Chem. Commun.*, 2019, **55**, 9661.
66. R. A. Cormier and B. A. Gregg, *RSC Adv.*, 2014, **4**, 2368.
67. Z. Ma, C. Xiao, C. Liu, D. Meng, W. Jiang, and Z. Wang, *Org. Lett.*, 2017, **19**, 4331−4334.
68. S. K. Lee, Y. Zu, A. Herrmann, Y. Geerts, K. Müllen, A. J. Bard, *J. Am. Chem. Soc.* 1999, **121**, 3513–3520.
69. T. Maki, H. Hashimoto, *Bull. Chem. Soc. Jpn.* 1952, **25**, 411–413.
70. C. W. Tang, *Appl. Phys. Lett.* 1986, **48**, 183 – 185.
71. P. Peumans, V. Bulović, and S. R. Forrest, *Appl. Phys. Lett.* 2000, **76**, 2650.
72. K. Takahashi, N. Kuraya, T. Yamaguchi, T. Komura, and K. Murata, S*ol. Energy Mater. Sol. Cells* 2000, **61**, 403.

73. D. Gebeyehu, M. Pfeiffer, B. Maennig, J. Drechsel, A. Werner, and K. Leo, *Thin solid films*, 2004, **451**, 29-32.
74. J. Xue, B. P. Rand, S. Uchida, and S. R. Forrest, *J. Appl. Phys.*, 2005, 98(12), 124902.
75. P. Dhagat, H. M. Haverinen, R. J. Kline, Y. Jung, D. A. Fischer, D. M. DeLongchamp, and G. E. Jabbour, *Adv. Funct. Mater.* 2009, **19**, 2365–2372.
76. J. Mizuguchi, and N. Shimo, *J. Imaging Sci. Tech* 2006, **50**, 115.
77. R. K. Gupta, and A. A. Sudhakar, *Langmuir* 2019, **35**, 2455–2479.
78. Z. Yuan, Y. Xiao, Z. Li, and X. Qian, *Org. Lett.*, 2009, **11**, 2808-2811.
79. L. Perrin, and P. Hudhomme, Synthesis, *Eur. J. Org. Chem.*, 2011, 5427–5440.
80. A. Wicklein, P. Kohn, L. Ghazaryan, T. Thurn-Albrecht, and M. Thelakkat, *Chem. Commun.* 2010, **46**, 2328–2330.
81. A. Wicklein, M.-A. Muth and M. Thelakkat, *J. Mater. Chem.*, 2010, **20**, 8646-8652.
82. S. J. Hein, C. Edder, M. Kowalczyk, A. Borzenko, L. Mourokh, and P. Lazarev, *RSC Adv.*, 2019, **9**, 361–364.
83. S. H. Oh, B. G. Kim, S. J. Yun, M. Maheswara, K. Kim, and J. Y. Do, *Dyes and Pigments*, 2010, **85**, 37-42.

Chapter 2

Columnar liquid crystals based on hetero atom *bay*-annulated perylene bisimides derived from tri-n-alkyl anilines and their application in OLEDs

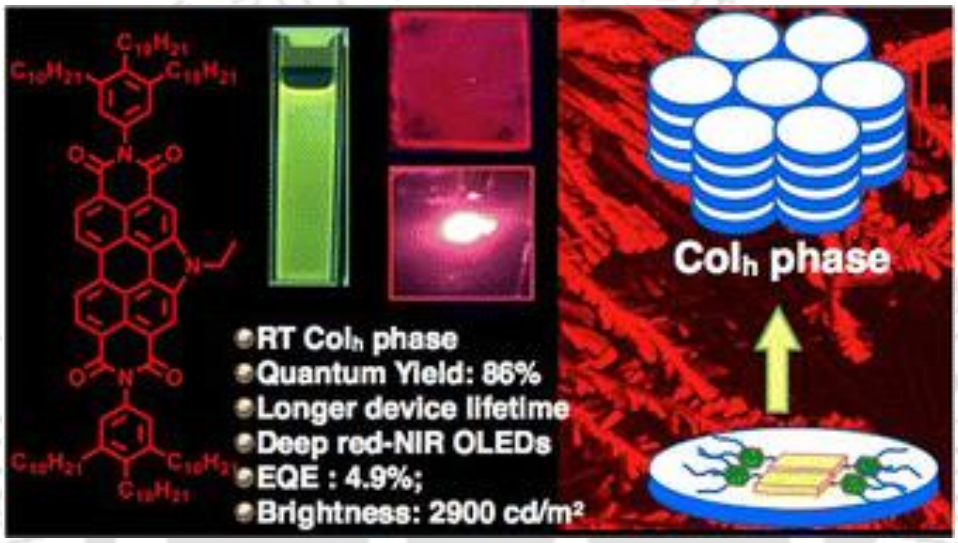

2.1. Introduction

It is almost a century passed after the discovery of perylenebisimides (PBIs), with their journey from red colored industrial vat dyes,[1] to one of the important class of functional dyes which can also work as highly tunable organic semiconductors.[2] Much of the synthetic efforts from different research groups were devoted to alter the solubility, self-assembly, pigment color, photophysical as well as electrochemical behavior[3] and also driven by the aim to realize new perylene derivatives with a potential in organic electronics[4-21] and supramolecular self-assembly.[22-24] High fluorescence quantum yield, facile tunability of the emission color, high thermal/photo/chemical stability[25-29], good electron mobility, ease of the molecular structure tunability make perylene derivatives as materials of choice in the detection of different organic amines including illicit drugs.[22-24] The electron deficient nature of perylene bisimides makes them a good class of inexpensive n-type semiconductors that are inevitable for the growth of organic semiconducting materials. This is because there are many electron-rich, hole conducting p-type organic semiconductors are available, but not many n-type counterparts.[3]

Perylene bisimides (PBIs) as such, are highly insoluble pigments often associated with high melting points. This often limits their application in the above-said avenues. In order to make them processable, one has to improve their solubility. Furthermore, if such molecular systems are able to self-assemble then it will improve their applicability in organic electronic devices due to their enhanced intermolecular order. Thus, the development of such self-organized organic semiconductors is considered to be a unique area. Here, in addition to the molecular property, their intermolecular interactions through several secondary interactions (π-π interactions, H-bonding, hydrophobic interactions, van der Waals interactions, dipole-dipole interactions) need to be considered during the molecular design.[22-24] Obviously due to the large aromatic core, the perylene derivatives exhibit strong π-π interactions. However, the availability of twelve functionalizable (four each *peri*-, *bay*- and *ortho*-) positions, provide much required handles to control the self-assembly as well as functional behaviors of these molecules.[4-8] PBIs, synthesized by the condensation of perylene tetracarboxylic acid dianhydride (PTCDA) with appropriate alkyl amines or aryl amines bearing flexible alkyl/alkoxy chains have exhibited the ability to stabilize different supramolecular self-assemblies like fluorescent J-aggregates, light harvesting complexes, vesicles, liquid crystals and so on. *Bay*-substitution provides an another useful tunable handle to alter their

physical properties and self-assembling behavior.[22-24] This strategy alters the molecular planarity and in turn impacts the self-assembly behavior of the PBIs. However, annulating the *bay*-position with heteroatoms is a powerful strategy to alter the physical properties while preserving the planarity and self-assembly.[30-33] Using this methodology, a series of hetero atom *bay*-annulated perylene tetraesters,[30-33] perylene diester imides[34-35] and their bisimide analogues[36-37] were also prepared, which exhibited promising photophysical, electrochemical properties and self-assembling behavior.

PBIs and their derivatives are often considered as potential substitutes to fullerenes, which are commonly utilized as n-type materials in organic photovoltaics.[4-24] However, they have a long way to reach that stage which requires structural modification and studies. Incorporation of various hetero-atoms for example, oxygen, nitrogen, sulphur and selenium in the *bay*-region of perylene derivatives by annulation is one such attempt. In particular, sulfur and selenium incorporation in organic semiconductors is a theme of intese research due to the additional intermolecular S···S and Se···Se interactions, that promote the molecular self-assembly and 1D conductivity.[38-46] Especially, chalocogen atoms like S and Se when form covalent bonds, their bonding orbital have a deficiency of electronic charge in its outer (noninvolved) lobe, which is known as a σ-hole. If the atom is sufficiently polarizable, the σ-hole may have a positive electrostatic potential which can interact with a nucleophilic site in its proximity to form a noncovalent bond or it can form the same with the regions of negative electrostatic potential on the same atoms. This is similar to the case of thiazole and selenazole nucleoside drugs exhibiting antitumor activity depending upon the particular conformations that are stabilized by intramolecular S···O and Se···O electrostatic interactions, which is shown to involve sulfur and selenium σ-holes.[47,48] This kind of secondary bonding interactions also play a role in the organization of organic semiconductor materials on a molecular scale.[49] Thus in addition to S-S, Se-Se interactions, there is a possibility of S···O and Se···O interactions in the case of S and Se-*bay* annulated PBIs (with the carbonyls of imide units). Thus there is a possibility to have an enhanced intermolecular interaction, assisted by strong intermolecular orbital coupling leading to a higher charge carrier mobility[50] when such molecules are assembled in a columnar structure.

Thus the the design and the syntheses of self-assembling perylene based materials, aimed at the application in organic electronics, motivated to prepare hetero atom *bay*-annulated PBIs by

condensing tri-*n*-alkyl benzeneamines with PTCDA. The molecular design with a central perylene core attached with flexible peripheral chains was aimed to obtain columnar (Col) liquid crystalline phases which act as one dimensional (1D) nanostructured channel for the conduction of charge carriers along the packing direction. [24,51] Further there are not much reports on OLEDs based on perylene derivatives, in comparison to their utilization in organic solar cells (OSCs) and organic field effect transistors (OFETs). There are few reports based on perylene tetraesters and PBIs as emitter materials in OLEDs.[52-57] In the past, there are reports on bright green electroluminescent room temperature columnar LCs based on heteroatom (N, S and Se) *bay*-annulated perylene tetraesters. They exhibited better efficiency when doped in polyvinylcarbzole (PVK) host.[33] A white electroluminescence was also reported in such host guest OLEDs prepared by doping *bay*-annulated perylene ester imides (PEIs) doped in PVK with TPBi as an electron injecting layer.[35] Welch's group extensively used *N*-annulated PBI dimer for the realization of air stable red OLEDs.[58,59] Considering the few reports on the application of PBI based fluorescent Col LCs, further encouraged to synthesize highly fluorescent hetero atom *bay*-annulated PBIs, which could self-assemble into highly ordered Col phases with a bright potential in the fabrication of OLEDs. Further, it is a distant dream to have a single layer OLED, with a solution processable self-assembling organic semiconductor with good conductivity, high quantum yield, and a proper match with the electrode work function. Though it is difficult to achieve all the functions in a single material, it was a pleasant surprise to find that these derivaties are the first examples of PBIs/*bay*-annulated PBIs which are liquid crystalline at room temperature exhibiting high EQE. In particular, the solution processable NIR fluorescent OLED based on **PBI-N^{10}**, displayed a maximum EQE of 4.9%, with a lifetime of 12.4 h with an initial brightness of 2900 cd/m^2 and a deep red/NIR emission.

2.2. Results and discussion

2.2.1. Synthesis and molecular structural characterization

The synthetic approach utilized for the preparation of target PBIs is outlined in scheme 2.1. Heteroatom *bay*-annulated PTCDAs (**2-4**) were achieved starting from PTCDA in good yields as per the earlier reports.[36] The tri-*n*-alkyl phenyl-functionalized PBIs have been synthesized in four steps similar to the reported method (outlined in scheme 2.2).[60]

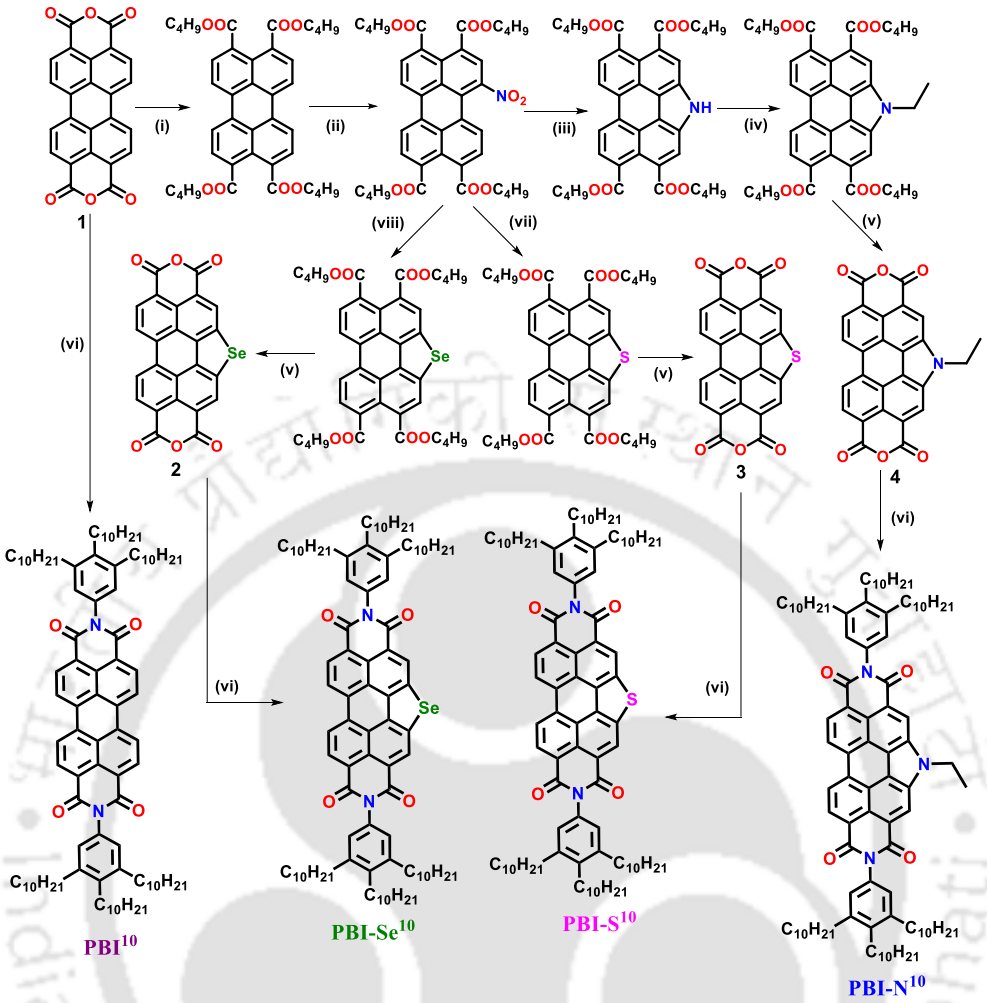

Scheme 2.1. Synthesis of target perylene bisimides. Reagents and conditions: (i) KOH, H_2O, 70 °C, 0.5 h, 1 M HCl, Aliquat 336, KI,1-bromobutane, reflux, 12 h (76 %); (ii) $NaNO_2$, HNO_3, 0 °C, 1 h (90 %); (iii) Triethyl phosphite, 160 °C, reflux, 4 h, N_2 (60 %); (iv) NaH, 1-Iodoethane, Dry THF, reflux, 17 h (75 %); (v) *p*-Toluene sulphonic acid monohydrate, toluene, 100 °C, 30 h (90%); (vi) **8**, zinc acetate, imidazole, 165 °C, microwave, 30 min. (80–90%); (vii) Sulfur powder, anhydrous NMP, N_2, 70 °C, 0.5 h, 180 °C, 17 h (55%); (viii) Selenium powder, anhydrous NMP, N_2, 70 °C, 0.5 h, 180 °C, 17 h (55 %).

First the precursor 1,2,3-triiodo-5-nitrobenzene (**6**) was prepared by diazotization reaction from 2,6-diiodo-4-nitro aniline (**5**). Then it was subjected to Sonogashira coupling reaction with 1-decyne to obtain the product 3,4,5-tris(1-decynyl)-nitrobenzene (**7**) in 70 % yield. Hydrogenation of the precursor **7** in the presence of catalyst Pd/C, reduced the nitro group and carbon-carbon triple bonds to get the aniline **8**.[60] Finally, the perylene tetracarboxylic bisanhydrides and its heteroatom *bay*-annulated derivatives were separately condensed with the aniline **8** in presence of imidazole and zinc acetate in a microwave reactor to give the final desired product with 85 % yield.[36] The crude compounds were then subjected for repeated column purifications on neutral

alumina with ethyl acetate-hexane mixture as an eluent to obtain the final products as gummy solids. All these PBIs were completely characterized by ^{1}H NMR, ^{13}C NMR, IR spectroscopy and mass spectrometry.

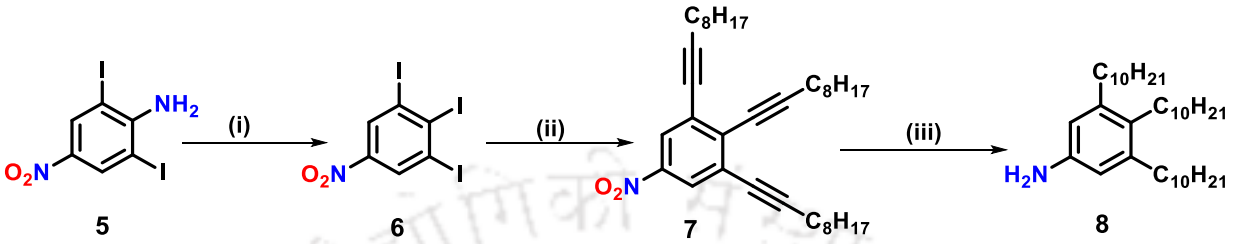

Scheme 2.2. Synthesis of 3,4,5-tri-*n*-decylaniline. Reagents and conditions. (i) $NaNO_2$, H_2SO_4, AcOH, H_2O, KI, 90 ^{o}C, (91 %) (ii) CuI, Et_3N, $Pd(PPh_3)_2Cl_2$, 80 ^{o}C, 4 h, (89 %), (iii) EtOAc, MeOH, H_2-Pd/C, RT, overnight (95 %).

2.2.2. Thermal behavior

The thermal behavior of heteroatom *bay*-annulated PBIs was investigated by polarizing optical microscopy (POM), differential scanning calorimetery (DSC), thermogravimetric analysis (TGA) and X-ray diffraction (XRD) studies. The phase transition from crystal to LC phase was at first examined with the help of POM observation, which showed the appearance of strong birefringence coupled with an increase in the fluidity of the compounds on heating. The phase transition temperatures and the corresponding changes in enthalpy were confirmed by DSC thermograms. These values were in agreement with peak temperatures noted in POM studies (Table A 2.2). Analysis of the optical textures observed in POM and the information obtained from XRD studies showed the nature of the mesophase under examination. From the TGA, it was found that, all the PBIs exhibit almost equal thermal stability. The temperature at which the 5 weight percent weight loss was observed varied from 346 ^{o}C to 356 ^{o}C (Fig. 2.1a, Table A 2.2). Under POM observation all the three PBIs (**PBI^{10}**, **PBI-N^{10}** and **PBI-Se^{10}**) exhibited textures corresponding to columnar hexagonal (Col_h) phase, whereas **PBI-S^{10}** showed columnar oblique (Col_{ob}) phase (Fig. 2.1b). DSC thermograms showed that the mesophases were stable over a broad thermal range including ambient temperature. The assignment of the Col phases was confirmed from the powder XRD studies carried out at different temperatures (Table A 2.3, Fig. A17-18).

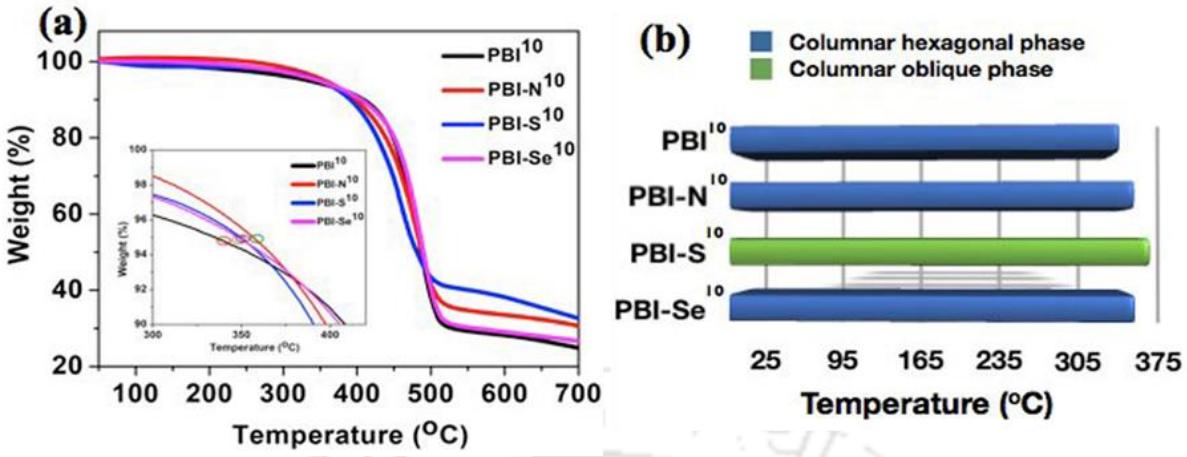

Figure 2.1. TGA plots (heating rate of 10 °C/min, Nitrogen atmosphere, inset shows the temperatures at which 5 wt% decomposition occurs) (a); and bargraph showing the thermal behavior (b) of compounds **PBI^{10}, PBI-N^{10}, PBI-S^{10}** and **PBI-Se^{10}** (considered the second heating scan).

For example, compound **PBI^{10}** which was a sticky mass, sandwiched between a glass slide and coverslip, on slow heating in a programmable hotstage placed under a POM showed an increase in the fluidity and birefringence. The viscous mass was shearable on the application of mechanical stress and transformed into an isotropic liquid at ≈ 328 °C (Fig. 2.2a). Slow cooling of the isotropic liquid at a rate of 5 °C/min, showed the growth of broad leaf like texture emerging from large homeotropic domains, which is a characteristic feature of Col_h phases (Fig. 2.2a). The texture remains unaltered even at room temperature, while the DSC shows no signature of crystallization, confirming that the Col phase is stable even at room temperature (Fig. 2.2b). Powder XRD studies were carried out at different thermal intervals to analyze the mesophase structure. XRD patterns obtained at 200 °C, 100 °C and at room temperature were almost identical. As an example, the plot of intensity *vs* 2θ obtained for compound **PBI^{10}** at 100 °C (Fig. 2.2c) showed a strong peak corresponding to a *d* spacing of 27.74 Å, followed by weaker peaks centered at smaller *d* spacings in the ratio of 1: 1/√3: 1/√4: 1/3: 1/√12. These values could be indexed to the (10), (11), (20), (30) and (22) reflections of the Col_h phase (Fig. 2.2c). In the wide angle region, two diffuse peaks were found with *d*-spacings of 4.65 Å and 4.12 Å. The first diffuse peak is arising from the packing of aliphatic tails, while the second peak corresponds to the stacking of the cores within the columns. The intercolumnar distance or the lattice constant '*a*' was found to be 32 Å, which is much lower than the molecular diameter of the compound **PBI^{10}** in its all extended form (44.8 Å) (Fig. 2.2d). This difference of around 30% can be accredited to the folding of alkyl chains or their interdigitaion with the neighbouring columns. Further confirmation of

interdigitation being responsible comes from the following observation. As seen in Table A2.3, the *d* spacing decreases by 2.5% when the temperature is lowered from 200 °C to room temperature. Generally, the columnar phase exhibits a negative thermal expansion in the column diameter owing to the stretching of the peripheral alkyl chains when the temperature is lowered. Consequently, the *d* value should increase on lowering the temperature contrary to the experimental data quoted in Table A2.3. This is, however, possible if interdigitation is the governing mechanism, the extent of which increases as the temperature is lowered. A third possibility is that the discs are tilted within the columns, but the tilt direction is not correlated. This argument gets further support from the fact that the extent of interdigitation expected otherwise would be nearly over the entire length of the chain, which would make the discs completely flat and thus, the core-core peak should be very strong and sharp. But the peak due to core-core correlations is quite weak (see Fig. 2.2c, inset). The reduction in the d_{10} values as the temperature is lowered would thus be due to increased tilt of the discs. Tetracatenars exhibiting the columnar phase have been proposed to have tilted-but-uncorrelated columns.[61] A more realistic situation in the present case is perhaps a combination of both tilt and interdigitation.

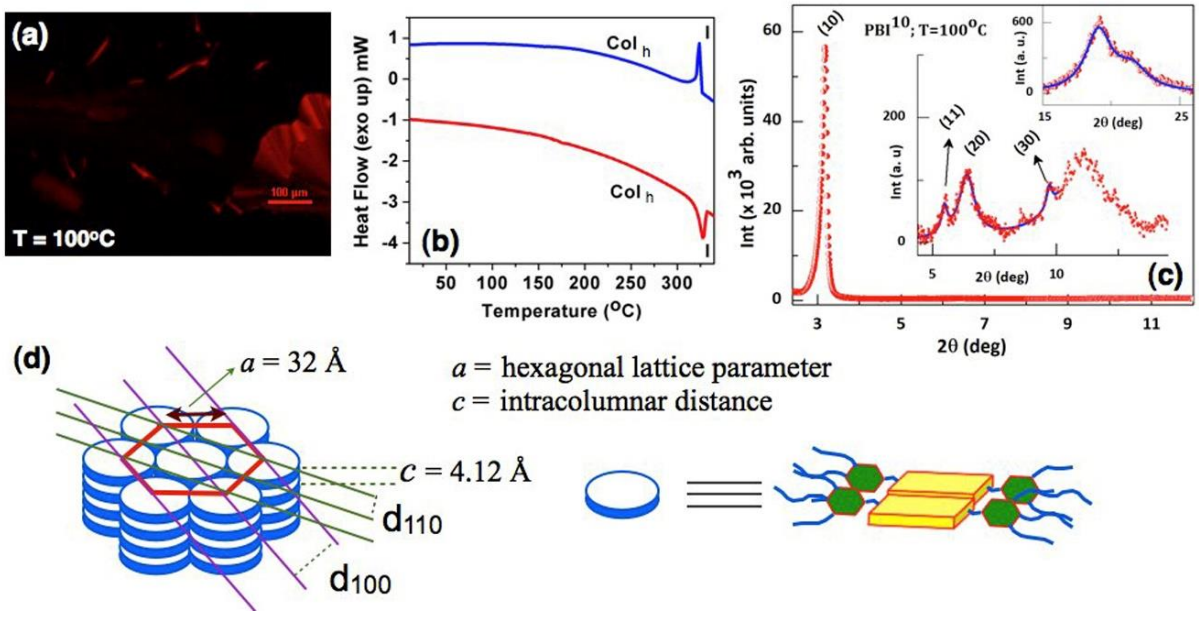

Figure 2.2. POM image of the Col_h phase at 100 °C for compound **PBI[10]** (a); DSC thermogram for the first cooling (blue trace) and second heating (red trace) taken at 5 °C/min (b); Powder XRD pattern at 100 °C over the low angle region, with the lattice indices marked against the lowest angle peak (main panel) and subsidiary peaks (middle inset). The top inset depicts the diffraction in the wide angle region with the two vertical lines pointing to the maxima arising from the alkyl chain and correlated core-core regions, respectively. (c); Schematic diagram showing the Col_h phase and the formation of a disc by the side by side arrangement of two molecules (d).

Another feature to be noted in the XRD pattern is the presence of a weak, but diffuse peak in the intermediate angles (~ 8 Å), labelled as halo in Table A2.3. The unmistakable presence of this peak, suggests the possibility of some sort of dimer formation within the column, but loosely held. From the lattice constant '*a*' the lattice area (*S*) and molecular volume (*V*) were calculated. The number of molecules forming an individual disc was found to be approximately 2 (Fig. 2.2d, Table A2.3), where the individual disc is formed by the lateral arrangement of two **PBI^{10}** molecules. Similar arrangement of PBI molecules in the Col_h phase is reported earlier.[62] Observation of Col_h phase in **PBI^{10}** is in line with the earlier report on the stabilization of Col_h phase in the case of PBI with six dodecyl chains.[63]

Perylene bismides **PBI-N^{10}** and **PBI-Se^{10}** showed Col_h phase for a wide thermal range including room temperature as confirmed by the DSC thermograms (Fig. 2.3b and 2.3e). However, **PBI-N^{10}** exhibited a fernlike texture, while the compound **PBI-Se^{10}** exhibited a mosaic texture (Fig. 2.3a and 2.3d), which are usually observed for Col_h phases.[64] The XRD scans at three different temperatures are shown in Fig. A17, exhibiting features qualitatively similar to those for **PBI^{10}**. The most notable difference being the presence of many peaks arising from the 2D lattice. However, just as for **PBI^{10}**, the reflections index to the Col_h phase (See Table A2.3). This compound also presents two diffuse reflections in the wide angle region corresponding to the spacing between the alkyl chains of neighbouring discs and the correlation between the molecular cores. Again, there is a quantitative difference with respect to the data for the unsubstituted perylene bismide. For example, at 200 ^oC, the latter has an alkyl chain spacing of 4.85 Å, whereas the **PBI-N^{10}** compound has a much larger value of 5.68 Å suggesting that the chains are more disordered in the latter case. The temperature dependence of this spacing is also more for the *N*-annulated PBI. Concomitantly, the cores are also more separated than in the unsubstituted compound, indicating a slightly more disordered column. This could be arising from the fact that the (*N*-ethyl) substitution is quite bulky taking more space in the out-of -plane direction. Fom the data it was revealed that the molecules forming a disc was found to be almost one, with the intracolumnar distance lower than that observed for **PBI^{10}**. The XRD pattern of **PBI-Se^{10}**, indexed to a Col_h phase, exhibited no surprises, but for the fact that the spacing corresponding to the core-core correlation is substantially reduced (~10%) with respect to that for the unsubstituted compound. However, the peak is broader than for **PBI^{10}**, indicating a less packed system, arguably

due to the presence of the bulky Se entity. In view of the data on the **PBI-S[10]** compound, to be discussed below, it may be said that the Se-Se interaction is still weak.

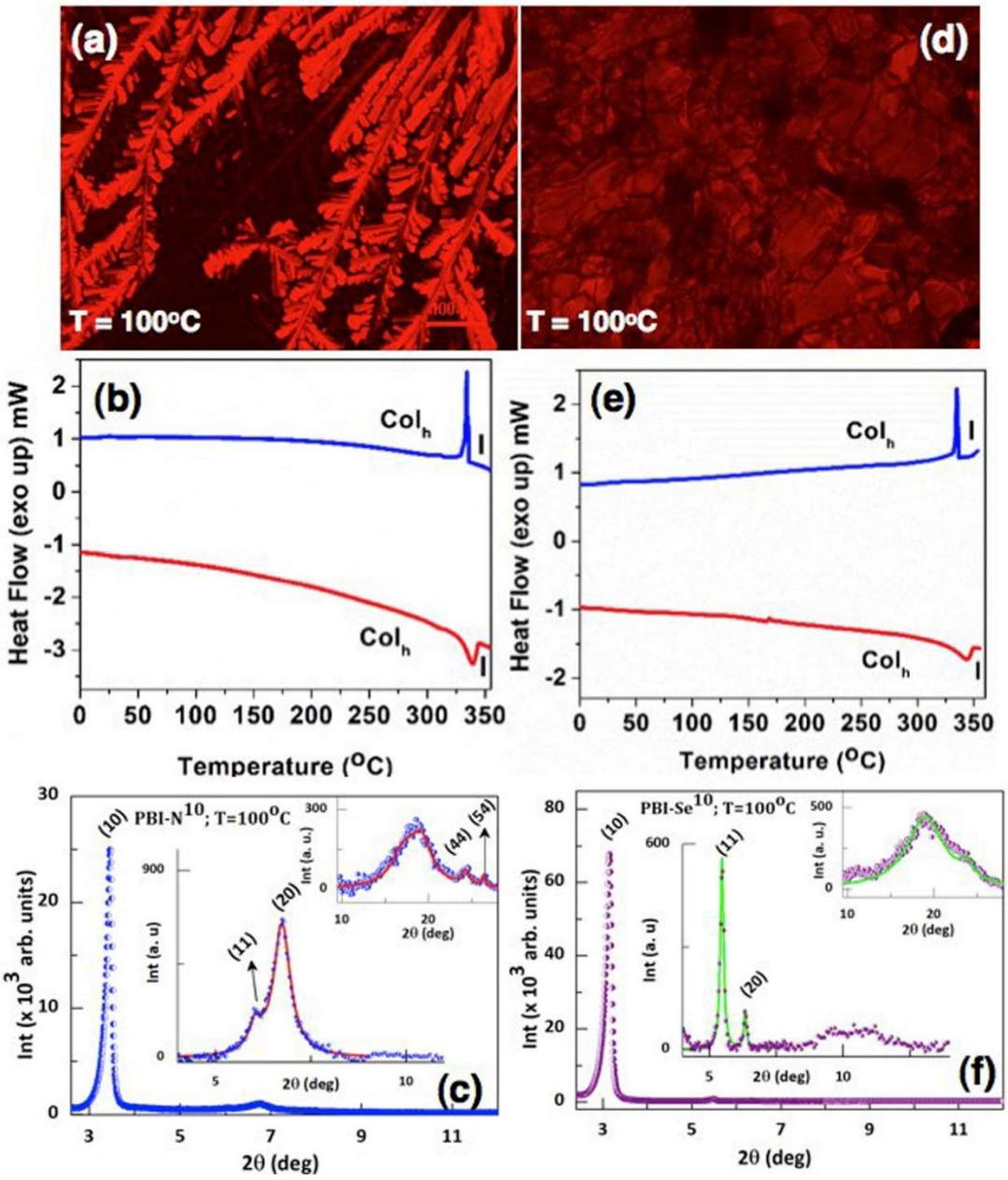

Figure 2.3. POM image of the Col$_h$ phase at 100 °C (a); DSC thermogram for the first cooling (blue trace) and second heating (red trace) taken at 5 °C/min (b) for compound **PBI-N[10]**; Powder XRD pattern at 100 °C obtained for compound **PBI-N[10]** (c); POM image of the Col$_h$ phase at 100 °C (d); DSC thermogram for the first cooling (blue trace) and second heating (red trace) taken at 5 °C/min (e) for compound **PBI-Se[10]**, Powder XRD pattern at 100 °C obtained for compound **PBI-Se[10]** (f).

The compound **PBI-S^{10}** stands apart from the other compounds in many respects. It exhibits an optical texture, which is different from those for the other compounds (Fig. 2.4a). As seen in the DSC thermogram, the compound has a mesophase spanning over a broad thermal range including ambient temperature (Fig. 2.4b). The POM images obtained at different thermal intervals and XRD patterns obtained at 200 ^{o}C, 100 ^{o}C and at room temperature are essentially similar (Fig. 2.4c, Table A2.3 and A18), but again are different from those for the other bisimides studied here. For example, the diffraction pattern obtained at 100 ^{o}C (Fig. 2.4c) showed many peaks at low angle that can be indexed into Col phase with a parallelogram lattice bearing an oblique symmetry (Col_{ob}), with lattice parameters a = 30.5Å, b = 28.9 Å and a tilt angle γ = 65.2^{o}. Interestingly, the core-core separation distance between the discs in a column was 3.98 Å.

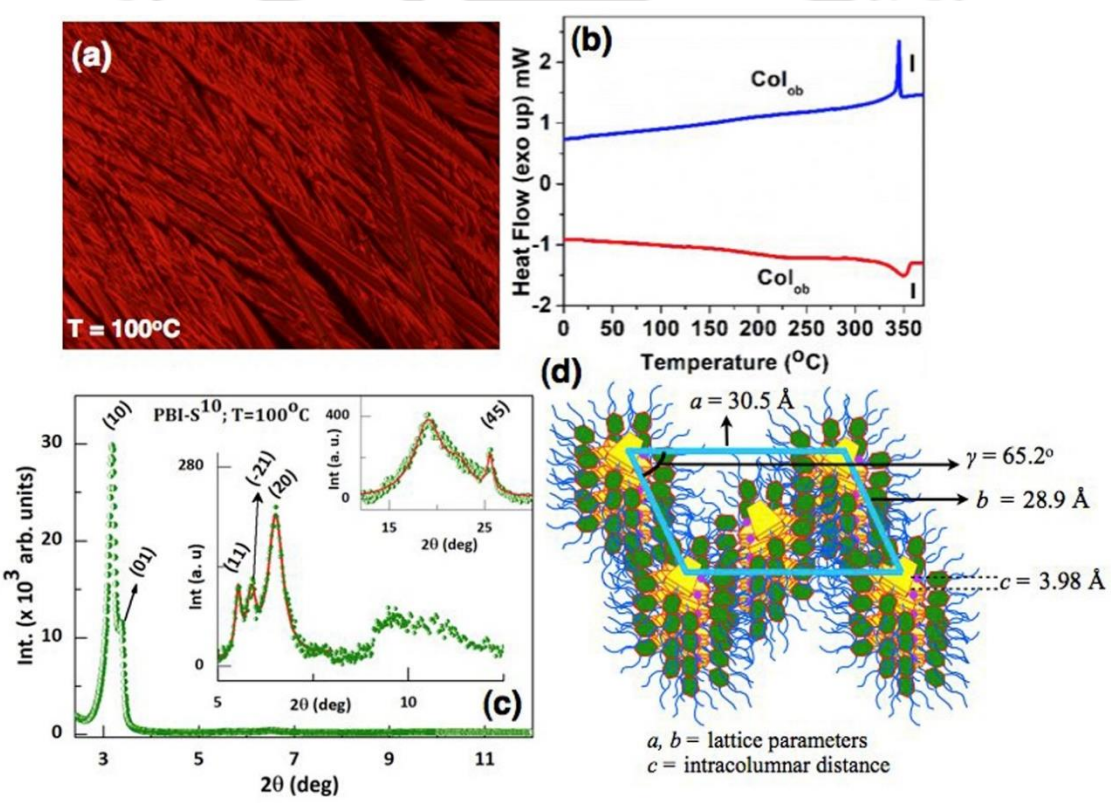

Figure 2.4. POM image of the Col_{ob} phase at 100 ^{o}C (a); DSC thermogram for the first cooling (blue trace) and second heating (red trace) taken at 5 ^{o}C/min (b); Powder XRD pattern at 100 ^{o}C obtained for compound **PBI-S^{10}** (c); Schematic diagram showing the Col_{ob} phase formed by compound **PBI-S^{10}** (d).

From these values, it is evident that each unit cell is comprising of 1 molecule (Table A2.3, Fig. 2.4c, d). Col_{ob} phase is often found with the molecules with greater core-core interactions[51,64]. However, considering that both the *Se* and *N*-ethyl PBIs show a smaller core-core distance indicate

that this parameter is not the only one that decides the presence of an oblique lattice. The second obvious reason is the strength of the secondary interaction, being the S···S interaction and/or S···O σ-hole interaction for **PBI-S^{10}**. It is possible that these secondary interactions are present in each of the hetero atom annulated compounds, but is maximized for the sulphur compound, as also suggested by the highest clearing point observed amongst the four compounds studied. Such organization of columns in oblique lattice is not often seen in literature, one example is a PBI bearing siloxane substituents at imide position.[65]

2.2.3. Photophysical properties

Photophysical behavior of these PBIs were investigated by measuring their absorption and fluorescence spectra in solutions and spin coated thin films on quartz substrates (Table 2.1 and Fig. 2.5). Well-structured absorption spectra with characteristic four vibronic bands were observed for all PBIs in solution state with the longest absorption wavelength was positioned in the range of 503-532 nm. Compound **PBI-N^{10}** was slightly red-shifted with respect to **PBI^{10}**, whereas **PBI-S^{10}** and **PBI-Se^{10}** exhibited hypsochromic absorption spectra. All the PBIs showed high molar extinction coefficients at their absorption maxima (ε: 70,500 to 1,27,000 $Lmol^{-1}cm^{-1}$). The optical band gap deduced from the red edge of the absorption spectra showed a similar value for **PBI^{10}** and **PBI-N^{10}**, whereas that of the **PBI-S^{10}** and **PBI-Se^{10}** showed an increase. Fluorescence spectra of these compounds displayed two maxima, with the high intensity one was in the range of 509-539 nm (Fig. 2.5b). These PBIs exhibited bright yellowish green fluorescence in solution state (Fig. 2.6). The Stokes shift was in the range of 191–249 cm^{-1}. Relative quantum yield of these compounds were measured with respect to Rhodamine 6G and was found to be in the range of 0.02 to 0.86 (Fig. A15). Among these compounds **PBI-N^{10}** exhibited a highest quantum yield of 0.86. **PBI-Se^{10}** exhibited a weak emission along with the lowest quantum yield, which was attributed to the heavy atom quenching effect.[66-68] All the compounds in the neat state showed a hypsochromic absorption and bathochromic emission spectra corresponding to their solutions (Fig. 2.5). **PBI^{10}, PBI-N^{10}** and **PBI-S^{10}** exhibited a bright red emission, while **PBI-Se^{10}** did not show any perceivable emission (Fig. 2.6). The hypsochromic shift in the absorption maxima in the solid state indicate the formation of H-aggregates with the molecules arranged in a cofacial (head-head) manner. Although the H-aggregates are known to be non-emissive, there are some examples with emissive H-aggregates in literature.[69]

Table 2.1. Photophysical properties of PBIs in solution[a] and thin film[b] state.

Entry	Absorption [nm]	Emission[c] [nm]	Stokes Shift (cm^{-1})	Molar extinction coefficient (ε) (L mol^{-1} cm^{-1})	Quantum yield[d] (Q_S)	$\Delta E_{g,opt}$[e] [eV]	Absorption [nm]	Emission[f] [nm]	Stokes Shift (cm^{-1})
PBI^{10}	429, 459, 491, 527	534, 580, 622	249	98,000	0.62	2.29	490, 545	642	4832
PBI-N^{10}	433, 465, 496, 532	539, 595, 625	244	1,27,000	0.86	2.28	499, 547	638	4368
PBI-S^{10}	413, 440, 469, 503	509, 550, 593	234	94,500	0.39	2.41	473, 519	618	4960
PBI-Se^{10}	421, 446, 475, 509	517, 531, 552	191	70,500	0.02	2.37	478, 530	624	4895

[a] Micromolar solutions in $CHCl_3$. [b]Prepared by spin coating of millimolar solution in toluene. [c] The excitation wavelength λ_{ex} = 527, 532, 503 and 509 nm respectively, for compounds **PBI^{10}**, **PBI-N^{10}**, **PBI-S^{10}** and **PBI-Se^{10}**. [d] Relative quantum yields are calculated with respect to Rhodamine-6G (λ_{ex} = 530 nm) in ethanol solution as the standard and compounds in $CHCl_3$. [e] Calculated from the red edge of the absorption band. [f] Excited at the absorption maxima.

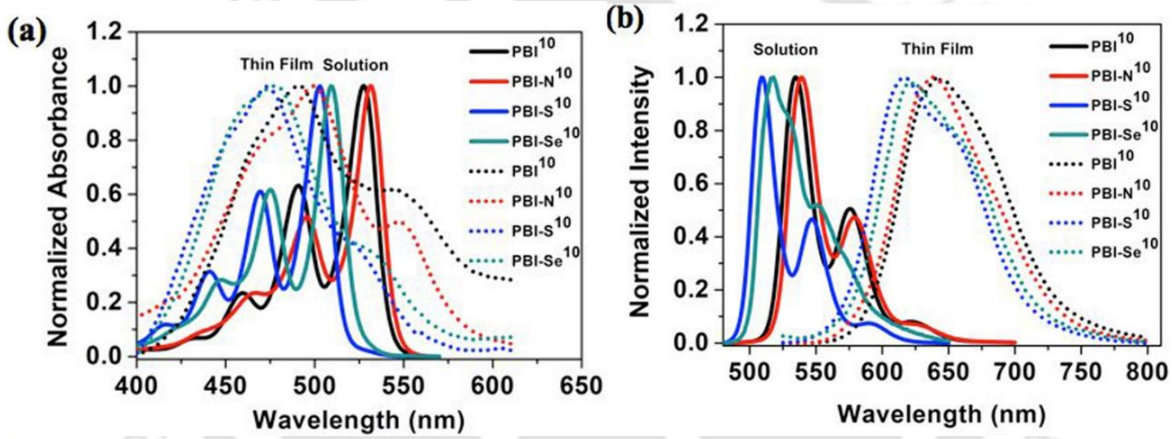

Figure 2.5. Absorption spectra (a) and emission spectra (b) of compounds **PBI^{10}**, **PBI-N^{10}**, **PBI-S^{10}** and **PBI-Se^{10}** **(**Solid lines represent the spectra obtained for micromolar chloroform solutions and dotted line represent the spectra obtained for thin films).

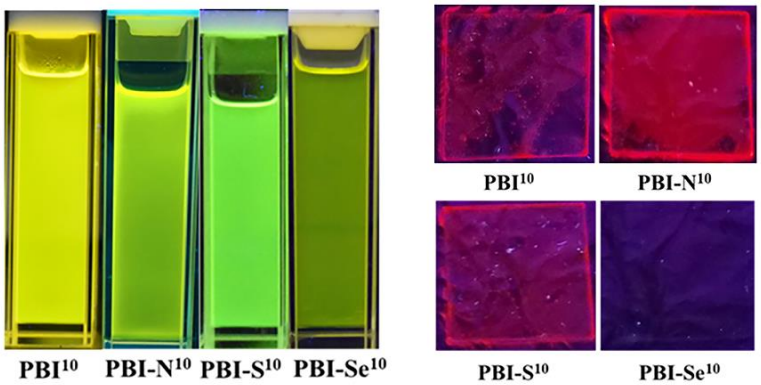

Figure 2.6. Micromolar solutions and spin coated thin-films of PBIs under the illumination of UV light (λ = 365 nm).

Thermal and solvent vapour annealing treatments were tried on the drop-casted films in order to understand the occurrence of any rearrangement in the solid phase. Nearly similar result was obtained either by heating the films at 100 ^{o}C for 10 minutes or by exposing them to dichloromethane vapour for 10 min. The dropcasted thin films on quartz plates did not show much difference in their absorption spectra, (Fig. A11 and A12) except a slight broadening of the absorption spectra and a slight increase in the intensity of the longer wavelength absorption maximum. This could be linked to the reorganization of these molecules into different aggregates upon annealing and a change of orientation to the quartz substrate, affecting their optical and electronic properties.[70] The time resolved fluorescence studies of PBIs in micromolar chloroform solution showed the monoexponential decay of the excited species (τ_1 = in the range of 0.9 to 40 ns for different PBIs Fig. A16 and Table A2.1).

2.2.4. Electrochemical properties

Cyclic voltammetry (CV) studies were conducted to understand the electronic levels of the molecules which play an important role in the energy and electron transfer process as well as the reversibility of a redox process. Electrochemical studies of PBIs were carried out in anhydrous dichloromethane solutions. The energy levels (HOMO and LUMO), band gap values of all the PBIs **PBI^{10}, PBI-N^{10}, PBI-S^{10}** and **PBI-Se^{10}** are tabulated in Table 2.2. PBIs due to their electron deficient nature are considered as n-type semiconductors and known to possess high electron affinity. The optical band gap $E_{g,opt}$ was then estimated from the red edge of the absorption spectra (Table 2.2). Energy levels of LUMO was deduced by using the formula $E_{LUMO} = -(4.8 - E_{1/2,\,Fc,Fc^+} + E_{red,\,onset})$ eV, while HOMO energy levels were determined by using the formula $E_{HOMO} = E_{LUMO} - E_{g,opt.}$. From the electrochemical studies, it was observed that the *bay*-annulated PBIs exhibited elevated LUMO levels in comparison to **PBI^{10}**.

A small increase of 0.20 eV in the HOMO level was observed in the case of **PBI-N^{10}**, whereas **PBI-S^{10}** and **PBI-Se^{10}** showed a lowering of HOMO levels by 0.05 and 0.02 eV, respectively. The values obtained from CV studies showed the same general trend and were comparable to the values obtained from DFT calculations. In comparison to PBIs prepared from alkylamines, **PBI^{10}** exhibited an increased LUMO level and a decreased HOMO level. It is to be noted that in comparison to heteroatom *bay*-annulated PBIs prepared from alkylamines, **PBI-N^{10}**, **PBI-S^{10}** and **PBI-Se^{10}** exhibited lowered HOMO and LUMO levels.[37]

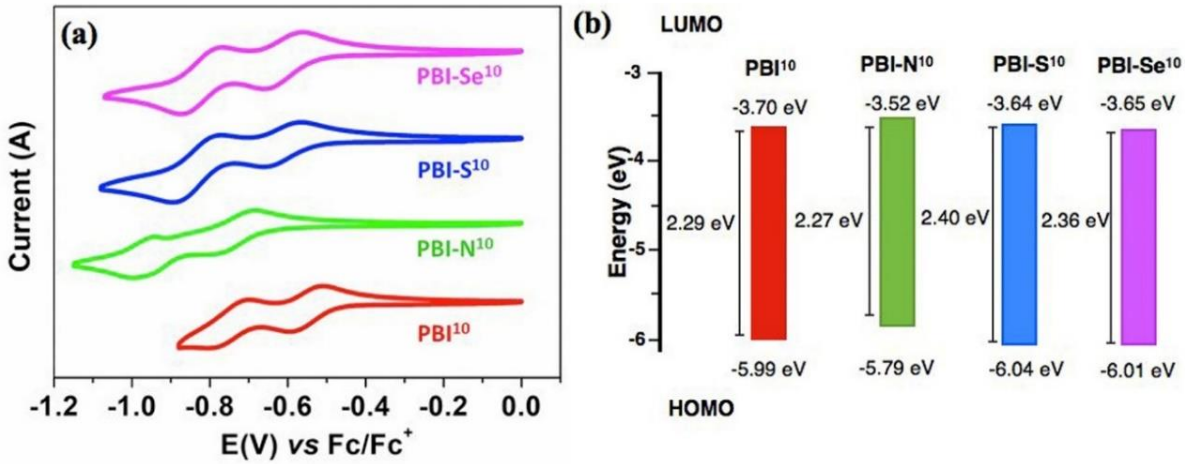

Figure 2.7. Cyclic voltammograms of PBIs (a); Energy band level diagram showing HOMO and LUMO energy levels of PBIs (b).

Table 2.2. Electrochemical[a,b] data and data obtained from DFT[h] calculations for compounds **PBI[10], PBI-N[10], PBI-S[10]** and **PBI-Se[10]**.

Electrochemical data					Data from DFT calculations		
Entry	$E_{1st\ red}$ [c]	E_{LUMO}[d,e]	E_{HOMO}[d,f]	$\Delta E_{g,\ opt}$ [d,g]	E_{LUMO}[d,h]	E_{HOMO}[d,h]	$\Delta E_{g,}$[d,h]
PBI[10]	-0.60	-3.70	-5.99	2.29	-3.35	-5.88	2.53
PBI-N[10]	-0.78	-3.52	-5.79	2.27	-3.23	-5.87	2.64
PBI-S[10]	-0.66	-3.64	-6.04	2.40	-3.31	-6.02	2.71
PBI-Se[10]	-0.65	-3.65	-6.01	2.36	-3.29	-5.99	2.70

[a] 0.5 mM Dichloromethane solutions; [b]experimental conditions: $Ag/AgNO_3$ as reference electrode, glassy carbon working electrode, platinum wire counter electrode, TBAP (0.1M) as a supporting electrolyte, room temperature; [c] in volts (V); [d] in eV; [e] estimated from the formula by using E_{LUMO}= -(4.8 - $E_{1/2,\ Fc/Fc+}$ + $E_{red,\ onset}$) eV; [f] estimated from the formula E_{HOMO} = E_{LUMO} - $E_{g,opt}$) eV; $E_{1/2,\ Fc/Fc+}$ = 0.50 V. [g]calculated from the red edge of the absorption band of each compound.[h] Obtained from DFT calculations by employing the combination of Becke3-Lee-Yang-Parr (B3LYP) hybrid functional and 6-31G(d,p) basis set using the Gaussian 09 package

2.2.5. Density Functional Theory Studies

Density functional theory (DFT) quantum mechanical calculations were carried out to cross check the experimental data obtained from photophysical and electrochemical studies, by employing the combination of Becke3-Lee-Yang-Parr (B3LYP) hybrid functional and 6-31G(d,p) basis set using the Gaussian 09 package. Further, this is also expected to afford information on the geometry, electronic structure, molecular conformation and frontier molecular orbitals (FMOs: HOMO and LUMO) of **PBI[10], PBI-N[10], PBI-S[10]** and **PBI-Se[10]**. Fig. 2.8 shows the energy

minimized space filling models of all the PBIs studied. Pictures of FMOs and the differences in their energies gives us a knowledge about the length of conjugation, the energy levels of HOMO and LUMO and band gap, which in turn helps in the comparison of the PBIs with their hetero atom *bay*-annulated PBIs.

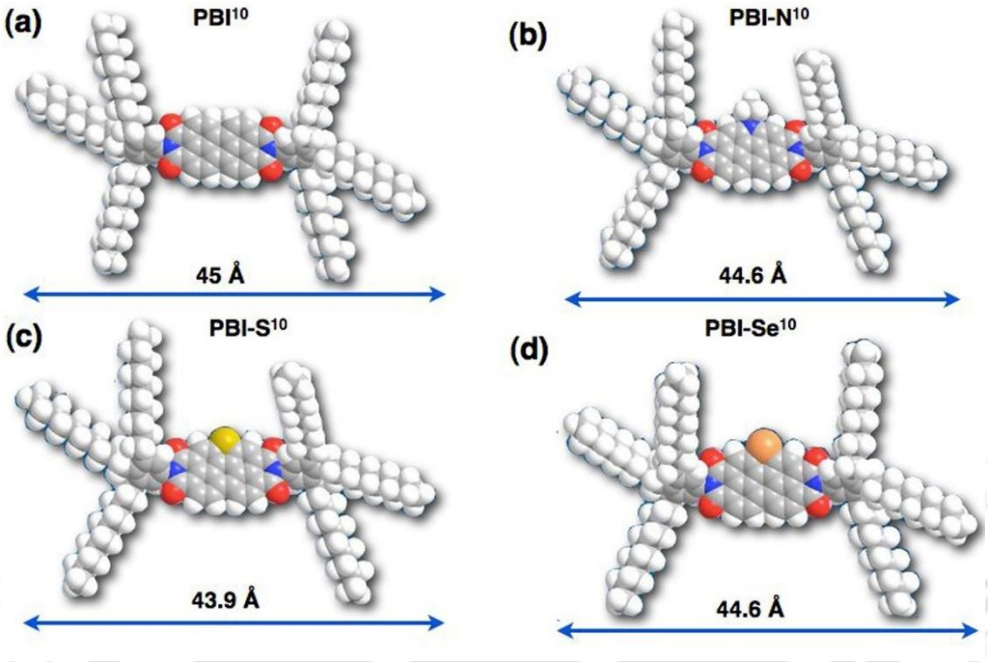

Figure 2.8. Optimized geometry of compounds **PBI[10]** (a), **PBI-N[10]** (b), **PBI-S[10]** (c) and **PBI-Se[10]** (d).

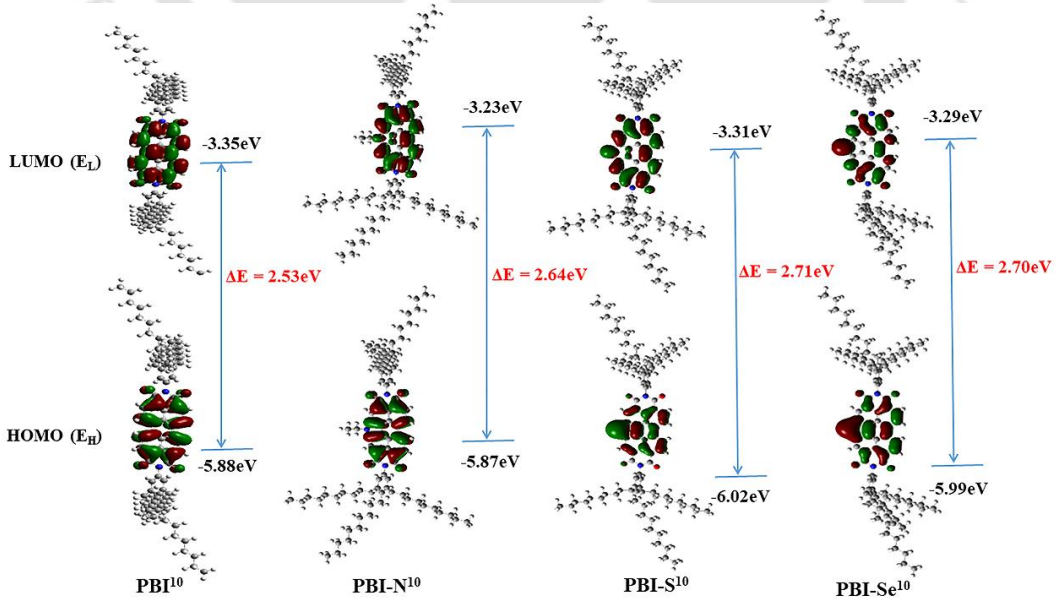

Figure 2.9. Frontier molecular orbitals of compounds **PBI[10]** (a); **PBI-N[10]** (b); **PBI-S[10]** (c) and **PBI-Se[10]** (d) obtained from DFT calculations at the B3LYP/6-31G(dp) level. E_H and E_L denote energies of the highest occupied molecular orbital (HOMO) and the lowest unoccupied molecular orbital (LUMO), respectively.

The contours of the HOMO and LUMO of PBIs are provided in Fig. 2.9. It is seen that the HOMO-LUMO energy levels of these PBIs are dispersed on the central aromatic ring, but not on the trialkyl benzene moieties because of the nodes on the nitrogen atoms of imide units. In the case of *bay*-annulated PBIs, LUMO was found to be spreading over hetero atom. The theoretical band gaps obtained for **PBI[10], PBI-N[10], PBI-S[10]** and **PBI-Se[10]** were 2.53 eV, 2.64 eV, 2.71 eV and 2.7 eV respectively, found to be slightly higher than the optical bandgap (Table 2.2).

2.3. Electroluminescence Studies

The bright deep red or near infrared emission of the liquid crystalline PBIs in solid state and their high solubility in organic solvents motivated us to investigate their applicability in the fabrication of OLEDs. Solution-processed OLEDs were fabricated by following device structures: indium tin-oxide (ITO)/PEDOT:PSS (35 nm)/ PVK (20 nm)/ Neat-Films of **PBI-N[10]** or **PBI[10]** or **PBI-S[10]** or **PBI-Se[10]** (20 nm)/ TPBi (40 nm)/ LiF (1 nm)/Al (200 nm) and indium tin-oxide (ITO)/PEDOT:PSS (35 nm)/ PVK (20 nm)/CBP: 1, 3 and 5 wt% **PBI-N[10]** or **PBI[10]** or **PBI-S[10]** or **PBI-Se[10]** (20 nm)/ TPBi (40 nm)/ LiF (1 nm)/Al (200 nm). In which, Neat films were prepared by **PBI-N[10]** or **PBI[10]** or **PBI-S[10]** or **PBI-Se[10]**. PEDOT:PSS and LiF were incorporated as a hole-injecting and electron-injecting layer, respectively. Poly(vinyl carbazole) or PVK served as a hole-transporting and electron blocking layer. Different emissive layers were prepared by doping CBP host with 1, 3 and 5 wt% **PBI-N[10]** or **PBI[10]** or **PBI-S[10]** or **PBI-Se[10]**. TPBi was used as electron-transporting and hole-blocking layer. ITO and Al served as anode and cathode. The energy-level diagram of the studied OLEDs having LCs as neat films or doped with CBP host is displayed in Fig. 2.10 (a).

The key electroluminscent (EL) properties of all organic LEDs are shown in Fig. A19-A22 (see appendix 2.6) and pertinant data are summarized in Table A2.4 (see annexure 2.6). As observed, the neat films based solution-processed OLEDs displayed poor performance. The **PBI-N[10]**, **PBI[10]**, **PBI-S[10]**, and **PBI-Se[10]** neat-film based devices displayed a maximum luminance of 676, 294, 293, and 177 cd/m^2. The key reasons why the neat films based devices displayed poor performances may be the mismatch of hole-injection and electron-injection barriers which causes

the imbalance of charge carriers in emissive layer, formation of non-radiative exciton formation at HTL and neat-films interface, and concentration quenching due to the aggregation of liquid crystals.[71-78] It is reported that the employement of appropriate host and effective emissive layer formation improves the performance of fluorescent liquid crystals.[63] Hence, by observing both photophysical and electrochemical properties, a carbazole based bipolar organic host CBP has been utilized as an appropriate material for making efficient emissive layer matrix.

The doping concentration of the Col LCs affects the device performance and light emission process. It can be observed that the devices fabricated with **PBI-N^{10}**, **PBI^{10}**, **PBI-S^{10}**, and **PBI-Se^{10}** displayed the best EL performance at 1 wt%. For example, 1 wt% **PBI-N^{10}** based device exhibited a compartively good performance among all of the emitters. The resultant device displayed the best EQE of 4.9% with CIE coordinates of (0.46,0.32) (see Table A2.4 in supporting information). As observed, doped devices exhibited reduced current densities with sufficient enhancement in the brightness. As the dopant concentration increases from 1 to 5%, the current density and luminance decreases from higher to lower brightness (see in Fig. A19a-b, A20a-b, A21a-b, and A22a-b in appendix 2.6). It can be observed that the doped devices showed lower operating voltage and it increases with the dopant concentration from 1 to 5 wt%. The reason why the device shows this behaviour may be attributed to following key factors: imbalanced charge transport in the emissive layer, injection of less charge carriers, trapping of charge carriers, and aggregation of materials at the higher doping concentration.[76-79] We have also observed that the power efficacies and current efficacies of doped devices decrease as the doping concentration increases resulting in the reduced device performance (Fig. A19c-d, A20c-d, A21c-d, and A22c-d in annexure 2.6).

The increase in the concentration may also alter the crystallinity and the thin film morphology of composite material.[80-84] Furthermore, higher doping concentrations of emitters may lead to nonradiative decay of excitons due to the Auger recombination [85,86]. We have also observed the effects of doping concentration on EL spectra of these devices. With the increase in dopant concentration from 1 to 5 wt%, the EL spectra of the devices shifted more towards red region. It also exhibited higher increment in intensity of IR emission peaks as the concentration increases from 1 to 5 wt% (Fig. A19e, A20e, A21e, and A22e in the appendix 2.6). Interestingly, theoretical singlet and triplet energy levels of CBP are significantly higher than that of the LCs, **PBI-N^{10}, PBI^{10}, PBI-S^{10},** and **PBI-Se^{10}**, which helps in efficient energy-transfer from host to guest.[87] The

energy transfer paths are shown in Figure A23.

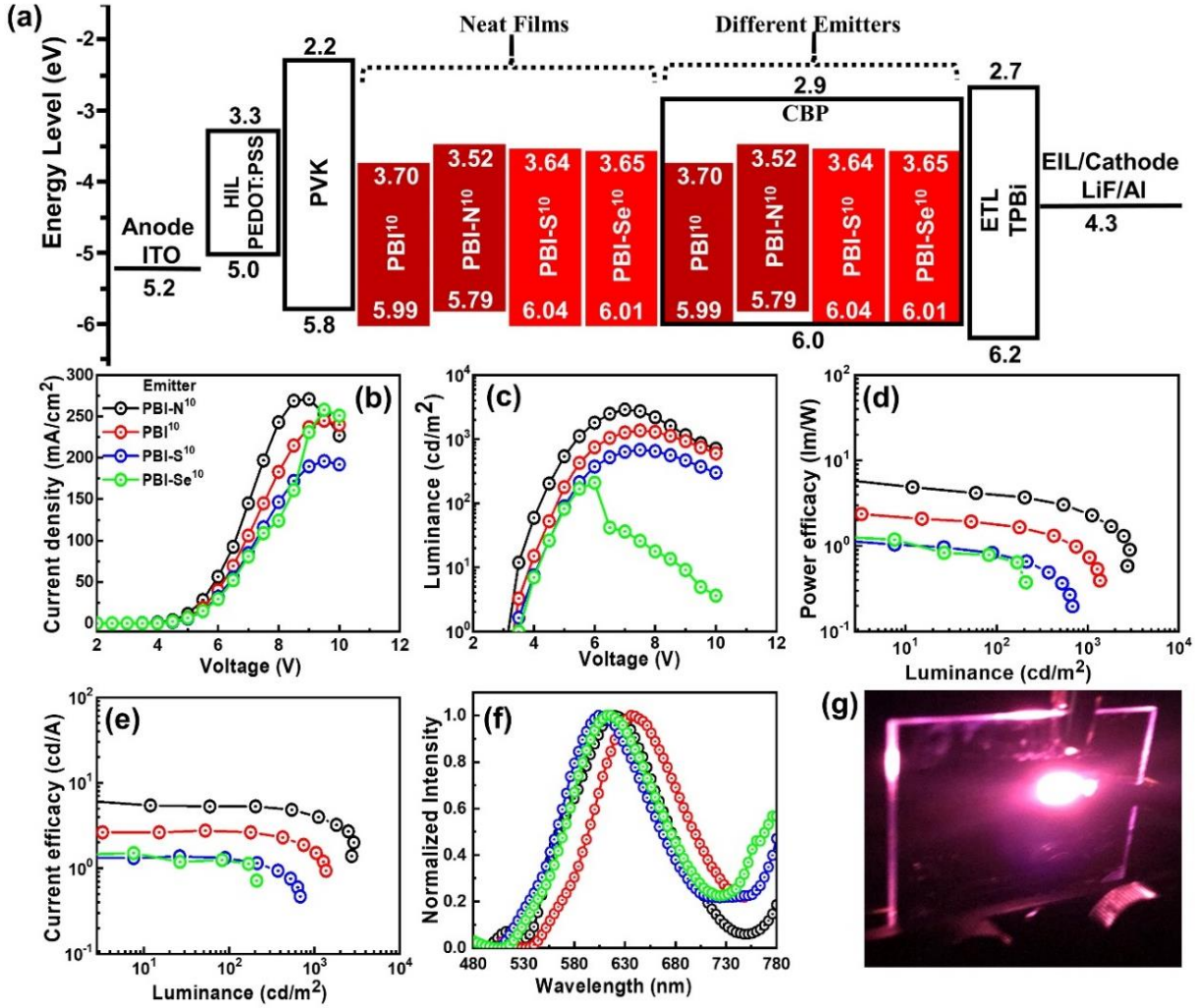

Figure 2.10. (a) Energy-level diagram of OLEDs consisting of neat films and CBP-doped with different emitters, **PBI-N^{10}, PBI^{10}, PBI-S^{10},** and **PBI-Se^{10}**. The electrolumniescent performance of Deep-red-NIR OLEDs fabricated by **PBI-N^{10}, PBI^{10}, PBI-S^{10},** and **PBI-Se^{10}** respectively: (b) current density versus voltage curves, (c) luminance versus voltage curves, (d) power efficacy versus luminance curves, (e) current efficacy versus luminance curves, and (f) EL spectra. (g) Photograph of an electricity-operated NIR organic LED based on best performing emitter **PBI-N^{10}**.

The comparative key EL performances of best performing device at optimized concentration are displayed in Figure 2.10(b-f) and pertinant data are listed in Table 2.3. The 1 wt% **PBI-N^{10}** LC based OLED exhibited a PE_{max} of 7.2 lm/W, a CE_{max} of 6.9 cd/A, an EQE_{max} of 4.9 %, and a L_{max} of 2,900 cd/m^2. While, 1 wt% PBI based device displayed a PE_{max} of 2.4 lm/W, a CE_{max} of 2.7 cd/A, an EQE_{max} of 4.3 %, and a L_{max} of 1,366 cd/m^2. The 1 wt% **PBI-S^{10}** based device demonstrated a PE_{max} of 1.3 lm/W, a CE_{max} of 1.3 cd/A, an EQE_{max} of 2.1 %, and a L_{max} of 683

cd/m^2. The 1 wt% **PBI-Se^{10}** based device exhibited a PE_{max} of 1.2 lm/W, a CE_{max} of 1.4 cd/A, an EQE_{max} of 1.6 %, and a L_{max} of 210 cd/m^2.

Table 2.3. Summarized of OLEDs Consisting of 1.0 wt % Emitters, **PBI-N^{10}**, **PBI^{10}**, **PBI-S^{10}**, and **PBI-Se^{10}** doped in the CBP Host.

Guests	Dopant Con. (wt%)	V_{on} (V)	Power efficacy (lm/W)			Current efficacy (cd/A)			External quantum efficiency (%)			CIE_{xy} @100 cd/m^2	L_{max} cd/m^2
			Max.	100 cd/m^2	1,000 cd/m^2	Max.	100 cd/m^2	1,000 cd/m^2	Max.	100 cd/m^2	1,000 cd/m^2		
PBI-N^{10}	**1.0**	3.0	7.2	4.0	2.4	6.9	5.3	4.2	4.9	4.4	3.2	(0.46,0.32)	2,900
PBI^{10}		3.0	2.4	1.8	0.8	2.7	2.7	1.6	4.3	4.3	1.8	(0.44,0.28)	1,366
PBI-S^{10}		3.3	1.3	0.8	-	1.3	1.3	-	2.1	2.0	-	(0.43,0.25)	683
PBI-Se^{10}		4.0	1.2	1.2	-	1.4	1.3	-	1.6	1.6	-	(0.40,0.23)	210

As observed, the **PBI-N^{10}** based device showed superior performance in terms of higher current-density and luminance in comparison to **PBI^{10}, PBI-S^{10}** and **PBI-Se^{10}**, as shown in Fig. 2.10b and 2.10c. This higher current-density may be attributed to more electron charge-trapping in **PBI-N^{10}** as comparison with other liquid crystals. We also observed that all the devices displayed diode characteristics. Moreover, a rapid increment in forward bias current is observed for **PBI-N^{10}** based OLED, indicating a smaller sheet resistance of the device in comparison to other LCs. Additionally, **PBI-N^{10}** based device displayed low turn-on voltage (3.0 V) in comparison to other devices, which may be attributed to higher hole-mobility, lower hole-injection layer (-0.01) and efficient charge balance into emissive layer. The maximum power efficacy attained for **PBI-N^{10}** based organic LED is 7.2 lm/W which is higher than that of **PBI^{10}** (2.4 lm/W) based device at 5 cd/m^2, as shown in Fig. 2.10d, and current efficacy also exhibited similar trend in curves, as shown in Fig. 2.10e.

The normalized electroluminescence (EL) spectra of all OLED devices is shown in Fig. 2.10f. These EL spectra were obtained from the device fabricated with 1 wt% **PBI-N^{10}**, **PBI^{10}**, **PBI-S^{10}**, and **PBI-Se^{10}** doped in CBP host, at a brightness of 100 cd/m^2. The main emission peaks are displayed at 620, 636, 604, and 616 nm for **PBI-N^{10}, PBI^{10}, PBI-S^{10}**, and **PBI-Se^{10}** based devices, respectively. These main emission peaks almost matched to the solid-state emission spectra of the PBIs, confirming the direct excitation of PBI cores. A shoulder peak with lower intensity at 780 nm was also observed in EL spectra of all devices extending the emission to NIR region. The

shoulder peaks may be attributed to the extensive aggregation of these molecules.[88] The extensive aggregation may lead to the excimer emission, which gave extra peak of 780 nm in the EL spectra.[89,90] Moreover, EL spectra of **PBI-N^{10}** based OLED is wider than that of the other liquid crystals, which suggest that the recombination zone of the charge carriers is wider as compared to other devices. The proper dispersion of guest LCs in host matrix facilitates the radiative decay of singlet excitons, resulting in the efficient electroluminescence. A photograph of the electricity-operated NIR emitting OLED based on the best performing emitter **PBI-N^{10}** is shown in Fig. 2.10g.

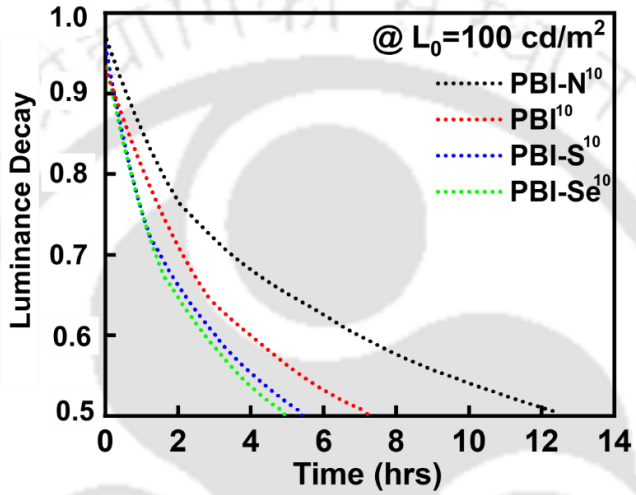

Figure 2.11. Operational lifetime of organic LEDs with emitter **PBI-N^{10}**, **PBI^{10}**, **PBI-S^{10}**, and **PBI-Se^{10}**.

The significant performance of the liquid crystals inspired us to check their device operational stability. Operating lifetime of the devices, fabricated with these LCs, was measured at the initial brightness of 100 cd/m^2. The operational device lifetimes are shown in Fig. 2.11. The lifetimes up to 50% of initial luminance were found 12.4, 7.2, 5.4, and 4.9 h, for **PBI-N^{10}, PBI^{10}, PBI-S^{10},** and **PBI-Se^{10}** respectively. **PBI-N^{10}** LC-based device displayed ~2.5 folds longer device lifetime than that of **PBI-Se^{10}** based device. This longer device lifetime may be attributed to high current-efficacy of **PBI-N^{10}** based device as compared with other devices. These results indicate that the **PBI-N^{10}** based device is comparably stable while applying external voltages. Thus, excellent efficiencies and longer device lifetime of **PBI-N^{10}** based device, confirms that the present design approach is promising to achieve efficient and stable deep red-NIR OLEDs. Although further improvement of the luminance and operational lifetime is required to realize the commercial value of these materials, present results will encourage the researchers working in this area.

2.4. Conclusions

In essence, we have synthesized highly fluorescent electron deficient PBI and heteroatom *bay*-annulated PBIs stabilizing ordered columnar phase over a broad thermal range including ambient temperature. These PBIs are appended with tri-*n*-decylphenyl groups to provide the flexibility and stabilize the liquid crystallinity. Compounds **PBI^{10}, PBI-N^{10}** and **PBI-Se^{10}** exhibited columnar hexagonal phase, whereas the *S*-annulated perylene bisimide **PBI-S^{10}** exhibited columnar oblique phase. The absorption spectra of these molecules exhibited high molar extinction coefficients which will be promising for organic solar cells with a scope to improve further and also to cover the entire visible spectrum by the suitable structural modulation. All the compounds except **PBI-Se^{10}** were found to be highly fluorescent with good quantum yield. The optical band gaps were found to be around 2.3-2.4 eV, with slight differences observed in the HOMO and LUMO levels. Considering the need of new n-type semiconductors with good emission properties, this class of compounds is unique and promising with the additional advantage of columnar self-assembly. The PBIs alone did not show good electroluminescence, however, the host-guest OLEDs prepared by using a carbazole based bipolar host CBP showed a significant improvement. Among the studied PBIs, host-guest OLED with **PBI-N^{10}** as the emitter exhibited a promising electroluminescence with low turn on voltage. This deep red-NIR OLED also showed better operational device lifetime in comparison to other PBIs. Thus, these compounds can be considered as potential solution processable, stable emissive materials for the application in technologically important deep red-NIR OLEDs.

2.5. Experimental section

In this section the detailed synthesis procedure and the molecular structural characterization data have been presented for the intermediates and target compounds mentioned in the scheme.

Procedure for the synthesis of 3, 4, 5-triiodonitrobenzene (6): [91]

An ice-cold solution of sodium nitrite (1.37 g) in concentrated sulfuric acid (7.7 mL) was added dropwise into a well-stirred suspension of 2,6-diiodo-4-nitroaniline (5.5 g, 0.014 mol) in acetic acid (33 mL) in an ice-bath. The reaction mixture was kept below 25 °C with stirring until all diiodonitroaniline was dissolved. The resulting deep yellow solution was poured into ice water (200 mL). Urea (0.5 g) was added into the above reaction solution to remove the excess nitrous

acid and then filtered. The filtrate was added with the solution of potassium iodide (3.30 g) in water (16.5 mL) dropwise with vigorous stirring, leading to the formation of a yellow precipitate. The reaction mixture was heated to 85-90 °C in a water-bath, and afterwards cooled to room temperature. Sodium bisulfite (0.5 g) was added into the reaction solution to remove excess iodine. The yellow precipitate was separated by filtration and washed with water, then dried in vacuum. The crude product was purified by silica gel column chromatography with *n*-hexane /dichloromethane (1:1) as eluent to give a yellow solid. (6.40 g, 91%). R_f = 0.6 (5% EtOAc-Hexane). ^{1}H-NMR (600 MHz, $CDCl_3$, 299 K): δ = 8.61 (s, 2H, Ar-H). ^{13}C NMR (150 MHz, $CDCl_3$, 298.1K): δ 147.50, 132.86, 131.02, 106.96; MALDI-TOF exact mass calculated for $C_6H_3I_3NO_2$ ($M+H^+$): 501.73, found: 501.89.

Procedure for the synthesis of 3,4,5-tris(1'-decynyl)-nitrobenzene (7): [63]

To a well stirred suspension of 3,4,5-triiodonitrobenzene (3.0 g, 6.0 mmol), bis(triphenylphosphine)-palladium(II) dichloride (252 mg, 0.30 mmol), copper(I) iodide (115 mg, 0.60 mmol) in triethylamine (80 mL) under argon atmosphere at 80 °C, 1-decyne (2.737 g, 19.8 mmol) was added dropwise and the reaction mixture was stirred for another 4 h, maintaining the same conditions. After cooling to room temperature, the solid precipitate was filtered and the filtrate was concentrated by rotary evaporation. The residue was purified by silica gel column chromatography with *n*-hexanes to obtain a brown oil (2.9 g, 89%). R_f = 0.70 (5% EtOAc-Hexane). ^{1}H NMR (600 MHz, $CDCl_3$, 299 K): δ = 8.08 (s, 2H, Ar-H), 2.54-2.46 (t, 6H, J = 7.0 Hz, C≡CCH_2), 1.65 (m, 6H, CH_2), 1.4-1.1 (m, 30H, CH_2), 0.88 (t, 9H, J = 6.7 Hz, CH_3). MALDI-TOF exact mass calculated for $C_{36}H_{54}NO_2$ ($M+H^+$): 532.42, found: 532.67.

Procedure for the synthesis of 3,4,5-trisdecylaniline (8): [63]

1,2,3-Tri(1-decynyl)-5-nitrobenzene (1.5 g, 2.82 mmol) was dissolved in a mixture of ethyl acetate (25 mL) and methanol (5 mL). Argon was bubbled through the solution for 15 minutes after which Pd/C (160 mg) was carefully added and the mixture was subsequently subjected to hydrogenation in a Parr hydrogenation apparatus at 150 psi for 24 h. Upon completion of the reaction, the suspension was filtered and the filtrate was concentrated *in vacuo* to yield a reddish brown viscous liquid (1.38 g, 95%). R_f = 0.3 (5% EtOAc-Hexane). ^{1}H NMR (600MHz, $CDCl_3$, 299 K): δ = 6.38 (s, 2H, Ar-H), 2.47 (t, J = 7.4 Hz, 6H, ArCH_2),1.6–1.0 (m, 48H, aliphatic), 0.88 (t, J = 6.8 Hz, 9H, -CH_3). MALDI-TOF exact mass calculated for $C_{36}H_{65}NH_2$ ($M+H^+$): 514.94, found: 514.64.

General procedures for synthesis of PBIs [36]

Compounds **1-4** (1 eq.), tridecyl aniline (2.2 eq.), zinc acetate (2 eq.) and imidazole (1 g) were taken in a microwave vessel, flushed with nitrogen and put in microwave reactor. The mixture was heated to 165 °C for 35 minutes at 35 W and 100 psi pressure. After cooling, reaction mixture was poured into a 2N HCl (10 mL) solution and extracted with chloroform. Organic layer was washed with water and saturated sodium chloride solution. The crude compound was purified by

neutral alumina column chromatography using 50% chloroform-hexane system. Further purification was done by recrystallization from chloroform-methanol system.

PBI[10] : R_f = 0.6 (10% EtoAc-Hexane); Dark red waxy solid, yield: 86%; IR: ν_{max} in cm^{-1}: 2955, 2924, 2854, 1698, 1664, 1592, 1504, 1464, 1439, 1404, 1371, 1332, 1240, 1196, 1114, 858, 809, 744, 722; ^{1}H NMR (600 MHz, $CDCl_3$, 299 K): 8.73 (d, *J* = 12 Hz, 4H, H_{Ar}), 8.63 (d, *J* = 6 Hz, 4H, H_{Ar}), 6.98 (s, 4H, H_{Ar}), 2.65 (m, 12H, 6 × -CH_2), 1.6 (m, 12H, 6 × -CH_2), 1.5-1.1 (m, 84H, 42 × -CH_2), 0.88 (m, 18H, 6 × -CH_3); ^{13}C NMR (150 MHz, $CDCl_3$, 298.1 K): δ 163.85, 142.41, 139.52, 134.99, 132.34, 131.91, 129.87, 126.78, 126.40, 123.84, 123.41, 33.39, 32.18, 32.14, 31.50, 30.98, 30.67, 30.25, 29.92, 29.88, 29.86, 29.74, 29.66, 29.64, 22.59, 22.91, 14.37, 14.35; MALDI-TOF exact mass calculated for $C_{96}H_{139}N_2O_4$ $(M+H)^+$: 1384.07, found: 1384.031.

PBI-N[10] : R_f = 0.6 (10% EtOAc-Hexane); Dark red waxy solid, yield: 86%; IR: ν_{max} in cm^{-1}: 2955, 2923, 2854, 1706, 1667, 1595, 1561, 1466, 1427, 1364, 1351, 1319, 1244, 1185,1127, 845, 807, 744, 722; ^{1}H NMR (600 MHz, $CDCl_3$, 299 K): 9.03 (s, 2H, H_{Ar}), 8.94 (d, *J* =12Hz, 2H, H_{Ar}), 8.87 (d, *J* =12 Hz, 2H, H_{Ar}),7.06 (s, 4H, H_{Ar}), 4.98 (d, *J* = 6 Hz, 2H, N-$\underline{CH_2}$) 2.69 (m, 12H, 6 × -CH_2), 1.66 (m, 3H, N-CH_2-$\underline{CH_3}$), 1.58 (m, 12H, 6 × -CH_2), 1.42-1.26 (m, 84H, 42 × -CH_2), 0.88 (m, 18H, -CH_3); ^{13}C NMR (150 MHz, $CDCl_3$, 298.1 K): δ 165.67, 164.54, 142.47, 139.57, 134.63, 133.87, 132.76, 130.25, 128.20, 126.69,124.06, 123.14, 122.99, 120.16, 119.21, 41.96, 32.17, 30.29, 30.24, 29.92, 29.79, 29.75, 29.71, 29.68, 29.60, 22.94, 22.90, 17.07, 14.38, 14.34; MALDI-TOF exact mass calculated for $C_{98}H_{142}N_3O_4$ $(M+H)^+$: 1425.10, found: 1425.049.

PBI-S[10] : R_f = 0.6 (10% EtoAc-Hexane); Orange red waxy solid, yield: 78%; IR: ν_{max} in cm^{-1} :2955, 2923, 2854, 1706, 1667, 1595, 1561, 1466, 1427, 1364, 1351, 1319, 1244, 1185,1127, 845, 807, 744, 722; ^{1}H NMR (600 MHz, $CDCl_3$, 299 K): 9.39 (s, 2H, H_{Ar}), 9.03 (d, *J* = 12 Hz, 2H, H_{Ar}), 8.99 (d, *J* =12 Hz, 2H, H_{Ar}),7.03 (s, 4H, H_{Ar}), 2.67 (m, 12H, 6 × -CH_2), 1.6 (m, 12H, 6 × -CH_2), 1.5-1.1 (m, 84H, 42 × -CH_2), 0.88 (m, 18H, 6 × -CH_3); ^{13}C NMR (150 MHz, $CDCl_3$, 298.1 K): δ 164.54, 164.09, 142.48, 139.57, 138.63, 133.87, 132.76, 132.13, 130.25, 128.20, 126.69, 126.50, 124.06, 123.73, 123.38, 122.99, 33.40, 32.17, 32.13, 31.50, 30.97, 30.68, 30.24, 29.92, 29.88, 29.86, 29.75, 29.66, 29.64, 29.59, 29.05, 22.94, 22.90, 14.38, 14.34; MALDI-TOF exact mass calculated for $C_{96}H_{137}N_2O_4S(M+H)^+$: 1414.03, found: 1414.509.

PBI-Se[10] : R_f = 0.6 (10% EtoAc-Hexane); Dark red waxy solid, yield: 76%; IR: ν_{max} in cm^{-1}: 2955, 2923, 2854, 1706, 1667, 1595, 1561, 1466, 1427, 1364, 1351, 1319, 1244, 1185, 1127, 845, 807, 744, 722; ^{1}H NMR (600 MHz, $CDCl_3$, 299 K): 9.37 (s, 2H, H_{Ar}), 8.94 (d, *J* =12 Hz, 2H, H_{Ar}), 8.92 (d, *J* =12 Hz, 2H, H_{Ar}), 7.03 (s, 4H, H_{Ar}), 2.67 (m, 12H, 6 × -CH_2), 1.6 (m, 12H, 6 × -CH_2), 1.5-1.1 (m, 84H, 42 × -CH_2), 0.88 (m, 18H, 6 × -CH_3); ^{13}C NMR (150 MHz, $CDCl_3$, 298.1 K): δ 164.54, 164.05, 142.46, 140.99, 138.63, 139.53, 134.88, 133.95, 132.69, 130.50, 126.50, 124.95, 123.55, 123.08, 122.53, 33.40, 32.18, 32.14, 31.49, 30.99, 30.69, 30.26, 29.93, 29.88, 29.87, 29.75, 29.67, 29.65, 29.59, 29.05, 22.95, 22.91, 14.38, 14.35; MALDI-TOF exact mass calculated for $C_{96}H_{137}N_2O_4Se(M+H)^+$: 1461.97, found: 1461.935.

2.6. Appendix

2.6.1. NMR Spectra

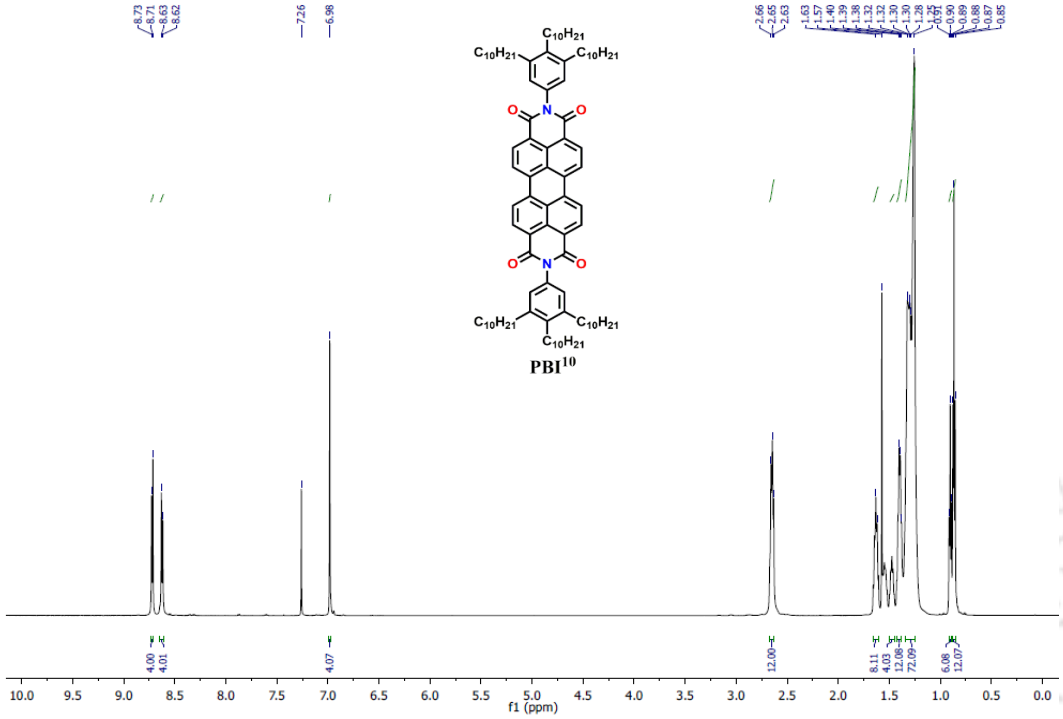

Figure A1. ^{1}H NMR (600 MHz) spectra of **PBI^{10}** in $CDCl_3$.

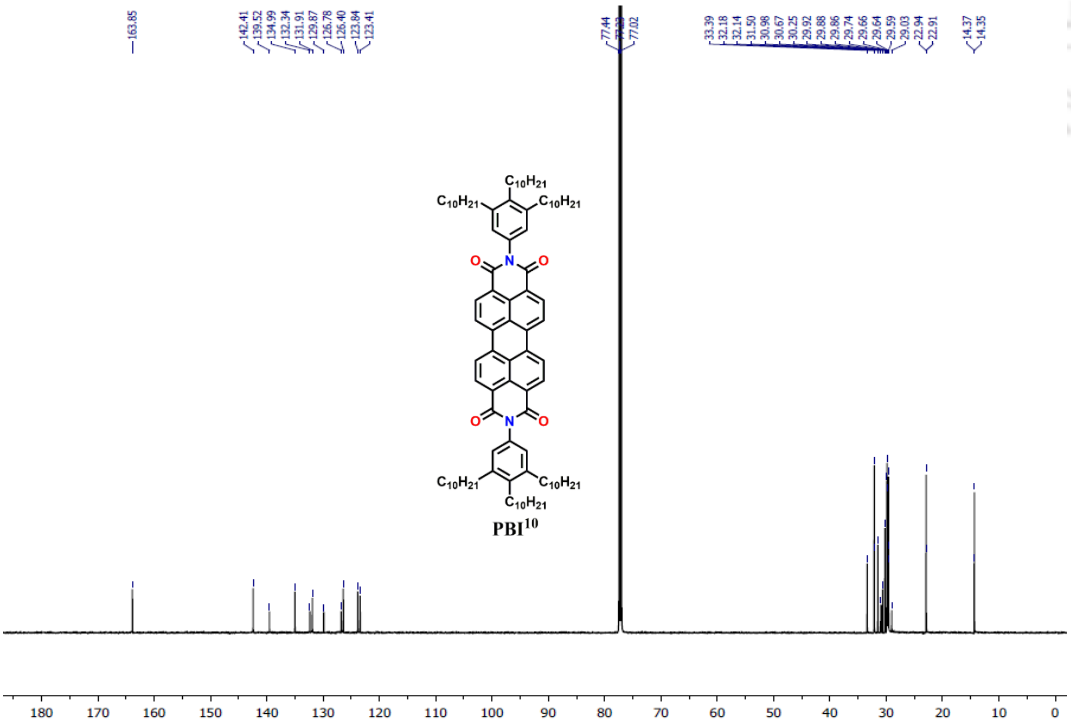

Figure A2. ^{13}C NMR (150 MHz) spectra of **PBI^{10}** in $CDCl_3$.

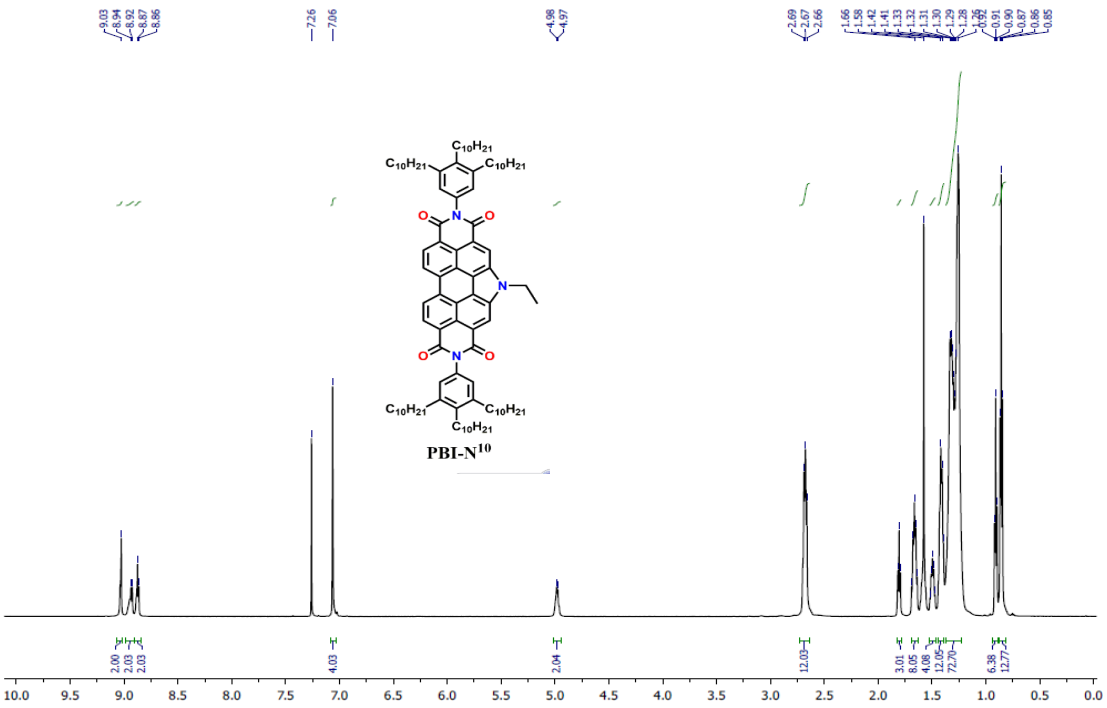

Figure A3. ^{1}H NMR (600 MHz) spectra of **PBI-N^{10}** in $CDCl_3$.

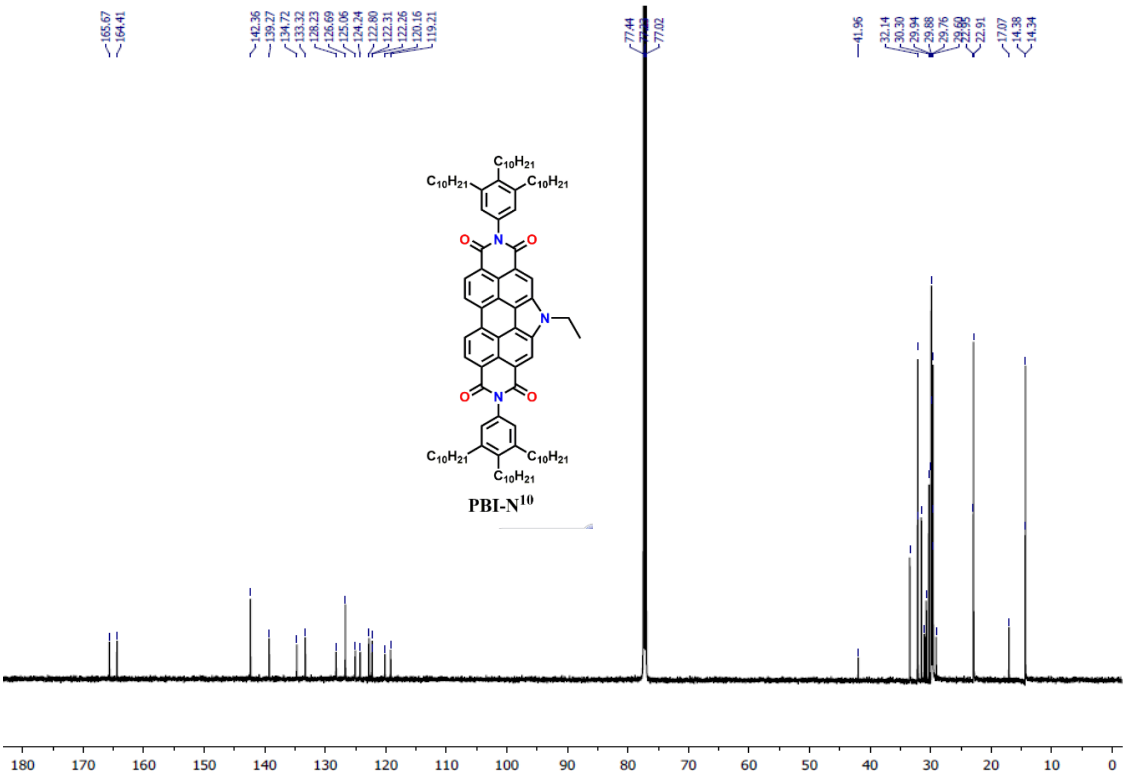

Figure A4. ^{13}C NMR (150 MHz) spectra of **PBI-N^{10}** in $CDCl_3$.

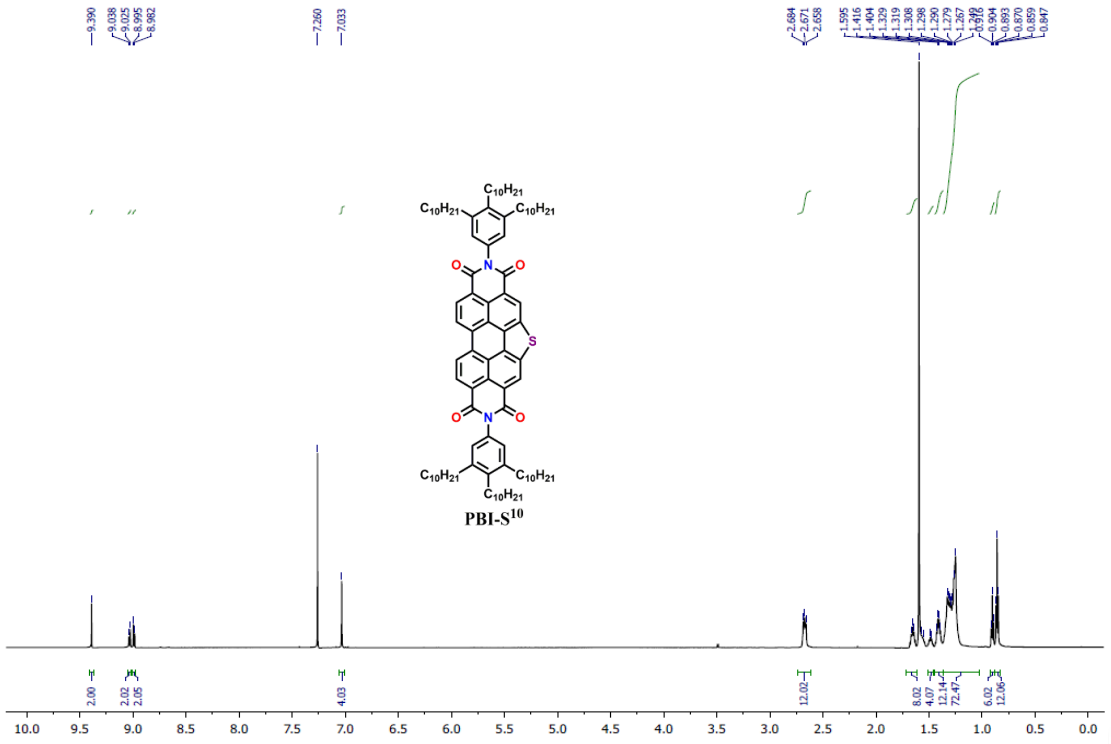

Figure A5. ^{1}H NMR (600 MHz) spectra of **PBI-S^{10}** in $CDCl_3$.

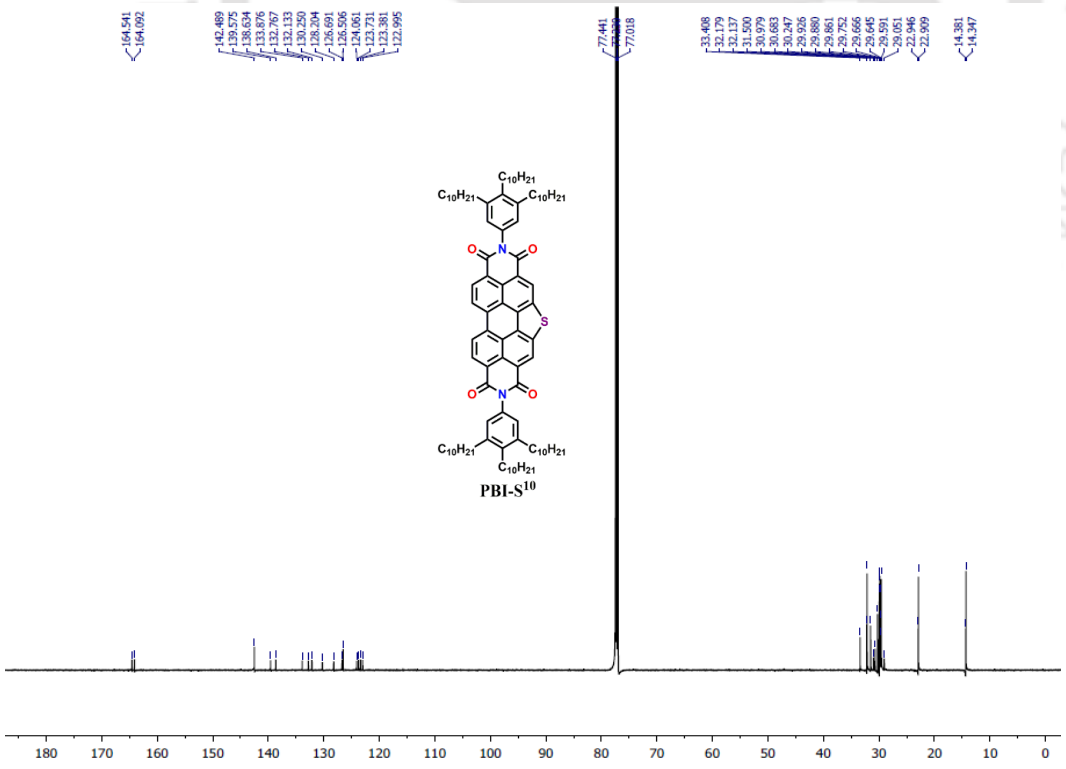

Figure A6. ^{13}C NMR (150 MHz) spectra of **PBI-S^{10}** in $CDCl_3$.

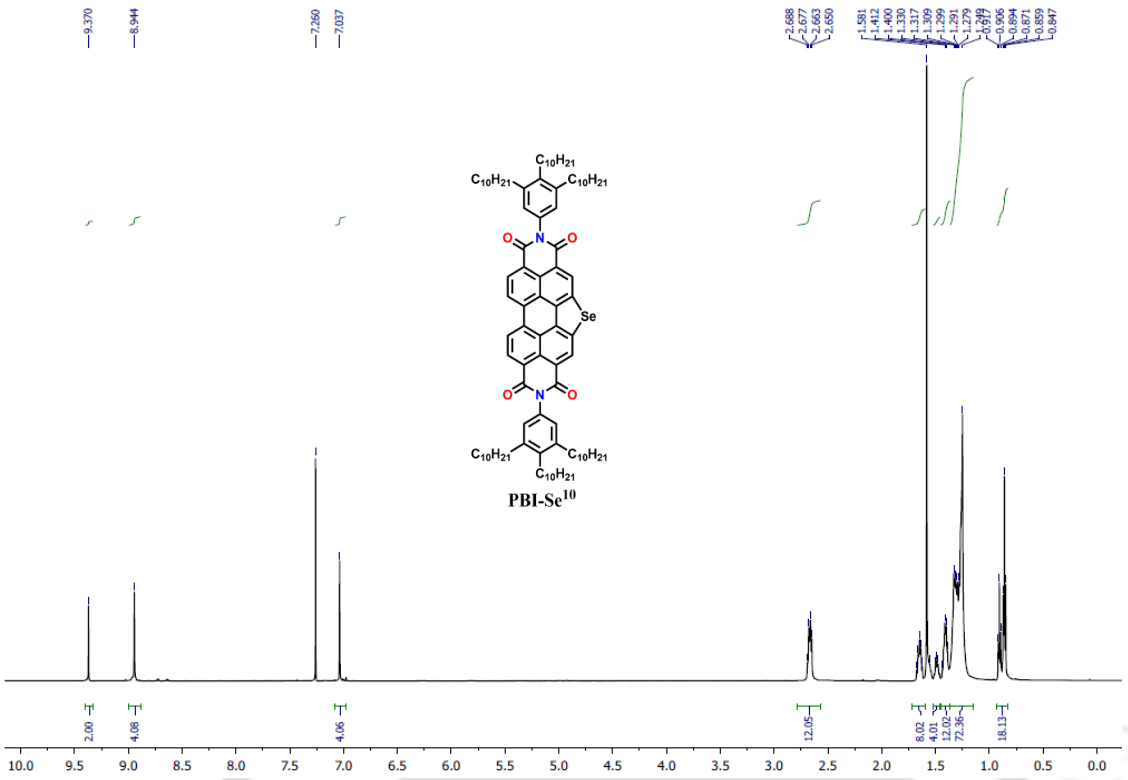

Figure A7. ^{1}H NMR (600 MHz) spectra of **PBI-Se^{10}** in $CDCl_3$.

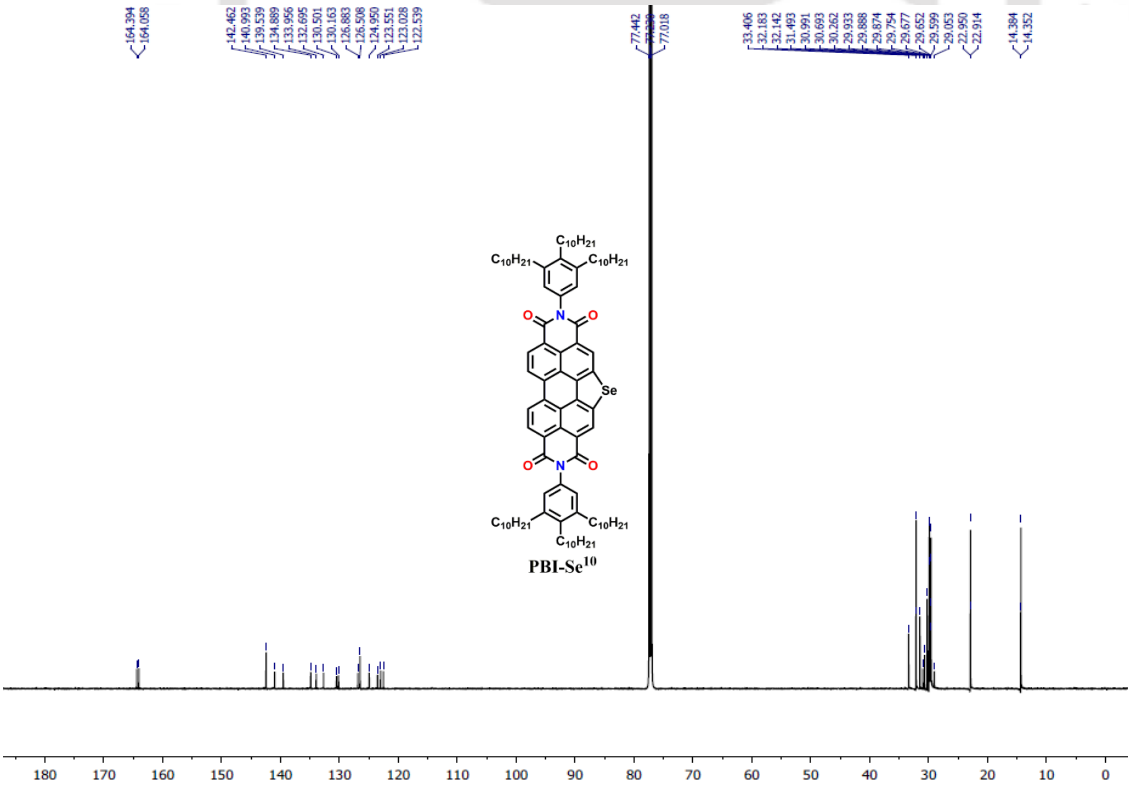

Figure A8. ^{13}C NMR (150 MHz) spectra of **PBI-Se^{10}** in $CDCl_3$.

2.6.2. Photophysical studies

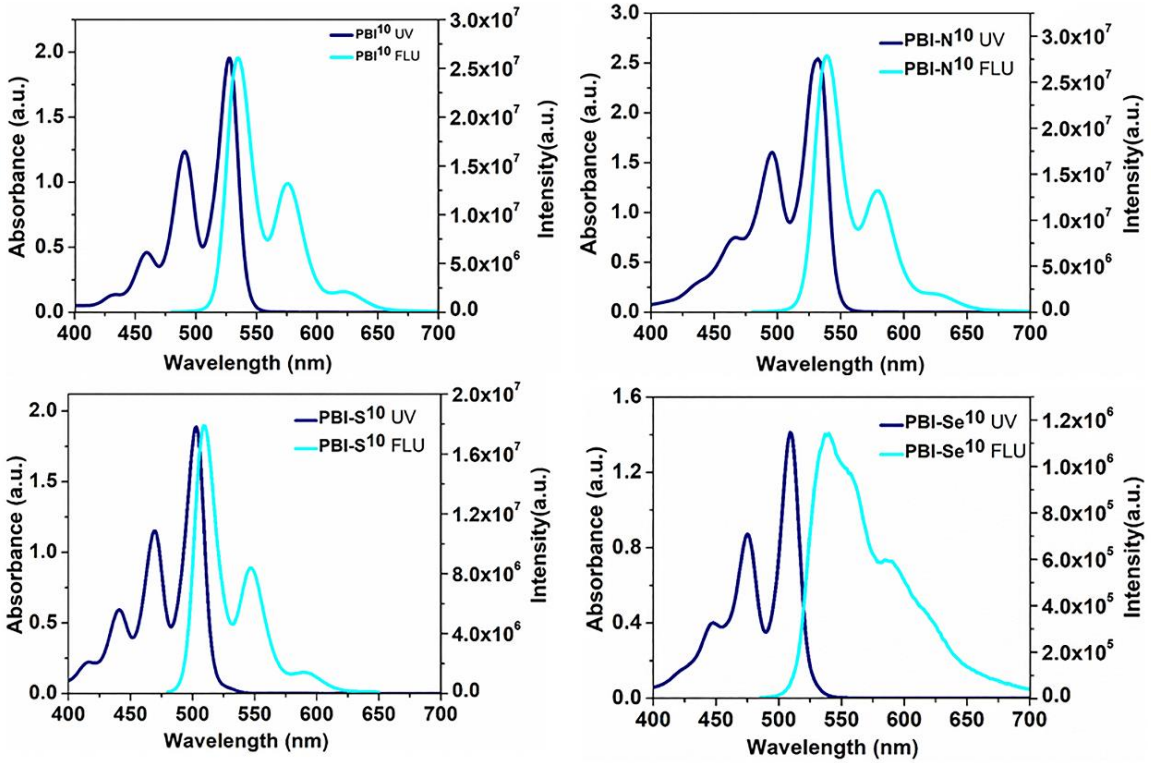

Figure A9. Overlay of absorption (blue trace) and emission (cyan trace) spectra of PBIs in micromolar chloroform solutions**.**

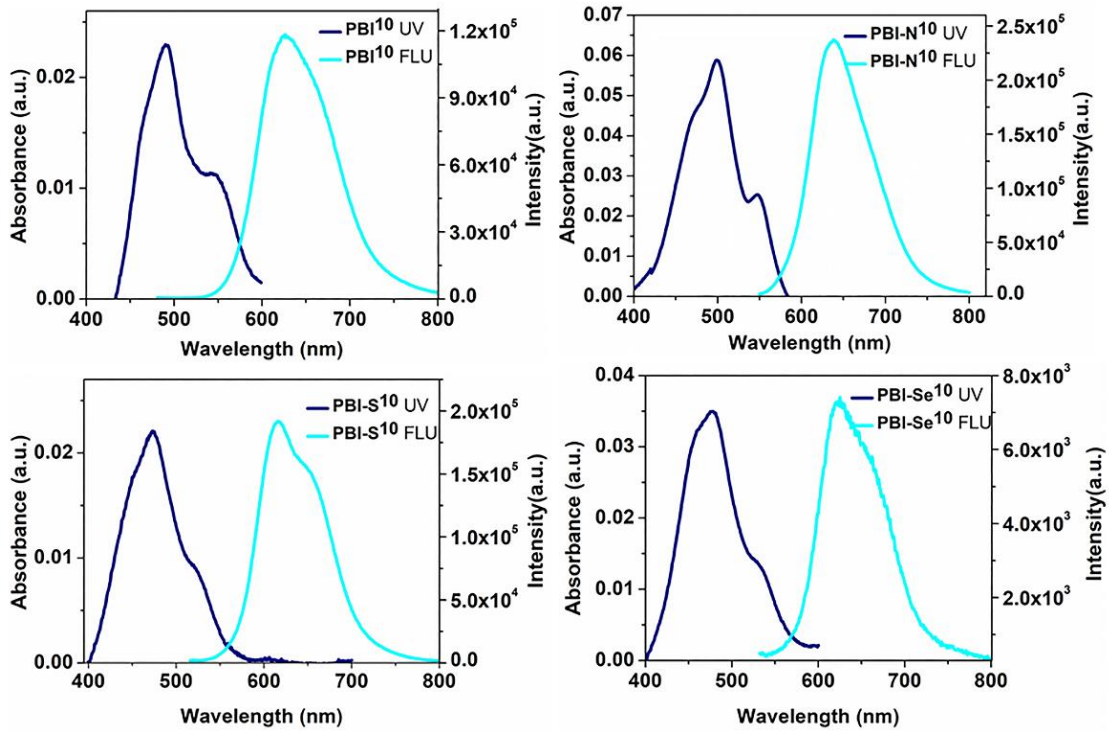

Figure A10. Overlay of absorption (blue trace) and emission (cyan trace) spectra of PBIs in thin film state**.**

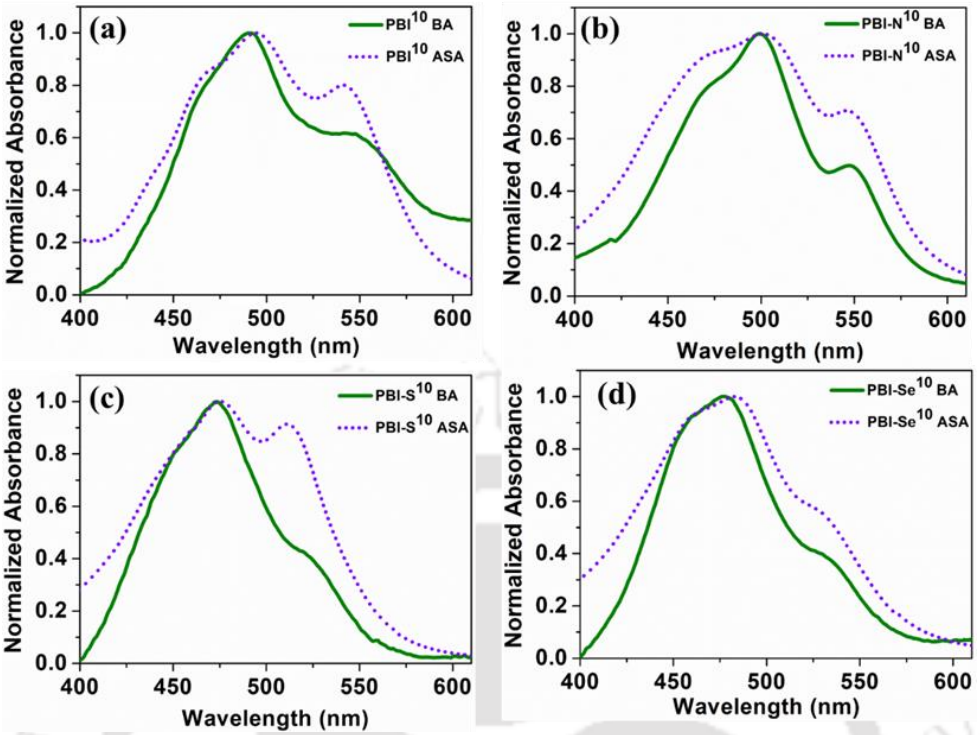

Figure A11. Overlay of the absorption spectra of drop casted thin films of PBIs before (solid line) and after (dotted line) solvent annealing.

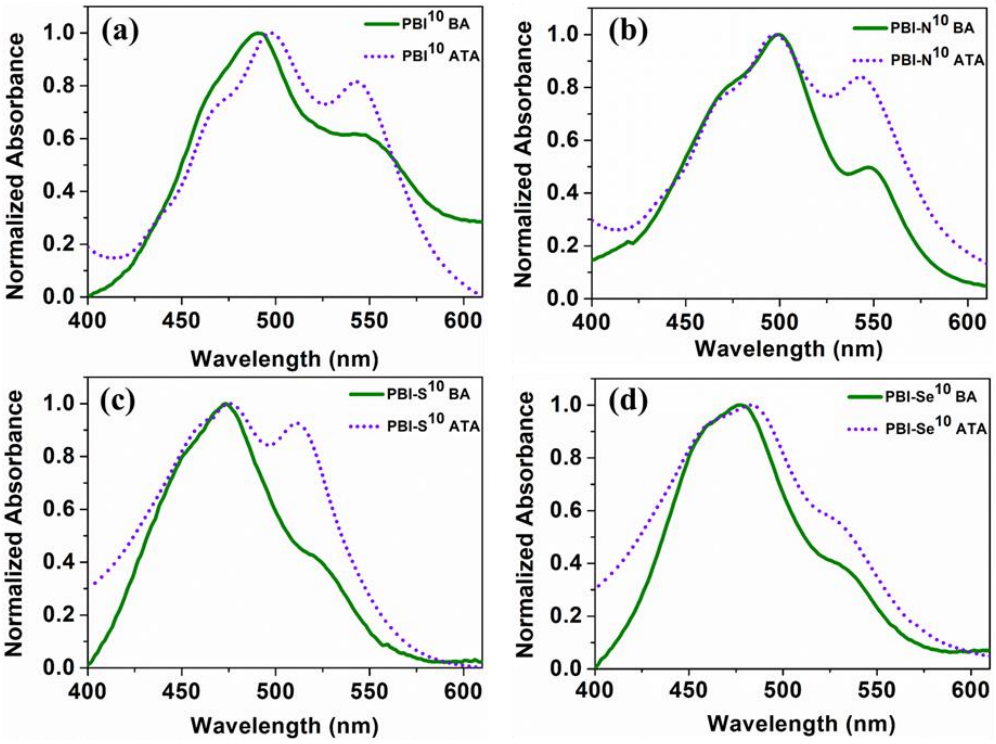

Figure A12. Overlay of the absorption spectra of drop casted thin films of PBIs before (solid line) and after (dotted line) thermal annealing.

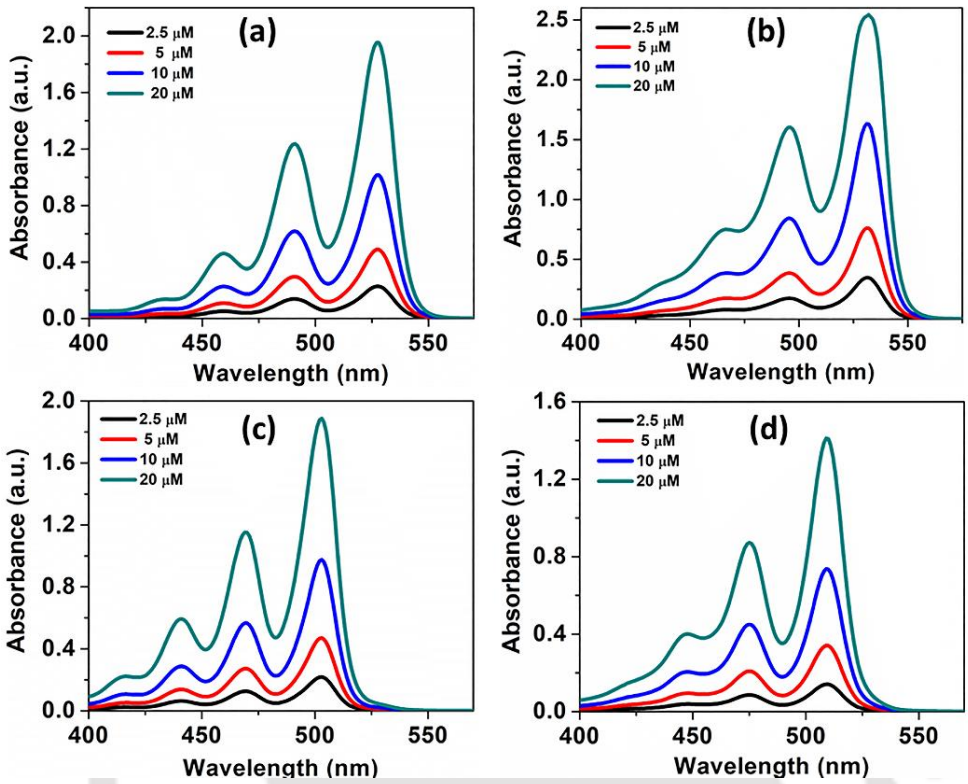

Figure A13. Absorption spectra of **PBI**[10] (a), **PBI-N**[10] (b), **PBI-S**[10] (c) and **PBI-Se**[10] (d) in chloroform solution as a function of concentration.

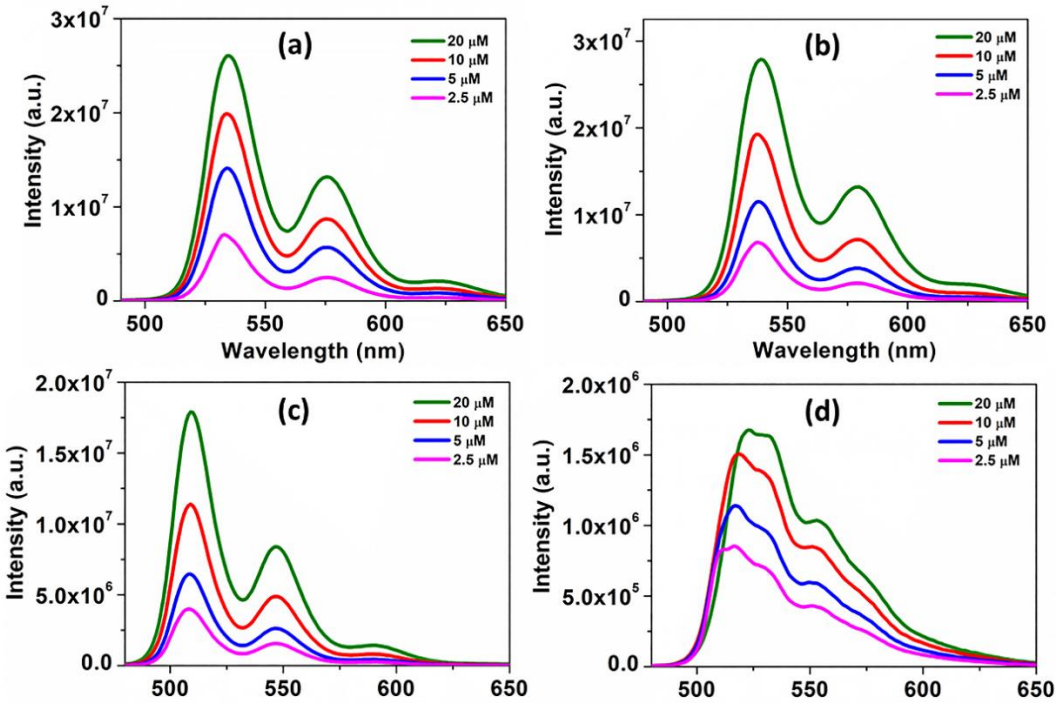

Figure A14. Emission Spectra of **PBI**[10] (a), **PBI-N**[10] (b), **PBI-S**[10] (c) and **PBI-Se**[10] (d) in chloroform solution as a function of concentration.

2.6.3. Quantum yield measurement (Relative)

Quantum yield was measured according to established procedure by using rhodamine 6g in ethanol as the standard. Absolute values were calculated according to the following equation: $Q_S = Q_R \times (m_S / m_R) \times (n_S / n_R)^2$, Where, Q: Quantum yield, m: Slope of the plot of integrated fluorescence intensity vs absorbance (Calculated from Fig.A13), n: refractive index (1.361 for ethanol and 1.445 for chloroform). The subscript R refers to the reference fluorophore i.e. rhodamine 6G solution in EtOH and subscript S refers to the sample under investigation. In order to minimize re-absorption effects, absorbance was kept below 0.15 at the excitation wavelength of 527, 532, 503 and 509 nm respectively for compounds **PBI**[10], **PBI-N**[10], **PBI-S**[10] and **PBI-Se**[10]. Quantum Yield of Rhodamine 6G in EtOH is 0.95. Simplified equation for the calculation after substituting the appropriate values is given below and values obtained are given in table below.

$$Q_S = 0.95 \times (m_s / m_R) \times (1.445/1.361)^2$$

Compounds	m_S	m_R	Q_S [a,b,c]
PBI[10]	8.44794×10^8	1.4208×10^9	0.62
PBI-N[10]	1.26959×10^{10}	1.5694×10^{10}	0.86
PBI-S[10]	5.10306×10^8	1.3867×10^9	0.39
PBI-Se[10]	2.73086×10^7	1.3942×10^9	0.02

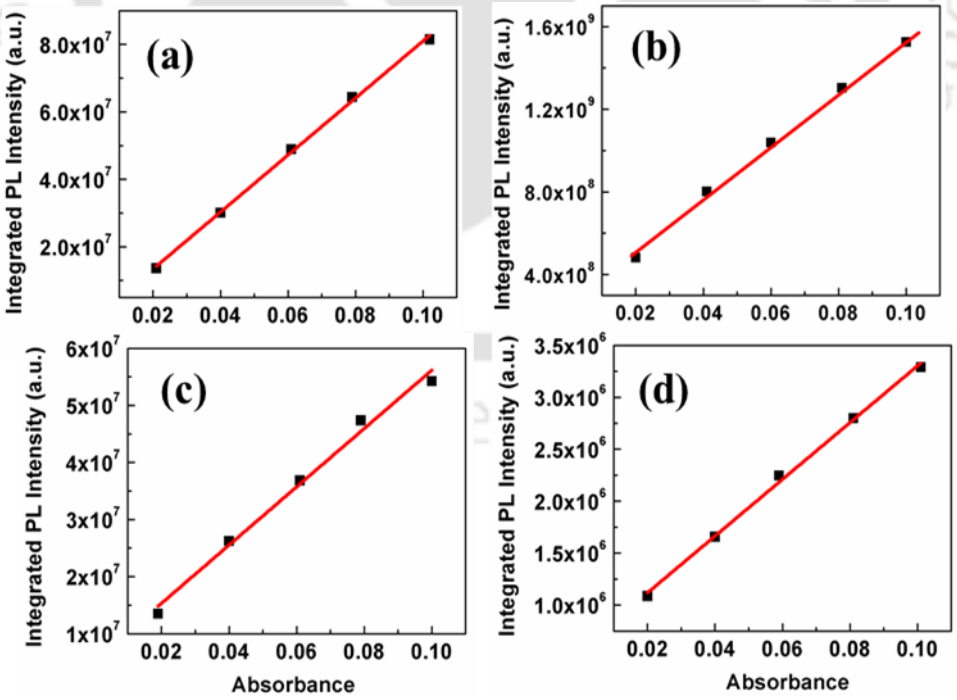

Figure A15. Plots of integrated photoluminescence intensity vs absorbance of reference compound **PBI**[10] (a), **PBI-N**[10] (b), **PBI-S**[10] (c) and **PBI-Se**[10] (d) respectively.

2.6.4. Time resolved photoluminescence studies

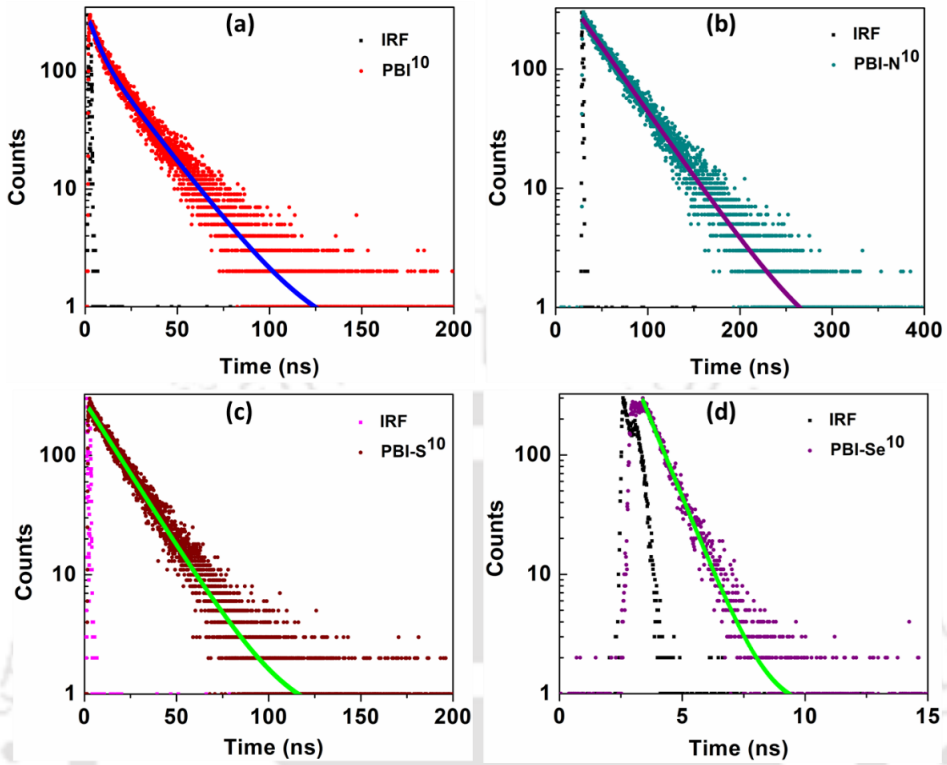

Figure A16. Fluorescence decay plots of compounds **PBI**[10] (a), **PBI-N**[10] (b), **PBI-S**[10] (c) and **PBI-Se**[10] (d) respectively. (IRF: Instrument response function).

Table A2.1. Data obtained from the time resolved photoluminescence experiments of compounds **PBI**[10], **PBI-N**[10], **PBI-S**[10] and **PBI-Se**[10] respectively.

Sl no.	Compound	τ_1 (ns)
1	**PBI**[10]	17.701
2	**PBI-N**[10]	39.693
3	**PBI-S**[10]	17.850
4	**PBI-Se**[10]	0.859

2.6.5. Thermal behavior

Table A2.2. Phase transition temperatures (°C), corresponding enthalpies (kJmol^{-1})[a] and decomposition temperatures obtained by TGA.

Compounds	Phase Sequence (kJ/mol)		
	Second heating	First Cooling	Temperature at which 5 wt% decomposition occurred (°C)
PBI[10]	Col_h 327.66 (7.82) I	I 323.40 (7.84) Col_h	346
PBI-N[10]	Col_h 338.86 (6.12) I	I 334.32 (5.63) Col_h	356

PBI-S[10]	Col_{ob} 349.23 (4.67) I	I 346.00 (3.67) Col_{ob}	349
PBI-Se[10]	Col_h 343.63 (4.02) I	I 334.76 (3.50) Col_h	348
[a] Peak temperatures in the DSC thermograms obtained during the second heating and first cooling cycles at 5 ^{o}C min $^{-1}$. Col_h = Columnar hexagonal phase; Col_{ob} = Columnar oblique phase; I = Isotropic phase.			

2.6.6. XRD Studies

Table A2.3. Results of (*hkl*) indexation of XRD profiles of the compounds at a given temperature (T) of mesophases.[a]

Compounds (D/Å)	Phase (T/^{o}C)	Space Group	d_{obs} (Å)	d_{cal} (Å)	Miller indices *hk*	Lattice parameters (Å), Lattice area S (Å^2), Molecular volume (Å^3)
PBI[10] (44.8) MW: 1384.17	Col_h (200)	P6mm	28.11 16.16 14.64 4.85 (h_a)	28.11 16.23 14.06	10 11 20	a = 32.46 S = 912.6 V = 4426.9 Z = 1.9 [b]
	Col_h (100)		27.74 16.33 13.90 4.65 (h_a) 4.12 (h_c)	27.74 16.02 13.87	10 11 20	a = 32.03 S = 888.7 V = 3667 Z = 1.6
	Col_h (28)		27.44 15.79 13.71 4.60 (h_a) 4.12 (h_c)	27.43 15.84 13.72	10 11 20	a = 31.68 S = 869.2 V = 3584 Z = 1.6
PBI-N[10] (44.6) MW: 1425.22	Col_h (200)	P6mm	25.98 14.94 13.21 5.68(h_a) 4.87 (h_c) 3.67 3.41	25.98 15.00 12.99 -- -- 3.71 3.33	10 11 20 53 54	a = 29.99 S = 779.1 V = 3795.7 Z = 1.6
	Col_h (100)		25.53 14.58 13.11 5.19(h_a) 4.63 (h_c) 3.66 3.38	25.53 14.74 12.76 - - 3.63 3.22	10 11 20 -- -- 44 54	a = 29.48 S = 752.6 V = 3487.7 Z = 1.47(1.5)
	Col_h (25)		25.18 14.06 12.63 4.90 (h_a) 4.52 (h_c) 3.64 3.36	25.18 14.54 12.59 3.63 3.22	10 11 20 -- -- 44 54	a = 29.08 S = 732.4 V = 3307.6 Z = 1.4
PBI-S[10]			28.28	28.28	10	a = 31.39

(43.9) MW: 1414.21	Col_{ob} (200)		16.32 14.04 9.20 8.36 7.99 4.75 (h_a) 3.99 (h_c)	16.32 14.14 9.23 8.16 7.87	11 02 30 22 13	b = 32.04 γ = 61.95° S = 887.6 V = 3541.6 Z = 1.50
	Col_{ob} (100)	P1	27.67 26.18 15.96 15.03 13.57 4.63 (h_a) 3.98 (h_c) 3.49	27.67 26.18 15.96 15.14 13.84 3.52	10 01 11 -21 20 45	a = 30.50 b = 28.86 γ = 65.15° S = 798.5 V = 3177 Z = 1.4
	Col_{ob} (28)		27.31 25.68 15.02 13.38 4.60 (h_a) 4.0 (h_c) 3.47	27.31 25.68 15.02 13.66 3.35	10 01 11 20 54	a = 32.81 b = 30.85 γ = 56.4° S = 842.68 V = 3365.3 Z = 1.4
PBI-Se[10] (44.6) MW: 1461.13	Col_h (200)		28.30 16.30 14.08 5.90 4.82 (h_a)	28.30 16.34 14.15	10 11 20	a = 32.68 S = 925.1 V = 4459.8 Z = 1.8
	Col_h (100)	P6mm	28.00 16.14 13.93 4.65 (h_a) 3.73 (h_c)	28.01 16.17 14.00	10 11 20	a = 32.34 S = 905.8 V = 3384.9 Z = 1.4
	Col_h (28)		27.58 15.89 13.71 4.56 4.176 (h_a) 3.74 (h_c)	27.58 15.93 13.79 3.83	10 11 20 62	a = 31.85 S = 878.5 V = 3660.2 Z = 1.2

[a]The diameter (D) of the disk (estimated from Chem 3D Pro 8.0 molecular model software from Cambridge Soft). d_{obs}: spacing observed; d_{cal}: spacing calculated (deduced from the lattice parameters; a for Col_h phase; a, b for Col_{ob} phase; γ is the tilt angle for Col_{ob} phase; c is height of the unit cell). The spacings marked h_a and h_c correspond to diffuse reflections in the wide-angle region arising from correlations between the alkyl chains and core regions, respectively. Z indicates the number of molecules per columnar slice of thickness h_c estimated from the lattice area S and the volume V. [b] In the absence of h_c, h_a is considered for the calculation of Z.

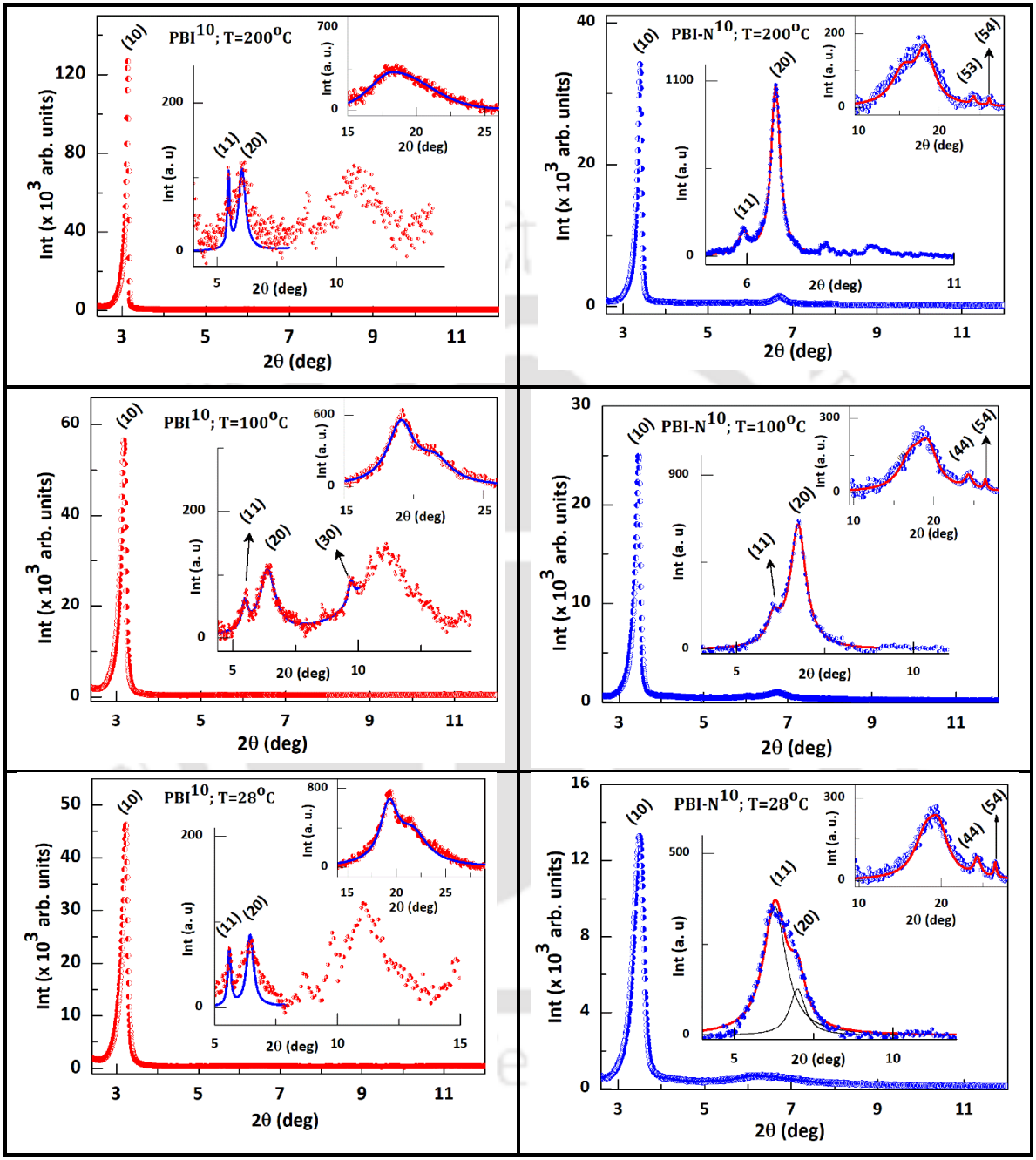

Figure A17. XRD pattern obtained for compound **PBI[10]** (left) and **PBI-N[10]** (right) at different temperature intervals.

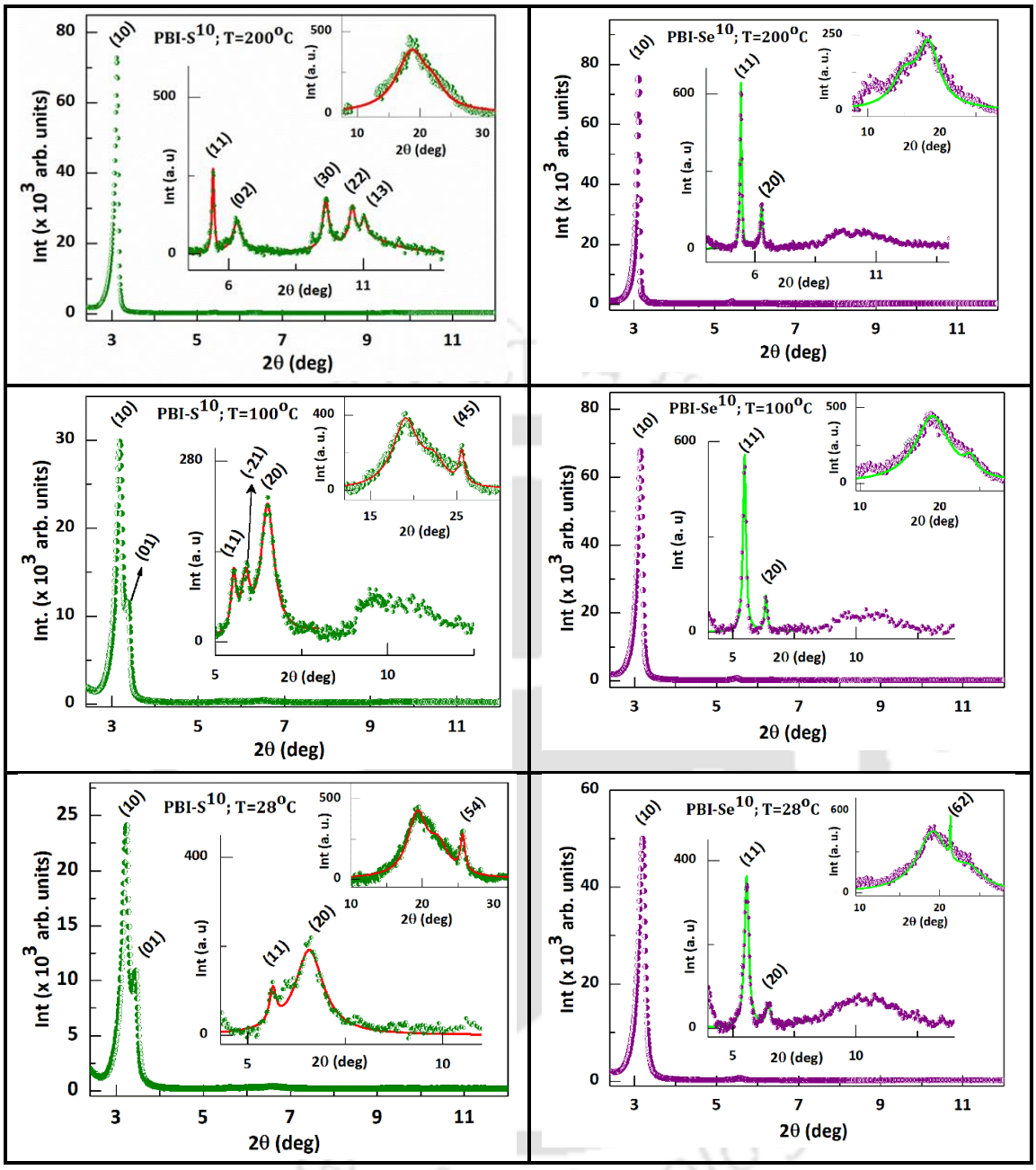

Figure A18. XRD pattern obtained for compound **PBI-S^{10}** (left) and **PBI-Se^{10}** (right) at different temperature intervals.

2.6.7. Device Fabrication and Characterizations

Based on superior photophysical and electrochemical properties, the electroluminescent properties of **PBI-N[10], PBI[10], PBI-S[10]**, and **PBI-Se[10]** emitter materials. Multi-layered solution processed OLEDs were fabricated consisting of following device configurations: indium tin-oxide (ITO)/ PEDOT:PSS (35 nm)/ PVK (20 nm)/ **PBI-N[10]** or **PBI[10]** or **PBI-S[10]**, or **PBI-Se[10]** (20 nm)/ TPBi (40 nm)/ LiF (0.5 nm)/ Al (200 nm) for non-doped device and ITO/ PEDOT:PSS (35 nm)/ PVK (20 nm)/ CBP: **PBI-N[10]** or **PBI[10]** or **PBI-S[10]**, or **PBI-Se[10]** (1,3 and 5 wt%) (20 nm)/ TPBi (40 nm)/ LiF (0.5 nm)/ Al (200 nm) for doped device. Initially, ITO-coated glass substrates were cleaned to remove greasy layer. The cleaning process was carried-out with soap-solution, deionized water, acetone, and alcohol in water-bath sonicator at optimized time. Cleaned substrates were kept in ultra-violet ozone system to expose in UV-light for removing residual solvents and further impurities. Then, these substrates were transferred into nitrogen purged glovebox for further processing of layers.

Simultaneously, the PVK for HTM and CBP as host and newly synthesized emitters for emissive solution layer were dispersed into suitable solvents with water-bath sonicator. Prepared solutions were filtered with 0.45 µm PTFE filters and mixed in desired ratio to prepare emissive layer. First, a hole-injection layer was prepared by spin-coating an aqueous solution of PEDOT:PSS at 4,000 rpm for 20 s. Subsequently, these substrates were annealed at 130 ^{o}C for 15 minutes. Then, a solution of HTM was spin-coated onto hole-injection layer to form a thin-layer of hole transport layer. After that, these samples were treated by 70 ^{o}C for 30 minutes to remove the solvent. After cooled down the substrates, neat solution or emissive layer solution were spin-coated onto hole-transport layer at 2,500 rpm for 20 s.

Then, these substrates were transferred into thermal evaporator to deposit subsequent layers. Then, TPBi was deposited as an electron-transport layer followed by the deposition of 0.5 nm LiF as an electron-injection layer and 200 nm Al as a cathode. All the layers of TPBi, LiF and Al were deposited subsequentially via thermal evaporation method at base pressure of 4.0×10^{-6} Torr. After that, Fabricated devices were kept in the mini vacuum chamber during testing process and then measured at room temperature conditions. To analyse the device, the electroluminescence (EL) spectrum, luminance, and the CIE coordinates were obtained using a photo research (PR-655) spectrometer. The current density-voltage-luminance (J-V-L) characteristics were obtained by a computer mounted voltmeter (Keithley 2400) and spectrophotometer CS-100 Minolta. Lifetime measurement was carried-out with computer mounted Lifetime Test System. Lifetime was investigated without encapsulation of devices.

Table A2.4. Effect of doping concentration on the operation voltage (Von), power efficacy (PE), current efficacy (CE), external quantum efficacy (EQE), CIE coordinates, and maximum luminance of solution-processed deep-red/NIR OLED devices with the CBP host for **PBI-N[10]**, **PBI[10]**, **PBI-S[10]**, and **PBI-Se[10]**.

Hosts	Dopant Concen. (wt%)	V_{on} (V)	Power efficacy (lm/W)			Current efficacy (cd/A)			External quantum efficiency (%)			CIE_{xy} @100 cd/m²	L_{max} cd/m²
			Max.	100 cd/m²	1,000 cd/m²	Max.	100 cd/m²	1,000 cd/m²	Max.	100 cd/m²	1,000 cd/m²		
PBI-N[10]	1.0	3.0	7.2	4.0	2.4	6.9	5.3	4.2	4.9	4.4	3.2	(0.46,0.32)	2,900
	3.0	3.2	2.1	1.3	0.8	2.3	2.0	1.6	2.9	2.9	1.7	(0.54,0.30)	1,820
	5.0	3.5	0.6	0.4	0.5	1.1	0.8	1.0	1.9	1.3	1.2	(0.52,0.27)	1294
	100	3.6	0.6	0.3	-	0.7	0.5	-	0.9	0.9	-	(0.52,0.27)	676
PBI[10]	1.0	3.0	2.4	1.8	0.8	2.7	2.7	1.6	4.3	4.3	1.8	(0.44,0.28)	1,366
	3.0	3.6	0.9	0.8	-	1.3	1.3	-	2.9	2.9	-	(0.39,0.20)	886
	5.0	3.7	0.5	0.4	-	0.6	0.6	-	2.0	1.8	-	(0.33,0.16)	612
	100	4.0	0.2	0.1	-	0.4	0.3	-	0.9	0.8	-	(0.33,0.15)	294
PBI-S[10]	1.0	3.3	1.3	0.8	-	1.3	1.3	-	2.1	2.0	-	(0.43,0.25)	683
	3.0	3.8	0.5	0.3	-	0.6	0.6	-	1.4	1.4	-	(0.39,0.20)	443
	5.0	4.0	0.2	0.2	-	0.3	0.3	-	0.9	0.9	-	(0.33,0.16)	306
	100	4.1	0.2	0.1	-	0.3	0.3	-	0.8	0.8	-	(0.33,0.16)	293
PBI-Se[10]	1.0	4.0	1.2	1.2	-	1.4	1.3	-	1.6	1.6	-	(0.40,0.23)	210
	3.0	4.1	0.7	0.7	-	1.1	1.1	-	1.6	1.6	-	(0.40,0.23)	191
	5.0	4.2	0.6	0.4	-	0.8	0.8	-	1.5	1.5	-	(0.40,0.23)	140
	100	4.0	0.3	0.2	-	0.3	0.3	-	0.9	0.9	-	(0.33,0.16)	177

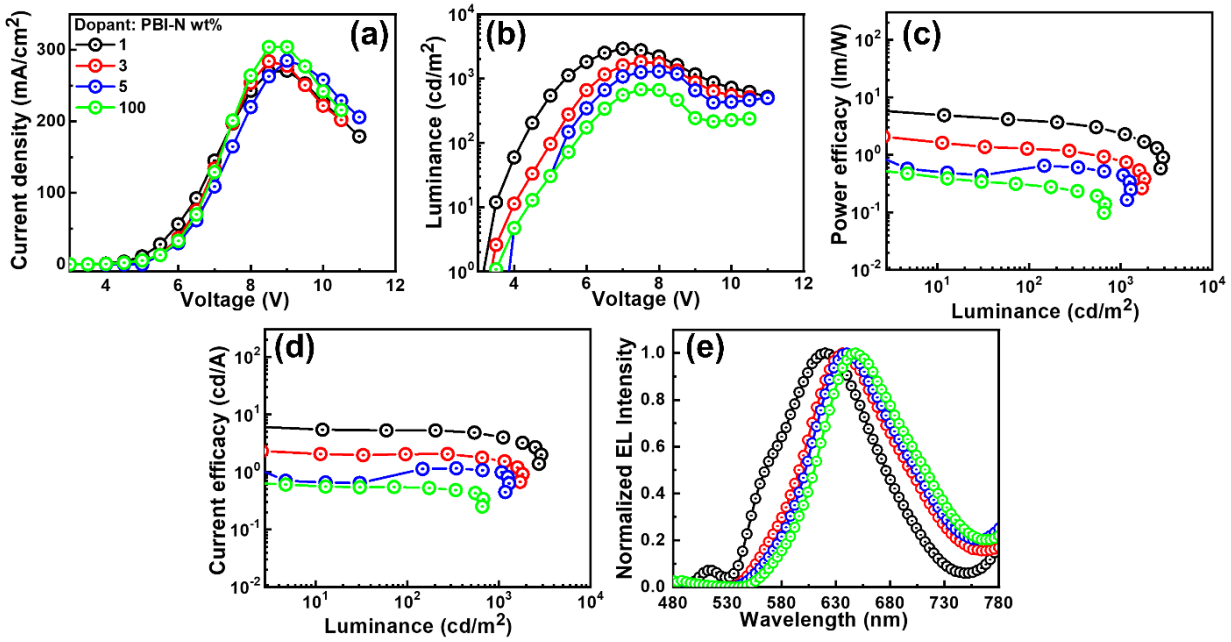

Figure A19. (a) Current density-voltage, (b) luminance-voltage, (c) power efficacy-luminance, (d) current efficacy-luminance, and (e) EL spectra curves of the solution-processed deep-red/NIR OLED using CBP host with 1, 3, 5, and 100 wt% **PBI-N[10]** concentration.

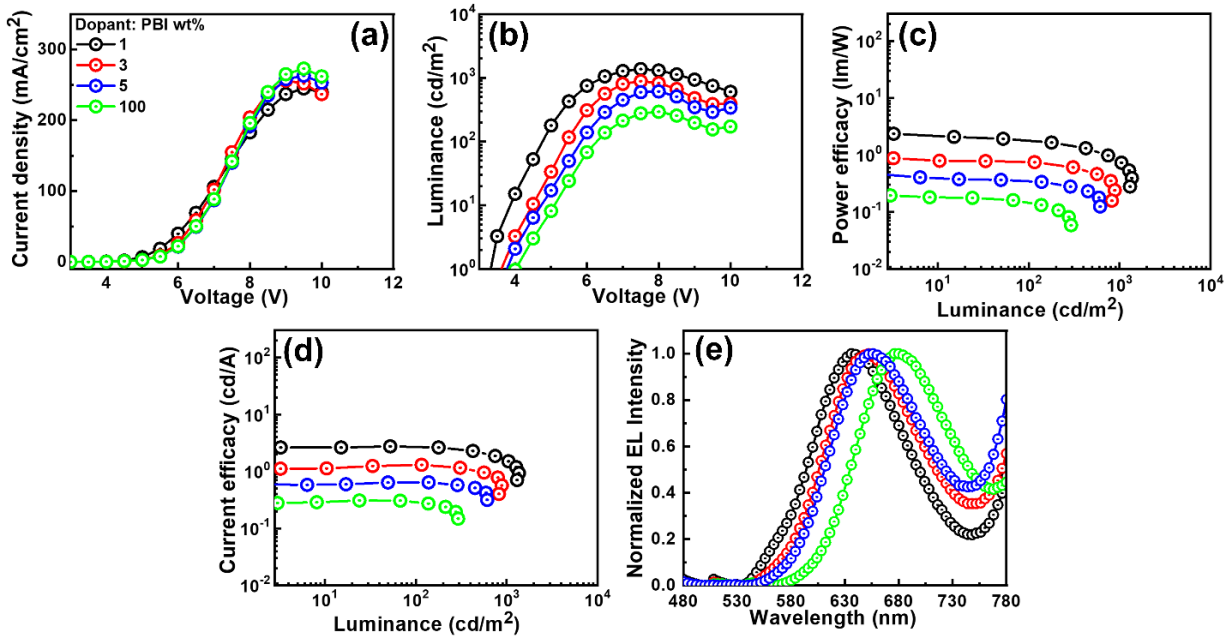

Figure A20. (a) Current density-voltage, (b) luminance-voltage, (c) power efficacy-luminance, (d) current efficacy-luminance, and (e) EL spectra curves of the solution-processed deep-red/NIR OLED using CBP host with 1, 3, 5, and 100 wt% **PBI**[10] concentration.

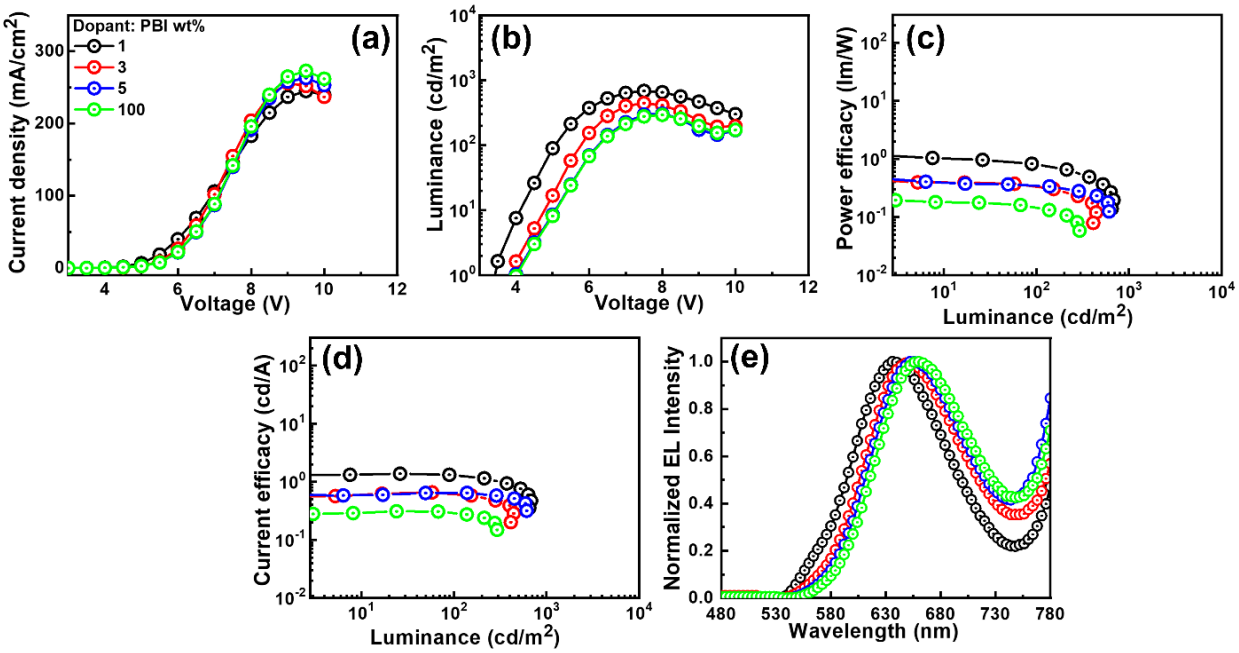

Figure A21. (a) Current density-voltage, (b) luminance-voltage, (c) power efficacy-luminance, (d) current efficacy-luminance, and (e) EL spectra curves of the solution-processed deep-red/NIR OLED using CBP host with 1, 3, 5, and 100 wt% **PBI-S**[10] concentration.

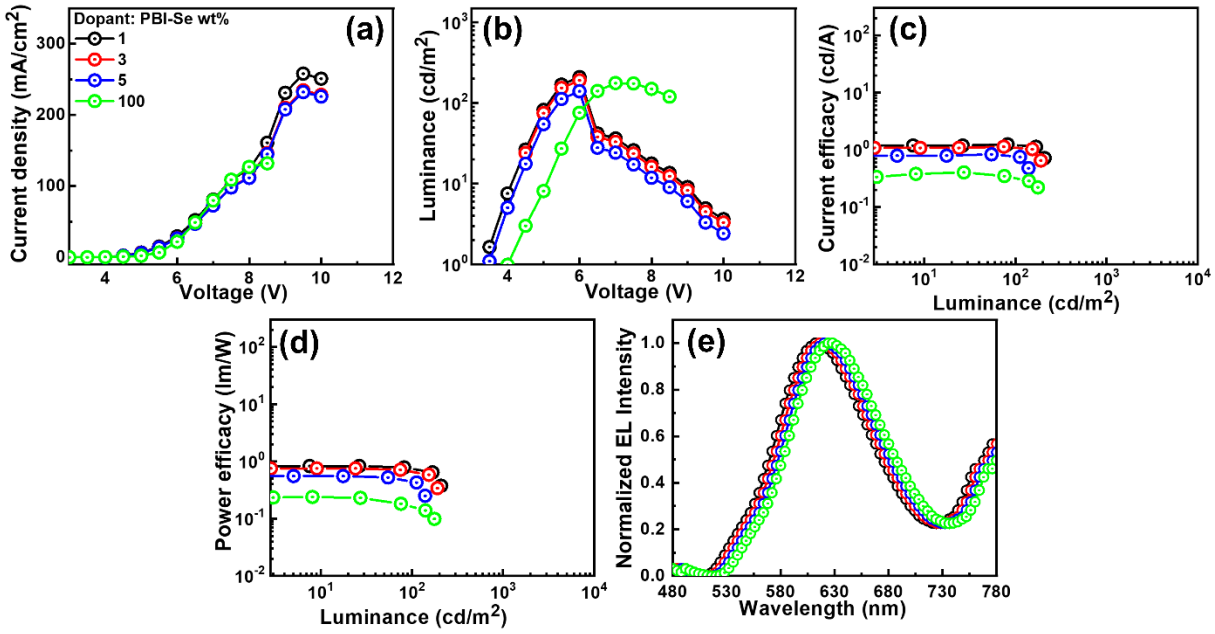

Figure A22. (a) Current density-voltage, (b) luminance-voltage, (c) power efficacy-luminance, (d) current efficacy-luminance, and (e) EL spectra curves of the solution-processed deep-red/NIR OLED using CBP host with 1, 3, 5, and 100 wt% **PBI-Se**[10] concentration.

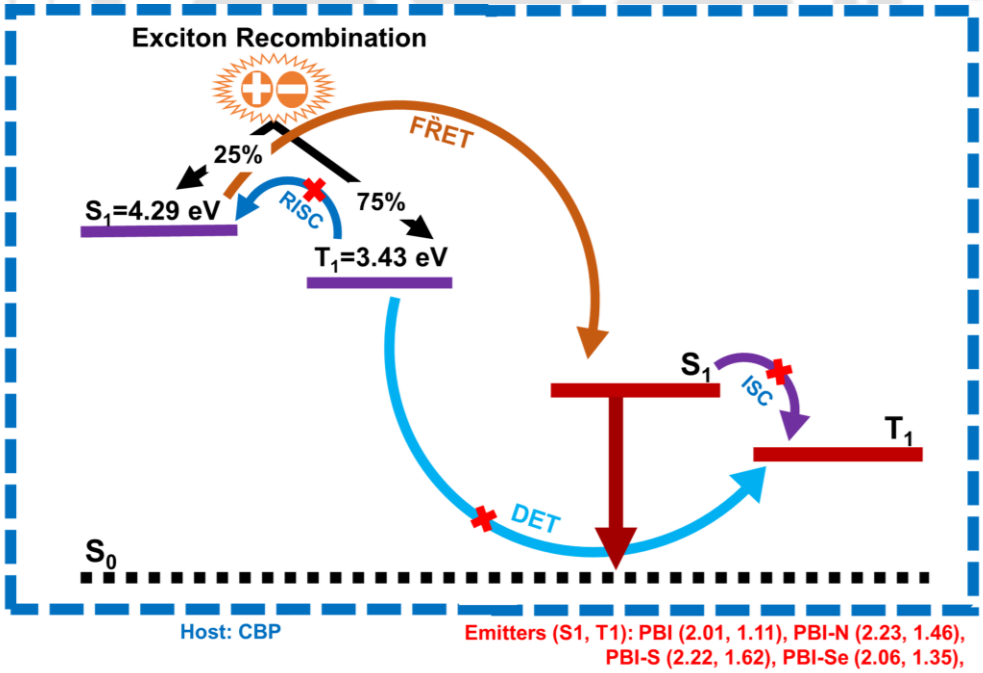

Figure A23. Energy-transfer routes from host-to-guest.

2.7. References

1. W. Herbst and K. Hunger, *Industrial Organic Pigments, Wiley-VCH, Weinheim*, 2004.
2. H. Klauk, Ed. *Organic Electronics: Materials, Manufacturing and Applications*, Wiley-VCH, *Weinheim*, 2006.
3. F. W. Agnieszka Nowak-Król, F. Wurthner, *Org. Chem. Front.*, 2019, **6**, 1272.
4. L. Schmidt-Mende, A. Fechtenkötter, K. Müllen, E. Moons, R. H. Friend and J. D. MacKenzie, *Science,* 2001, **293**, 1119- 1122.
5. B. A. Gregg and R. A. Cormier, *J. Am. Chem. Soc.*, 2001, **123**, 7959–7960.
6. A. J. Breeze, A. Salomon, D. S. Ginley, B. A. Gregg, H. Tillmann and H. H. Horhold, *Appl. Phys. Lett.,* 2002, **81**, 3085–3087.
7. B. A. Gregg, *J. Phys. Chem.*, 1996, **100**, 852–859.
8. A. D. Hendsbee, J.-P. Sun, W. K. Law, H. Yan, I. G. Hill, D. M. Spasyuk, and G. C. Welch, *Chem. Mater.*, 2016, **28**, 7098−7109.
9. H. E. Katz, Z. Bao and S. L. Gilat, *Acc. Chem. Res.*, 2001, **34**, 359-369.
10. F. Wu¨rthner, *Angew. Chem., Int. Ed.*, 2001, **40**, 1037- 1039.
11. P. Jonkheijm, N. Stutzmann, Z. Chen, D. M. de Leeuw, E. W. Meijer, A. P. H. J. Schenning and F. Würthner, *J. Am. Chem. Soc.*, 2006, **128**, 9535–9540.
12. M. A. Angadi, D. Gosztola and M. R. Wasielewski, *Mater. Sci. Eng. B,* 1999, **63**, 191-194.
13. A. Kraft, A. C. Grimsdale and A. B. Holmes, *Angew. Chem., Int. Ed.*, 1998, **37**, 402-428.
14. P. Ranke, I. Bleyl, J. Simmerer, D. Haarer, A. Bacher and H. W. Schmidt, *Appl. Phys. Lett.,* 1997, **71**, 1332-1334.
15. S. Alibert-Fouet, S. Dardel, H. Bock, M. Oukachmih, S. Archambeau, I. Seguy, P. Jolinat and P. Destruel, *Chem. Phys. Chem.*, 2003, **4**, 983–985.
16. S.C. Lo and P. L. Burn, *Chem. Rev.,* 2007, **107**, 1097–1116.
17. E. Kozma, W. Mro´z, F. V.-Monteleone, F. Galeotti, A. A.´-Eckstein, M. Catellani and C. Botta, *RSC Adv.*, 2016, **6**, 61175-61179.
18. J. Vollbrecht, S. Blazy, P. Dierks, S. Peurifoy, H. Bock, and H. Kitzerow, *ChemPhysChem*, 2017, **18**, 2024 – 2032.
19. T. E. Wood and A. Thompson, *Chem. Rev.,* 2007, **107**, 1831–1861.
20. R. S. Loewe, K. Tomizaki, W. J. Youngblood, Z. Bo and J. S. Lindsey, *J. Mater. Chem.,* 2002, **12**, 3438–3451.

21. K. Tomizaki, R. S. Loewe, C. Kirmaier, J. K. Schwartz, J. L. Retsek, D. F. Bocian, D. Holten and J. S. Lindsey, *J. Org. Chem.*, 2002, **67**, 6519–6534.
22. F. Würthner, *Chem. Commun.*, 2004, 1564–1579.
23. F. Würthner, C. R. Saha-Möller, B. Fimmel, S. Ogi, P. Leowanawat and D. Schmidt, *Chem Rev*, 2016, **116**, 962–1052.
24. R. K. Gupta and A. S. Achalkumar, *Langmuir*, 2019, **35**, 2455-2479
25. D. Pfeifer, I. Klimant and S. M. Borisov, *Chem. Eur. J.*, 2018, **24**, 10711–10720.
26. B. P. Jiang, D. S. Guo, Y. Liu, *J. Org. Chem.*, 2010, **75**, 7258−7264.
27. Q. Liu, T. Liu and Y. Fang, *Langmuir*, 2020, **36**, 2155−2169.
28. S. Malkondu, S. Erdemir, *Dyes and Pigments*, 2015, **113**, 763-769.
29. P. Singh, A. Hirsch and S. Kumar, TrAC, *Trends Anal. Chem.* 2021, **138**, 116237.
30. R. K. Gupta, S. K. Pathak, B. Pradhan, D.S.S. Rao, S. K. Prasad, A. A. Sudhakar, *Soft Matter*, 2015, **11**, 3629-3636.
31. R. K. Gupta, B. Pradhan, S. K. Pathak, M. Gupta, S. K. Pal, A. A. Sudhakar, *Langmuir*, 2015, **31**, 8092-8100.
32. R. K. Gupta, S. K. Pathak, B. Pradhan, M. Gupta, S. K. Pal, A. A. Sudhakar, *ChemPhysChem*, 2016, **17**, 859-872.
33. R. K. Gupta, D. Das, M. Gupta, S. K. Pal, P. K. Iyer, A. A. Sudhakar, *J. Mater. Chem. C*, 2017, **5**, 1767-1781.
34. R. K. Gupta and A. S. Achalkumar, *J. Org. Chem.*, 2018, **83**, 6290−6300.
35. R. K. Gupta, D. Das, P. K. Iyer, and A. S. Achalkumar, *ChemistrySelect*, 2018, **3**, 5123 – 5129.
36. R. K. Gupta, D. S. S. Rao, S. K. Prasad, and A. S. Achalkumar, *Chem. Eur. J.*, 2018, **24**, 3566 – 3575.
37. R. K. Gupta, A. Dey, A. Singh, P. K. Iyer, and A. A. Sudhakar, *ACS Appl. Electron. Mater.*, 2019, **1**, 1378−1386.
38. J. Dhar, N. Venkatramaiah, A. Anitha, S. Patil, *J. Mater. Chem. C*, 2014, **2**, 3457 – 3466.
39. Y. Sun, L. Tan, S. Jiang, H. Qian, Z. Wang, D. Yan, C. Di, Y. Wang, W. Wu, G. Yu, S. Yan, C. Wang, W. Hu, Y. Liu, D. Zhu, *J. Am. Chem. Soc.*, 2007, **129**, 1882 – 1883.
40. L. Tan, W. Jiang, L. Jiang, S. Jiang, Z. Wang, S. Yan, W. Hu, *Appl. Phys. Lett.*, 2009, **94**, 153306.

41. Y. Zagra- nyarski, L. Chen, D. Jänsch, T. Gessner, C. Li, K. Müllen, *Org. Lett.*, 2014, **16**, 2814 – 2817.
42. W. Jiang, Y. Zhou, H. Geng, S. Jiang, S. Yan, W. Hu, Z. Wang, Z. Shuai, J. Pei, *J. Am. Chem. Soc.*, 2011, **133**, 1 – 3.
43. H. Iino, T. Usui, J. Hanna, *Nat. Commun.*, 2015, **6**, 6828.
44. A. Patra, Y. H. Wijsboom, S. S. Zade, M. Li, Y. Sheynin, G. Leitus, M. Bendi- kov, *J. Am. Chem. Soc.*, 2008, **130**, 6734.
45. D. J. Schipper, L. C. H. Moh, P. Müller, T. M. Swager, *Angew. Chem., Int. Ed.*, 2014, **53**, 5847-5851; D. J. Schipper, L. C. H. Moh, P. Müller, T. M. Swager, *Angew. Chem.* 2014, **126**, 5957.
46. A. Bedi, S. Debnath, S. S. Zade, *Chem. Commun.* 2014, **50**, 13454–13456.
47. F. T. Burling and B. M. Goldstein, *J. Am. Chem. Soc.*, 1992, **114**, 2313 —2320.
48. J. S. Murray, P. Lane and P. Politzer, *Int. J. Quantum Chem.*, 2008, **108**, 2770 —2781.
49. M. Gsänger, D. Bialas, L. Huang, M. Stolte, and F. Würthner, *Adv. Mater.* 2016, **28**, 3615–3645.
50. S. Shinamura, I. Osaka, E. Miyazaki, and K. Takimiya, *Heterocycles*, **2011**, 83(6), 1187 – 1204.
51. T. Wohrle, I. Wurzbach, J. Kirres, A. Kostidou, N. Kapernaum, J. Litterscheidt, J. C. Haenle, P. Staffeld, A. Baro, F. Giesselmann, S. Laschat, *Chem. Rev.*, 2016, **116,** 1139–1241.
52. T. Hassheider, S. A. Benning, H. S. Kitzerow, M. F. Achard, and H. Bock, *Angew. Chem., Int. Ed.*, 2001, **40**(11), 2060-2063.
53. C. Keum, D. Becker, E. Archer, H. Bock, H. Kitzerow, M. C. Gather, and C. Murawsk, *Adv. Optical Mater.*, 2020, **8**, 2000414.
54. I. Bala, N. Singh, R. A. K. Yadav, J. De, S. P. Gupta, D. P. Singh, D. K. Dubey, J. H. Jou, R. Doualid and S. K. Pal, *J. Mater. Chem. C*, 2020, **8**, 12485—12494.
55. V. Bozkus, E. Aksoy and C. Varlikli, *Electronics*, 2021, **10**(725), 1-12.
56. G. Li, Y. Zhao, J. Li, J. Cao, J. Zhu, X. W. Sun, and Q. Zhang, *J. Org. Chem.*, 2015, **80**, 196−203.
57. L. Zong, Y. Gong, Y. Yu, Y. Xie, G. Xie, Q. Peng, Q. Li, Z. Li, *Science Bulletin*, 2018, **63**, 108–116.

58. S. V. Dayneko, M. Rahmati, M. Pahlevani, G. C. Welch, *J. Mater. Chem. C*, 2020, **8**, 2314-2319.
59. M. Rahmati, S. V. Dayneko, M. Pahlevani, and G. C. Welch, *ACS Appl. Electron. Mater.* 2020, **2**, 48−55.
60. V. Dehm, Z. Chen, U. Baumeister, P. Prins, L. D. A. Siebbeles and F. Würthner, *Org. Lett.*, 2007, **9**, 1085–1088.
61. T. Cardinaels, J. Ramaekers, P. Nockemann, K. Driesen, K. V. Hecke, L. V. Meervelt, S. D. Feyter, E. F. Iglesias, D. Guillon, B. Donnio, K. Binnemans and D. W. Bruce; *Soft Matter*, 2008, **4**, 2172-2185.
62. M.-A. Muth, G. Gupta, A. Wicklein, M. Carrasco-Orozco, T. Thurn-Albrecht, and M. Thelakkat, *J. Phys. Chem. C*, 2014, **118**, 92−102.
63. Z. Chen, V. Stepanenko, V. Dehm, P. Prins, L. D. A. Siebbeles, J. Seibt, P. Marquetand, Volker Engel, and F. Würthner, *Chem. Eur. J.*, 2007, **13**, 436– 449.
64. S. Laschat, A. Baro, N. Steinke, F. Giesselmann, C. Hägele, G. Scalia, R. Judele, E. Kapatsina, S. Sauer, A. Schreivogel and M. Tosoni, *Angew. Chem., Int. Ed.*, 2007, **46**, 4832–4887.
65. D. Zhang, J. Liu, S.Y. Gao, M. V. Bermeshev, Z. Chen and X.-K. Ren, *J. Mater. Chem. C*, 2021, **9**, 9236–9241.
66. D. S. McClure, *J. Chem. Phys.*, 1949, **17**, 905–913.
67. M. Kasha, *J. Chem. Phys.*, 1952, **20**, 71–74.
68. M. N. B. Santos, *PhysChemComm*, 2000, **3**, 18–23.
69. J. Gierschner, L. Lu¨er, B. Milan-Medina, D. Oelkrug and H.-J. Egelhaaf, *J. Phys. Chem. Lett.*, 2013, **4**, 2686–2697.
70. A. Goujon, L. Rocard, H. Melville, T. Cauchy, C. Cabanetos, S. D. Seignon and P. Hudhomme, *J. Mater. Chem. C*, 2022, **10**, 14939-14945.
71. D. Thakur, M. R. Nagar, A. Tomar, D. k. Dubey, S. Kumar, S. S. Swayamprabha, S. Banik, J. H. Jou, and S. Ghosh, *ACS Appl. Electron. Mater.*, 2021, **3**, 2317−2332.
72. Anupriya, K. R. J. Thomas, M. R. Nagar, J. H. Jou, *Opt. Mater.* 2022, **124**, 112017.
73. Anupriya, K. R. J. Thomas, M. R. Nagar, Shahnawaz, J. H. Jou, *J. Photochem. Photobio., A*, 2022, **423**, 113600.

74. Anupriya, K. R. J. Thomas, M. R. Nagar, Shahnawaz, and J. H. Jou, *J. Mater. Sci.: Mater. Electron.*, 2021, **32**, 26838–26850.
75. A. Sharma, K. R. J. Thomas, M. R. Nagar and J. H. Jou, *Mater. Adv.*, 2021, **2**, 6326-6338.
76. S. M. Jung, T. H. Lee, S. Y. Bang, S. D. Han, D. W. Shin, S. Lee, H. W Choi, Y. H. Suh, X. B. Fan, J. W. Jo, S. Zhan, J. Yang, C. Samarakoon, Y. Kim, L. G. Occhipinti, G. Amaratunga and J. M. Kim, *npj Comput. Mater.*, 2021, 7, 122.
77. N. C. Erickson and R. J. Holmes, *Adv. Funct. Mater.*, 2013, **23**, 5190–5198.
78. N. C. Erickson and R. J. Holmes, *Adv. Funct. Mater.*, 2014, **24**, 6074–6080.
79. C. Murawski, K. Leo, M. C. Gathe, *Adv.Mater.*, 2013, **25**, 6801–682.
80. D. Liu, F. Zhu and D. Yan, *J. Mater. Chem. C*, 2022, **10**, 2663-2670.
81. O. F. Pascui, R. Lohwasser, M. Sommer, M. Thelakkat, T. T. Albrecht, and K. Saalwächter, *Macromolecules*, 2010, **43**(22), 9401–9410.
82. C. M. Keum, S. Liu, A. A. Shadeedi, V. Kaphle, M. K. Callens, L. Han, K. Neyts, H. Zhao, M. C. Gather, R. J. Twieg, A. Jakli and B. Lüssem, *Sci. Rep.*, 2018, **8**, 699.
83. Jeffrey Neato. Modeling the Effect of Film Morphology on the Performance of an OLED Device. United States: N. p., 2020.
84. D. Cui, S. Wang, S. Li, Y. Liu, X. Gao, W. Wang, and X. Dong, *Opt. Express*, 2021, 29(11), 16846.
85. B. S. B. Karunathilaka, U. Balijapalli, C. A. M. Senevirathne, S. Yoshida, Y. Esaki, K. Goushi, T. Matsushima, A. S. D. Sandanayaka, and C. Adachi, *Nat. Commun.*, 2020, **11**, 4926.
86. J. Song, F. Zhang, L. Yang, K. Chen, A. Li, R. Sheng, Y. Duan, and P. Chen, *Mater. Adv.*, 2021, **2**, 3677-3684.
87. J. H. Jou, S. Sahoo, S. Kumar, H. H. Yu, P. H. Fang, M. Singh, G. Krucaite, D. Volyniuk, J. V. Grazulevicius and S. Grigalevicius, *J. Mater. Chem. C*, 2015, **3**, 12297.
88. Y. Q. Zhang, G. Y. Zhong, and X. A. Cao, *J. Appl. Phys.*, **108**, 083107.
89. T. Tsuboi and N. Aljaroudi, *Opt. Mater.*, 2008, **30**, 1375–1381.
90. A. Soman, A. K. Sajeev, K. Rajeev, and N. Unni K.N.; *ACS Omega* 2020, **5**, 1698−1707.
91. X. Zhang, Z. Chen, and F. Wu¨rthner; *J. Am. Chem. Soc*. 2007, **129**, 4886-4887.

Chapter 3

Columnar self-assembly of liquid crystalline hetero atom *bay*-annulated perylene bisimides adorned with tri-n-alkoxy anilines and their charge carrier mobility studies

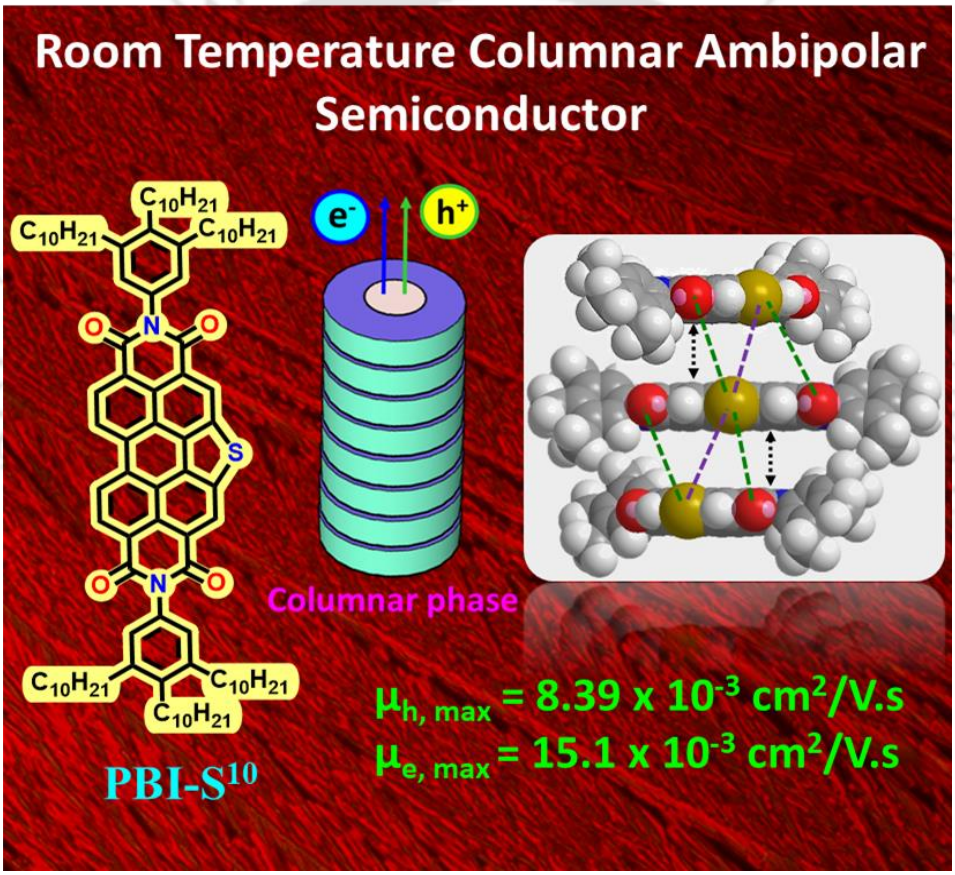

3.1. Introduction

Understanding of the charge transport behaviour in organic semiconductors with respect to their structure is of ultimate importance for the progress of organic electronics. The charge carrier mobility is one such crucial parameter that determines the performance of organic semiconductor based electronic devices like light emitting diodes (OLEDs), field effect transistors (OFETs) and photovoltaics (OPVs). Though the charge carrier mobility is of several orders lower than that of their inorganic counterparts, there is an inevitable requirement to explore organic semiconductors with respect to their molecular structure for further advancement towards the light weight, large area, low cost and flexible devices. These semiconductors can be solubilized in various organic solvents to create inks, which can be used later to print them on flexible substrates to reduce the cost. Most of the known organic semiconductors are hole-transporting (p-type), which accept and transport holes, while electron-transporting (n-type) semiconductors are rare and face stability issues. Thus, there is huge requirement of research dedicated to the synthesis of new processable n-type organic semiconductors.[1] From the viewpoint of organic electronic devices, having separate n- and p-type semiconductors (unipolar charge transport) lead to the utilization of these materials as blends or to use them as bilayers to ensure the hole and electron transport. In contrast, to have a single component ambipolar semiconductor capable of transporting both electrons and holes, simplifies the device fabrication process and thus promise low cost, light weight, flexible and portable electronic devices. Further it will also reduce the number of boundaries that cause charge carrier traps. Thus it is necessary to develop ambipolar organic semiconductors with a balanced hole and electron carrier mobility along with a lowered band gap.[2,3]

Perylene bismides (PBIs) are one of the most studied n-type semiconductors with high thermal, chemical and photochemical stability. Their low lying LUMO level and highly reversible redox behaviour makes them ambient oxidation resistant n-type organic semiconductors. In addition, they can be functionalized (at *bay*- and *headland* positions, 12 functionalizable positions) to alter the electronic properties and the nature of self-assembly. This tunability of the molecular structure opens the possibility to utilize the realization of elaborate molecular architectures aimed at various applications. Functionalization at the imide positions do not alter the optical property of the PBI due to the presence of imide nodes, while definitely control the self-organizing ability of the PBI. Substitution at imide nitrogen can be used to tune the solubility and hence the solution processability of the material.[4] In contrast, substitution at the *bay*-position alter the planarity of the

molecule due to the steric hindrance of the bay substituents, and thus alter the packing of the PBIs and their self-assembly. However, the hetero atom *bay*-annulation will keep the planarity intact, and hence without affecting the self-assembly, provide a handle to tune the electronic properties.[5-7] In addition, sulfur and selenium incorporated organic semiconductors are gaining importance due to the additional intermolecular S···S and Se···Se interactions.[8-16] Considering the presence of oxygen (O) atoms from the carbonyls of imide units in PBIs, Further, there is a possibility of S···O and Se···O interactions which involve sulfur and selenium σ-holes.[17,18] This compliments the molecular self-assembly and also could play a major role in enhancing 1D charge transport.[19,20]

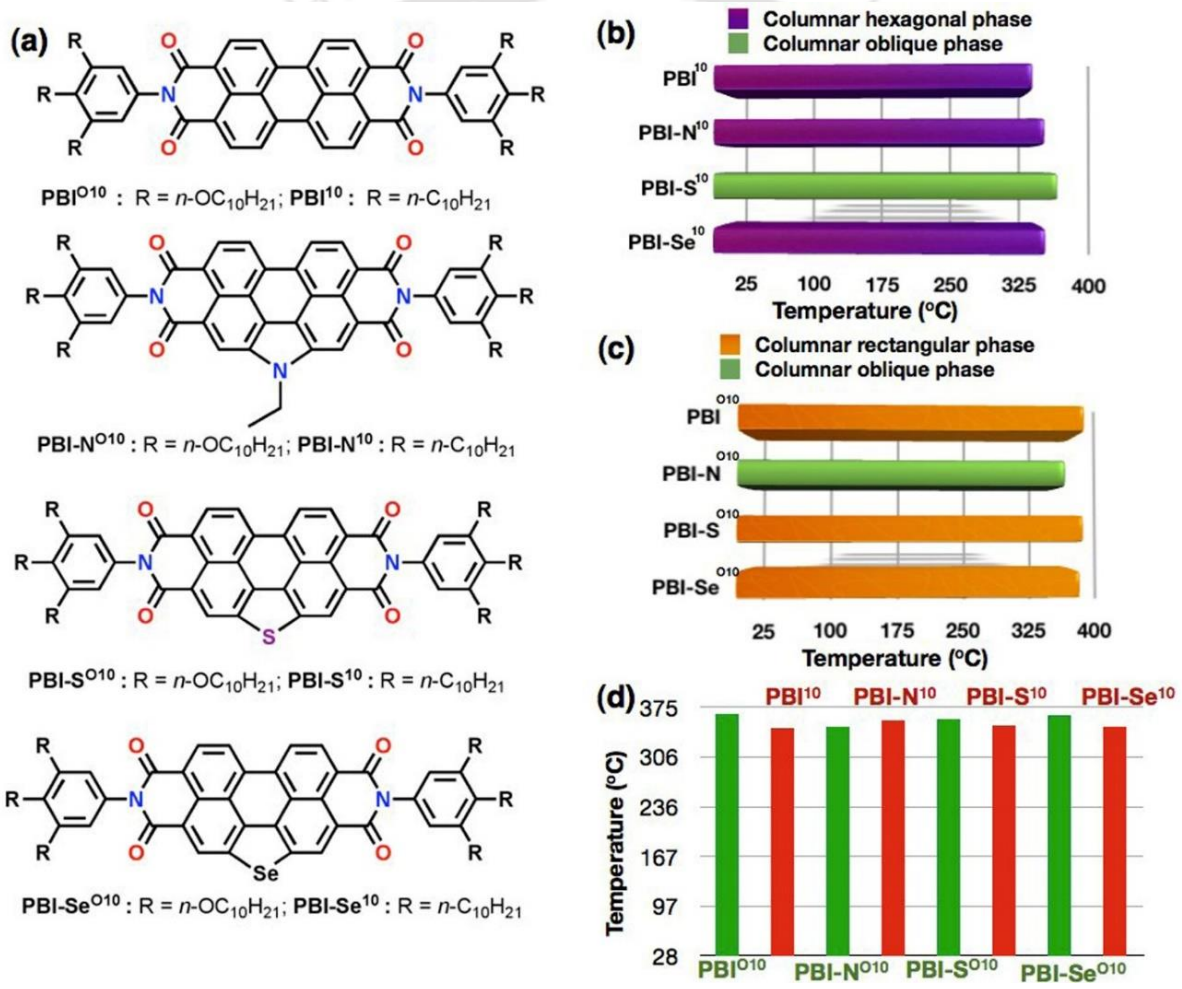

Figure 3.1. Structures of PBIs derived from tri-*n*-alkoxy anilines (**PBI^{O10}, PBI-N^{O10}, PBI-S^{O10}** and **PBI-Se^{O10}**) and PBIs derived from tri-*n*-alkyl anilines (**PBI^{10}, PBI-N^{10}, PBI-S^{10}** and **PBI-Se^{10}**) (a); Bargraph showing the thermal behaviour of **PBI^{10}, PBI-N^{10}, PBI-S^{10}** and **PBI-Se^{10}** (b); Bargraph showing the thermal behaviour of **PBI^{O10}, PBI-N^{O10}, PBI-S^{O10}** and **PBI-Se^{O10}** (considered the second heating scan in DSC) (c); Thermal stability of PBIs obtained from TGA studies (considering the temperature at which 5 weight % decomposition occurs) (d).

It is also documented that, PBIs with tri-*n*-alkoxy phenyl group in the imide position have showed lower photoluminescence quantum yield due to the intramolecular charge transfer, while their tri-*n*-alkyl counterparts exhibited high photoluminescence (see chapter 2). Recently, the substitutions at *bay*-positions have also been noticed to stabilize a unique kind of favourable J-aggregates with columnar self-assembly.[22] The strong π-π interaction of the PBI cores results in electron mobilities of 0.1-1cm^2/V.s in PBI-based small molecules.[23] When used as a blend with polythiophene, PBIs exhibited better charge photogeneration than their blend with fullerene derivative PCBM.[24] Thus, they have bright potential in organic photovoltaic devices as non-fullerene acceptors (NFAs). The tendency of this class of materials to form large crystals, however resulted in the poor device performance and thus, there is a pressing need for a processable form of the PBIs and their derivatives.[25] There are several classes of organic semiconductors like polymers, single crystals and liquid crystals. Usually polymeric semiconductors exhibit excellent mechanical stability, but have disadvantages in terms of charge transport due to their amorphous nature in thin films, presence of defects acting as charge traps and recombination centres, difficulty in the processing due to their low solubility. In addition, batch to batch variation also affects all the aspects of the optoelectronic properties due to the variation in the molecular weight or the synthetic method.[26] Growth of the single crystals with large monodomain is a tough and expensive task. Further, such crystals may not find application in the fabrication of large area devices due to their inherent brittleness. Thus, liquid crystalline organic semiconductors with an intermediate order, solution processability, self-healing ability of structural defects have clear advantages over polymeric and crystalline organic semiconductors.[27] Thus the organic semiconductors capable to form columnar LCs can be considered as molecular wires with a huge potential to become the mainstay of organic electronics.[28,29,30]

In this work, a series of hetero atom *bay*-annulated perylenes functionalized with tri-*n*-alkoxy phenyl group at the imide positions stabilizing a long range room temperature Col phase has been presented. Their structural characterization, photophysical properties, thermal behaviour and charge carrier mobilities were investigated. Further, these compounds were compared with tri-*n*-alkyl phenyl substituted analogues to understand the effect of molecular structure on their optoelectronic properties. It should be noted that most of the PBI based semiconductors are of n-type, while to our surprise the compounds presented here are ambipolar.

3.2. Results and discussion

3.2.1. Synthesis and molecular structural characterization

The synthesis of the hetero atom *bay*-annulated PBIs is described in Scheme 3.1 and 3.2. Heteroatom *bay*-annulated perylene tetracarboxylic bisanhydrides (**5-7**) from perylene tetracarboxylic dianhydride (PTCDA) and their functionalization with trialkoxy phenyl group was carried out in good yields as reported earlier.[31,32] The key intermediate tri-*n*-decyloxybenzene (**1**) was prepared as reported earlier (Scheme 3.1).[48] The aniline obtained was condensed with PTCDA and its heteroatom *bay*-annulated analogues in presence of molten imidazole as solvent and zinc acetate as a catalyst under microwave conditions to yield the corresponding PBIs in 85 % yield.[31] Similarly, the trialkyl phenyl-funtionalized PBIs have been synthesized in four steps as reported before.[33,21] The crude compounds were purified by column chromatography on neutral alumina using chloroform-hexane mixture (50%) as an eluent to furnish gummy red colored solids. All the PBIs were characterized by routine spectroscopic techniques (see 3.6 appendix).

Scheme 3.1. Synthesis of 3,4,5-tridecyloxyaniline

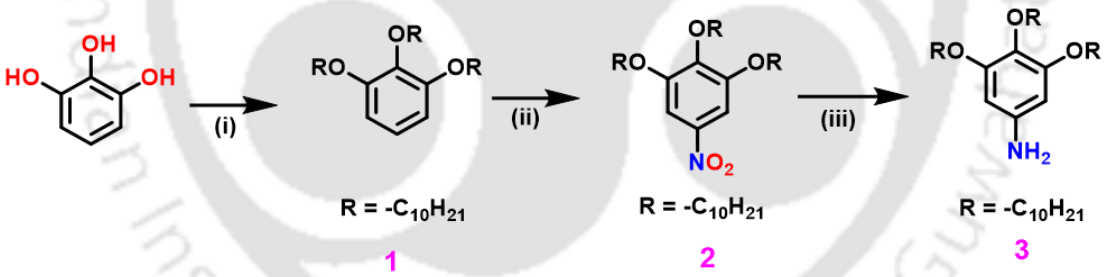

Reagents and conditions. (i) K_2CO_3, Dry DMF, $C_{10}H_{21}Br$, 80 °C, 12 h, 75% yield, (ii) $NaNO_2$, HNO_3, 0 °C, 1h, 90% yield, (iii) $N_2H_4.H_2O$, EtOH, H_2 -Pd/C, rt, overnight, 67% yield.

Scheme 3.2. Synthesis of heteroatom *bay*-annulated PBIs

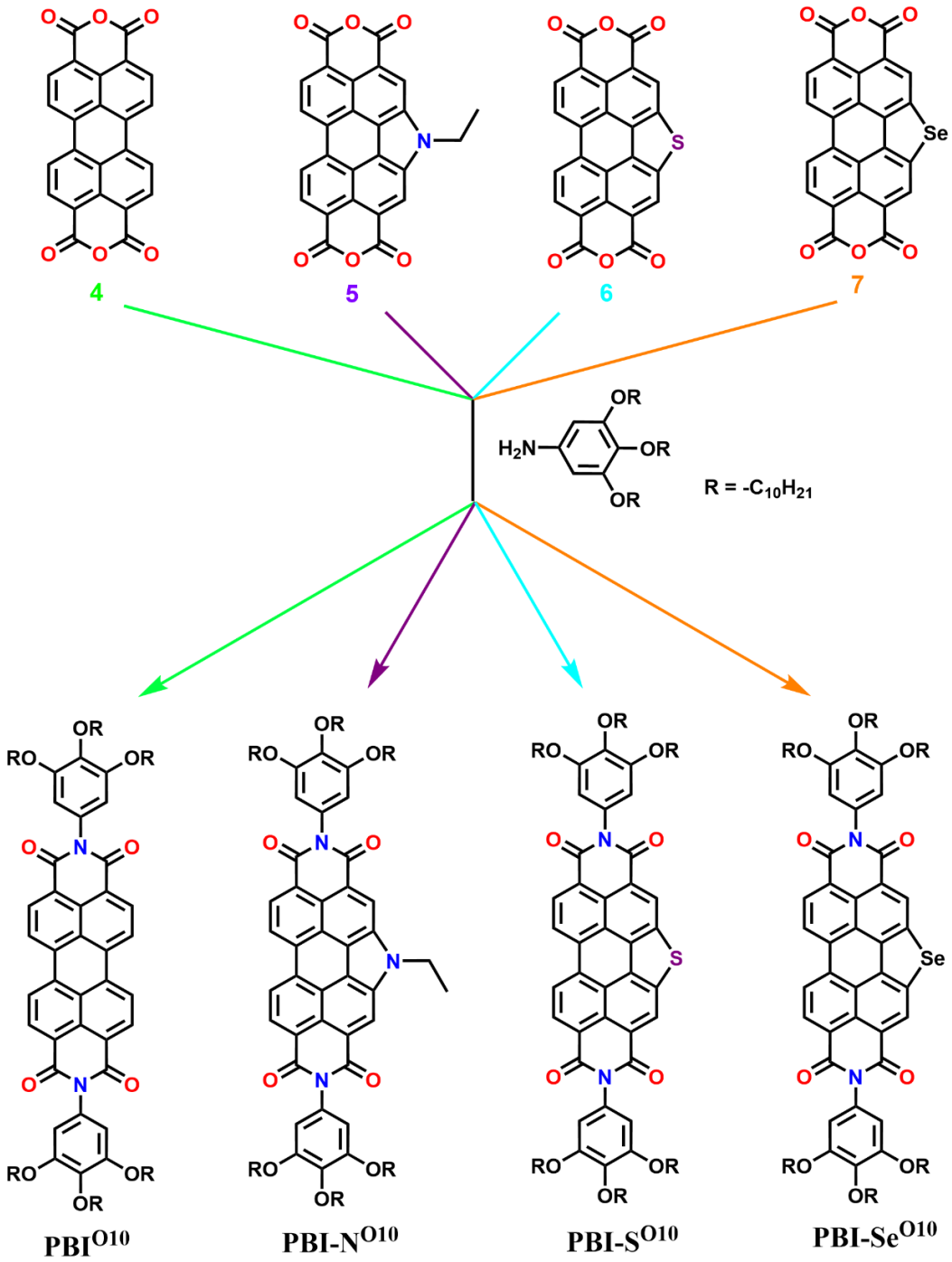

Reagents and conditions: (i) $Zn(OAc)_2$, imidazole, microwave irradiation, 35 W, 35 min, 165 ^{o}C, 80-85%.

3.2.2. Thermal behavior

The mesomorphic properties of the PBIs was examined initially with polarizing optical microscopy (POM) revealed by the fluidic nature of the sample along with strong birefringence

even at room temperature. Differential scanning calorimetry (DSC) corroborated the mesophase to isotropic transition temperature observed by POM with associated enthalpy changes, as well as the absence of crystallization on cooling run. These values were concordant with transition temperatures noted in POM studies (Table 3.1). Further the nature of mesophase was analysed with the help of X-ray diffraction (XRD) studies conducted at different temperature intervals along with the room temperature.

Table 3.1. Phase transition temperatures (^{o}C), corresponding enthalpies (kJmol^{-1}) of PBIs and the data on thermal stability.[a]

Compounds	Phase Sequence (kJ/mol)		T_5[b] (^{o}C)
	Second heating	First Cooling	
PBI^{O10}	Col_r 359.23 (2.87) I	I 354.92 (2.10) Col_r	366
PBI-N^{O10}	Col_{ob} 340.31 (1.55) I	I 336.04 (1.13) Col_{ob}	348
PBI-S^{O10}	Col_r 356.52 (4.01) I	I 353.57 (3.13) Col_r	358
PBI-Se^{O10}	Col_r 353.57 (2.26) I	I 351.12 (1.61) Col_r	364

[a] Peak temperature in the DSC thermograms obtained during the second heating and first cooling cycles at 5 ^{o}C min^{-1}. Col_r = Columnar rectangular phase; Col_{ob} = Columnar oblique phase; I = Isotropic phase. [b]Temperature at which 5 weight % decomposition occurs as noted in TGA.

Analysis of the POM images and the powder XRD data helped in the mesophases identification. The mesomorphic behaviour and thermal stability data was compared with respect to PBIs derived from tri-*n*-alkyl anilines (**PBI^{10}, PBI-N^{10}, PBI-S^{10}** and **PBI-Se^{10}**) (Fig. 3.1b-d). From the TGA, it was found that, all the four PBIs derived from tri-*n*-alkoxy anilines (**PBI^{O10}**, **PBI-N^{O10}**, **PBI-S^{O10}** and **PBI-Se^{O10}**), exhibited high thermal stability at least upto 370 ^{o}C (Fig. 3.1d and Fig. A14). **PBI^{O10}**, **PBI-S^{O10}** and **PBI-Se^{O10}** exhibited columnar rectangular (Col_r) phase, whereas **PBI-N^{O10}** showed columnar oblique (Col_{ob}) phase (Fig. 3.1c). DSC thermograms showed that the mesophases were stable over a wide thermal range including room temperature. The high clearing temperatures indirectly confirm the strong interactions between the perylene cores. The assignment of the Col phases was confirmed from the powder XRD studies carried out at different thermal intervals (Table A3.1). In comparison to PBIs derived from tri-*n*-alkoxylanilines, the PBIs derived from tri-*n*-alkylanilines exhibited lower decomposition temperatures (346-356 ^{o}C) (Fig. 3.1c).[42] Except **PBI-S^{10}**, all the PBIs exhibited columnar hexagonal (Col_h) phase, while **PBI-S^{10}** exhibited Col_{ob} phase (Fig. 3.1b). It is remarkable to note that all the PBIs were liquid crystalline over a wide thermal range including RT, while higher isotropic temperatures were seen for PBIs

derived from tri-*n*-alkoxylanilines, probably due to the higher molecular weight accounted from the six oxygen atoms. Following section details the mesomorphic behaviour of these compounds in detail.

POM examination of **PBI^{O10}** exhibited mosaic pattern intermixed with homeotropic regions on cooling from isotropic liquid state from 359 ^{o}C which is a characteristic of Col phase (Table 3.1, Fig. 3.2a). No signs of crystallization were observed in POM and DSC scans (Fig. A9 and Fig. A13a), confirmed the stability of the Col phase at room temperature. The nature of Col phase is analysed from the powder XRD patterns obtained at 100 and at 28 ^{o}C, which were essentially similar, although more number of low angle peaks observed in the low temperature scan. The XRD studies at 28 ^{o}C revealed the mesophase under investigation as Col phase with a rectangular lattice (Col$_r$ phase) with a unit rectangular cell is formed by one molecule with an intracolumnar distance of 3.37 Å (Fig. 3.3a). Such low core-core separation ensures the intimate interaction of the PBI cores within the Col phase and very important from the view point of 1D charge transport along the columnar axis. The XRD pattern obtained at 100 ^{o}C (Table A3.1) also exhibited a similar pattern but with lesser number of peaks at small angle and with the absence of core-core peak confirming the Col$_r$ phase. Absence of core-core peak is reasonable due to the increased fluidity of the columnar structure at higher temperature (Table A3.1). It is to be noted that the PBI with six *n*-dodecyloxy chains exhibited Col$_h$ phase with a higher clearing temperature of 373 ^{o}C without any core-core separation peak in the wide angle region.[34] It is also interesting to note that the PBI with six *n*-decyl chains exhibited columnar hexagonal phase, which differ from **PBI^{O10}** by the absence of oxygen atoms (Fig. 3.1c) (see chapter 2).

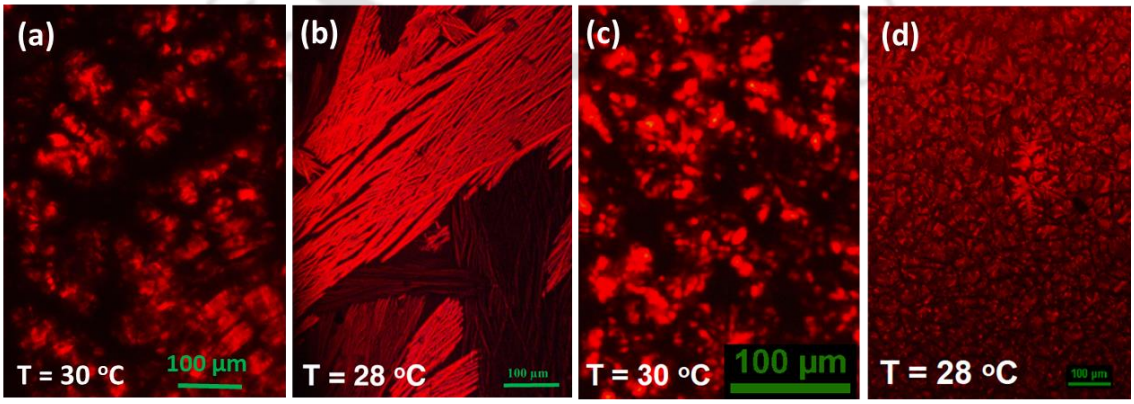

Figure 3.2. POM image of the Col$_r$ phase at 30 ^{o}C for **PBI^{O10}** (a); Col$_{ob}$ phase at 28 ^{o}C for **PBI-N^{O10}** (b); Col$_r$ phase at 30 ^{o}C for **PBI-S^{O10}** (c); Col$_r$ phase at 28 ^{o}C for **PBI-Se^{O10}** (d).

N-annulated PBI, compound **PBI-N^{O10}** exhibited broad birefringent leaf-like texture (Fig.3.2b), which is quite uncharacteristic for Col phases. Again the mesophase was stable at ambient temperature (Fig. A10 and Fig. A13b), with a slight decrease in the clearing temperature in comparison to **PBI^{O10}**. The XRD pattern obtained at 280 ^{o}C and 230 ^{o}C were complicated exhibiting many peaks in the low to mid angle region along with the diffused peak at wide angle region (Table A3.1). The core-core separation peak in the wide angle region was not observed. However, the XRD pattern obtained at 28 ^{o}C exhibited this core-core separation peak corresponding to the packing of discs with in the column with an intracolumnar distance of 3.31 Å (Fig. 3.3b). The low angle and mid angle region were composed of many peaks with *d*-spacings of 25.20 Å, 12.99 Å, 11.26 Å, 10.20 Å and 6.85 Å which can be assigned to Miller indices (01), (12), (22), (-12), (42) of an oblique lattice with lattice parameters a = 28.1 Å, b = 26.4 Å and γ = 72.7^{o} (Fig. 3.3b). Considering the height of unit cell as 3.31 Å, the number of discs present in the unit cell Z was found to be 1.

Perylene bisimides **PBI-S^{O10}** and **PBI-Se^{O10}** also exhibited Col$_r$ phase for a wide temperature range including RT as confirmed by the DSC thermograms (Fig. A13c and A13d). Both the compounds exhibited mosaic texture as shown in Fig. 3.2c and 3.2d, and the presence of Col$_r$ phase was confirmed by XRD studies conducted at different temperatures (at 200 ^{o}C, 100 ^{o}C and at 28 ^{o}C, Table A3.1). All the POM images (Fig. A11 and A12) diffraction patterns were found to be similar confirming that the compounds are monomesomorphic. For example, in the case of **PBI-S^{O10}**, for the XRD pattern obtained at 28 ^{o}C, the *d*-spacings observed at low angle were at 27.78 Å, 24.04 Å, 13.45 Å, 5.60 Å along with two diffused peaks at *d*-spacings of 4.36 and 3.43 Å at wide angle (Fig. 3.3c, Table A3.1). The *d*-spacings corresponding to low angle reflections can be assigned with the Miller indices (01), (10), (02), (42) of a rectangular lattice, with the lattice parameters a = 24 Å, b = 27.8 Å with the lattice area of 667.8 Å^2. Considering the unit cell height (c) as 3.43 Å, the cell volume was found to be 2290.7 Å^3, and the number of molecules forming a unit cell (Z) is ≈ 1. **PBI-Se^{O10}** also exhibited Col$_r$ phase at both high and low temperatures, where a columnar slice is made from 1 molecule, similar to that observed for **PBI^{O10}** (Fig. 3.3d, and Table A3.1).

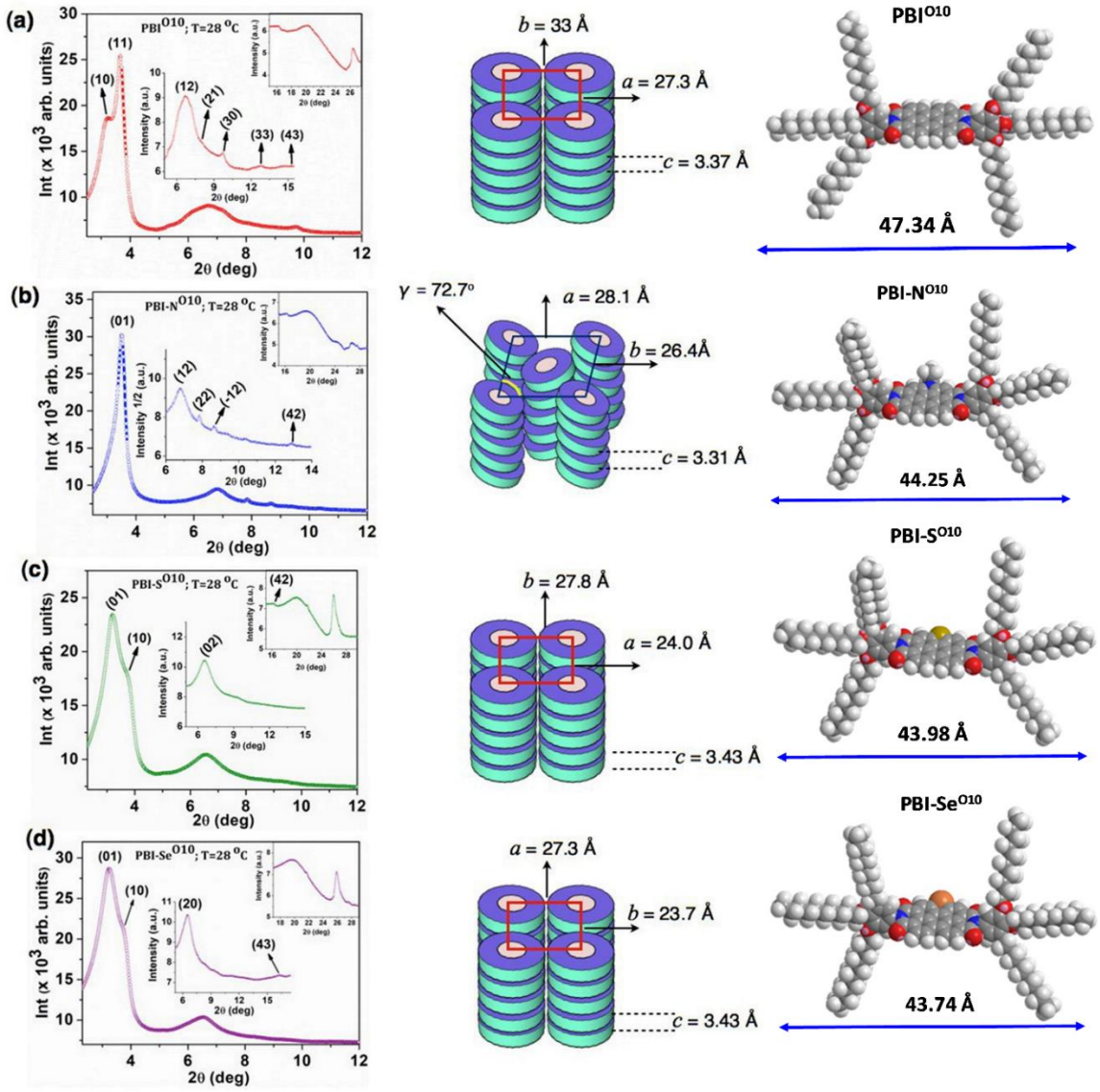

Figure 3.3. Powder XRD pattern obtained for the Col_r phase at 28 °C for compound **PBI^{O10}** (a); Col_{ob} phase at 28 °C for **PBI-N^{O10}** (b); Col_r phase at 28 °C for **PBI-S^{O10}** (c); Col_r phase at 28 °C for **PBI-Se^{O10}** (d) (Corresponding schematic diagram showing the columnar packing and the molecular diameter calculated from the energy minimized structures obtained from Chem3D are also given in the right hand side).

3.2.3. Photophysical properties

The data obtained from the absorption and emission spectra in micromolar chloroform solutions is presented in Table 3.2 and Fig. 3.4. Well-resolved absorption spectra with typical four vibronic bands were witnessed for all PBIs with the absorption maxima positioned in the range of 503-532 cm^{-1} with high extinction coefficients (ε: 67,500 to 1,08,000 $Lmol^{-1}cm^{-1}$). The optical band gap

obtained from the absorption onset showed a similar value for **PBI^{O10}** and **PBI-N^{O10}**, whereas that of the **PBI-S^{O10}** and **PBI-Se^{O10}** showed an increase. However, these values did not change much from the PBIs derived from tri-*n*-alkylanilines, though they are on the higher side. The absorption and emission spectra were similar to the PBIs derived from tri-*n*-alkylanilines.

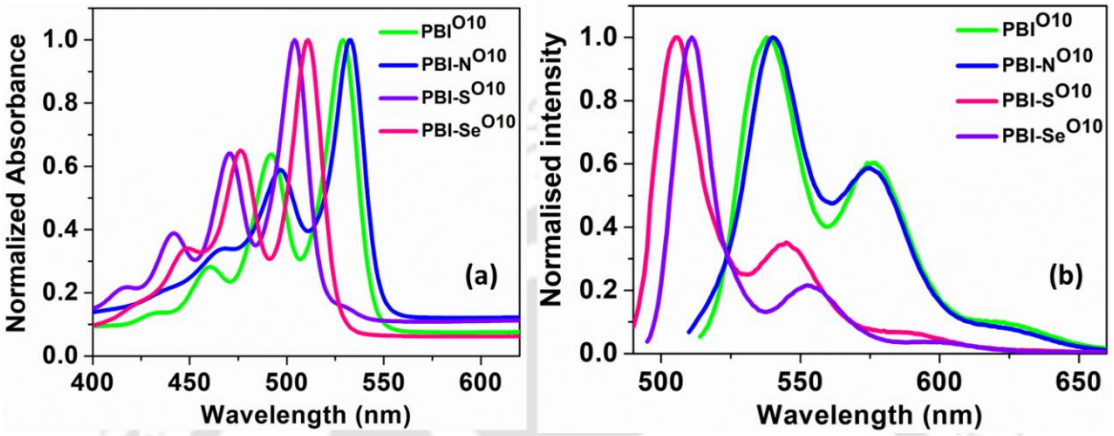

Figure 3.4. Absorption spectra (a) and emission spectra (b) of compounds **PBI^{O10}, PBI-N^{O10}, PBI-S^{O10}** and **PBI-Se^{O10}** in micromolar chloroform solutions.

Table 3.2. Photophysical[a] properties of PBIs in solution state.

Entry	Absorption [nm]	Emission[b] [nm]	Stokes Shift (cm^{-1})	Molar extinction coefficient (ε) (L mol^{-1} cm^{-1})
PBI^{O10}	431, 459, 491, 528	530, 575, 625	72	103,000
PBI-N^{O10}	430, 466, 496, 532	534, 576, 626	70	108,000
PBI-S^{O10}	417, 442, 469, 503	505, 544, 593	79	67,500
PBI-Se^{O10}	419, 447, 476, 510	511, 553, 600	38	79,500

[a] Micromolar solutions in $CHCl_3$; [b] The excitation wavelength λ_{ex} = 528, 532, 503 and 510 nm respectively, for compounds **PBI^{O10}**, **PBI-N^{O10}**, **PBI-S^{O10}** and **PBI-Se^{O10}**.

These PBIs exhibited two emission maxima, with the high intensity one was in the range of 505-534 nm. However, the solutions did not show any perceivable fluorescence under UV light (λ = 365 nm) (Fig. A15e). This could be due to the quenching of the fluorescence by the intramolecular charge transfer from the peripheral tri-*n*-alkoxy aniline group to the central perylene core.[35] It should be noted that in contrast, the PBIs derived with tri-*n*-alkyl aniline exhibited excellent quantum yield (see chapter 2).[33] In the concentration dependent UV-Vis studies, with the increase in concentration the enhancement of absorption was seen, without any shift in the absorption maxima, while the emission spectra showed an reduced intensity with a red shift (Fig. A16-A17).

3.2.4. Electrochemical properties

Electrochemical properties were investigated with the help of cyclic voltammetry (CV) carried out in anhydrous dichloromethane solutions (Fig. A18) and the details are tabulated in Table 3.3. In general, PBIs are known as n-type semiconductors with high electron affinity. From the electrochemical studies, it was observed that the hetero atom *bay*-annulated PBIs exhibited elevated LUMO levels in comparison to **PBI^{O10}** (Fig. A18b, Fig. 3.5a). A small elevation of 0.18 eV in the HOMO level was observed in the case of **PBI-N^{O10}**, whereas **PBI-S^{O10}** and **PBI-Se^{O10}** showed a decreased HOMO levels by 0.06 and 0.05 eV, correspondingly. These values were analogous with the one obtained from DFT calculations (Fig. 3.5b).

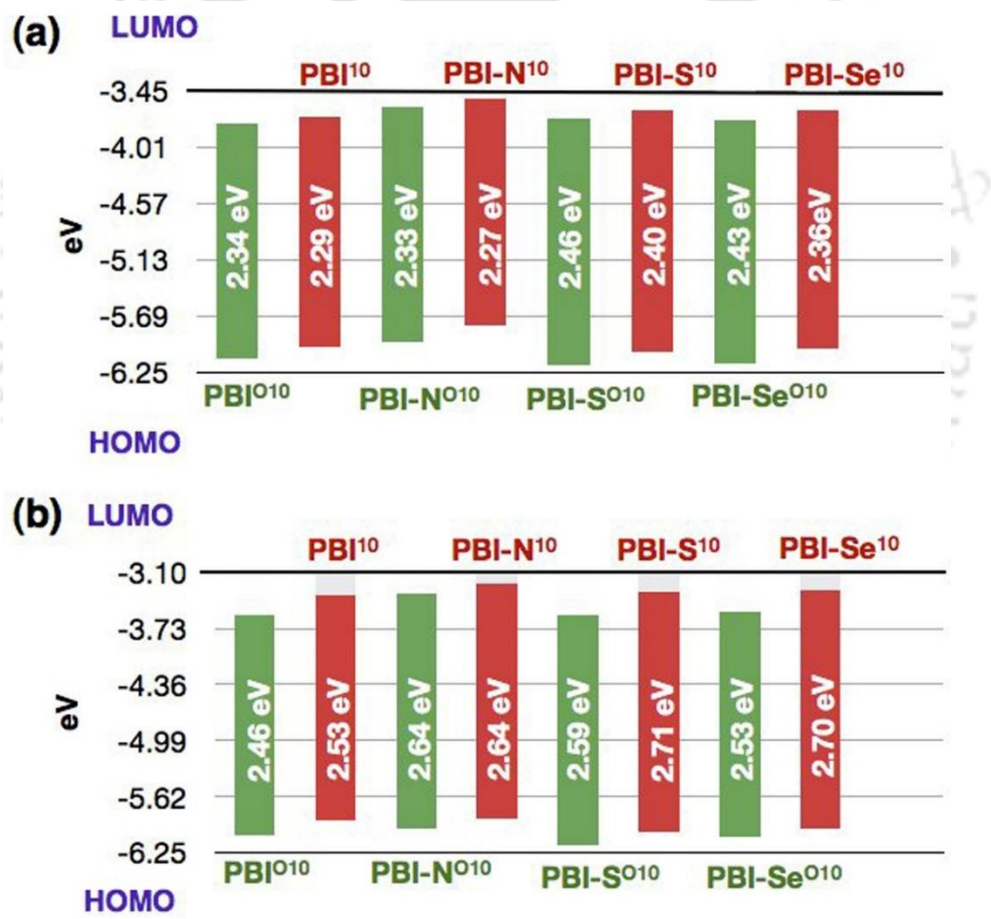

Figure 3.5. Energy band level diagram showing HOMO and LUMO energy levels of PBIs (from the data obtained from cyclic voltammetry) (a); Energy band level diagram showing HOMO and LUMO energy levels of PBIs (from the data obtained from DFT studies) (b).

In contrast to PBIs prepared from aliphatic amines, **PBI^{O10}** showed an elevated LUMO level and a diminished HOMO level. It is to be noted that in comparison to heteroatom *bay*-annulated PBIs prepared from aliphatic amines and tri-*n*-alkylanilines, **PBI-N^{O10}**, **PBI-S^{O10}** and **PBI-Se^{O10}** displayed lowered HOMO and LUMO levels (see chapter 2).[36] In comparison to PBIs derived from tri-*n*-alkylanilines, PBIs derived from tri-*n*-alkoxylanilines exhibited higher band gaps (Fig. 3.5a). Overall, all the molecules exhibited LUMO levels lower than 3.5 eV, confirming their potential as good electron acceptors and could be a new class of non-fullerene acceptors (NFAs) for organic photovoltaics. [37]

3.2.5. Density Functional Theory Studies

Density functional theory (DFT) quantum mechanical calculations were conducted to understand the molecular conformation and frontier molecular orbital (FMOs: HOMO and LUMO) energy levels of **PBI^{O10}**, **PBI-N^{O10}**, **PBI-S^{O10}** and **PBI-Se^{O10}**. Fig. 3.3 shows the energy minimized space filling models of all the PBIs studied (Fig. A19). It is evident that the FMOs of these PBIs are spread predominantly on the central ring, but not on the peripheral benzene moieties because of the nodes present on the nitrogen atoms of imide units.

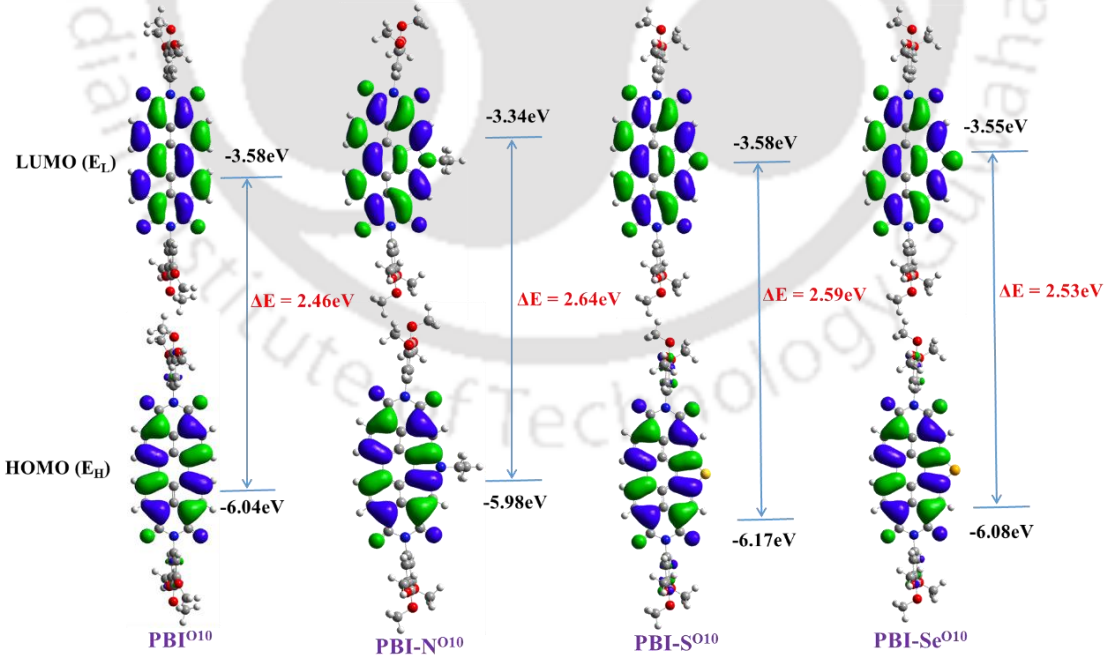

Figure 3.6. Frontier molecular orbitals of compounds **PBI^{O10}** (a); **PBI-N^{O10}** (b); **PBI-S^{O10}** (c) and **PBI-Se^{O10}** (d) obtained from DFT calculations at the B3LYP/6-31G(d,p) level. E_H and E_L denote energies of the highest occupied molecular orbital (HOMO) and the lowest unoccupied molecular orbital (LUMO), respectively.

In the case of *bay*-annulated PBIs, HOMOs and LUMOs distributed over hetero atom, showing their integration in the central aromatic core. 3D molecular electrostatic potential contour map of optimized structures of **PBI^{O10}, PBI-N^{O10}, PBI-S^{O10}** and **PBI-Se^{O10}** showed that the central perylene unit is electron deficient while the electron density is concentrated on the imide and alkoxy oxygen atoms (Fig. A20). PBIs derived from tri-*n*-alkylanilines, also exhibited similar electrostatic potential distribution, except the absence of electron density corresponding to the oxygens on peripheral phenyl units (Fig. A21). The theoretical band gaps obtained for **PBI^{O10}, PBI-N^{O10}, PBI-S^{O10}** and **PBI-Se^{O10}** were (Fig. 3.6), found to be slightly greater than the optical bandgap (Table 3.3, Fig. 3.5a-b). In comparison to PBIs derived from tri-*n*-alkylanilines, PBIs derived from tri-*n*-alkoxylanilines exhibited lowered LUMO, HOMO levels and reduced band gaps (Fig. 3.5b, Fig. A22).

Table 3.3. Electrochemical[a,b] data and data obtained from DFT[h] calculations for compounds **PBI^{O10}, PBI-N^{O10}, PBI-S^{O10}** and **PBI-Se^{O10}**.

	Electrochemical data				Data from DFT calculations		
Entry	$E_{1st\ red}$ [c] (eV)	E_{LUMO} [d,e] (eV)	E_{HOMO} [d,f] (eV)	$\Delta E_{g,\ opt}$ [d,g] (eV)	E_{LUMO} [d,h] (eV)	E_{HOMO} [d,h] (eV)	$\Delta E_{g,}$ [d,h] (eV)
PBI^{O10}	-0.52	-3.78	-6.12	2.34	-3.58	-6.04	2.46
PBI-N^{O10}	-0.69	-3.61	-5.94	2.33	-3.34	-5.98	2.64
PBI-S^{O10}	-0.58	-3.72	-6.18	2.46	-3.58	-6.17	2.59
PBI-Se^{O10}	-0.56	-3.74	-6.17	2.43	-3.55	-6.08	2.53

[a] 0.5 mM Dichloromethane solutions; [b]experimental conditions: $Ag/AgNO_3$ as reference electrode, glassy carbon working electrode, platinum wire counter electrode, TBAP (0.1M) as a supporting electrolyte, room temperature; [c] in volts (V); [d] in eV; [e] estimated from the formula by using E_{LUMO}= -(4.8 - $E_{1/2,\ Fc/Fc+}$ + $E_{red,\ onset}$) eV; [f] estimated from the formula $E_{HOMO} = E_{LUMO} - E_{g,opt}$) eV; $E_{1/2,\ Fc/Fc+}$ = 0.50 V. [g]calculated from the red edge of the absorption band of each compound.[h] Obtained from DFT calculations by employing the combination of Becke3-Lee-Yang-Parr (B3LYP) hybrid functional and 6-31G(d,p) basis set using the Gaussian 09 package.

3.3. Charge Carrier Mobility Studies

The study of charge carrier mobility in reported PBI based compounds were carried out using Space Charge Limited Current (SCLC) technique. A device with ITO/PEDOT: PSS / PBIs /MoO_3/Ag architecture was fabricated for extraction of hole mobility whereas ITO/ZnO/ PBIs/Ag was used for electron-mobility extraction. In hole only devices ITO/PEDOT: PSS electrode combination was chosen for hole injection whereas ITO/ZnO electrode combination was chosen for electron injection. To achieve SCLC regime an Ohmic contact is fundamental requirement with material under test in both hole (Injecting electrode-HOMO) as well as electron (Injecting electrode-LUMO) only devices. It is to be noted that solution-processed thin films using spin

coating technique was used to fabricate PBIs derived from tri-*n*-alkoxy anilines (**PBI^{O10}, PBI-N^{O10}, PBI-S^{O10}** and **PBI-Se^{O10}**) and PBIs derived from tri-*n*-alkyl anilines (**PBI^{10}**, **PBI-N^{10}, PBI-S^{10}** and **PBI-Se^{10}**) based SCLC devices. All the PBIs formed good quality thin films in chloroform (Fig. A23). Detailed experimental details can be find in the SI section.

In SCLC technique at initial low voltages current follows ohmic regime with slope of one whereas at higher voltages, where injected charges dominate over intrinsic charges SCLC regime with a slope two is observed. Considering material to be trap free charge mobility of the material can be extracted using Mott-Gurney law given by equation 1.[38]

$$J = \frac{9}{8}\varepsilon_0\varepsilon_r\mu\frac{V^2}{d^3} \quad (1)$$

Where ε_0 is the permittivity of free space (8.86×10^{-14} *F/cm*), ε_r represents the relative dielectric constant of the material (PBIs derived from tri-*n*-alkoxy anilines ~ 4.2 and PBIs derived from tri-*n*-alkyl anilines ~ 4.5), *V* is the applied voltage, *d* is the thickness of the material and *J* is density. In thin films where applied electric field is much higher as compared to the bulk, modified Mott−Gurney equation is widely used where a field-dependent charge mobility correction is introduced for the charge mobility calculation shown in equation 2.

$$J = \frac{9}{8}\varepsilon_r\varepsilon_0\mu\frac{V^2}{d^3}\exp\left(0.891\gamma\sqrt{\frac{V}{d}}\right) \quad (2)$$

where γ is the fitting parameter that represents the strength of the field dependence of mobility.

In this work modified Mott-Gurney equation was used for fitting the measured *J*−*V* curves for both PBIs derived from tri-*n*-alkyl anilines (**PBI^{10}, PBI-N^{10}, PBI-S^{10}** and **PBI-Se^{10}**) and PBIs derived from tri-*n*-alkoxy anilines (**PBI^{O10}, PBI-N^{O10}, PBI-S^{O10}** and **PBI-Se^{O10}**) to extract their hole and electron mobilities, summarized in Table 3.4 and 3.5 respectively. Fig. 3.7a-d represents the observed as well as SCLC fitted curves for both PBIs derived from tri-*n*-alkyl anilines and PBIs derived from tri-*n*-alkoxy anilines respectively. The reported mobility values for both electron and hole are an average of at least 5 devices (Table A3.2).

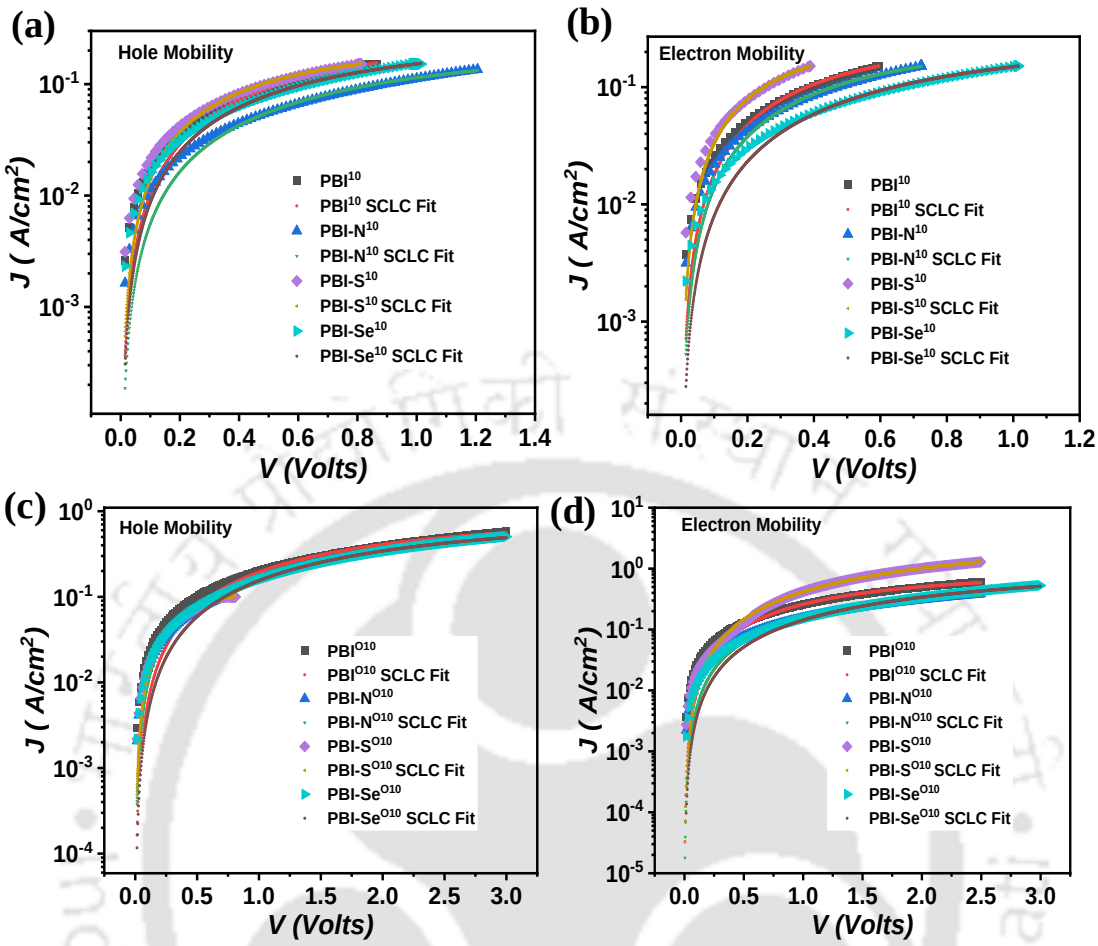

Figure 3.7. *J-V* curves along with SCLC fitting for *J-V* curves along with SCLC fitting for PBIs derived from tri-*n*-alkyl anilines (**PBI^{10}, PBI-N^{10}, PBI-S^{10}** and **PBI-Se^{10})** on semi log scale (a) for hole mobility; (b) for electron mobility; Same for PBIs derived from tri-*n*-alkoxy anilines (**PBI^{O10}, PBI-N^{O10}, PBI-S^{O10}** and **PBI-Se^{O10}**) on semi log scale (c) for hole mobility and (d) for electron mobility.

From the comparison of charge carrier mobility values (Table 3.4, 3.5 and Fig 3.8), we can conclude that overall, PBIs derived from tri-*n*-alkyl anilines (**PBI^{10}, PBI-N^{10}, PBI-S^{10}** and **PBI-Se^{10})** exhibit higher mobility values than the PBIs derived from tri-*n*-alkoxy anilines (**PBI^{O10}, PBI-N^{O10}, PBI-S^{O10}** and **PBI-Se^{O10}**). Only exception is found in the hole mobility value of **PBI-N^{O10}** which is almost double than the **PBI-N^{10}**. *S*-annulated PBI derived from tri-*n*-alkyl aniline (**PBI-S^{10}**) was the best among these compounds exhibiting highest hole (8.39×10^{-3} cm^2/ V.s) and electron (1.51×10^{-2} cm^2/ V.s) mobility values.

Table 3.4. Hole and electron mobility values for PBIs derived from tri-*n*-alkyl anilines (**PBI^{10}, PBI-N^{10}, PBI-S^{10}** and **PBI-Se^{10}**).

Entry	Hole mobility (μ_h) $\times 10^{-3}$ (cm^2/ V.s)	Electron mobility (μ_e) $\times 10^{-3}$ (cm^2/ V.s)	μ_e/ μ_h
PBI^{10}	6.20±1.10	10.2±2.51	1.7
PBI-N^{10}	2.81±0.585	6.56±1.67	2.3
PBI-S^{10}	8.39±0.455	15.1±11.1	1.8
PBI-Se^{10}	2.95±1.57	5.08±0.819	1.7

Table 3.5. Hole and electron mobility values both PBIs derived from tri-*n*-alkoxy anilines (**PBI^{O10}, PBI-N^{O10}, PBI-S^{O10}** and **PBI-Se^{O10}**).

Entry	Hole mobility (μ_h) $\times 10^{-3}$ (cm^2/ V.s)	Electron mobility (μ_e) $\times 10^{-3}$ (cm^2/ V.s)	μ_e/ μ_h
PBI^{O10}	2.08±0.24	2.91±0.486	1.4
PBI-N^{O10}	6.30±1.74	2.09±0.228	0.3
PBI-S^{O10}	6.91±0.95	2.82±0.650	0.4
PBI-Se^{O10}	1.42±0.72	0.97±0.523	0.7

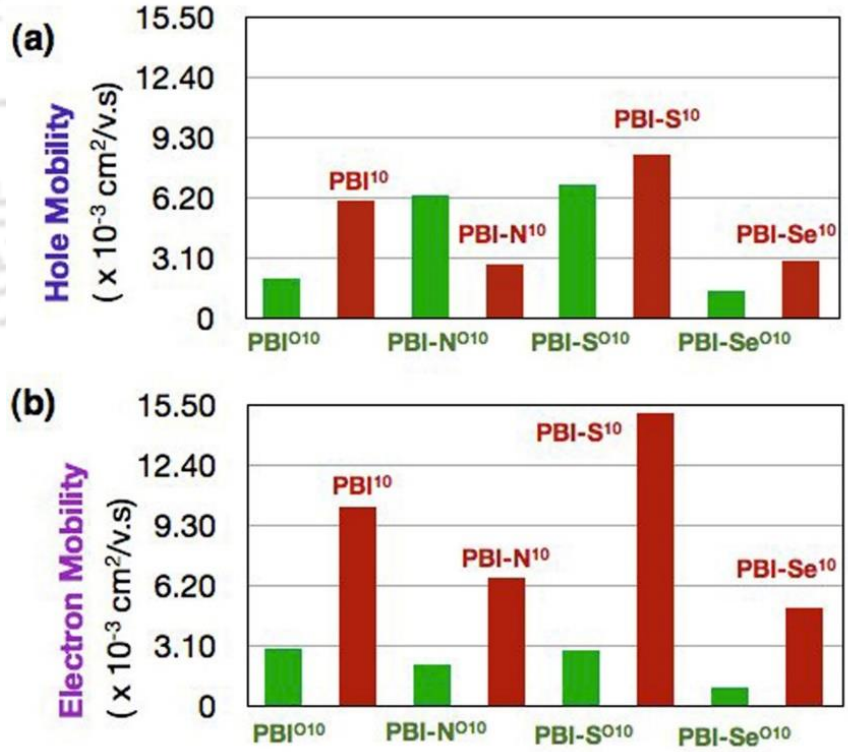

Figure 3.8. Comparison of hole mobility values (a) and electron mobility values (b) for PBIs derived from tri-*n*-alkoxy anilines (**PBI^{O10}, PBI-N^{O10}, PBI-S^{O10}** and **PBI-Se^{O10}**) and PBIs derived from tri-*n*-alkyl anilines (**PBI^{10}, PBI-N^{10}, PBI-S^{10}** and **PBI-Se^{10}**).

The better charge carrier transport abilities of could be attributed to the S···S and S···O σ-hole interactions, which was also evidenced by the observation of higher order peak at 3.47 Å in XRD studies (Table A3.1).[42] In the case of *S*-annulated PBIs, it is possible that they stack one upon another to form a Col phase with a rotational offset, due to the steric bulk of S atom and also to accommodate the out of plane phenyl rings at imide position. This will bring the two sulphur atoms staggered with respect to each other, but still they can have interaction with the S atoms of the same column or from the neighbouring column. Further they may have interaction with the oxygen atoms of the imide carbonyls of the PBIs of same column or from the neighbouring columns as shown in Fig. 3.9 below. As a result, intermolecular π-π interaction also increases.

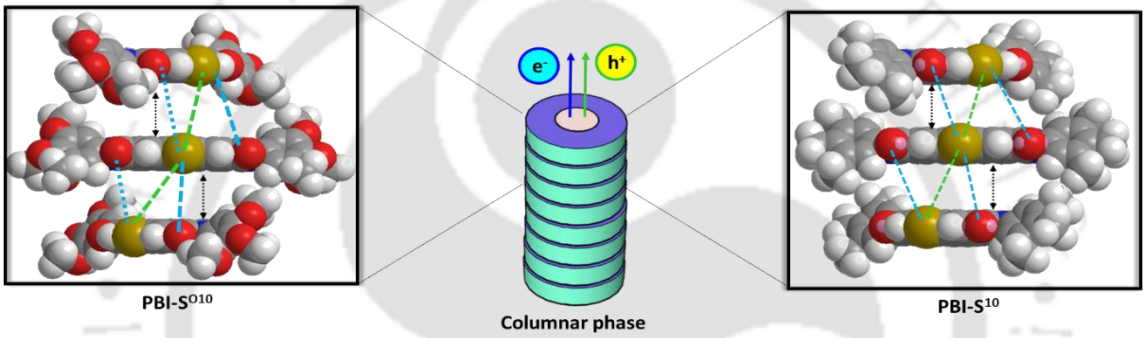

Figure 3.9. Schematic showing the self-assembly of **PBI-S^{O10}** and **PBI-S^{10}** in Col phase (Chain length is limited to methyl for clarity purpose, S···S and S···O interactions are shown in dotted lines, π-π interactions in double headed arrows).

Moreover, favourable energy level matching in hole and electron only devices for **PBI-S^{10}** over **PBI-S^{O10}** can also be an additional factor for its higher mobility value. Again it should be noted that Se based compounds and **PBI-S^{O10}** also could have shown high mobility values, but did not, suggesting the complexity involved in the design of self-assembled organic semiconductors. It is to be noted that, in literature it has been established that SCLC mobilities are usually lower than that obtained using field effect transistor method. [39,40] Overall, these compounds exhibited impressive ambipolar conductivity, which are relatively balanced (μ_e/ μ_h ratio in Table 3.4 and 3.5) in comparison to the molecular designs where the p-type moieties like carbazole and thiophenes were deliberately introduced to achieve the same[41,42,43] or two component systems containing donors and acceptors in varying ratio[44-47]. This highlights the simplicity of the present molecular design in tweaking the properties of organic semiconductors.

3.4. Conclusions

A set of PBI and its heteroatom *bay*-annulated analogues bearing tri-*n*-decyloxyphenyl moieties has been synthesized. Compounds **PBI^{O10}, PBI-S^{O10}** and **PBI-Se^{O10}** exhibited columnar rectangular phase, whereas the *N*-annulated perylene bisimide **PBI-N^{O10}** exhibited columnar oblique phase, down to room temperature with a wide thermal range. These compounds exhibited intense absorption spectra with high molar extinction coefficients. This is promising considering their application potential in organic solar cells, where there is a scope to widen their absorption range by structural modification. With low LUMO levels they can also function as non-fullerene acceptors for organic solar cells which are also promising for providing higher stability in organic solar cells as compared to much explored fullerenes. Considering the requirement of new n-type semiconductors capable of self-assembly, this class of compounds is exceptional and encouraging. The PBIs were tested for their charge carrier mobility by space charge limited current (SCLC) method and found that they exhibit ambipolar conductivity. In general, PBIs derived from tri-*n*-alkyl anilines exhibit higher mobility values than the PBIs derived from tri-*n*-alkoxy anilines. Only exception is found in the hole mobility value of **PBI-N^{O10}** which is almost double than the **PBI-N^{10}**. *S*-annulated PBI derived from tri-*n*-alkyl aniline (**PBI-S^{10}**) was the best among these compounds exhibiting highest hole (8.39×10^{-3} cm^2/ V.s) and electron (1.51×10^{-2} cm^2/ V.s) mobility values, which could be due to the S···S, S···O σ-hole interactions, and better core-core interaction in the columnar phase. From the literature survey it is evident that most of the reported PBIs are known for n-type semiconducting behaviour, while the present set of compounds are unique by showing ambipolar conductivity. The present molecular design to achieve ambipolar conductivity can be further improved by tuning the mesophase clearing temperatures, type of the mesophase and enhancing the surface alignment. Further exploration of these compounds as a non-fullerene acceptor for solar cells is currently being explored.

3.5. Experimental section

In this section the detailed synthesis procedure and the molecular structural characterization data have been presented for the intermediates and target compounds mentioned in the scheme.

Procedure for the synthesis of synthesis of 3,4,5-tri-n-decyloxybenzene (1): [48]

A mixture of 1,2,3-trihydroxybenzene (4.0 g, 31.71 mmol, 1 eq.), anhydrous K_2CO_3 (21.8 g, 158.5 mmol, 5 eq.) were dissolved in anhydrous N, N-dimethylformamide (80 mL) and stirred for 40 min at 50 ^oC. After that 1-bromodecane (23.02 mL, 110.98 mmol, 3.5 eq.) was added dropwise to it. The resultant reaction mixture was heated at 90 °C for 48 h. After completion, the reaction mixture was then cooled to room temperature and filtered with celite bed. Then the solvent was extracted with ethyl acetate (3 × 50 mL). The combined extracts were washed with water three times (3 × 50 mL) followed by brine and dried over anhydrous Na_2SO_4 and the solvent was evaporated via rotary evaporation. The crude product was purified by column chromatography using hexane and ethyl acetate as eluent to obtain colourless liquid (hexane : ethyl acetate = 30 : 1).

Yield - 75%; ^{1}H NMR ($CDCl_3$, 400 MHz): δ 6.90 (t, 1H, J = 8.0 Hz, ArH), 6.54 (d, 2H, J = 8.0 Hz, ArH), 3.91-3.99 (m, 6H, -OCH_2), 1.27-1.86 (m, 48H, -CH_2), 0.91 (t, 9H, J = 6.0 Hz, -CH_3)

Procedure for the synthesis of 3,4,5-tri-n-decyloxynitrobenzene (2): [49]

An appropriate mixture of compound 1 (4 g, 7.31 mmol, 1 eq.) and $NaNO_2$ (0.07 g, 1.02 mmol, 0.14eq.) were dissolved in CH_2Cl_2 and was stirred at 0 ^oC for 30 mins. To this well stirred suspension, 70% HNO_3 (1.32 mL,30 mmol, 3 equiv., 10% solution in dichloromethane) was added dropwise. This mixture was stirred at room temperature for 1h. Then it was poured into water and the aqueous layer was extracted with CH_2Cl_2. The organic layer was washed with H_2O, brine and dried over Na_2SO_4, then it was evaporated to dryness. The crude product was purified by column chromatography on silica gel (60-120 mesh) using hexane and CH_2Cl_2 as eluent to obtain slightly yellowish liquid (hexane: CH_2Cl_2 = 20: 1).

Yield - 86%; ^{1}H NMR ($CDCl_3$, 400 MHz): δ 7.47 (s, 2H, ArH), 4.00-4.10 (m, 6H, -OCH_2), 1.28-1.84 (m, 48H, -CH_2), 0.89 (t, 9H, J = 5.8 Hz, -CH_3).

Procedure for the synthesis of 3,4,5-tri-n-decyloxyaniline (3): [32]

To a suspension of nitro compound **2** (3g, 5.06 mmol, 1 eq.) and 10% Pd-C (10% weight of the nitro compound) in absolute ethanol, hydrazine monohydrate (50 mmol, 5 eq.) was added and refluxed under N_2 atmosphere for 24 h. The reaction mixture was cooled to room temperature and CH_2Cl_2 was added and filtered through a celite bed. The filtrate was extracted with CH_2Cl_2 (3 × 50 mL). The combined extracts were washed with water, brine and dried over anhydrous Na_2SO_4

and the solvent was concentrated via rotary evaporation and cooled methanol was added to get precipitate, then filtered to get the product.

Yield -74%; ^{1}H NMR ($CDCl_3$, 400 MHz): δ 5.91 (s, 2H, ArH), 3.81-3.92 (m, 6H, -OCH_2), 3.50 (bs, 2H, NH_2), 1.28-1.84 (m, 60H, -CH_2), 0.89 (t, 9H, J = 6.4 Hz, -CH_3).

General procedure for synthesis of PBIs [31]

Compound **4, 5, 6 & 7** (1 eq.), tri-n-decyloxy aniline (2.2 eq.), zinc acetate (2 eq.) and imidazole (1 g) were taken in a microwave vessel, flushed with nitrogen and put in microwave reactor. The mixture was heated at 165 ºC for 35 minutes at 35 W and 100 psi pressure. After cooling, reaction mixture was poured in 2(N) HCl (10 mL) and extracted with chloroform. Organic mixture was washed with water and saturated sodium chloride solution. The crude compound was purified by neutral alumina column chromatography using 50% chloroform-hexane system. Further purification was done by recrystallization from chloroform-methanol system.

PBI^{O10}: R_f = 0.5 (30% EtoAc-Hexane); Red solid, yield: 82%; IR (KBr pellet) ν_{max} in cm^{-1} 2921, 2852, 1705, 1666, 1592, 1502, 1466, 1434, 1365, 1320, 1233, 1113, 795, 745, 722; ^{1}H NMR (600 MHz, $CDCl_3$, 299K): δ 8.66 (d, J = 6 Hz, 4H, H_{Ar}), 8.47 (d, J = 6 Hz, 4H, H_{Ar}), 6.58 (s, 4H, H_{Ar}), 4.03 (t, J = 6 Hz, 4H, 2 × -OCH_2), 3.90 (t, J = 6 Hz, 8H, 4 × -OCH_2), 1.81-1.26 (m, 96H, alkyl chain), 0.90 (t, J = 6 Hz, 6H, 2 × -CH_3), 0.86 (t, J = 6 Hz, 12H, 4 × -CH_3); ^{13}C NMR (150 MHz, $CDCl_3$, 299K); δ 162.89, 153.69, 138.14, 133.55, 130.87, 129.76, 128.33, 125.28, 123.14, 122.78, 106.92, 73.48, 69.15, 32.02, 31.97, 31.44, 30.58, 29.90, 29.81, 29.79, 29.75, 29.72, 29.60, 29.51, 29.49, 29.43, 26.29, 26.14, 22.76, 22.71, 14.15, 14.11. MALDI-TOF exact mass calcculated for $C_{96}H_{139}N_2O_{10}[M+H]^+$: 1480.04; found: 1480.071.

PBI-N^{O10}: R_f = 0.5 (30% EtoAc-Hexane); Red solid, yield: 78%; IR (KBr pellet) ν_{max} in cm^{-1} 2921, 2852, 1699, 1663, 1599, 1501, 1465, 1423, 1378, 1298, 1226,1173, 1112, 803, 739, 709; ^{1}H NMR (600 MHz, $CDCl_3$, 299K): δ 8.64 (s, 2H, H_{Ar}), 8.55 (s, 2H, H_{Ar}), 8.28 (bs, 2H, H_{Ar}), 6.77 (s, 4H, H_{Ar}), 4.99 (q, 2H, -N$\underline{CH_2}$), 4.07 (t, J = 6 Hz, 4H, 2 × -OCH_2), 3.89 (m, 8H, 4 × -OCH_2), 1.81-1.26 (m, 96H, alkyl chain), 1.72 (t, J = 6 Hz, 3H, -$NCH_2\underline{CH_3}$), 0.92 (t, J = 6 Hz, 6H, 2 × -CH_3), 0.85 (t, J = 6 Hz, 12H, 4 × -CH_3); ^{13}C NMR (150 MHz, $CDCl_3$, 299K) δ 164.80, 163.45, 153.67, 138.07, 133.57, 130.66, 127.26, 123.58, 123.20, 122.10, 121.47, 118.39, 117.59, 107.22, 73.50, 69.17, 41.68, 32.02, 31.97, 31.60, 31.44, 30.60, 29.91, 29.82, 29.75, 29.71, 29.60, 29.51, 29.43, 26.30, 26.17, 22.77, 22.71, 22.66, 18.44, 16.79, 14.16, 14.11. MALDI-TOF exact mass calcculated for $C_{98}H_{142}N_3O_{10}[M+H]^+$: 1521.07; found: 1521.165.

PBI-S^{O10}: R_f = 0.5 (30% EtoAc-Hexane); Red solid, yield: 76%; IR (KBr pellet) ν_{max} in cm^{-1} 2921, 2852, 1704, 1669, 1595, 1502, 1466, 1427, 1367, 1298, 1233,1173, 1112, 804, 772, 740, 707; ^{1}H NMR (600 MHz, $CDCl_3$, 299K): δ 9.08 (s, 2H, H_{Ar}), 8.70 (s, 2H, H_{Ar}), 8.37 (bs, 2H, H_{Ar}), 6.73 (s, 4H, H_{Ar}), 4.06 (t, J = 6 Hz, 4H, 2 × -OCH_2), 3.84 (m, 8H, 4 × -OCH_2), 1.86-1.25 (m, 96H, alkyl chain), 0.91 (t, J = 6 Hz, 6H, 2 × -CH_3), 0.84 (t, J = 6 Hz, 12H, 4 × -CH_3); ^{13}C NMR (150 MHz,

$CDCl_3$, 299K) δ 163.47, 162.99, 154.79, 153.74, 138.22, 137.84, 132.01, 130.26, 130.15, 129.41, 127.00, 124.99, 123.08, 122.40, 122.11, 121.67, 107.14, 73.54, 69.19, 32.03, 31.96, 31.44, 30.63, 29.93, 29.83, 29.75, 29.72, 29.61, 29.52, 29.43, 26.33, 26.16, 22.77, 22.70, 14.16, 14.10. MALDI-TOF exact mass calcculated for $C_{96}H_{137}N_2O_{10}S[M+H]^+$: 1510.01; found: 1510.167.

PBI-Se^{O10}: R_f = 0.5 (30% EtoAc-Hexane); Red solid, yield: 76%; IR (KBr pellet) ν_{max} in cm^{-1} 2921, 2852, 1704, 1669, 1595, 1502, 1466, 1427, 1367, 1298, 1233,1173, 1112, 804, 772, 740, 707; ^1H NMR (600 MHz, $CDCl_3$, 299K): δ 9.15 (s, 2H, H_{Ar}), 8.71(s, 2H, H_{Ar}), 8.46 (bs, 2H, H_{Ar}), 6.69 (s, 4H, H_{Ar}), 4.06 (t, J = 6 Hz, 4H, 2 × -OCH_2), 3.86 (m, 8H, 4 × -OCH_2), 1.85-1.25 (m, 96H, alkyl chain), 0.91 (t, J = 6 Hz, 6H, 2 × -CH_3), 0.85 (t, J = 6 Hz, 12H, 4 × -CH_3); ^{13}C NMR (150 MHz, $CDCl_3$, 298.1K): δ 163.40, 163.01, 153.75, 140.61, 138.23, 133.13, 132.12, 130.13, 129.46, 129.33, 125.17, 122.85, 122.58, 122.11, 121.43, 107.20, 73.55, 69.21, 37.12, 32.03, 31.96, 31.44, 30.64, 30.20, 30.05, 29.94, 29.83, 29.76, 29.73, 29.63, 29.53, 29.43, 26.34, 26.17, 22.77, 22.70, 18.44, 14.15, 14.10. MALDI-TOF exact mass calcculated for $C_{96}H_{137}N_2O_{10}Se[M+H]^+$: 1557.94; found: 1557.812.

3.6. Appendix

3.6.1. NMR Spectra

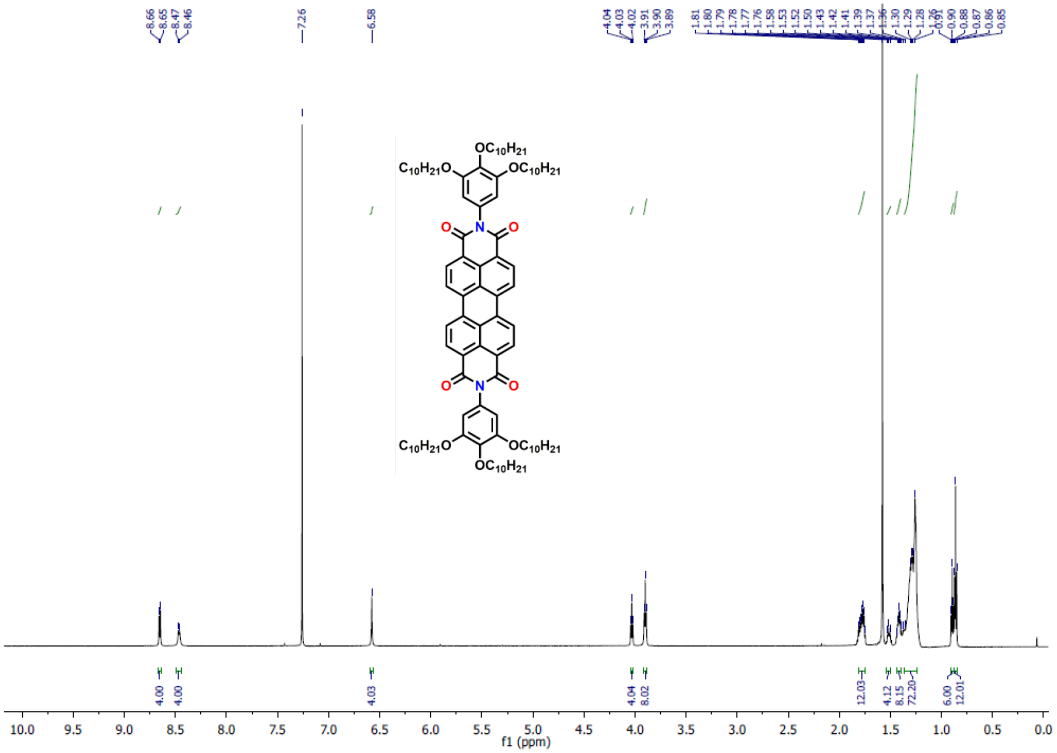

Figure A1. ^{1}H NMR (600 MHz) spectra of **PBI^{O10}** in $CDCl_3$.

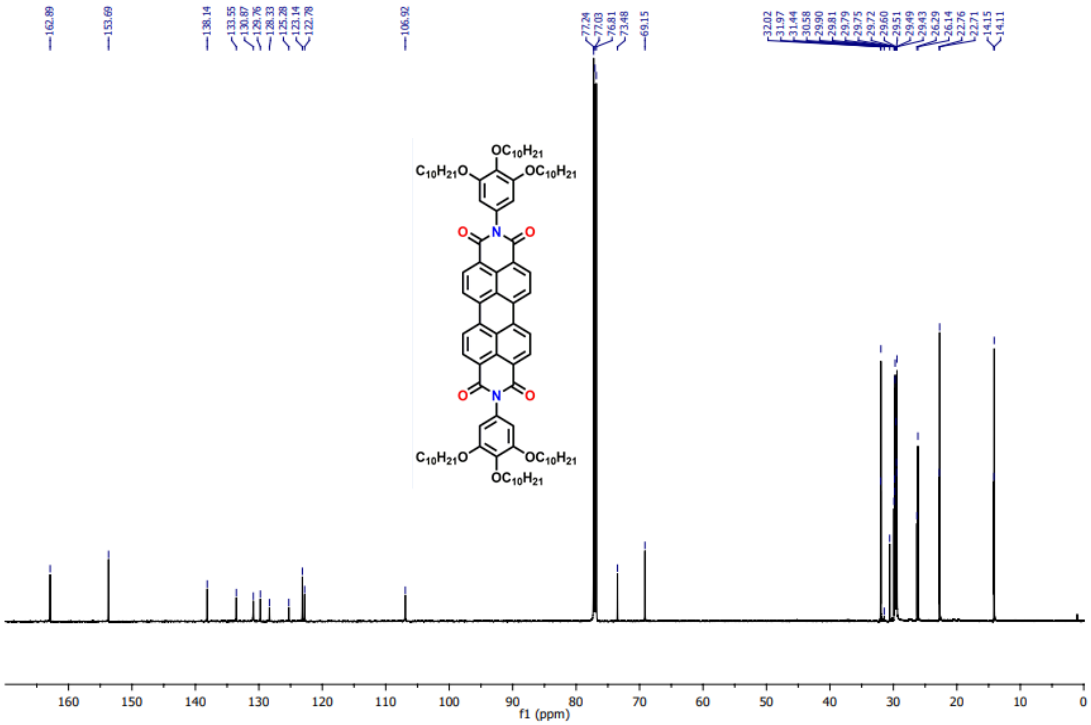

Figure A2. ^{13}C NMR (150 MHz) spectra of **PBI^{O10}** in $CDCl_3$.

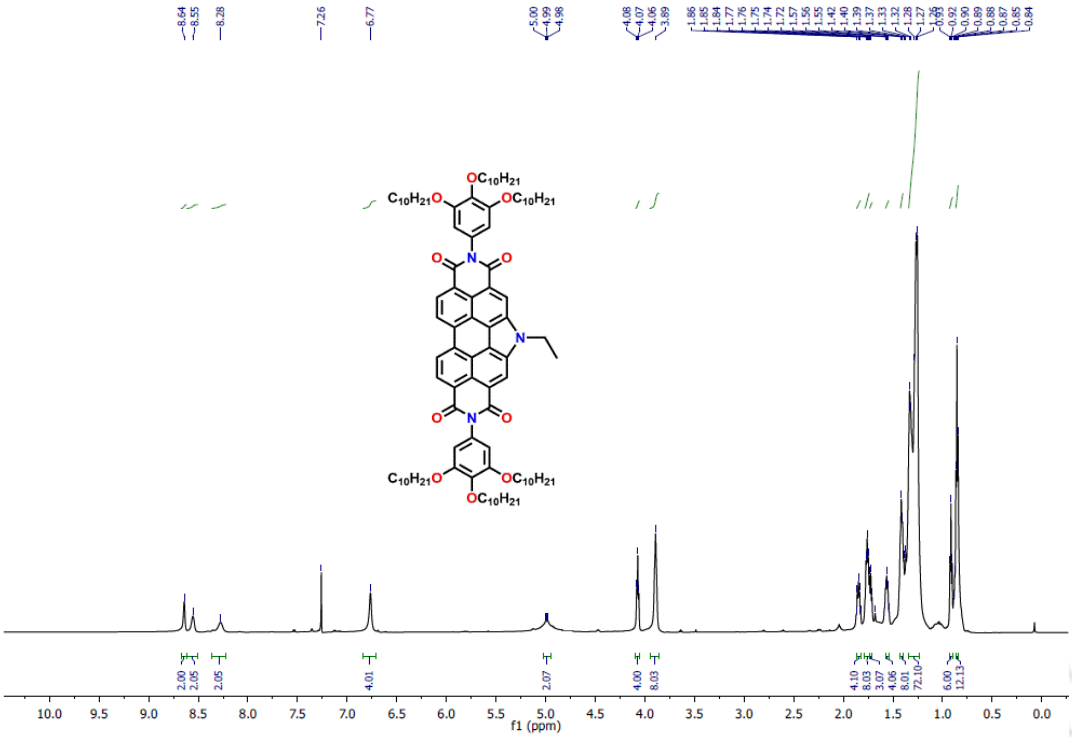

Figure A3. ^{1}H NMR (600 MHz) spectra of **PBI-N^{O10}** in $CDCl_3$.

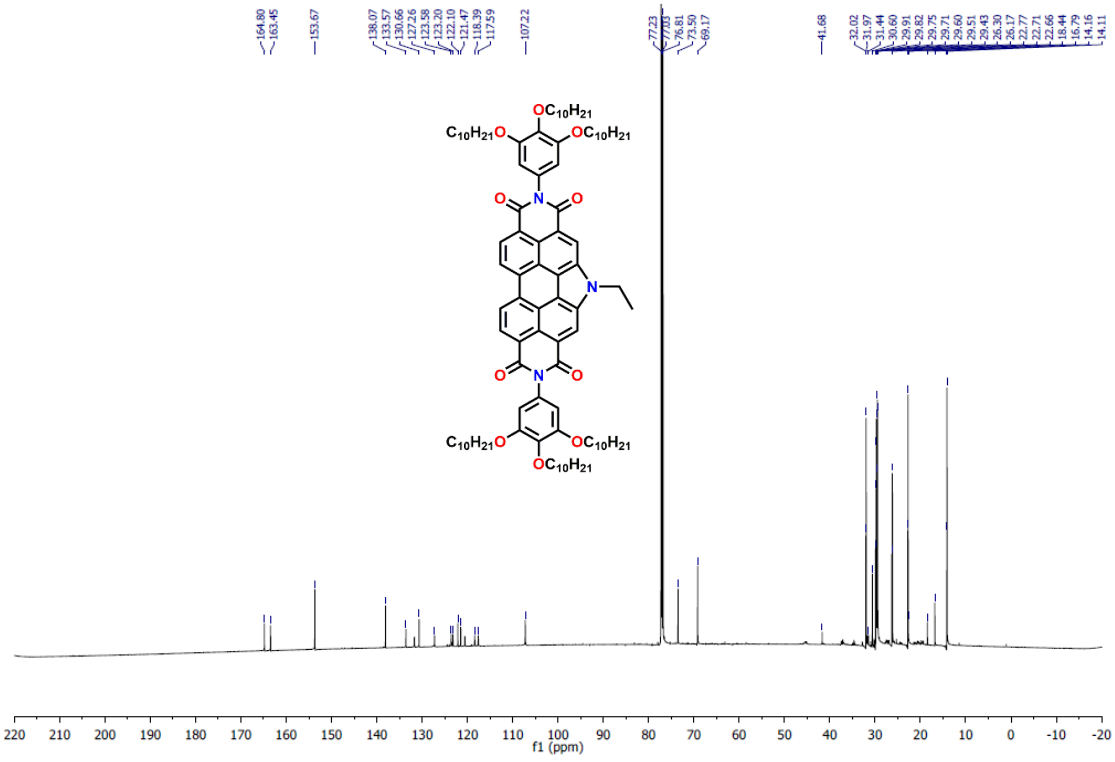

Figure A4. ^{13}C NMR (150 MHz) spectra of **PBI-N^{O10}** in $CDCl_3$.

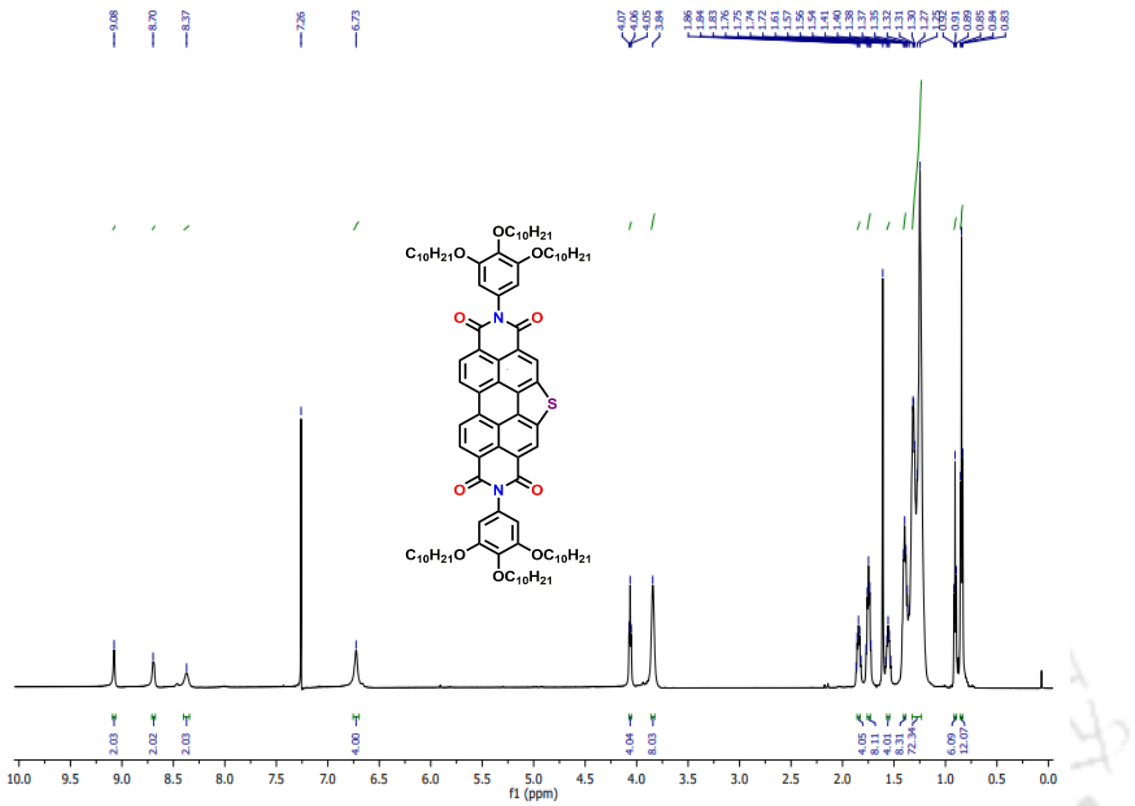

Figure A5. ^{1}H NMR (600 MHz) spectra of **PBI-S^{O10}** in $CDCl_3$.

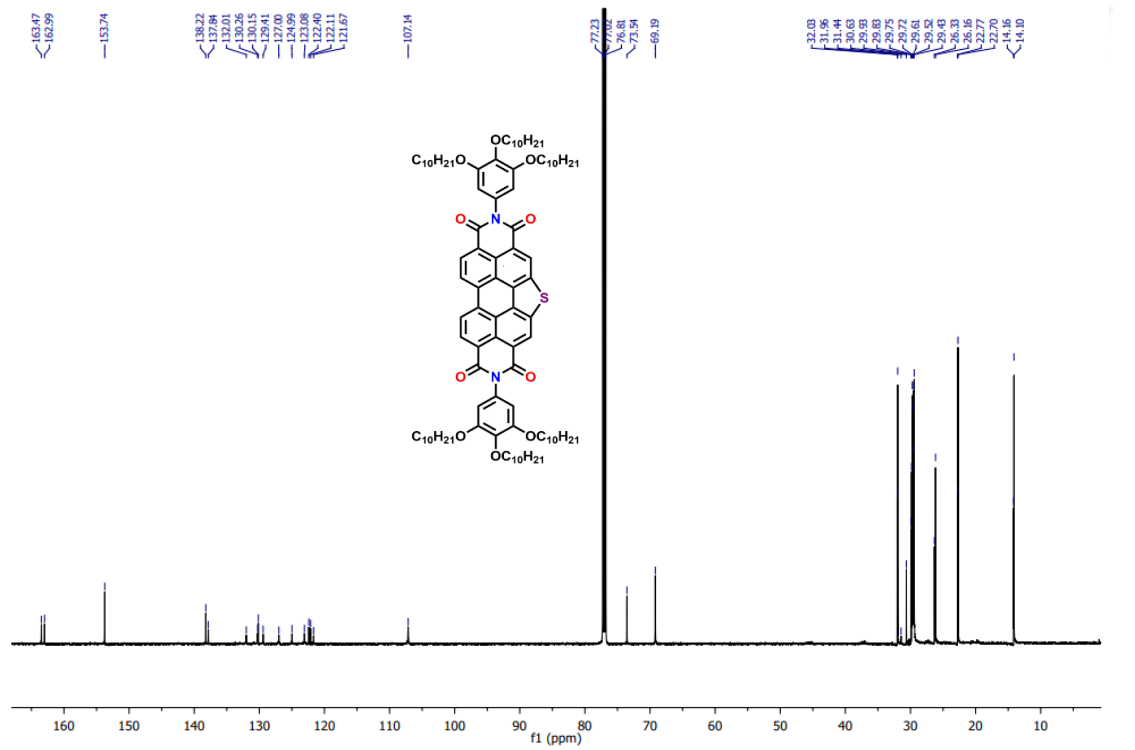

Figure A6. ^{13}C NMR (150 MHz) spectra of **PBI-S^{O10}** in $CDCl_3$.

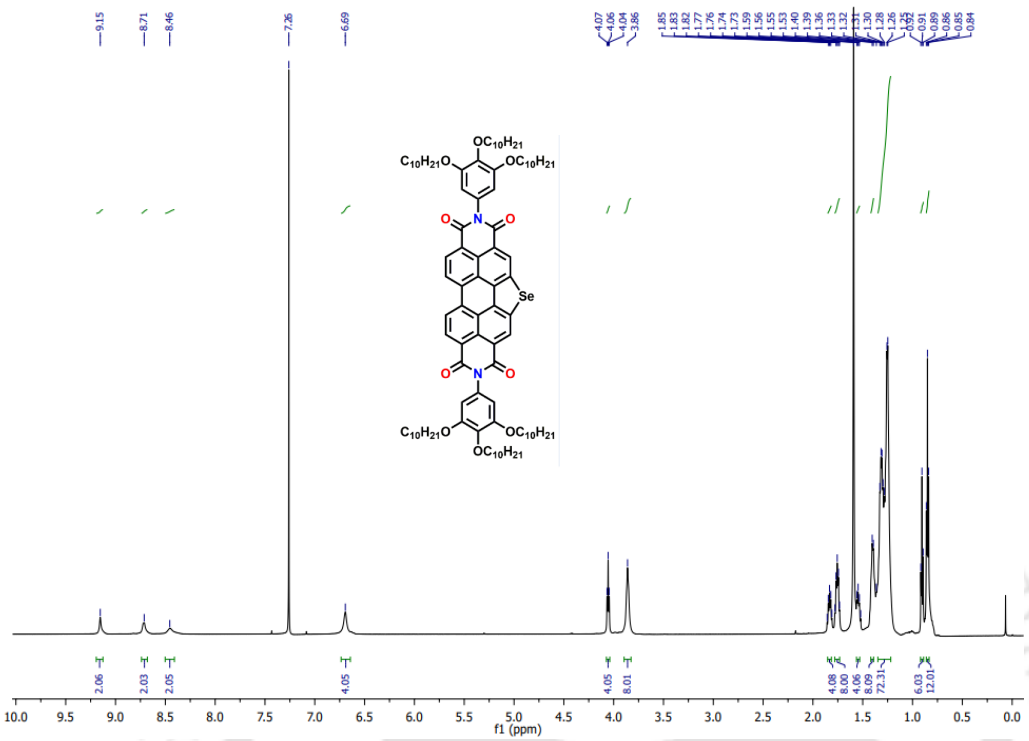

Figure A7. ^{1}H NMR (600 MHz) spectra of **PBI-Se^{O10}** in $CDCl_3$.

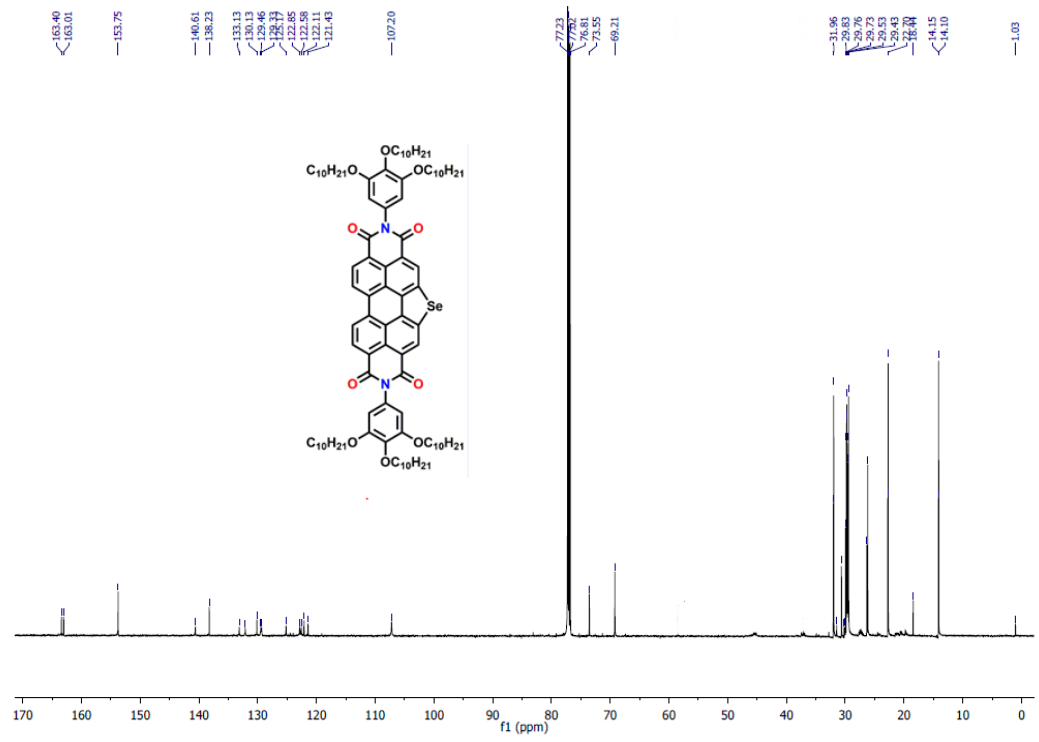

Figure A8. ^{13}C NMR (150 MHz) spectra of **PBI-Se^{O10}** in $CDCl_3$.

3.6.2. Polarizing optical microscopy (POM)

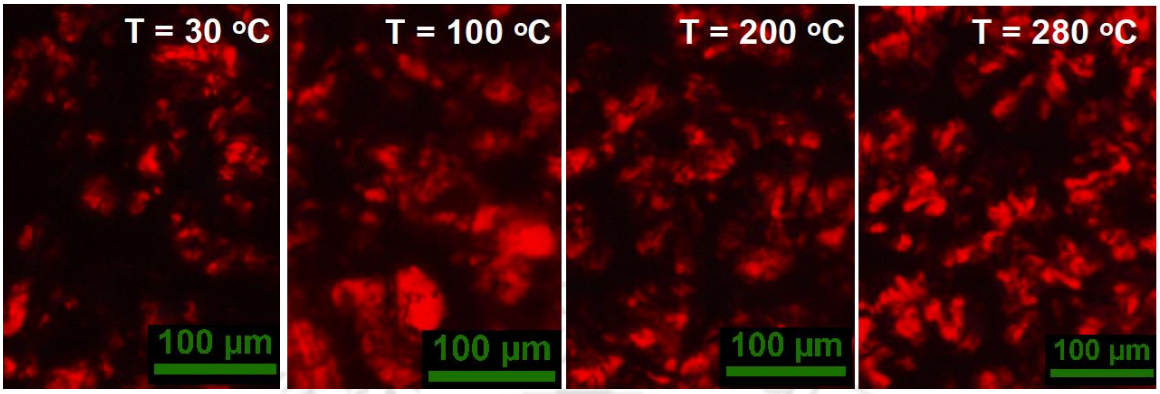

Figure A9. POM images of **PBI^{O10}** at different temperature intervals obtained on cooling the isotropic melt.

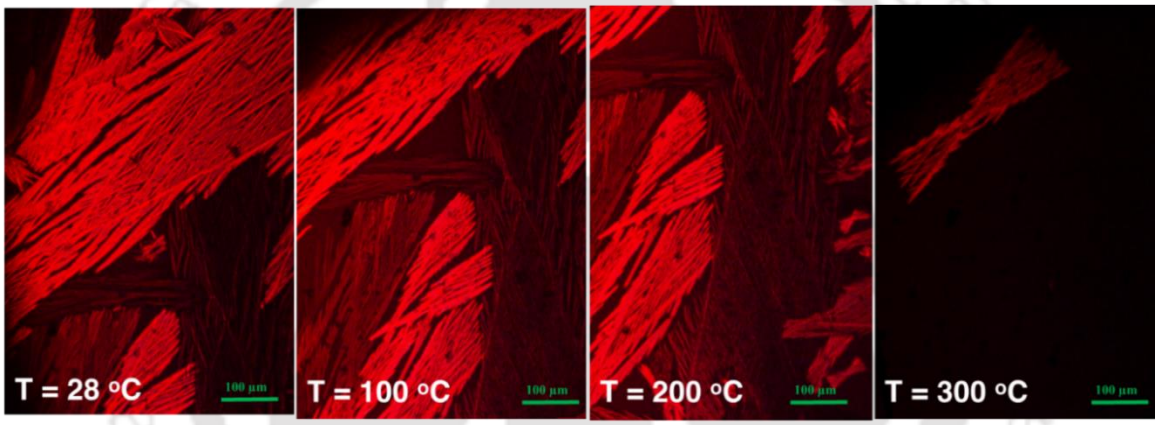

Figure A10. POM images of **PBI-N^{O10}** at different temperature intervals obtained on cooling the isotropic melt.

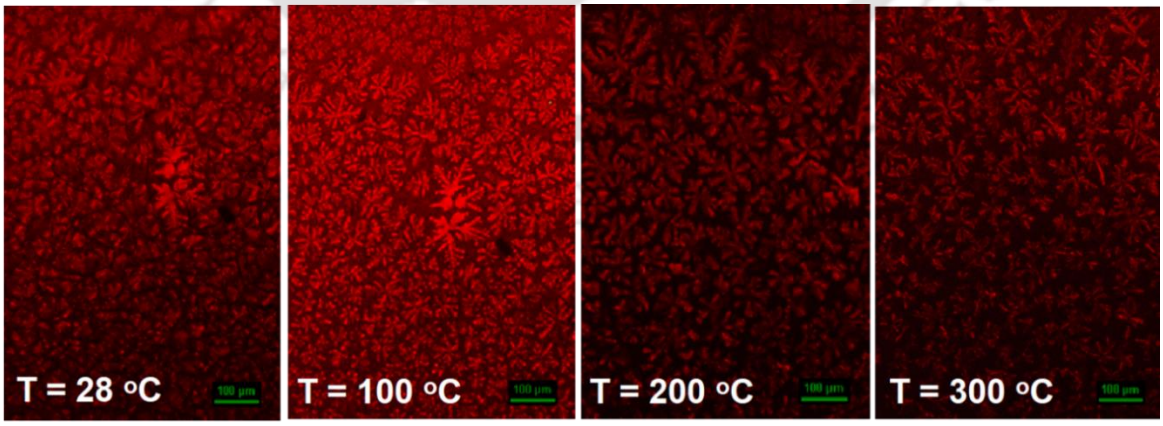

Figure A11. POM images of **PBI-S^{O10}** at different temperature intervals obtained on cooling the isotropic melt.

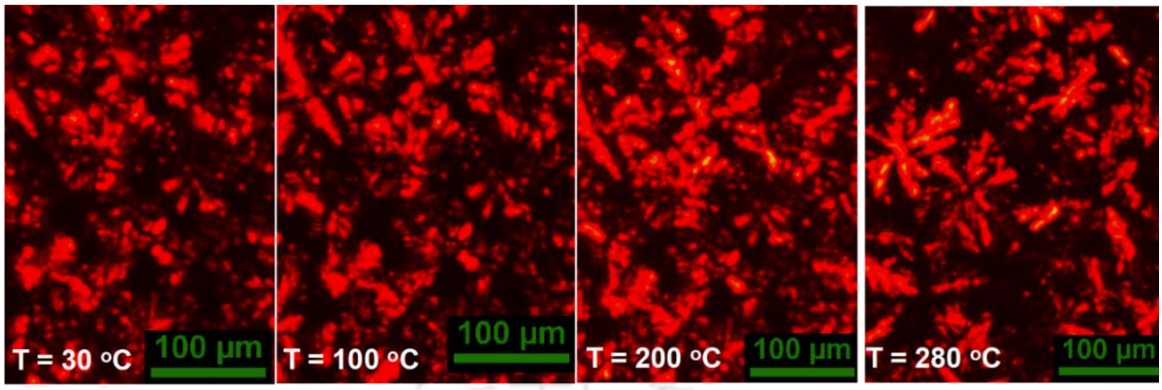

Figure A12. POM images of **PBI-Se^{O10}** at different temperature intervals obtained on cooling the isotropic melt.

3.6.3. Differential scanning calorimetry (DSC)

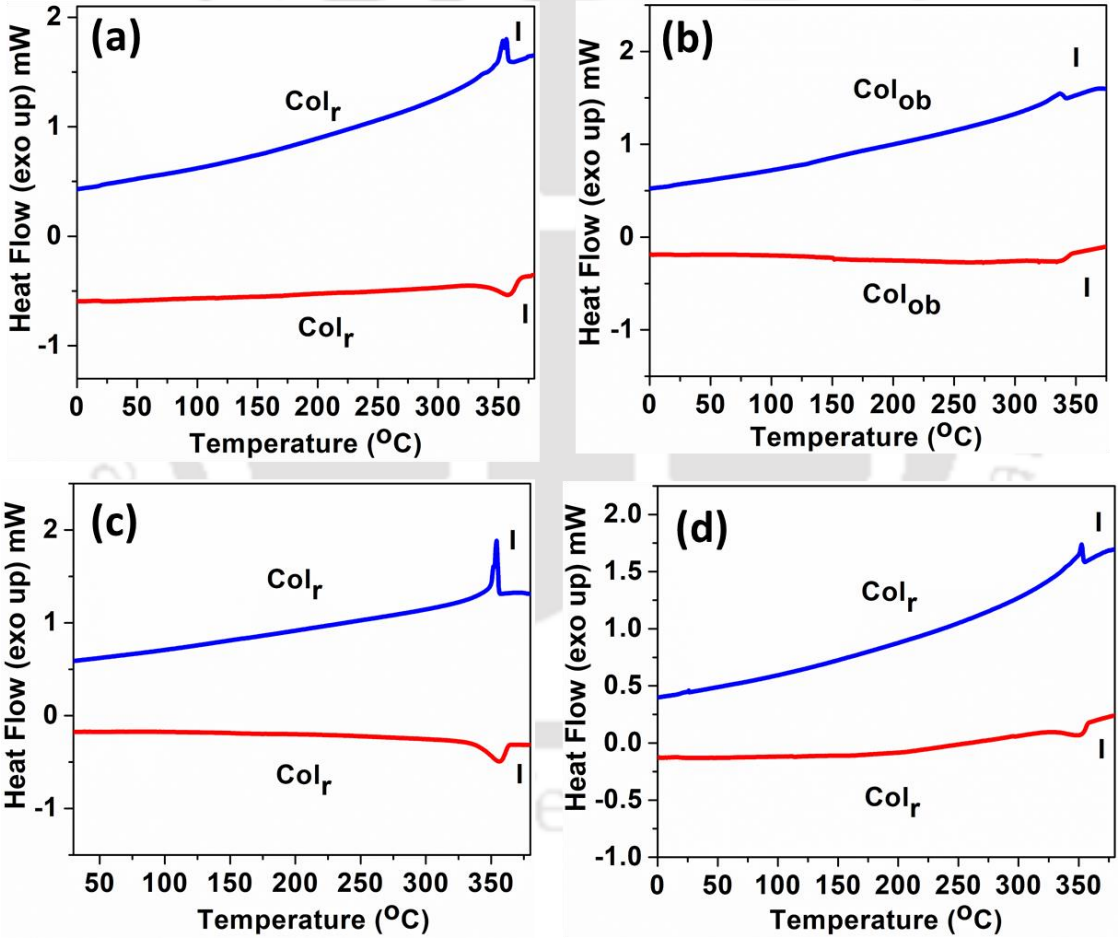

Figure A13. DSC thermograms of compounds **PBI^{O10}** (a)**, PBI-N^{O10}** (b)**, PBI-S^{O10}** (c)and **PBI-Se^{O10}** (d) at a rate 5 ^{o}C/min (Red trace: Second heating scan; Blue trace: First cooling scan).

3.6.4. Thermogravimetric analysis (TGA)

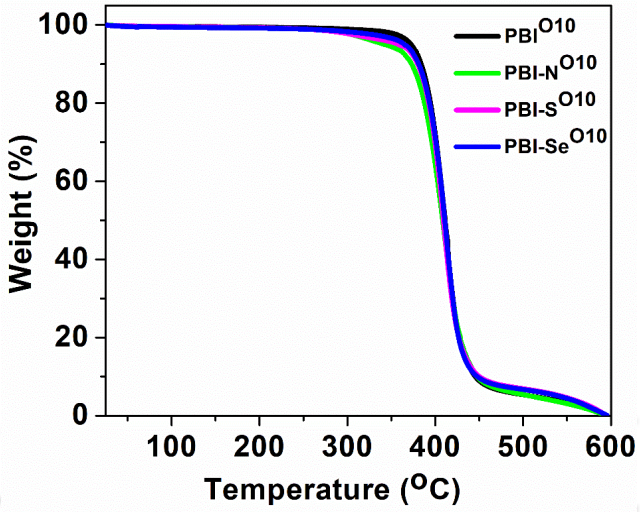

Figure A14. TGA plots of compound **PBI^{O10}**, **PBI-N^{O10}**, **PBI-S^{O10}** and **PBI-Se^{O10}** (heating rate of 10 ^{o}C/min, Nitrogen atmosphere).

3.6.5. X-ray diffraction studies (XRD)

Table A3.1. Results of (*hkl*) indexation of XRD profiles of the compounds at a given temperature (T) of mesophases[a]

Compounds (D/Å)	Phase (T/^{o}C)	Space Group	d_{obs} (Å)	d_{cal} (Å)	Miller indices *hk*	Lattice parameters (Å), Lattice area S (Å^2), Molecular volume (Å^3)
PBI^{O10} (47.34) MW: 1480.1	Col$_r$ (100)	P2mm	27.21 15.02 13.62 8.33 6.02 4.60 (h_a)	27.21 15.03 13.60 8.54 5.92	10 12 20 14 43	*a* = 27.2 *b* = 36.0 *S* = 979.4
	Col$_r$ (28)		27.29 24.10 14.12 12.75 9.15 6.93 5.69 4.36 (h_a) 3.37 (h_c)	27.30 21.03 14.12 12.61 9.10 7.01 5.80	10 11 12 21 30 33 43	*a* = 27.3 *b* = 33.0 *S* = 900.9 *V* = 3036 *Z* = 1.3
PBI-N^{O10} (44.25) MW: 1521.2	Col$_{ob}$ (280)	P1	29.97 26.42 13.23 11.28 10.36 9.99 8.82 8.61	29.97 26.42 13.23 11.23 10.12 9.99 8.81 8.72	10 01 12 22 31 30 03 -31	*a* = 30.8 *b* = 27.1 γ = 77.1^{o} *S* = 812.5

			6.92 3.70 (h_c)	6.94	-23	
	Col_{ob} (230)		26.38 13.27 11.29 9.98 5.08 3.68 (h_a)	26.38 13.27 11.29 9.98 5.75	01 12 22 30 -41	a = 32.3 b = 26.2 γ = 74^o S = 812.8
	Col_{ob} (28)		25.20 12.99 11.26 10.20 6.85 4.45 (h_a) 3.31 (h_c)	25.20 12.99 10.95 10.28 6.82	01 12 22 -12 42	a = 28.1 b = 26.4 γ = 72.7 ^{o} S = 707.4 V = 2341.4 Z = 0.9
PBI-S^{O10} (43.98) MW:1510.2	Col_r (200)	P2mm	31.20 27.83 8.49 5.08 (h_a)	31.20 27.83 8.33	10 01 32	a = 31.2 b = 27.8 S = 868.3
	Col_r (100)		31.31 27.18 8.81 5.50 4.62 (h_a)	31.31 27.18 8.70 5.92	10 01 13 43	a = 31.31 b = 27.18 S = 851
	Col_r (28)		27.78 24.04 13.45 5.60 4.36 3.43 (h_c)	27.78 24.04 13.89 5.52 4.55	01 10 02 42	a = 24.0 b = 27.8 S = 667.8 V = 2290.7 Z = 0.9
PBI-Se^{O10} (43.74) MW: 1556.9	Col_r (200)	P2mm	28.15 16.25 14.45 10.66 8.76 5.49 5.0 (h_a)	28.15 16.25 14.08 10.64 8.58	10 02 20 22 23	a = 28.1 b = 26.4 S = 741
	Col_r (100)		28.15 25.62 13.50 5.38 4.60 (h_a) 3.45 (h_c)	28.15 25.62 14.08 5.43	10 01 20 43	a = 28.2 b = 25.6 S = 721.2 V = 2488.1 Z = 1
	Col_r (28)		27.29 23.68 13.58 5.20 4.42 (h_a) 3.43 (h_c)	27.29 23.68 13.65 5.96	01 10 20 43	a = 27.3 b = 23.7 S = 646.2 V = 2216.5 Z = 0.9

[a]The diameter (D) of the disk (estimated from Chem 3D Pro 8.0 molecular model software from Cambridge Soft). d_{obs}: spacing observed; d_{cal}: spacing calculated (deduced from the lattice parameters; a, b for Col_r and Col_{ob} phase; γ tilt angle for Col_{ob} phase; c is height of the unit cell). The spacings marked h_a and h_c correspond to diffuse reflections in the wide-angle region arising from correlations between the alkyl chains and core regions, respectively. Z indicates the number of molecules per columnar slice of thickness h_c estimated from the lattice area S and the volume V; Z is only calculated when h_c was observed..

3.6.6. Photophysical studies

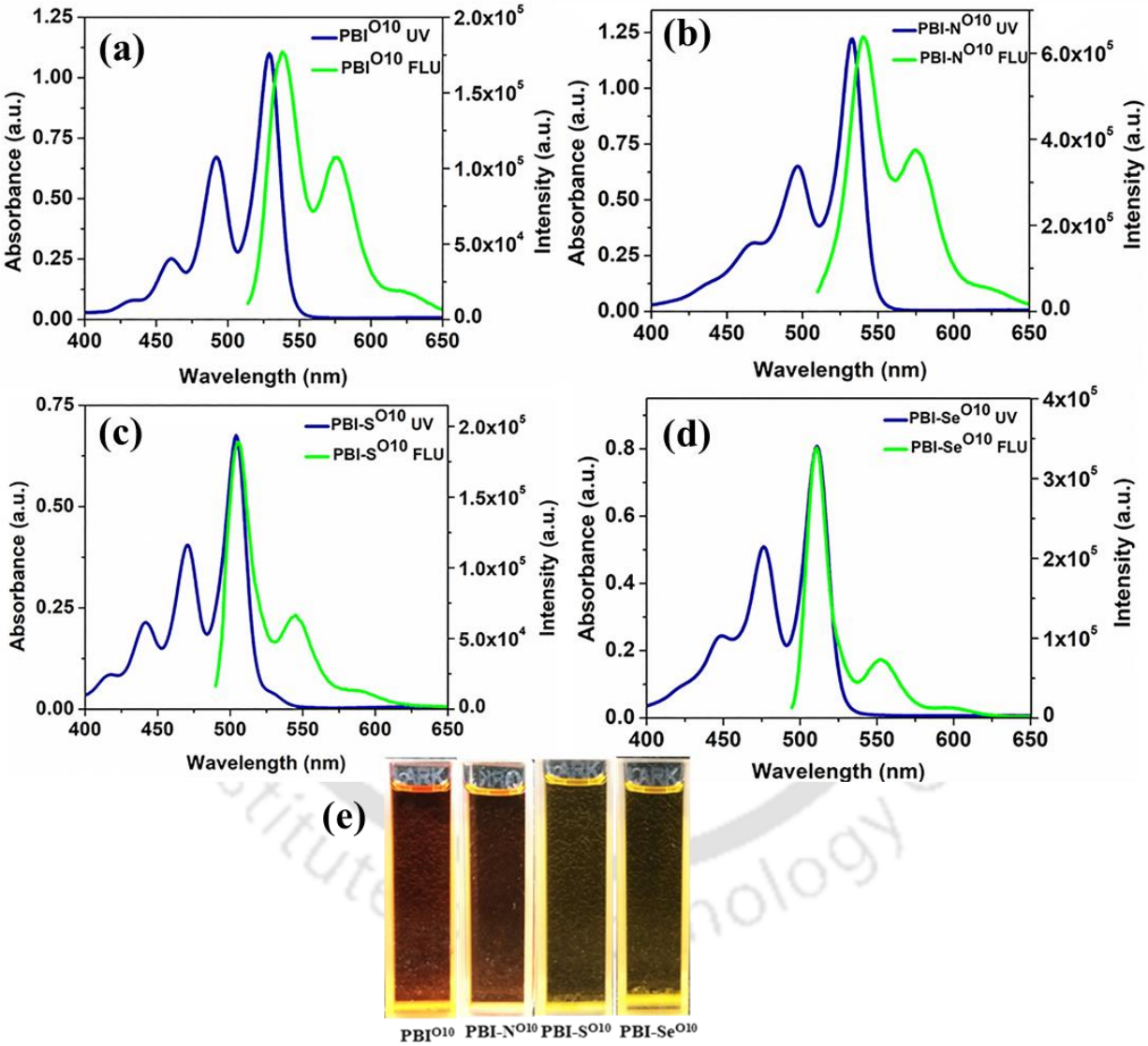

Figure A15. Overlay of absorption and emission Spectra of **PBI^{O10}** (a), **PBI-N^{O10}** (b), **PBI-S^{O10}** (c) and **PBI-Se^{O10}** (d) in solution state (in chloroform). Images of micromolar chloroform solutions under UV light (λ = 365 nm) (e).

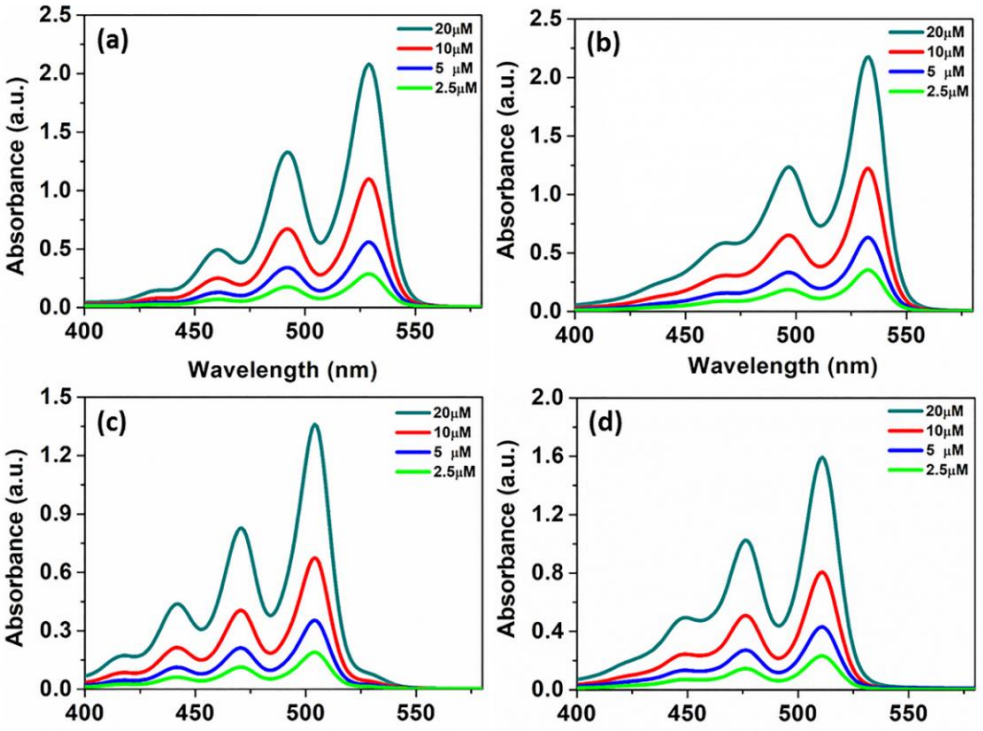

Figure A16. Absorption Spectra of **PBI^{O10}** (**a**), **PBI-N^{O10}** (**b**), **PBI-S^{O10}** (**c**) and **PBI-Se^{O10}** (**d**) with respect to change in concentration in solution state (in chloroform).

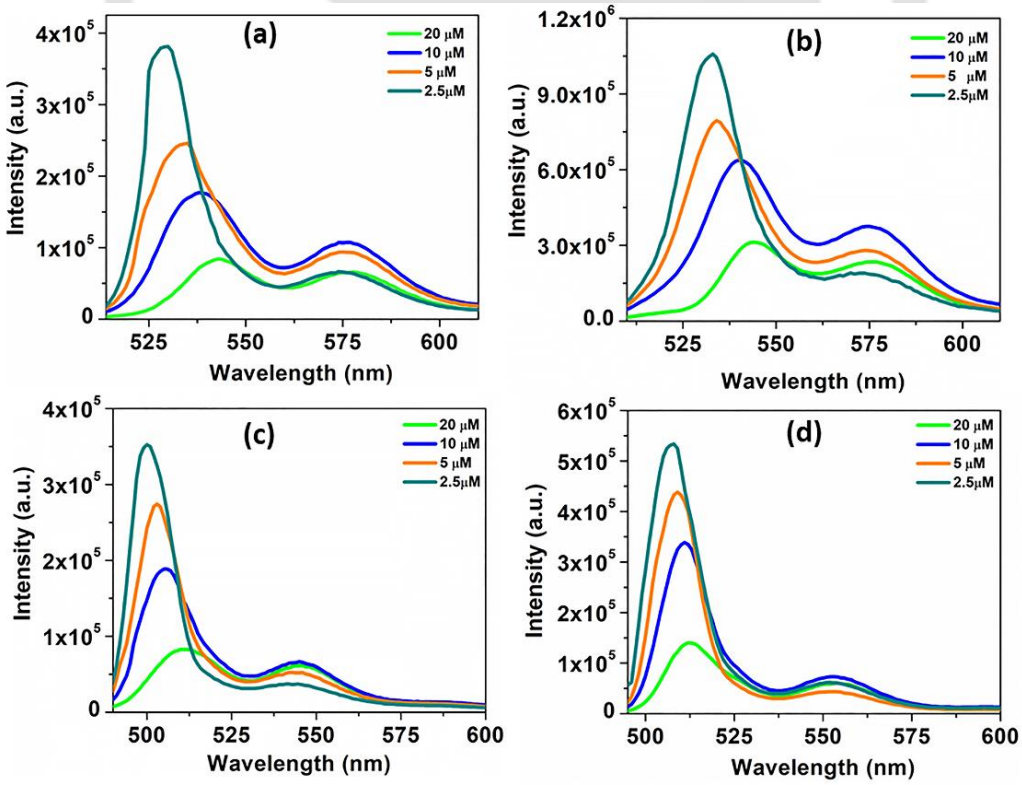

Figure A17. Emission Spectra of **PBI^{O10}** (**a**), **PBI-N^{O10}** (**b**), **PBI-S^{O10}** (**c**) and **PBI-Se^{O10}** (**d**) with respect to change in concentration in solution state (in chloroform).

3.6.7. Cyclic voltammetry (CV)

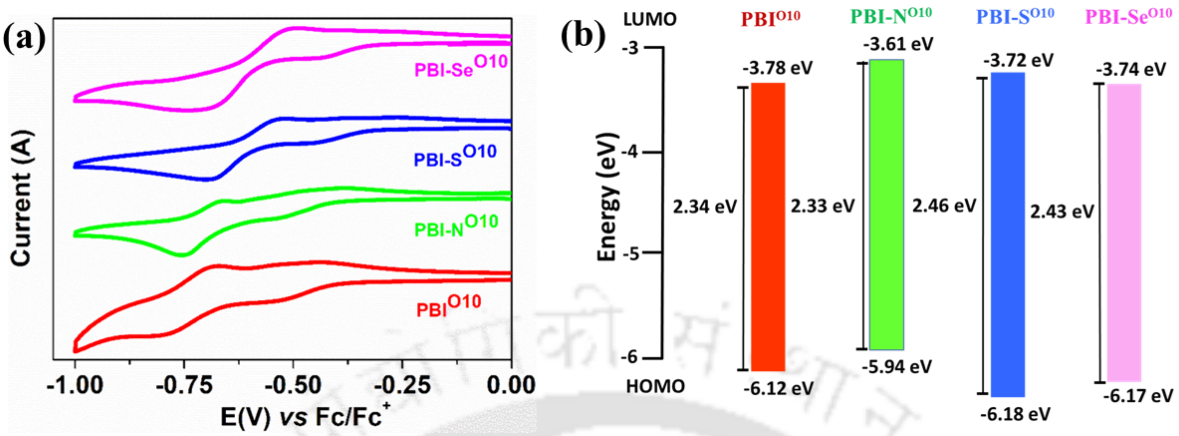

Figure A18. Cyclic voltammograms of PBIs (a); Energy band level diagram showing HOMO and LUMO energy levels of PBIs (b).

3.6.8. DFT Studies

To understand the electronic properties and frontier molecular orbital energy level of compounds **PBI^{O10}**, **PBI-N^{O10}**, **PBI-S^{O10}** and **PBI-Se^{O10}**, computational studies was carried out in B3LYP/6-311g(d,p) method using Gaussian 09 program package. The absence of imaginary frequency ensured the energy minimized structure of all the compounds.

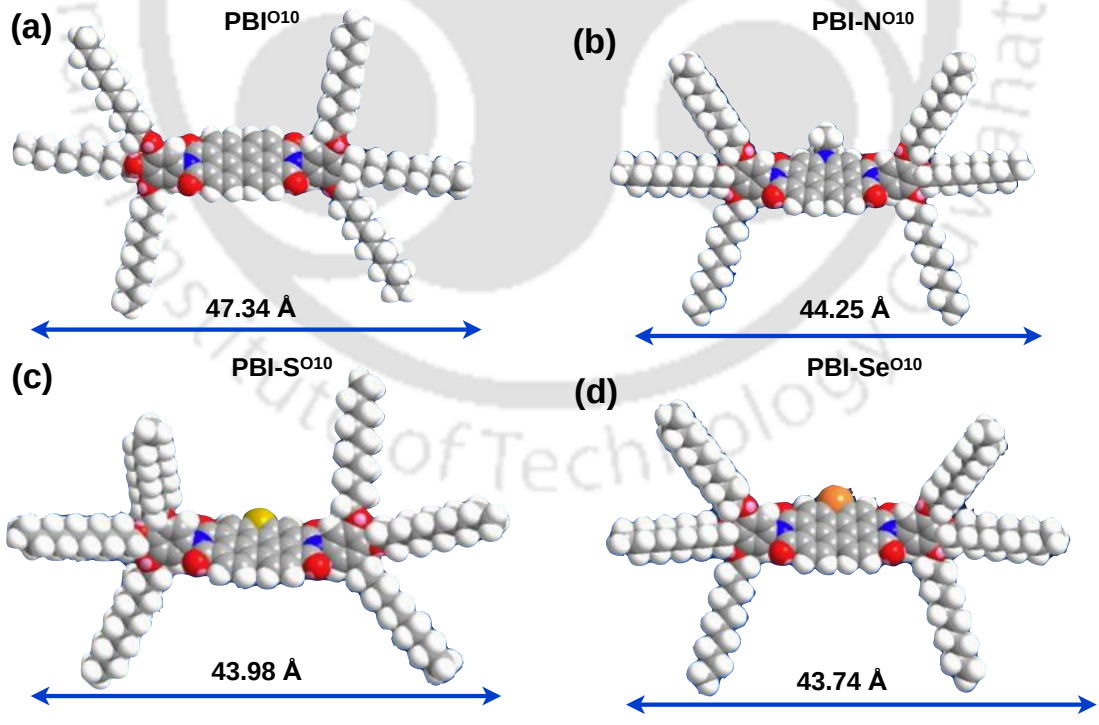

Figure A19. Optimized geometry of compounds **PBI^{O10}** (a), **PBI-N^{O10}** (b), **PBI-S^{O10}** (c) and **PBI-Se^{O10}** (d).

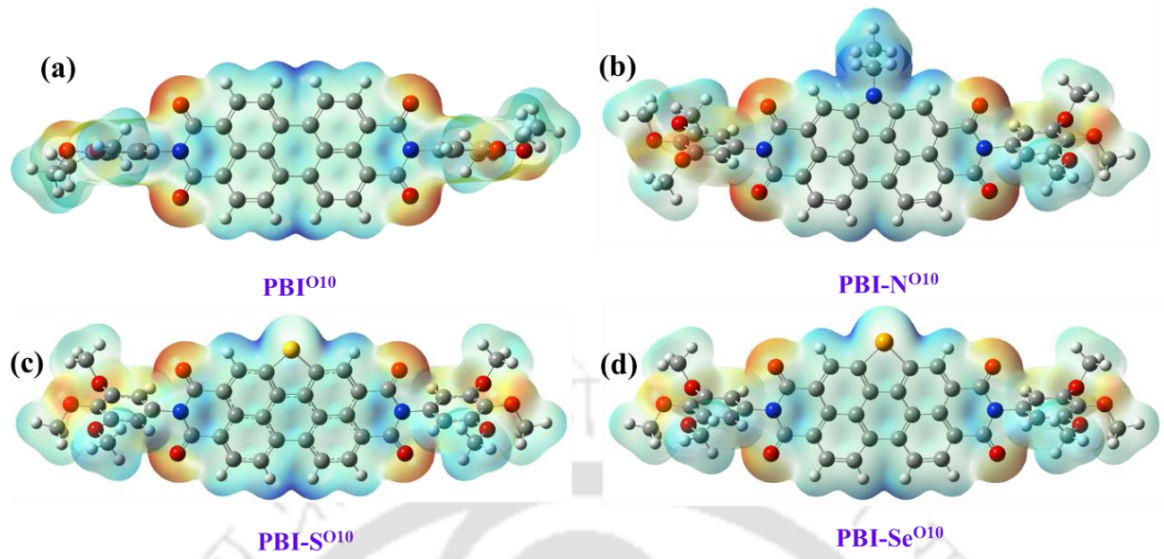

Figure A20. 3D molecular electrostatic potential contour map of optimized structure of PBIs derived from tri-*n*-alkoxyanilines (In the mapped electro-static potential surface, the red and blue colors refer to the electron-rich and electron-poor regions, respectively, whereas the green color signifies the zero electrostatic potential, chain length on the phenyl group is limited to methyl for clarity purpose).

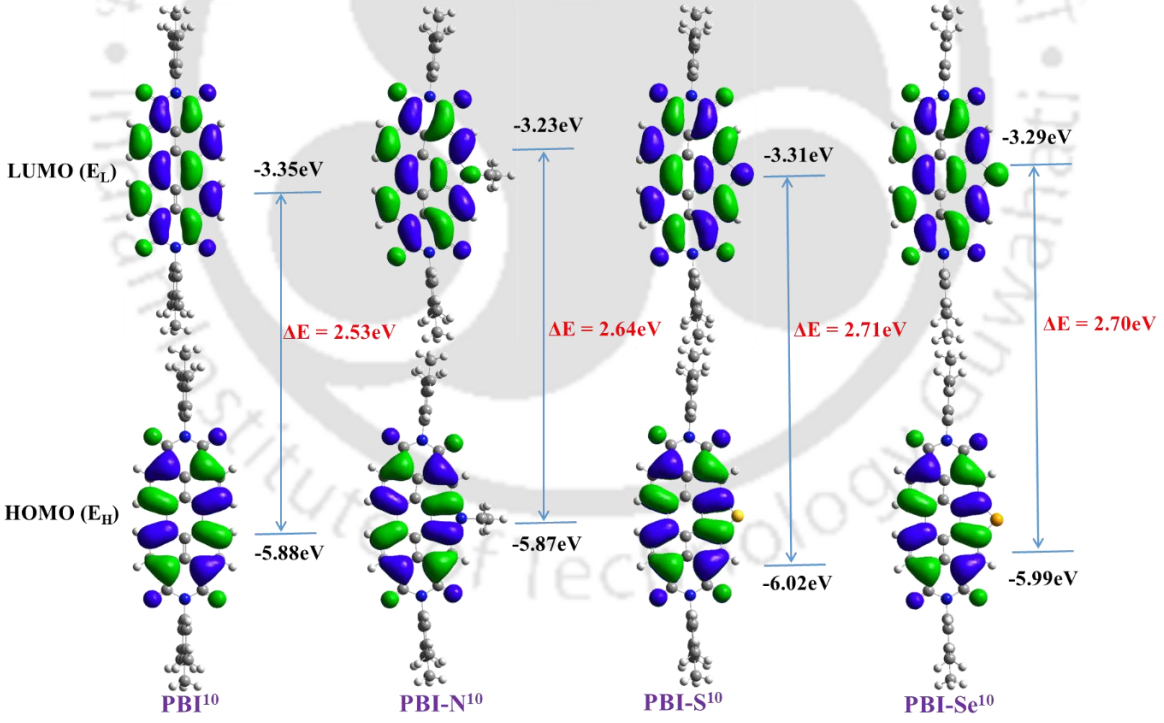

Figure A21. Frontier molecular orbitals of PBIs derived from obtained from tri-*n*-alkylanilines. DFT calculations at the B3LYP/6-31G(dp) level. E_H and E_L denote energies of the highest occupied molecular orbital (HOMO) and the lowest unoccupied molecular orbital (LUMO), respectively (chain length on the phenyl group is limited to methyl for clarity purpose).

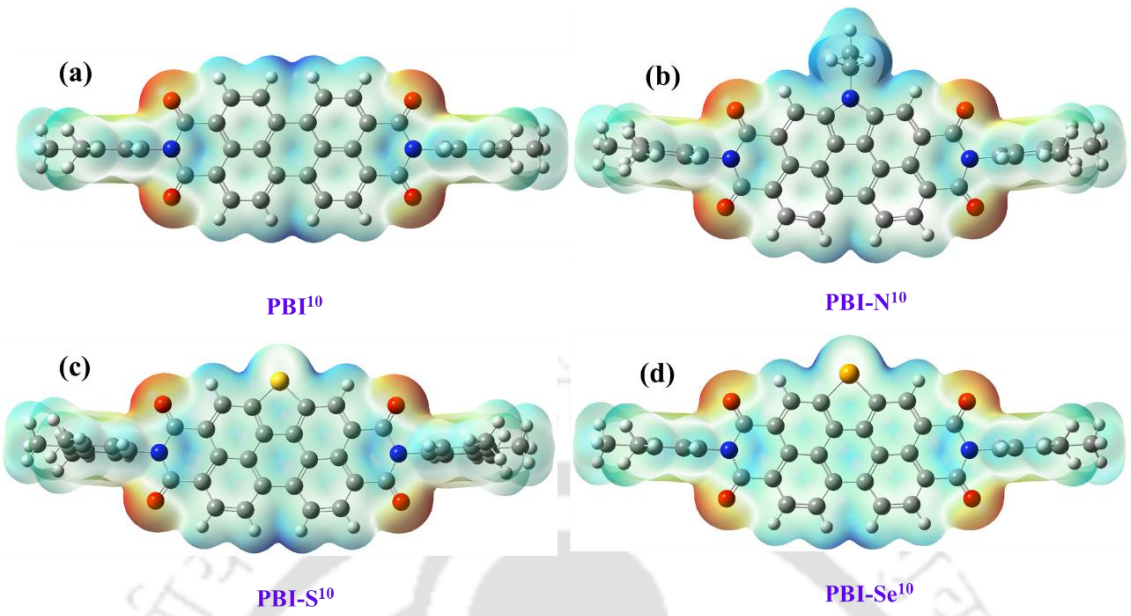

Figure A22. 3D molecular electrostatic potential contour map of optimized structure of PBIs derived from tri-*n*-alkylanilines (In the mapped electro-static potential surface, the red and blue colors refer to the electron-rich and electron-poor regions, respectively, whereas the green color signifies the zero electrostatic potential, chain length on the phenyl group is limited to methyl for clarity purpose).

3.6.9. Scanning Electron Microscopy

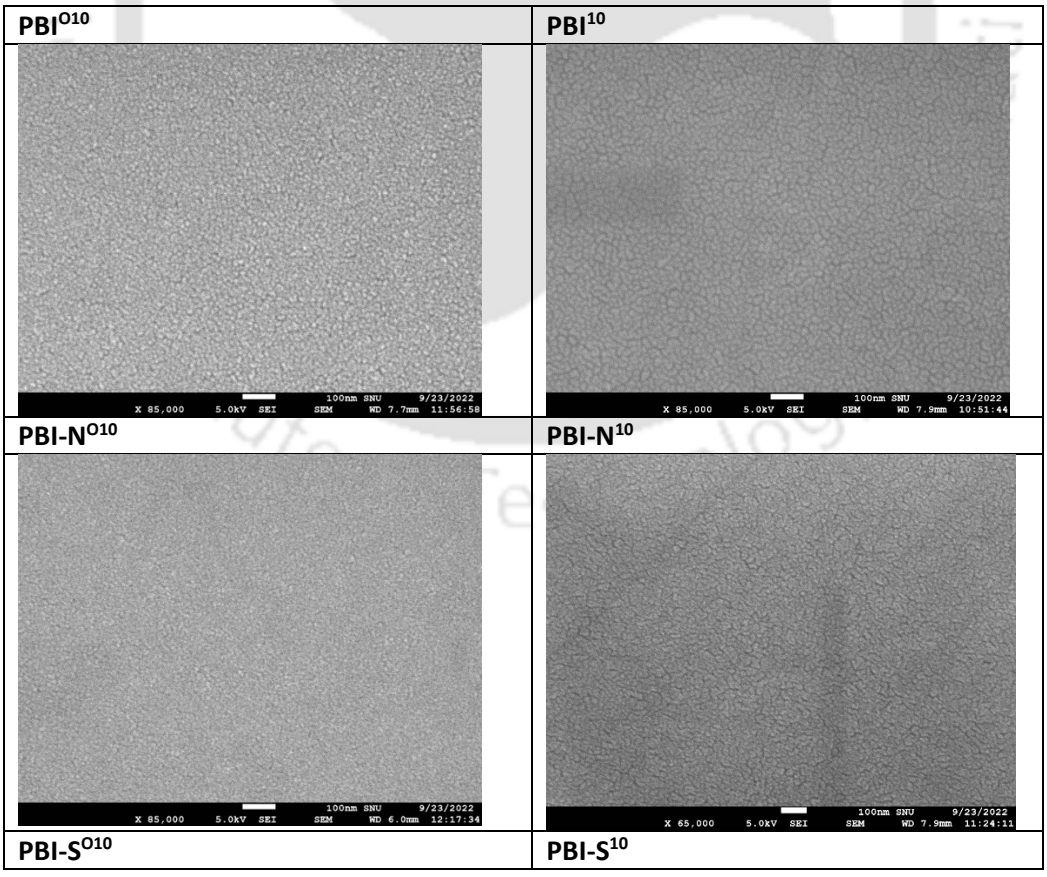

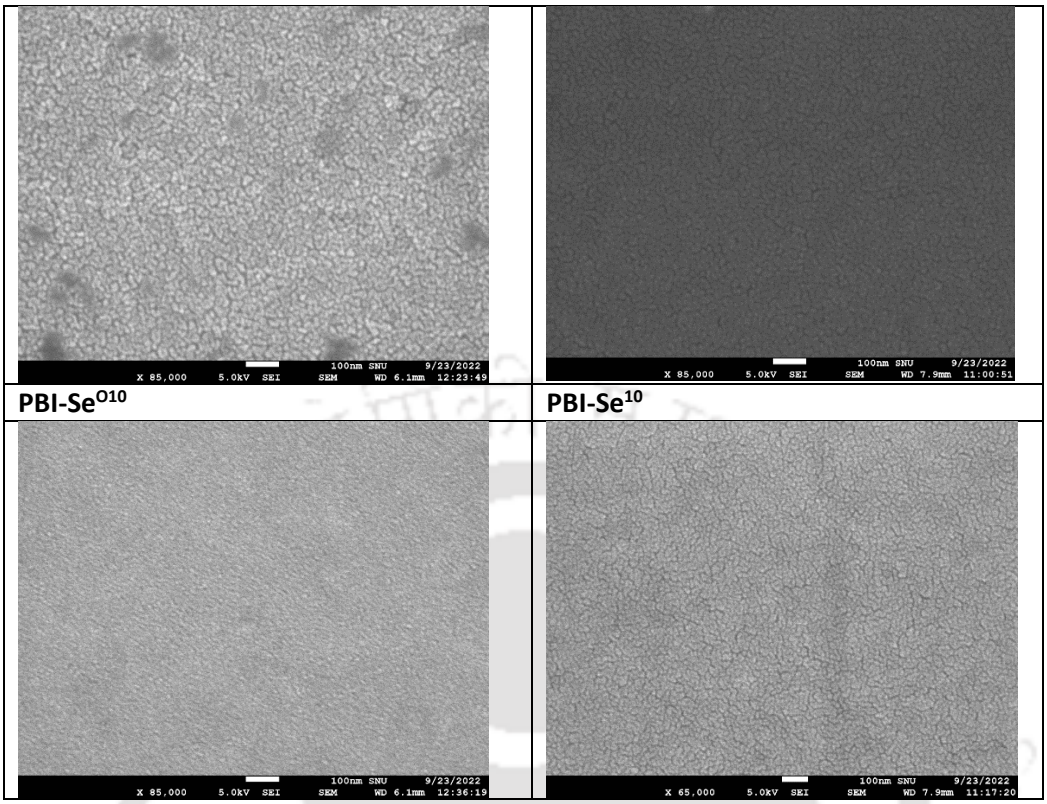

Figure A23. SEM images of spin coated PBIs in chloroform obtained after annealing 70 °C (Scale bar is 100 nm).

3.6.10. Device Fabrication and characterization:

In this work, charge transport features of PBIs derived from tri-*n*-alkoxy anilines (**PBI^{O10}, PBI-N^{O10}, PBI-S^{O10}** and **PBI-Se^{O10}**) and PBIs derived from tri-*n*-alkyl anilines (**PBI^{10}, PBI-N^{10}, PBI-S^{10}** and **PBI-Se^{10}**) were investigated using SCLC approach. For hole-only devices, ITO/PEDOT: PSS/PBIs/MoO_3-Ag were utilized, whereas, for electron-only devices, ITO/ZnO/PBIs/Ag were employed. For Device Fabrication, prepatterned indium tin oxide (ITO) substrates (Xinyan Technologies, Taiwan, 15 Ω /□) were used and cleaned using 5% soap solution in deionized water (Hellmanex III, Sigma-Aldrich), acetone, and isopropyl alcohol for 20 minutes sequentially in an ultrasonicator. The substrates were then dried with a gentle nitrogen gas blow and further exposed to UV ozone for 30 minutes (BioBEE Tech, India) at 50 °C to get rid of any organic residues. For both the PBI derivatives based on tri-*n*-alkoxy anilines (**PBI^{O10}, PBI-N^{O10}, PBI-S^{O10}** and **PBI-Se^{O10}**) and PBIs derived from tri-*n*-alkyl anilines (**PBI^{10}, PBI-N^{10}, PBI-S^{10}** and **PBI-Se^{10}**), ITO/PEDOT: PSS (40 nm)/PBIs (100 nm)/MoO_3 (5-7 nm)/Ag (100 nm) device structure was used for hole-only devices and ITO/ZnO (30 nm)/PBIs (100 nm)/Ag (100 nm) was used for electron-only devices in a diode like configuration.

For Fabrication of hole Only device (ITO/PEDOT: PSS/PBIs/MoO_3-Ag), first a 40 nm PEDOT: PSS (Sigma Aldrich) layer was spin coating at a speed of 4000 rpm for 65 secs with 2000 rpm as ramp rate. The film is then annealed at 150 °C on a hot plate for 20 minutes under ambient conditions. Active layer consisting of both PBI derivatives were then spin coated on PEDOT: PSS at 1500 rpm for 45 secs from a 10 mg/ml solution in chloroform to get a thickness ~ 100 nm.

Finally, ~ 7 nm of MoO_3 and 100 nm of Ag layer was subsequently thermally evaporated under high vacuum (2.2 x 10^{-6} mbar) on top of active layer as top contact to complete the devices.

For, electron only device, firstly ZnO sol gel solution (200 mg zinc acetate dihydrate ($Zn(CH_3COO)_2 2H_2O$) + 52 mg ethanolamine in 2 mL 2-methoxy ethanol, agitated heavily overnight and filtered using 0.45 µm PTFE filter) was spin coated on cleaned and UV Ozone treated ITO substrates to obtain a thickness of ~ 30 nm (4500 rpm for 45 sec followed by film annealing at 180 °C for 1 hour under ambient condition). An active layer of both PBI derivatives were then spin coated on top of the ZnO layer at 1500 rpm for 45 secs from a 10 mg/ml solution in chloroform to get a thickness ~ 100 nm. Lastly, 100 nm of Ag layer was evaporated at 2.2 x 10^{-6} mbar pressure on top of active layer to complete the devices. All fabricated devices have an active area of 0.066 cm^2 (measured through the overlap of ITO and top contact).

Table A3.2. Results of SCLC studies for PBIs derived from tri-*n*-alkylanilines and PBIs derived from tri-*n*-alkoxy anilines.

Entry	**PBI[10]**	**PBI-N[10]**	**PBI-S[10]**	**PBI-Se[10]**
Hole mobility (cm^2/ V.s)	5.74E-03 5.53E-03 5.00E-03 7.32E-03 7.42E-03	3.72E-03 2.99E-03 2.28E-03 2.34E-03 2.73E-03	8.38E-03 8.48E-03 7.63E-03 8.79E-03 8.68E-03	2.26E-03 4.26E-03 4.61E-03 2.89E-03 7.45E-04
Avg. **Stdev**	**6.20E-03** **1.10E-03**	**2.81E-03** **5.85E-04**	**8.39E-03** **4.55E-04**	**2.95E-03** **1.57E-03**
Electron mobility (cm^2/ V.s)	7.65E-03 7.36E-03 1.15E-02 1.15E-02 1.29E-02	8.44E-03 8.32E-03 5.23E-03 5.34E-03 5.45E-03	7.66E-03 8.59E-03 4.88E-03 2.72E-02 2.72E-02	4.16E-03 5.91E-03 5.90E-03 4.39E-03 5.05E-03
Avg. **Stdev**	**1.02E-02** **2.51E-03**	**6.56E-03** **1.67E-03**	**1.51E-02** **1.11E-02**	**5.08E-03** **8.19E-04**
Entry	**PBI[O10]**	**PBI-N[O10]**	**PBI-S[O10]**	**PBI-Se[O10]**
Hole mobility (cm^2/ V.s)	2.05E-03 2.08E-03 2.39E-03 2.17E-03 1.72E-03	5.64E-03 6.93E-03 6.89E-03 8.34E-03 3.70E-03	7.31E-03 7.68E-03 7.17E-03 7.13E-03 5.24E-03	1.89E-03 1.43E-03 1.78E-03 1.84E-03 1.61E-04
Avg. **Stdev**	**2.08E-03** **2.42E-04**	**6.30E-03** **1.74E-03**	**6.91E-03** **9.56E-04**	**1.42E-03** **7.27E-04**
Electron mobility (cm^2/ V.s)	3.21E-03 2.35E-03 2.41E-03 3.27E-03 3.31E-03	2.27E-03 2.37E-03 1.81E-03 1.99E-03 2.00E-03	2.03E-03 2.22E-03 3.40E-03 3.39E-03 3.12E-03	1.15E-03 1.12E-03 1.66E-03 6.68E-04 2.84E-04
Avg. **Stdev**	**2.91E-03** **4.86E-04**	**2.09E-03** **2.28E-04**	**2.82E-03** **6.50E-04**	**9.76E-04** **5.23E-04**

3.7. References

1. Z. Liu, G. Zhang, Z. Cai, X. Chen, H. Luo, Y. Li, J. Wang, D. Zhang, *Adv. Mater.* 2014, **26**, 6965–6977.
2. A. R. Mohebbi, J. Yuen, J. Fan, C. Munoz, M. F. Wang, R.S. Shirazi, J. Seifter, F. Wudl, *Adv. Mater.* 2011, **23**, 4644–4648.
3. J. Chen, J. Yang, Y. Guo, Y. Liu, *Adv. Mater.* 2022, **34**, 2104325.
4. Y. Ma, Z. Shi, A. Zhang, J. Li, X. Wei, T. Jiang, Y. Li, X. Wang, *Dyes and Pigments* 2016, **135**, 41-48.
5. R. K. Gupta, S. K. Pathak, B. Pradhan, D.S.S. Rao, S. K. Prasad, A. A. Sudhakar, *Soft Matter* 2015, **11**, 3629-3636.
6. R. K. Gupta, B. Pradhan, S. K. Pathak, M. Gupta, S. K. Pal, A. A., *Langmuir* **2015**, **31**, 8092-8100.
7. R. K. Gupta, S. K. Pathak, B. Pradhan, M. Gupta, S. K. Pal, A. A. Sudhakar, *ChemPhysChem* 2016, **17**, 859-872.
8. J. Dhar, N. Venkatramaiah, A. Anitha, S. Patil, *J. Mater. Chem. C* 2014, **2**, 3457-3466.
9. Y. Sun, L. Tan, S. Jiang, H. Qian, Z. Wang, D. Yan, C. Di, Y. Wang, W. Wu, G. Yu, S. Yan, C. Wang, W. Hu, Y. Liu, D. Zhu, *J. Am. Chem. Soc.* 2007, **129**, 1882-1883.
10. L. Tan, W. Jiang, L. Jiang, S. Jiang, Z. Wang, S. Yan, W. Hu, *Appl. Phys. Lett.* 2009, **94**, 108.
11. Y. Zagra- nyarski, L. Chen, D. Jänsch, T. Gessner, C. Li, K. Müllen, *Org. lett.* 2014, **16**, 2814-2817.
12. W. Jiang, Y. Zhou, H. Geng, S. Jiang, S. Yan, W. Hu, Z. Wang, Z. Shuai, J. Pei, *J. Am. Chem. Soc.* 2011, **133**, 1-3.
13. H. Iino, T. Usui, J. Hanna, *Nat. Commun.* 2015, **6**, 1-8.
14. A. Patra, Y. H. Wijsboom, S. S. Zade, M. Li, Y. Sheynin, G. Leitus, M. Bendi- kov, *J. Am. Chem. Soc*. 2008, **130**, 6734-6736.
15. D. J. Schipper, L. C. H. Moh, P. Müller, T. M. Swager, *Angew. Chem. Int. Ed.*, 2014, **53**, 5847. *Angew. Chem.* 2014, **126**, 5957-5961.
16. A. Bedi, S. Debnath, S. S. Zade, *Chem. Commun.* 2014, **50**, 13454-13456.
17. F. T. Burling, B. M. Goldstein, *J. Am. Chem. Soc.* 1992, **114**, 2313 —2320.
18. J. S. Murray, P. Lane, P. Politzer, *Int. J. Quantum Chem.* 2008, **108**, 2770 —2781.
19. M. Gsänger, D.Bialas, L. Huang, M. Stolte, F. Würthner, *Adv. Mater.* 2016, **28**, 3615–3645.

20. S. Shinamura, I. Osaka, E. Miyazaki, K. Takimiya, *Heterocycles* 2011, **83**, 6, 1187 – 1204.
21. V. Dehm, Z. Chen, U. Baumeister, P. Prins, L. D. A. Siebbeles and F. Würthner, *Org. lett.* 2007, **9**, 1085-1088.
22. S. Herbst, B. Soberats, P. Leowanawat, M. Lehmann, F. Würthner, *Angew. Chem.* 2017, **129**, 1 – 5.
23. B. A. Jones, A. Facchetti, M. R. Wasielewski, T. J. Marks, *J. Am. Chem. Soc.* 2007, **129**, 15259-15278.
24. S. Shoaee, Z. An, X. Zhang, S. Barlow, S. R. Marder, W. Duffy, M. Heeney, I. McCulloch, J. R. Durrant, *Chem. Commun.* 2009, 5445-5447.
25. J. J. Dittmer, E. A. Marseglia, R. H. Friend, *Adv. Mater.* 2000, **12**, 1270-1274.
26. R. J. Kline, M. D. McGehee, E. N. Kadnikova, J. Liu, J. M. Frechet, *Adv. Mater.* 2003, **15**, 1519-1522.
27. T. Wohrle, I. Wurzbach, J. Kirres, A. Kostidou, N. Kapernaum, J. Litterscheidt, J. C. Haenle, P. Staffeld, A. Baro, F. Giesselmann, *Chem. Rev.* 2016, **116**, 1139-1241.
28. W. Pisula, M. Zorn, J. Y. Chang, K. Müllen, R. Zentel, *Macromol. rapid commun.* 2009, **30**, 1179-1202.
29. M. A. Muth, M. Carrasco-Orozco, M. Thelakkat, *Adv. Funct. Mater.* 2011, **21**, 4510-4518.
30. R. K. Gupta and A. S. Achalkumar, *Langmuir* 2018, **35**, 2455-2479.
31. R. K. Gupta, D. S. S. Rao, S. K. Prasad, and A. S. Achalkumar, *Chem.–Eur. J.* 2018, **24**, 3566-3575.
32. V. Percec, M. Peterca, T. Tadjiev, X. Zeng, G. Ungar, P. Leowanawat, E. Aqad, M. R. Imam, B. M. Rosen, U. Akbey, R. Graf, *J. Am. Chem. Soc.* 2011, **133**, 12197-12219.
33. Z. Chen, V. Stepanenko, V. Dehm, P. Prins, L. D. Siebbeles, J. Seibt, P. Marquetand, V. Engel, F. Würthner, *Chem.– Eur. J.* 2007, **13**, 436-449.
34. F. Würthner, C. Thalacker, S. Diele, C. Tschierske, *Chem.– Eur. J.* 2001, **7**(10), 2245-2253.
35. Z. Chen, B. Fimmel, F. Würthner, *Org. Biomol. Chem.* 2012, **10**(30), 5845-5855.
36. R. K. Gupta, A. Dey, A. Singh, P. K. Iyer, and A. A. Sudhakar, *ACS Appl. Electron. Mater.* 2019, **1**, 1378-1386.
37. H. Zhylitskaya, M. Stępień, *Org. Chem. Front.* 2018, **5**, 2395-2414.
38. P. N. Murgatroyd, *J. Phys. D: Appl. Phys.* 1970, **3**, p.151.
39. P. W. Blom, V. D. Mihailetchi, L. J. A. Koster, D. E. Markov, *Adv. Mater.* 2007, **19**, 1551-

1566.

40. H. Yin, P. Bi, S. H. Cheung, W. L. Cheng, K.L. Chiu, C. H. Y. Ho, H. W. Li, S. W. Tsang, X. Hao, S. K. So, *Solar RRL* 2018, **2**, p.1700239.
41. R. R. Reghu, H. K. Bisoyi, J. V. Grazulevicius, P. Anjukandi, V. Gaidelisc, V. Jankauskas, *J. Mater. Chem.* 2011, **21**, 7811-7819.
42. G. Balaji, T. S. Kale, A. Keerthi, A. M. Della Pelle, S. Thayumanavan, S. Valiyaveettil, *Org. Lett.* 2011, **13**, 1, 18-21.
43. L. Zhang, I. Song, J. Ahn, M. Han, M. Linares, M. Surin, H. J. Zhang, J. H. Oh, J. Lin, *Nat Commun* 2021, **12**, 142.
44. R. Sato, D. Yoo, T. Mori, *CrystEngComm*, 2019, **21**, 3218-3222.
45. P. Yu, Y. Li, H. Zhao, L. Zhu, Y. Wang, W. Xu, Y. Zhen, X. Wang, H. Dong, D. Zhu, W. Hu, *Small* 2021, **17**, 2006574.
46. Y. Su, Y. Li, J. Liu, R. Xing, Y. Han, *Nanoscale*, 2015, **7**, 1944-1955.
47. B. Balambiga, R. Dheepika, P. Devibala, *Sci Rep.*, 2020, **10**, 22029.
48. Y. Huang, Y. Yuan, W. Tu, Y. Zhang, M. Zhang, H. Qu; *Tetrahedron*, 2015, **71**, 3221 – 3230.
49. C. V. Yelamaggad, A. S. Achalkumar, D. S. S. Rao, and S. K. Prasad; *J. Org. Chem.* 2007, **72**, 8308-8318.

Chapter 4

Solution processable Swallow Tail Perylene Bisimides Exhibiting Room Temperature Columnar Phases and Efficient Ambipolar Charge Carrier Mobility

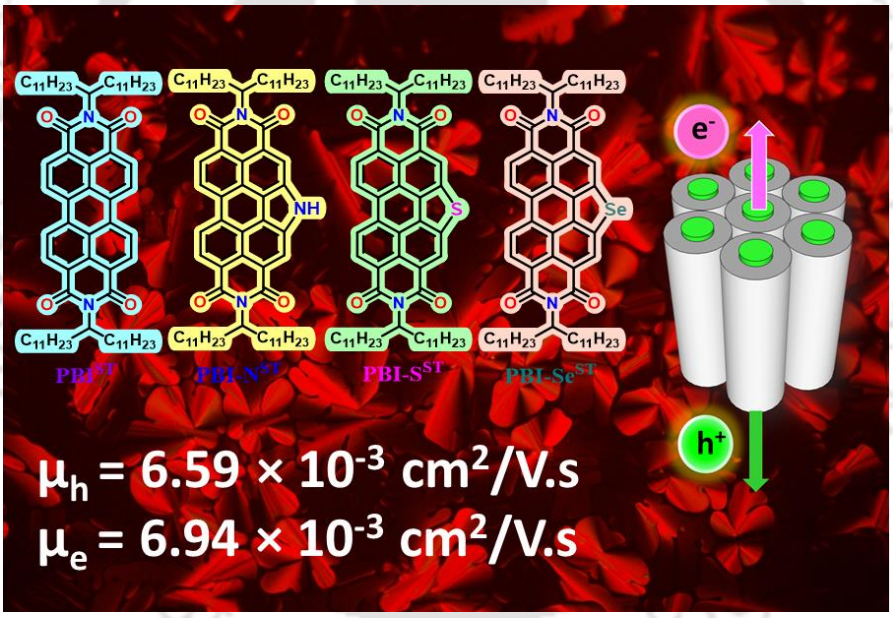

4.1. Introduction

The study of charge carrier mobility in organic semiconductors is crucial for the development of organic electronic devices and a critical factor for their performance.[1] Though organic semiconductors show low charge carrier mobility in comparison to their inorganic counterparts, they are inevitable to realize lightweight, large-area, low-cost, and flexible devices.[2] Most organic semiconductors are known for hole transport, and thus there is a dearth of electron carriers. Ambipolar organic semiconductors, which have the ability to transport both electrons and holes are further less in number and have great importance due to the simplicity they bring in device fabrication and the possible reduction in the number of charge carrier traps.[3] Therefore, it is imperative to foster the growth of versatile organic semiconductors that possess equitably distributed mobility for both holes and electrons, in addition to a reduced energy difference between valence and conduction bands.

Perylene bismide (PBIs) derivatives form an important class of structurally tunable, large bandgap, inexpensive n-type organic semiconductors known for their electron-deficient nature, high photo/thermal stability, and high quantum yield.[4,5] Therefore, they are considered favorable materials for application in organic electronic devices. The central large π-core leads to their strong intermolecular interaction leading to an increased order which is very important from the viewpoint of exciton diffusion or charge carrier mobility in organic electronic devices.[6] However, this also leads to a decreased solubility of the PBIs, which makes them, to be processed by vapor deposition techniques, which are expensive and only limited to a small area device. In such conditions introducing alkyl chains at the imide positions of PBIs will improve their solubility and also induce liquid crystallinity, thus making them easily processable. Liquid crystalline organic semiconductors are advantageous due to their intermediate order, solution processability, and self-healing ability of structural defects, which forms a productive area of research.[7] However, the structural design to achieve this goal is not that simple, because it requires a delicate balance between core rigidity and peripheral flexibility, which often requires the synthesis of different varieties of molecules to understand the exact rules governing the self-assembly behavior of PBIs.[8] Due to the large π-core, peripherally substituted PBI-based shape anisotropic molecules can stabilize a variety of columnar (Col) phases, where the molecules pack one above the other to form columns of indefinite length, which can be termed as ‘molecular wires’. Even then, the clearing

temperatures of these Col phases are very high.[9,10] In contrast, if the volume of the flexible chains is increased, then it leads to the dilution of the conductive cores in the columnar phase, which warrants a minimum amount of insulating peripheral alkyl chains to balance the self-assembly as well as the one-dimensional charge carrier mobility. Introduction of branched peripheral chains,[11] or swallow tailed groups, oligoethoxy chains or unsymmetrical substitution,[12] silyloxy chains,[13] connecting the trialkoxy benzene through a methylene unit[14] at the imide N are known to reduce the melting point of these PBIs and improve the solubility. The melting point and clearing point of a liquid crystal are governed by two different packing motifs, the first one is related to the unsettling of alkyl chains, while the second one corresponds to the displacement of discotic cores. Therefore, the introduction of disorder in the peripheral chains will not guarantee the reduction in clearing point. However, one needs to introduce subtle disorder in the intracolumnar packing of the discs in such a way that it should not entirely eliminate the liquid crystallinity, but bring down the clearing temperature as well, and hence reduce the processing cost of the organic electronic device.

Hetero atom incorporation in the molecular design of organic semiconductors brings about a multitude of new prospects, by affecting the charge carrier mobility, self-assembly behavior, and photophysical properties.[1] Therefore, the incorporation of heteroatoms like nitrogen, and chalcogens like sulphur, and selenium into the molecular structure of disc-like molecules stabilize the columnar liquid crystal phase in general, and PBIs, in particular, is an important topic.[8] Especially, chalcogen atoms like S and Se are known to facilitate intermolecular interactions (by S···S and Se···Se interactions) to promote beneficial molecular self-assembly.[15-17] The additional hetero atom to hetero atom interaction augments the existing π-π interaction among the perylene core, which can enhance the charge carrier mobility. Thus, hetero atom *bay*-annulation of perylene derivatives served as a good option to alter the optical, and electronic properties, solubility, and self-assembly of the perylene derivatives, while keeping the planarity intact.[8] The potential for these semiconductors to form columnar liquid crystals opens up possibilities for their use as molecular wires, playing a pivotal role in the field of organic electronics.

Thus to explore room temperature liquid crystalline heteroatom *bay*-annulated PBIs for various organic electronic devices, the issue of PBIs' high clearing temperature need to be addressed through the utilization of a systematic molecular design. In this regard, a study was

reported in literature, where the introduction of a swallow tail reduced the clearing point, albeit at the expense of sacrificing the liquid crystallinity.[12] In this work, the introduction of swallow-tail alkyl chains on the imide N atoms of the hetero atom *bay*-annulated PBIs was proposed, especially aiming to reduce their clearing point and reducing melting temperatures. However, it was found that PBI and its hetero atom *bay*-annulated PBIs exhibited a room-temperature columnar phase with a very low clearing point.

4.2. Results and Discussion

4.2.1. Synthesis and molecular structural characterization

The synthetic approach utilized for the preparation of swallow tailed **PBIST** and the *bay*-annulated PBIs (**PBI-NST**, **PBI-SST**, **PBI-SeST**) is illustrated in Scheme 4.1. The synthesis started from the reductive amination of commercially available 12-tricosanone by using ammonium acetate and sodium cyanoborohydride to give tricosa-12-amine.[18] The condensation of this amine with perylene tetracarboxylic dianhydride (PTCDA) in the presence of molten imidazole and anhydrous zinc acetate as a catalyst gives the corresponding perylene bisimide, **PBIST** (**3**). The controlled electrophilic aromatic mononitration of **PBIST** (**3**) was carried out with HNO_3 and $NaNO_2$ at 0 ^oC, giving compound **4** in good yield. This nitro derivative (**4**) was then treated with sodium azide in a DMF/THF (1:1) mixture to obtain the compound **PBI-NST**. The sulphur and selenium annulation at the bay positions of the PBI chromophore was accomplished by Cadogan cyclization, as previously reported by Langhals and co-workers[18] by heating the nitro compound (**4**) with sulphur and selenium powder in anhydrous *N*-methyl pyrrolidone (NMP) as a solvent to afford heteroatom annulated **PBI-SST** and **PBI-SeST**. The final products were recrystallized by chloroform-methanol system and obtained as red and orange gummy solids in good yield. The compounds were characterized by routine characterization techniques like ^1H NMR, ^{13}C NMR, IR and MALDI-TOF mass spectrometry (SI). (see 4.6 appendix).

Scheme 1. Synthesis of swallow tailed PBI (**PBIST**) and its heteroatom annulated derivatives (**PBI-NST**, **PBI-SST**, **PBI-SeST**).

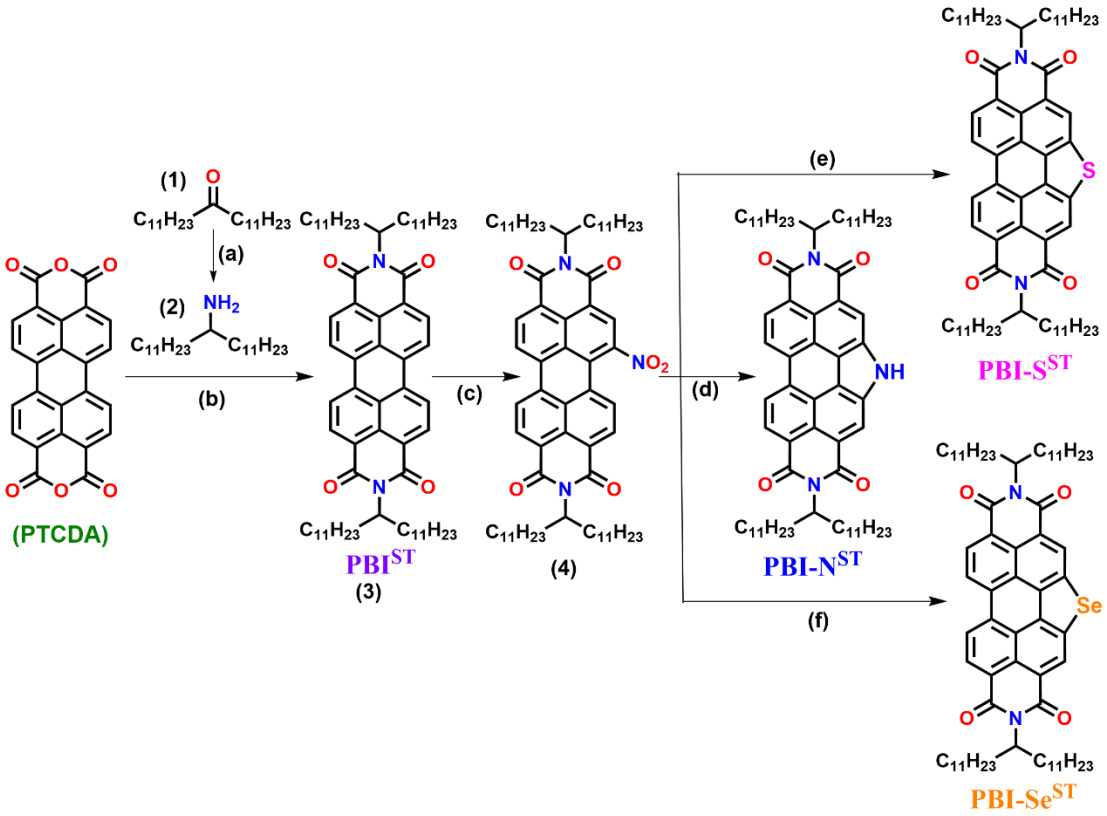

Reagents and conditions: (a) NH_4OAc, $NaBH_3CN$, MeOH, RT, 72 h (95%); (b) **2**, $Zn(OAc)_2$, imidazole, 160 °C, 2h, (91%); (c) $NaNO_2$, HNO_3, 0 °C, 30 min., rt, 1 h (90%); (d) NaN_3, DMF/THF mix.(1:1), rt, 18h (76%) (e) sulfur powder, anh. NMP, N_2, 70 °C, 0.5 h, 180 °C, 12 h (74%); (f) selenium powder, anh. NMP, N_2, 70 °C, 0.5 h, 180 °C, 12 h (68%).

4.2.2. Thermal behavior

The preliminary way of identifying mesomorphism was through the detection of optical textures when viewed under polarized optical microscopy (POM) with programmable hot stage. Additionally, double melting points and associated enthalpy changes were detected through differential scanning calorimetry (DSC) which further confirmed the mesomorphic behavior. Powder X-ray diffraction studies were performed to confirm different mesophases. The phase transition temperatures of all the compounds together with transition enthalpy values were summarized in Table 4.1.

Table 4.1. Phase transition temperatures (°C), corresponding enthalpies (kJmol^{-1}) of PBIs and the data on thermal stability.[a]

Compounds	Phase Sequence (kJ/mol)		T_5^b (°C)
	Second heating	First Cooling	
PBIST	Col_{ob1} 43.43 (0.33) Col_{ob2} 84.08 (6.30) I	I 74.28 (5.74) Col_{ob2} 28.12 (0.23) Col_{ob1}	387
PBI-NST	Col_{ob} 121.95 (3.35) I	I 111.23 (3.63) Col_{ob}	378
PBI-SST	Col_{h1} 56.01 (5.22) Col_{h2} 127.16 (0.93) I	I 122.04 (1.20) Col_{h2} 41.69(5.11) Col_{h1}	387
PBI-SeST	Col_h 69.01 (4.88) I	I 61.40 (3.69) Col_h	389

[a] Peak temperatures in the DSC thermograms obtained during the second heating and first cooling cycles at 5 °C min^{-1}. Col_{ob} = Columnar oblique phase; Col_h = Columnar hexagonal phase; I = Isotropic phase.

Thermogravimetric analysis (TGA) revealed that all PBIs exhibited nearly identical thermal stability. The temperature at which a 5% weight loss occurred ranged from 378°C to 389°C (Fig. 4.1c, Table 4.1, Fig. A17). Under POM observation, **PBIST** and **PBI-NST** displayed textures corresponding to a columnar oblique (Col_{ob}) phase, while **PBI-SST**, and **PBI-SeST** exhibited a columnar hexagonal (Col_h) phase (Fig. 4.1b). DSC thermograms showed that the mesophases were stable over a broad thermal range including ambient temperature. The assignment of the Col phases was confirmed from the powder XRD studies carried out at different temperatures (Table 4.2). The subsequent section provides a comprehensive analysis of the mesomorphic behavior of these compounds.

In literature there are contradicting reports, where the shorter swallow tail PBI derived from pentadecane-8-amine chains show monotropic columnar hexagonal (Col_h) phase, while the higher chain (tricosan-12-amine) derivative seems to be crystalline.[12] The **PBIST** compound sandwiched between a glass slide and coverslip was placed in a programmable hot stage and slowly heated. An increase in the birefringence was noted along with a slow increase of fluidity. Response to the mechanical shear confirmed that the compound was in a mesomorphic state. At ≈ 84 °C, the compound converted into an isotropic liquid (ΔH = 6.3 kJ/mol) (Fig. 4.2c, Table 4.1). Cooling the isotropic liquid at a rate of 5 °C/min shown the formation of long battonnets, which usually appear for Col_{ob} phases (Fig. 4.2a) (see chapter 2 and 3). The texture was similar to the earlier report.[12] Further cooling led to the coalescence of these structures to form a mosaic pattern confirming the transition to another mesophase as noted in DSC ($T \approx 28$ °C, ΔH = 0.2 kJ/mol) (Fig. 4.2b). Further

cooling to sub-ambient temperature showed no signs of crystallization in DSC, confirming the stability of the mesophase well below the room temperature.

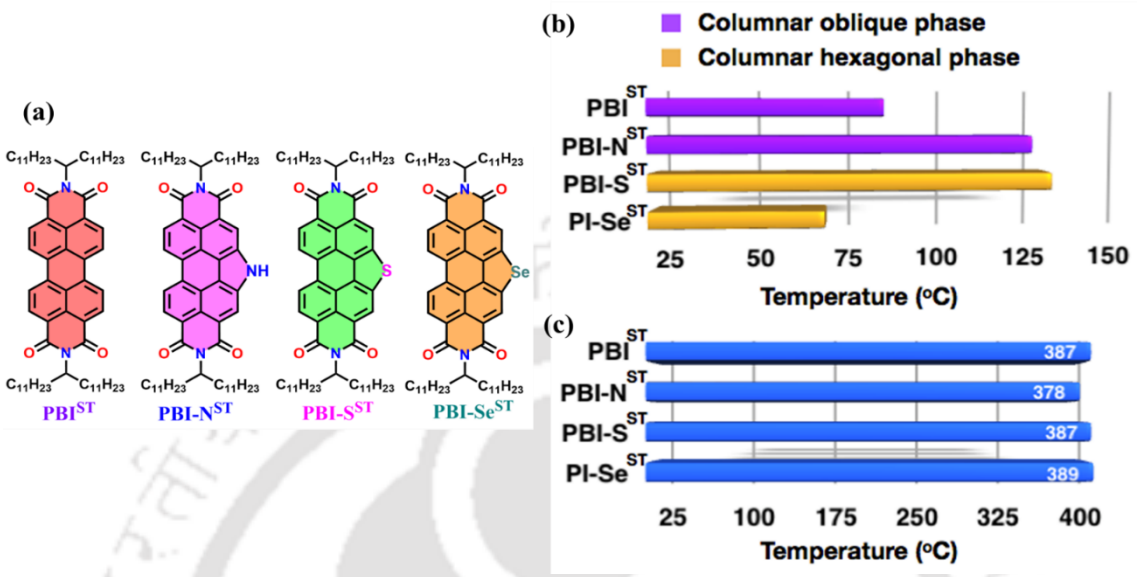

Figure 4.1. Structures of PBIs derived from tricosa-12-amine (**PBIST**, **PBI-NST**, **PBI-SST** and **PBI-SeST**) (a); Bargraph showing the thermal behaviour of **PBIST**, **PBI-NST**, **PBI-SST** and **PBI-SeST** (considered the second heating scan in DSC) (b); Thermal stability of PBIs obtained from TGA studies (considering the temperature at which 5 weight % decomposition occurs) (c).

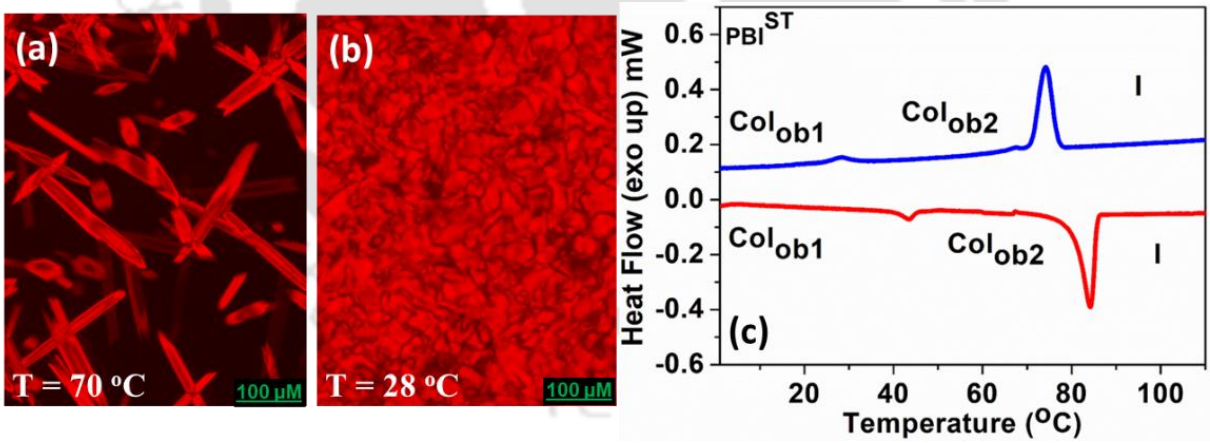

Figure 4.2. POM image of the Col_{ob} phase at 70 °C (a) and 28 °C (b) for compound **PBIST**; DSC thermogram for the first cooling (blue trace) and second heating (red trace) taken at a rate of 5 °C/min (c).

X-ray diffraction studies were conducted at high and room temperatures exhibited a complex pattern with many peaks in the small angle region which can be indexed into columnar phase of oblique symmetry (Col_{ob} phase) with lattice parameters a = 23.9 Å, b = 32.64 Å, and the angle

between them γ = 71.4° (Fig. 4.3a, b). The first diffuse peak corresponding to the alkyl chain packing was observed at 4.66 Å, while core-core stacking distance was not very prominent, which was seen at 3.99 Å. Calculation of the number of molecules forming unit oblique cell from the lattice area '*S*' and lattice volume '*V*', yielded the value of $Z \approx 2$ (Table 4.2). XRD pattern obtained at lower temperatures also showed a similar pattern, with *d*-spacings of 22.10, 21.25, 15.4, 9.47, 9.22, 8.82, 7.8, 6.96 Å that can be indexed into the 10, 11, 12, -21, 23, -13, 31, -23 corresponding to columnar phase with oblique lattice with lattice parameters *a* = 23 Å, *b* = 34.3 Å, and the angle between them γ = 74.1°. Calculation of the number of molecules forming unit oblique cell from the lattice area (S = 758.5 Å^2) and lattice volume (V = 3016.9 Å^3), yielded the value of $Z \approx 2$. This points to the formation of a columnar slice by the side-by-side arrangement of two PBIs as shown in Fig. 4.3c. This also shows that the two Col_{ob} phases slightly differ from each other but they are distinct as evidenced by the POM and DSC studies.

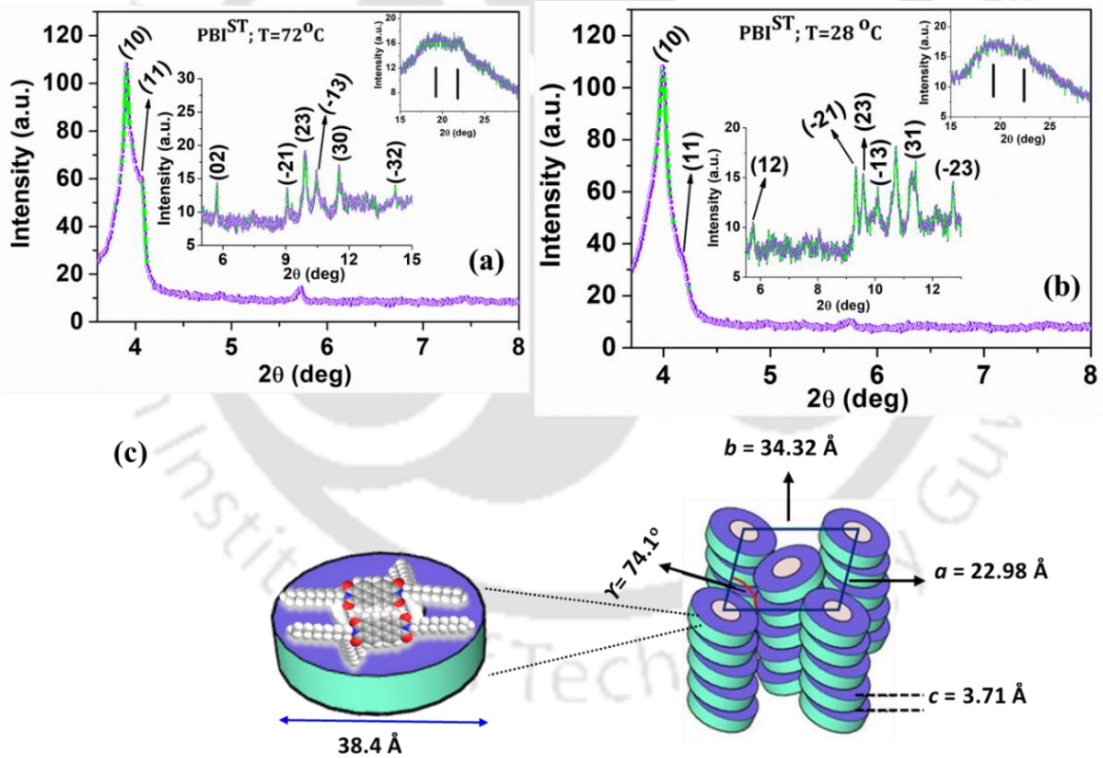

Figure 4.3. Powder XRD pattern obtained for the Col_{ob2} phase at 72 °C (a); Schematic diagram showing the Col_{ob1} phase of compound **PBIST** at 28 °C (b); Schematic diagram showing the Col_{ob1} phase formed by compound **PBIST** (c) (By considering the XRD pattern obtained at 28 °C).

Compound **PBI-NST** also exhibited a columnar phase with an oblique symmetry. At approximately 122 °C, the compound turned into an isotropic liquid with a ΔH of 3.4 kJ/mol. Cooling the liquid at a rate of 5 °C/min resulted in the formation of rectangular blocks with

diagonal lines on them (Fig. 4.4a), which is a signature of columnar oblique (Col_{ob}) phase (see chapter 2 and 3). These structures then coalesced to form a mosaic pattern, which remained stable down to room temperature (Fig. 4.4b). From the DSC, no crystallization was observed upon further cooling, indicating that the mesophase was stable even below room temperature (Fig. 4.4c).

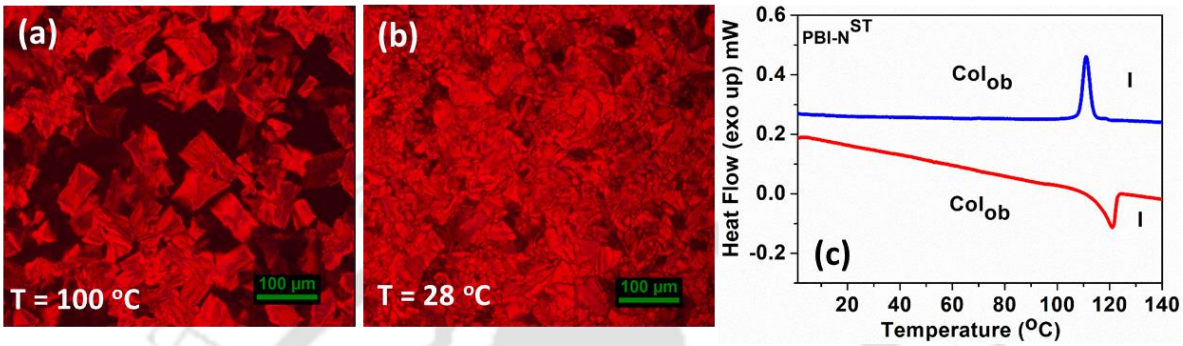

Figure 4.4. POM image of the Col_{ob} phase at 100 °C (a) and 28 °C (b). DSC thermogram for the first cooling (blue trace) and second heating (red trace) taken at 5 °C min^{-1} for compound **PBI-NST** (c).

X-ray diffraction studies were conducted at different temperature intervals including room temperature showed a complex pattern and were similar (Fig. A14). Thus for discussion, let us consider the XRD pattern obtained at 28 °C (Fig. 4.5a). The plot of intensity *vs* 2θ showed *d*-spacings of 25.52, 17.43, 10.49, 9.74, 6.24 Å that can be indexed into the 10, 01, 12, 32, -31 corresponding to columnar phase with oblique lattice with lattice parameters a = 32.68 Å, b = 22.32 Å, and the angle between them γ = 51.34 °. Calculation of the number of molecules forming unit oblique cell from the lattice area 'S' as 569.6 $Å^2$ and lattice volume 'V' as 2289.7 $Å^3$, yielded the value of $Z \approx 1$.

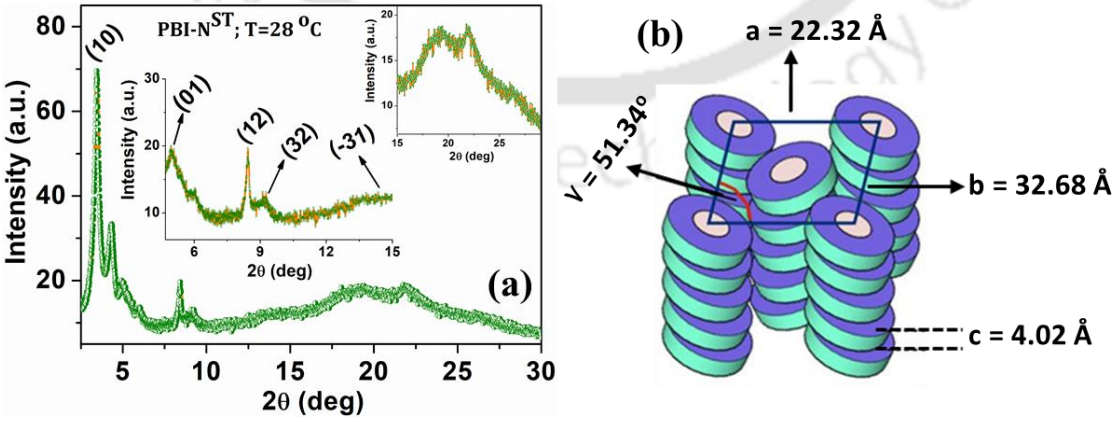

Figure 4.5. Powder XRD pattern obtained for the compound **PBI-NST** for the Col_{ob} phase at 28 °C (a); Schematic diagram showing the Col_{ob} phase formed by compound **PBI-NST** (By considering the XRD pattern obtained at 28 °C).

The POM images for **PBI-SST** taken at different temperatures including room temperature showed a hexagonal dendritic pattern commonly observed for the columnar hexagonal (Col_h) phase (Fig. 4.6b, c and Fig. A11-12). The DSC thermogram confirmed the existence of two mesophases, with the phase transition temperatures in good agreement with POM observations (Fig. 4.6a). Two peaks were observed in both the heating and cooling cycles of the DSC thermogram corresponding to the transition between columnar phases and for a transition from columnar to isotropic phase. From the POM observations, both the high and low-temperature mesophases were found to be similar except for a little change in birefringence (Fig. 4.6b, c).

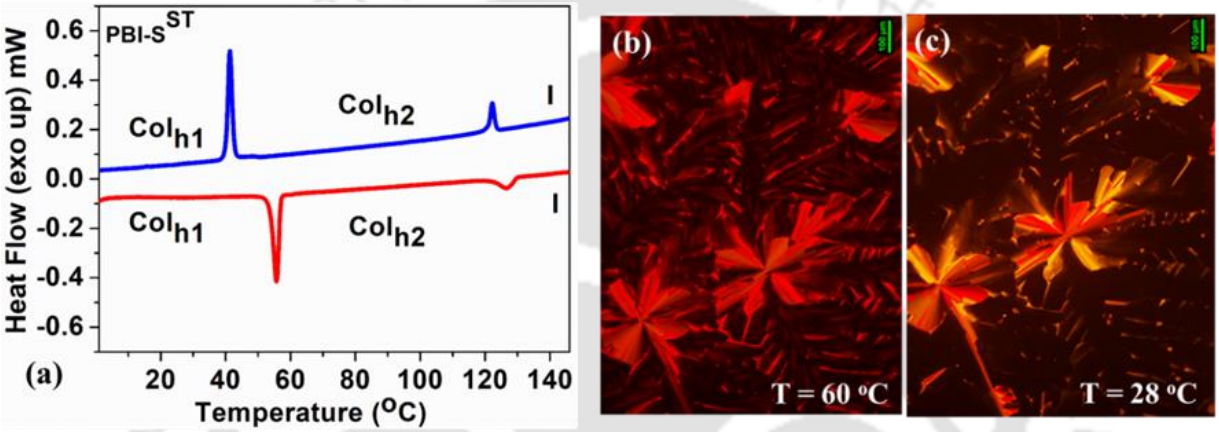

Figure 4.6. DSC thermogram for the first cooling (blue trace) and second heating (red trace) taken at 5 °C min^{-1} for compound **PBI-SST** (a); POM image of the Col_{h2} phase at 60 °C (b); Col_{h1} phase at 28 °C (c) (scale bar 100 μm).

Thus the mesophases were investigated with the help of powder XRD studies, at different temperature intervals and they showed a simpler pattern (Fig. A15, Table 4.2). The plot of intensity *vs* 2θ obtained at 60 °C, for example, showed *d*-spacings of 21.44, 12.31, 10.65 Å that can be indexed into Miller indices 10, 11, 20 corresponding to a reciprocal ratio of 1: √3: √4 of columnar phase with hexagonal symmetry. Further, two diffused peaks were noted at 4.64 Å and 3.52 Å, which are corresponding to the packing of flexible alkyl chains and the packing of cores (Fig. 4.7a, Table 4.2). The hexagonal lattice parameter '*a*' was found to be 24.76 Å. Calculation of the number of molecules forming a unit hexagonal cell from the lattice area '*S*' as 530.9 Å^2 and lattice volume '*V*' as 1868.8 Å^3, yielded the value of $Z \approx 1$. Further, the low-temperature XRD pattern obtained at 28 °C showed a very similar pattern to the high-temperature Col_h phase (Col_{h2} phase), but without the 20 peak and core-core separation peak (Fig. 4.7b). This has also shown a small increase in the hexagonal lattice parameter, but the value of Z still remains as 1 (Table 4.2). For

ease of identification, this low-temperature phase was termed as Col_{h1} phase. Such transition between Col_h phases is reported earlier and not very uncommon.[19,20] However, the absence of a core-core peak at low temperature was found to be a new observation which is unusual in the case of Col LCs. Considering the bulky alkyl chains at the imide *N*-positions, it can be assumed that each molecule forms a single disc and such molecules pack one above the other with a rotational offset to form a columnar structure.

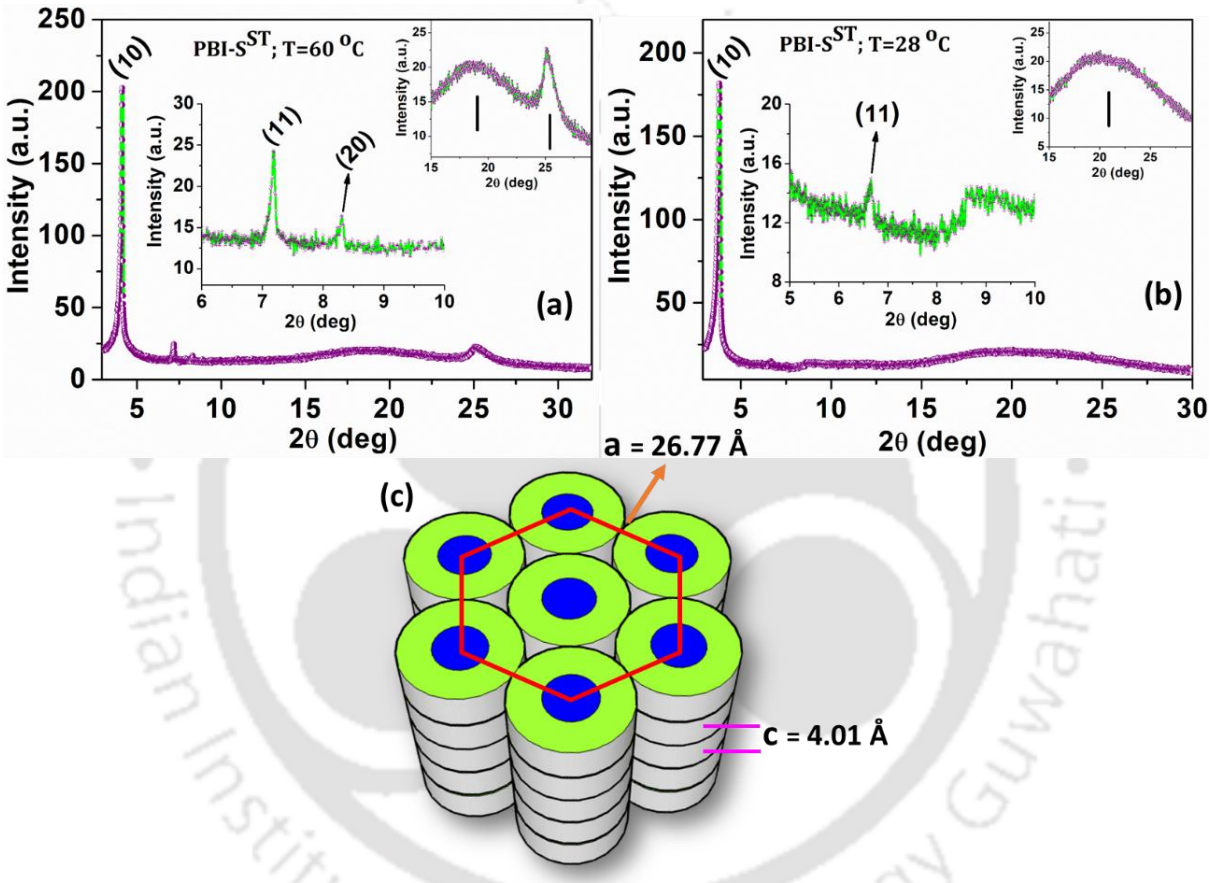

Figure 4.7. Powder XRD pattern obtained for the Col_{h2} phase at 60 °C (a) and the Col_{h1} phase at 28 °C (b) of compound **PBI-SST**; Schematic diagram showing the Col_h phase formed by compound **PBI-SST** (By considering the XRD pattern obtained at 28 °C).

For **PBI-SeST**, the POM images taken at different temperatures including room temperature showed a textural pattern with linear defects emerging from homeotropic domain,[22] that later coalesce to form a mosaic pattern observed for columnar hexagonal (Col_h) phase (Fig. 4.8a, b and Fig. A13). The DSC thermogram confirmed the existence of mesophase, with the phase transition temperatures in good agreement with POM observations (Fig. 4.8c). One peak was observed in both the heating and cooling cycles of the DSC thermogram corresponding to the transition from

columnar to isotropic phase. Nature of the columnar phase was examined by XRD studies at high and low-temperature intervals. The XRD patterns obtained at different temperature intervals showed a similar pattern (Fig. A16, Table 4.2). The plot of intensity *vs* 2θ obtained at 28 ^{o}C, for example, showed *d*-spacings of 23.11, 13.26, and 9.84 Å that can be indexed into Miller indices 10, 11, 20 of a Col phase with hexagonal symmetry with a reciprocal ratio of 1: √3: √4. The hexagonal lattice parameter '*a*' was found to be 26.7 Å. Calculation of the number of molecules forming unit hexagonal cells from the lattice area '*S*' as 616.9 Å^2 and lattice volume '*V*' as 2418.2 Å^3, yielded the value of $Z \approx 1$. Considering the bulky swallow tails at the imide *N*-positions, it can be assumed that each molecule forms a single disc and such molecules pack one above the other with a rotational offset to form a columnar structure, which further self-organizes to form the Col$_h$ phase.

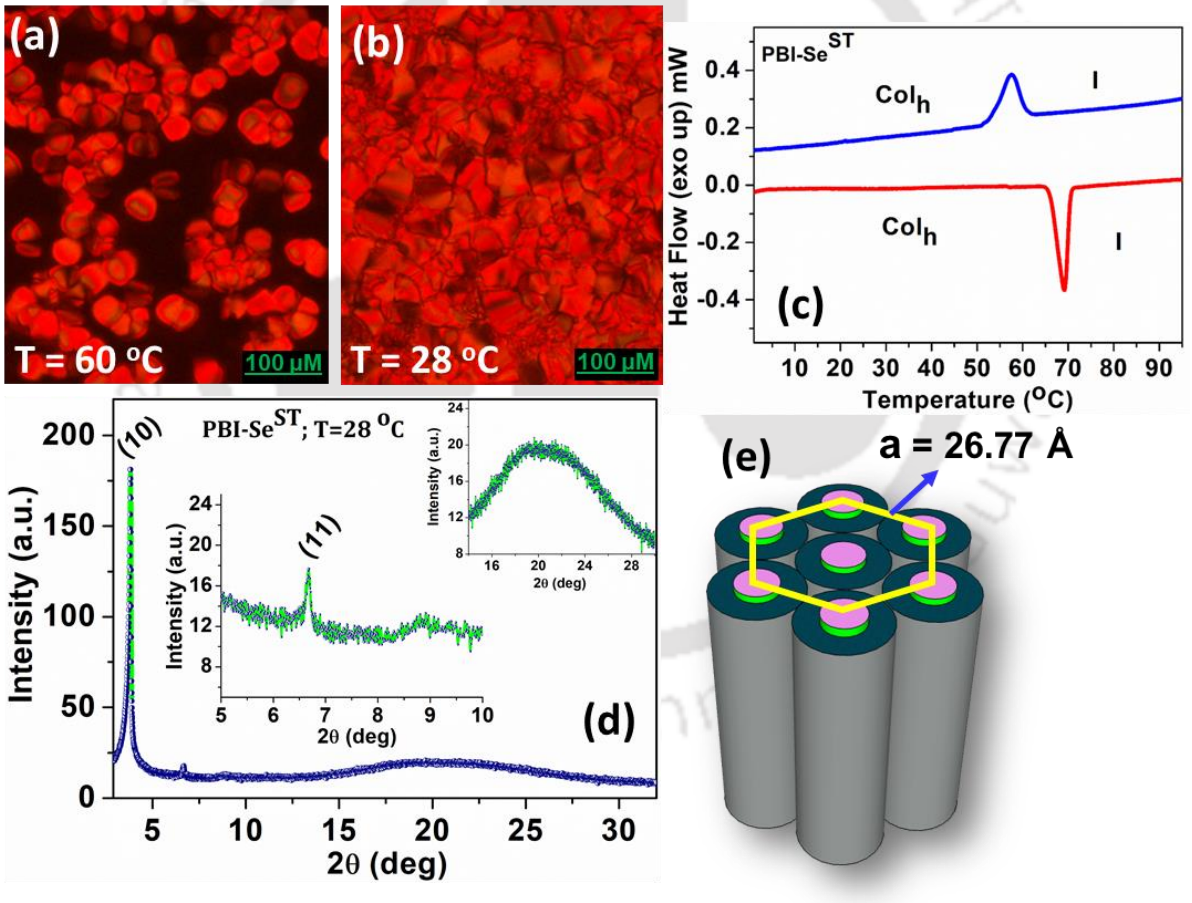

Figure 4.8. POM image of the Col$_{ob}$ phase at 70 ^{o}C (a) and 28 ^{o}C (b) for compound **PBI-SeST**; DSC thermogram for the first cooling (blue trace) and second heating (red trace) taken at a rate of 5 ^{o}C/min (c); Powder XRD pattern obtained at 28 ^{o}C for compound **PBI-SeST** (d); Schematic diagram showing the formation of Col$_{ob}$ phase by **PBI-SeST** (considered the XRD pattern obtained at 28 ^{o}C) (e).

Table 4.2. Results of (*hkl*) indexation of XRD profiles of **PBIST**, **PBI-NST**, **PBI-SST**, **PBI-SeST** at a given temperature (T) of mesophase[a].

Compounds (D/Å)	Phase (T/°C)	Space Group	d_{obs} (Å)	d_{cal} (Å)	Miller indices *hk*	Lattice parameters (Å), Lattice area S (Å^2), Molecular volume (Å^3)
PBIST (38.4) MW-1035.60	Col_{ob2} (72)	P1	22.64 21.91 15.46 9.75 8.91 8.45 7.67 6.26 4.66 (h_a) 3.99 (h_c)	22.65 21.91 15.46 9.68 9.23 8.42 7.55 6.06	1 0 1 1 0 2 -2 1 2 3 -1 3 3 0 -3 2	*a* = 23.90 *b* = 32.64 *γ* = 71.4 ° *S* = 739.1 *V* = 2953.9 *Z* ≈ 2
	Col_{ob1} (28)		22.10 21.25 15.40 9.47 9.22 8.82 7.80 6.96 4.68 (h_a) 3.98 (h_c)	22.10 21.26 15.40 9.71 9.15 8.92 7.65 6.91	1 0 1 1 1 2 -2 1 2 3 -1 3 3 1 -2 3	*a* = 22.98 *b* = 34.32 *γ* = 74.1 ° *S* = 758.5 *V* = 3016.9 *Z* ≈ 2
PBI-NST (37.665) MW-1048.60	Col_{ob} (100)	P1	23.67 16.67 15.83 10.62 9.68 6.31 4.81(h_a) 4.06(h_c)	23.68 16.67 10.63 9.93 6.37	10 11 02 -21 23	*a* = 23.80 b = 21.36 γ = 84.23 ° S = 505.79 V = 2.53.51 Z ≈ 1
	Col_{ob} (60)		23.58 16.55 10.54 9.74 6.32 4.79(h_a) 4.07(h_c)	23.59 16.55 10.54 9.89 6.32	10 11 02 -21 23	a = 23.70 b = 21.18 γ = 84.34 ° S = 499.51 V = 2033.04 Z ≈ 1
	Col_{ob} (28)		25.51 17.42 10.49 9.74 6.24 4.69(h_a) 4.02(h_c)	25.52 17.43 10.49 9.93 6.26	10 01 12 32 -31	a = 32.68 b = 22.32 γ = 51.34 ° S = 569.57 V = 2289.70 Z ≈ 1
PBI-SST MW-1065.69	Col_h (100)		22.06 21.66 12.43 10.74 4.72 3.54(h_c)	21.66 12.51 10.83	10 11 20	*a* = 25.01 S = 541.69 V = 1917.61 Z ≈ 1

	Col_h (60)	P6mm	21.44 12.31 10.65 4.64 3.52(h_c)	21.45 12.38 10.72	10 11 20	a = 24.76 S = 530.92 V = 1868.84 Z ≈ 1
	Col_h (28)		23.18 13.31 4.83 4.01	23.18 13.38	10 11	a = 26.77 S = 620.60 V = 2488.62 Z ≈ 1
PBI-SeST MW-1112.53	Col_h (50)	P6mm	23.09 13.25 9.61 4.75 3.93	23.10 13.34	10 11	a = 26.67 S = 615.97 V = 2420.78 Z ≈ 1
	Col_h (28)		23.11 13.26 9.84 4.69 3.92	23.12 13.35	10 11	a = 26.69 S = 616.90 V = 2418.24 Z ≈ 1

[a]The diameter (D) of the disk (estimated from Chem 3D Pro 22.2.0 molecular model software from Cambridge Soft). d_{obs}: spacing observed; d_{cal}: spacing calculated (deduced from the lattice parameters; a for Col_h phase, a, b for Col_{ob} phase; γ tilt angle for Col_{ob} phase; c is height of the unit cell). The spacings marked h_a and h_c correspond to diffuse reflections in the wide-angle region arising from correlations between the alkyl chains and core regions, respectively. Z indicates the number of molecules per columnar slice of thickness h_c estimated from the lattice area S and the volume V.

4.2.3. Photophysical properties

To learn more about the photophysical properties of these compounds, their absorption and fluorescence spectra in 10^{-6} M chloroform solutions and in drop casted thin films on quartz substrates was measured (Fig. 4.10, 4.11 and Table 4.3). All the PBIs exhibited well-structured absorption spectra with four characteristic vibronic bands in the solution. All PBIs exhibited distinct absorption spectra, characterized by well-defined four vibronic bands. A hypsochromic shift ($\Delta\lambda_{Hyps}$) was observed in the absorption spectra of *bay*-annulated PBIs (**PBI-NST**: $\Delta\lambda_{Hyps}$= 2 nm, **PBI-SST**: $\Delta\lambda_{Hyps}$= 24 nm and **PBI-SeST**: $\Delta\lambda_{Hyps}$= 18 nm with respect to **PBIST** (Fig. 4.9a). A high molar extinction coefficient value was observed for all PBIs, at their highest absorption (ε: 30,000 − 45,000 L mol^{-1} cm^{-1}). The absorption onset revealed a comparable optical band gap value for **PBIST** and **PBI-NST**, whereas **PBI-SST** and **PBI-SeST** exhibited an increase in their respective gaps. All these PBIs were excited at their longest absorption maximum (λ_{max}) to measure their photoluminescence spectra. The emission maxima for all the PBIs were found in the range of 510-537 nm. The emission spectra of **PBI-NST** showed a red shift while **PBI-SST** and **PBI-SeST** showed a hypsochromic shift in comparison to **PBIST** (Fig. 4.9b). Furthermore, both the absorption and

emission spectra of all the PBIs showed an increase in their intensity with an increase in concentration (Fig. A18, A19). **PBIST** and **PBI-NST** shows a yellowish fluorescence in their solution and a reddish emission in their film state, while **PBI-SST** showed a greenish and orange emission in its solution and thin film respectively (Fig. 4.11 insets). Solutions of **PBI-SeST** showed a weak yellow emission and a weak red emission was observed in its thin film. All these PBIs, except **PBI-SeST**, exhibited excellent quantum yield values measured with respect to Rhodamine 6G (Φ_f = 0.95). **PBIST**, **PBI-NST**, and **PBI-SST** displayed a quantum yield value of 0.88, 0.93, and 0.74 respectively (Table 4.3, Fig. A15). The incorporation of heavy atom selenium in the PBI core causes a superfast intersystem crossing (ISC) to the triplet excited state, resulting in an infinitesimally low photoluminescence for **PBI-SeST**, whereas this rate of ISC is comparatively lower to moderate for other PBIs making them high fluorescent.[22]

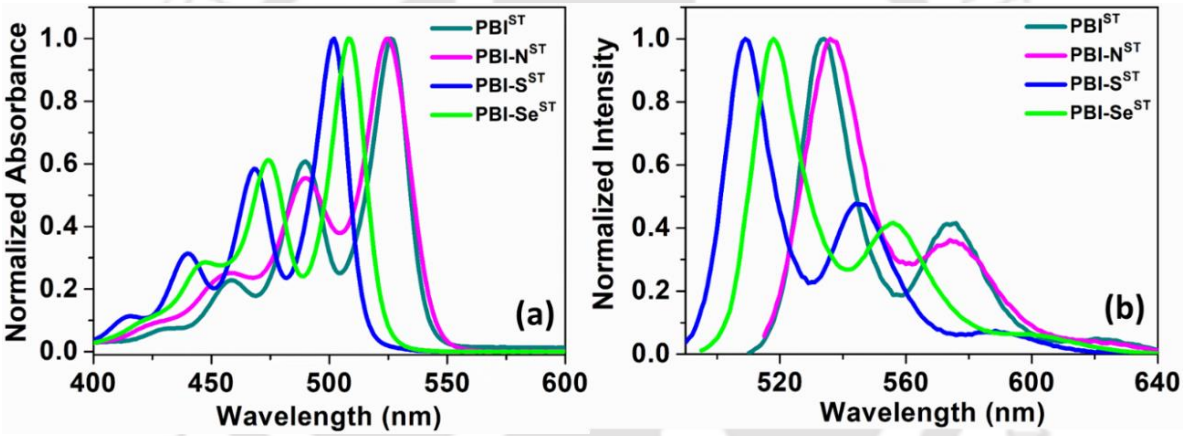

Figure 4.9. Absorption spectra (a) and emission spectra (b) of compounds **PBIST, PBI-NST, PBI-SST** and **PBI-SeST** in micromolar chloroform solutions.

PBIST and **PBI-NST** shows a yellowish fluorescence in their solution and a reddish emission in their film state, while **PBI-SST** showed a greenish and orange emission in its solution and thin film respectively (Fig. 4.11 insets). Solutions of **PBI-SeST** showed a weak yellow emission and a weak red emission was observed in its thin film. All these PBIs, except **PBI-SeST**, exhibited excellent quantum yield values measured with respect to Rhodamine 6G (Φ_f = 0.95). **PBIST**, **PBI-NST**, and **PBI-SST** displayed a quantum yield value of 0.88, 0.93, and 0.74 respectively (Table 4.3, Fig. A15). The incorporation of heavy atom selenium in the PBI core causes a superfast intersystem crossing (ISC) to the triplet excited state, resulting in an infinitesimally low photoluminescence for **PBI-SeST**, whereas this rate of ISC is comparatively lower to moderate for

other PBIs making them high fluorescent.[22] To investigate the photophysical properties in a thin film of PBIs, a drop casted film was created utilizing their micromolar toluene solution on a quartz surface, and the solvent was then totally evaporated at room temperature in order to analyze the solid state absorption and emission behavior. All PBIs exhibited solid-state absorption peaks in the 478–515 nm range and emission maxima in the 615–637 nm range. *Bay*-annulated PBIs were found to have significantly greater values of the Stokes shift than **PBIST** (Table 4.3).

Table 4.3. Photophysical properties of PBIs in solution[a] and thin film[b] state.

Entry	Absorption [nm]	Emission[c] [nm]	Stokes Shift (cm^{-1})	Molar extinction coefficient (ε) ($L\ mol^{-1}\ cm^{-1}$)	Quantum yield[d] (Q_S)	$\Delta E_{g,opt}$[e] [eV]	Absorption[b] [nm]	Emission[f] [nm]	Stokes Shift (cm^{-1})
PBIST	429, 458, 490, 526	534, 574	285	32,800	0.88	2.29	480, 515, 549	624	3392
PBI-NST	425, 457, 490, 524	537, 574	462	30,000	0.93	2.28	463, 493, 535	637	4585
PBI-SST	413, 440, 468, 502	510, 544	313	45,000	0.74	2.40	445, 478, 513	613	4607
PBI-SeST	421, 447, 474, 508	519, 556	418	33,900	0.06	2.36	458, 482, 520	619	4591

[a] Micromolar solution in $CHCl_3$. [b]Prepared by drop casting of millimolar solution in toluene. [c] The excitation wavelength λ_{ex} = 526, 524, 502, 508 nm for **PBIST**, **PBI-NST**, **PBI-SST**, **PBI-SeST**. [d] Relative quantum yield is calculated with respect to Rhodamine-6G (λ_{ex} = 530 nm) in ethanol solution as the standard and compound in $CHCl_3$. [e] Calculated from the red edge of the absorption band. [f] Excited at the absorption maxima.

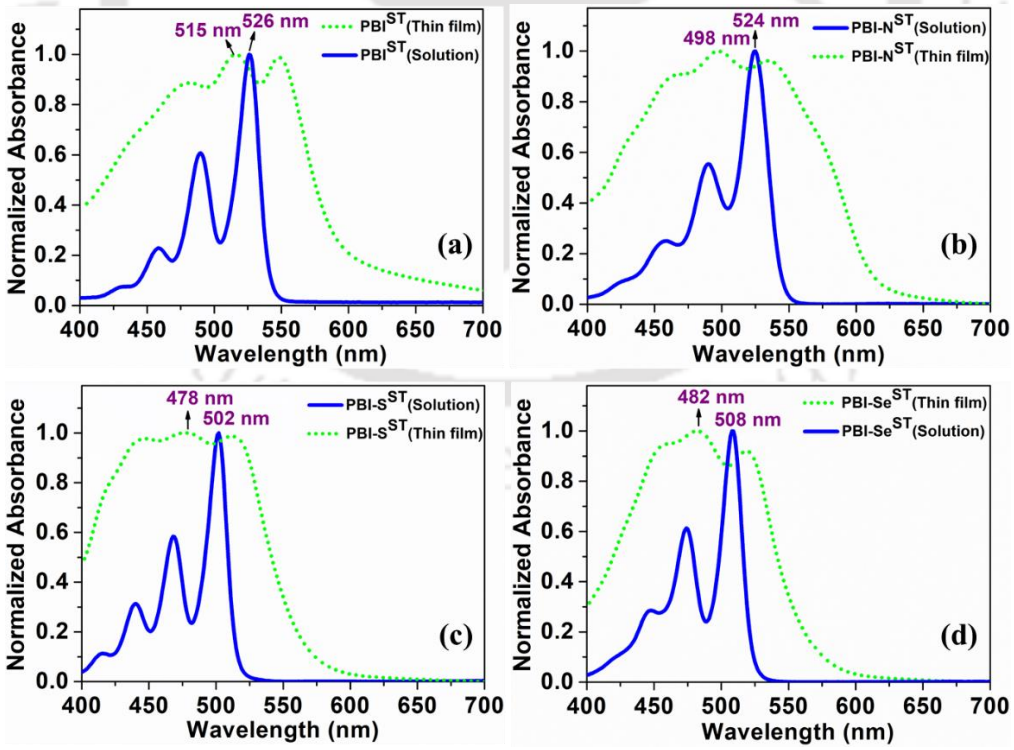

Figure 4.10. Overlay of absorption spectra in micromolar chloroform solutions and dropcasted thin films of compounds (a) **PBIST**;(b) **PBI-NST**; (c) **PBI-SST** and (d) **PBI-SeST**.

As compared with their solution state, all PBIs, in their neat state displayed a hypsochromically shifted absorption and bathochromically shifted emission spectra respectively (Fig. 4.10 and 4.11). The cofacial (head-to-head) arrangement of the molecules in the formation of H-aggregates is apparent through the hypsochromic shift in the absorption maxima in the solid state. Despite the fact that H-aggregates are known to be non-emissive, certain emissive H-aggregate examples may be found in the literature.[23] Here the rotational offset of the molecules due to the presence of bulky side chains at the imide nitrogen could be a reason that minimizes the core-core overlap in the aggregated state. The broadness in the film state could be ascribed due to the restrictions in the rotation of the molecules in the film state in contrast to solution state.

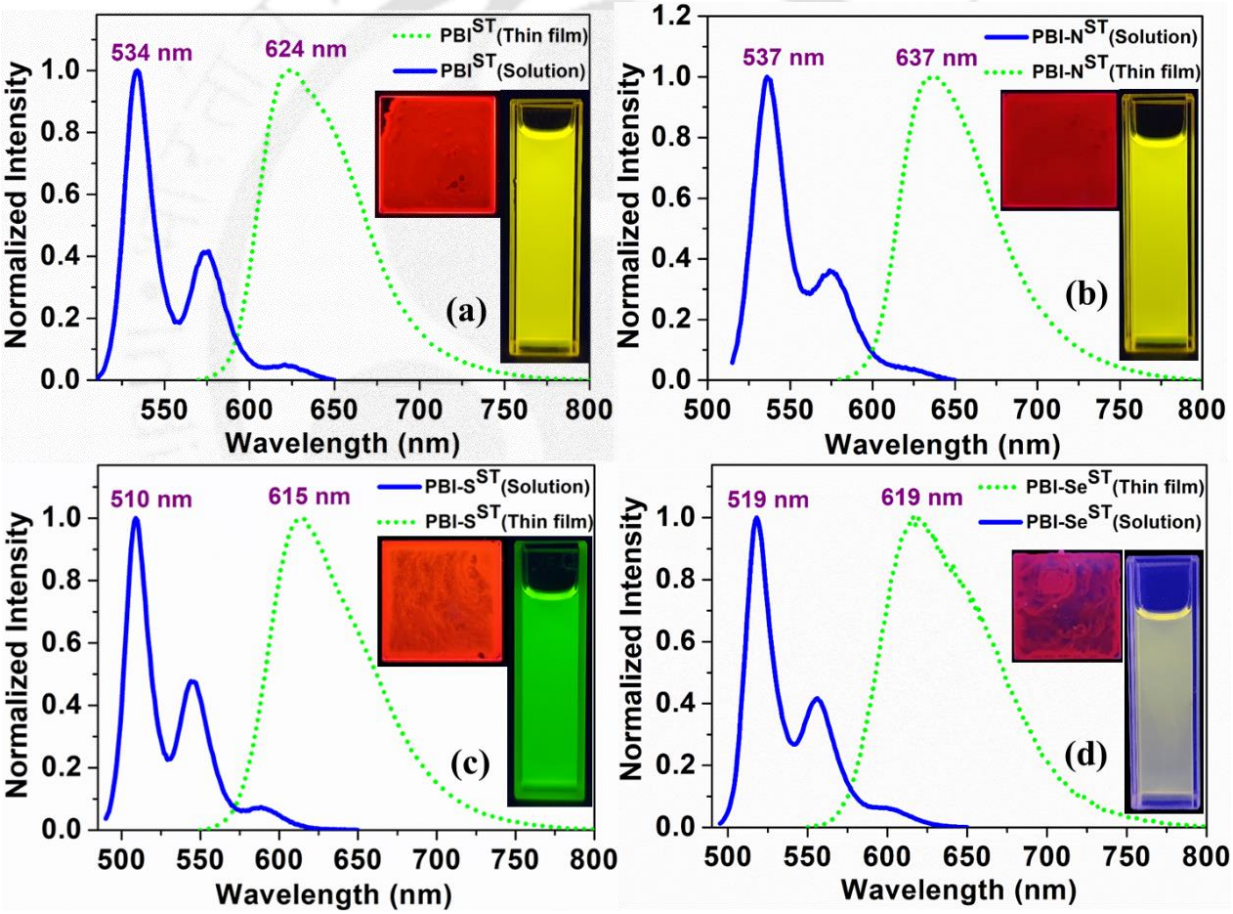

Figure 4.11. Overlay of emission spectra in micromolar chloroform solutions and dropcasted thin films of compounds (a) **PBIST**;(b) **PBI-NST**; (c) **PBI-SST** and (d) **PBI-SeST** (insets show the images of solutions and thin films under the UV light, λ_{max} = 365 nm).

4.2.4. Electrochemical properties

Cyclic voltammetry investigations were carried out to understand the electronic energy levels that govern the energy and electron transfer process, as well as the reversibility of a redox process. To conduct these investigations, CV tests were conducted in 0.5 mM solutions of PBIs in anhydrous dichloromethane with a supporting electrolyte tetrabutyl ammonium perchlorate (TBAP) of 0.1 M concentration, and all CV studies were recorded at a scan rate of 100 mVs^{-1} (Fig. 4.12). The results of the CV studies are depicted in Table 4.4. PBIs are well-recognized n-type semiconductors that are electron deficient and have a strong electron affinity. The neutral molecule of all PBIs was reduced to a radical anion in the first stage and to a dianion in the second step, resulting in two quasi-reversible reduction peaks. The first reduction's insertion of one electron raises the density of electrons on the imide's carbonyl. The ability of the core to delocalize this additional electron density to lessen the Coulombic repulsion of equivalent charges supports the insertion of the second electron in the second reduction.[24,25] The oxidation potentials of these electron-deficient compounds were challenging to determine even with a CV measuring window up to +1 V vs $Ag/AgNO_3$. To estimate the HOMO levels, the optical band gap ($\Delta E_{g,UV}$), which was determined from the absorption onset of the relevant compounds in solutions, was subtracted from the LUMO energy values.

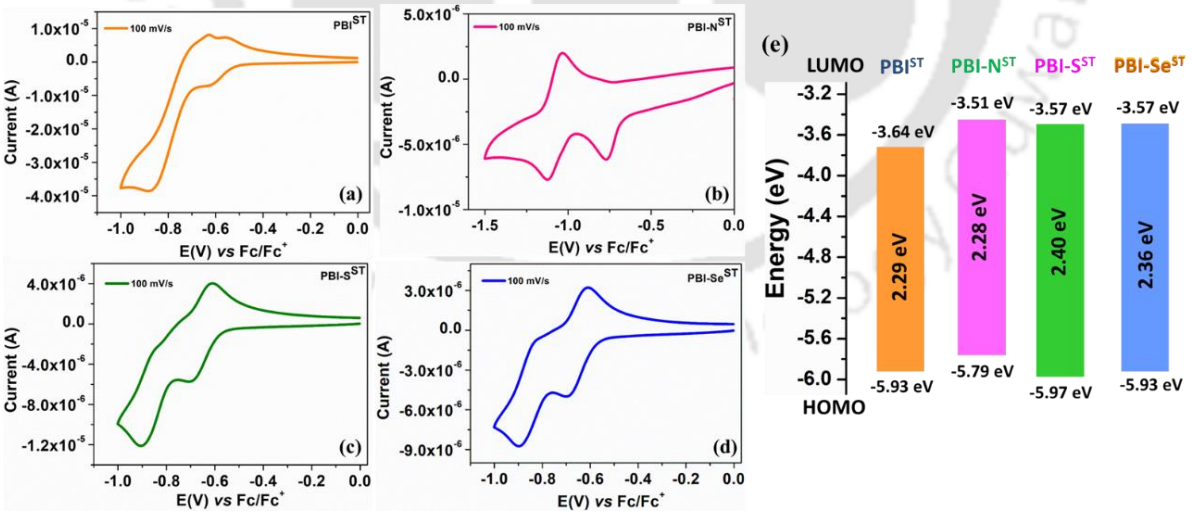

Figure 4.12. Cyclic voltammogram of **PBIST**(a), **PBI-NST**(b), **PBI-SST**(c), **PBI-SeST**(d) respectively; Energy band level diagram showing HOMO and LUMO energy levels of **PBIs** (e).

The electrochemical investigations revealed that the bay-annulated PBIs displayed higher LUMO levels when compared to **PBIST**. In the case of **PBI-NST**, there was a slight increase of 0.14 eV in the HOMO level, while **PBI-SST** and **PBI-SeST** exhibited a nearly same HOMO levels. The CV studies yielded similar results, consistent with the values obtained from DFT calculations. Overall, all the molecules demonstrated LUMO levels below 3.5 eV, indicating their potential as effective electron acceptors and suggesting their suitability as a novel category of non-fullerene acceptors (NFAs) for organic photovoltaics.

Table 4.4. Electrochemical[a,b] data and data obtained from DFT[h] calculations for compounds **PBIST, PBI-NST, PBI-SST** and **PBI-SeST**.

	Electrochemical data				Data from DFT calculations		
Entry	$E_{1st\ red}$ [c]	E_{LUMO} [d,e]	E_{HOMO} [d,f]	$\Delta E_{g,\ opt}$ [d,g]	E_{LUMO} [d,h]	E_{HOMO} [d,h]	$\Delta E_{g,}$ [d,h]
PBIST	-0.63	-3.64	-5.93	2.29	-3.44	-5.96	2.52
PBI-NST	-0.76	-3.51	-5.79	2.28	-3.21	-5.89	2.68
PBI-SST	-0.70	-3.57	-5.97	2.40	-3.39	-6.09	2.70
PBI-SeST	-0.70	-3.57	-5.93	2.36	-3.41	-6.09	2.68

[a] 0.5mM Dichloromethane solutions; [b]experimental conditions: $Ag/AgNO_3$ as reference electrode, glassy carbon working electrode, platinum wire counter electrode, TBAP (0.1M) as a supporting electrolyte, room temperature; [c] in volts (V); [d] in eV; [e] estimated from the formula by using E_{LUMO}= -(4.8 - $E_{1/2,\ Fc/Fc+}$ + $E_{red,}$ onset) eV; [f] estimated from the formula $E_{HOMO} = E_{LUMO} - E_{g,opt}$) eV; $E_{1/2,\ Fc/Fc+}$ = 0.50V. [g]calculated from the red edge of the absorption band of each compound. [h] Obtained from DFT calculations by employing the combination of Becke3-Lee-Yang-Parr (B3LYP) hybrid functional and 6-31G(d,p) basis set using the Gaussian 09 package..

4.2.5. Density Functional Theory Studies

In order to obtain a better understanding of the electronic properties of these PBIs from a theoretical perspective, density functional theory (DFT) quantum mechanical calculations were performed. These calculations offered valuable insights into several factors, including the molecule's geometry, electronic structure, molecular conformation, and the frontier molecular orbitals (FMOs) such as the HOMO and LUMO. The HOMO-LUMO energy levels of PBIs were found to be dispersed on the central aromatic ring, with nodes located on the imide units' nitrogen atoms, as evident from the HOMO and LUMO contours (Fig. 4.14). The energy minimized space-filling models of all the PBIs studied are shown in (Fig. 4.13).

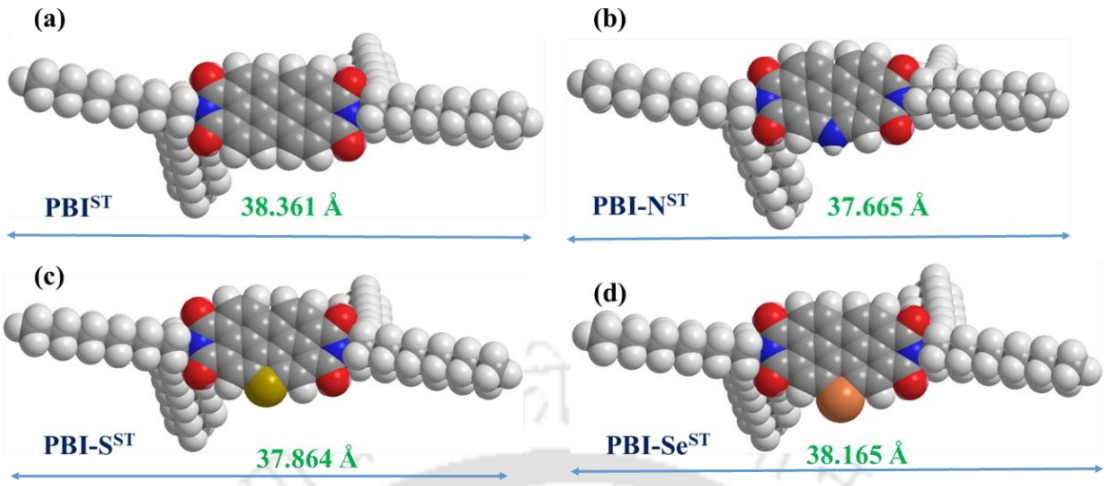

Figure 4.13. Optimized geometry of compounds **PBIST** (a), **PBI-NST** (b), **PBI-SST** (c) and **PBI-SeST** (d).

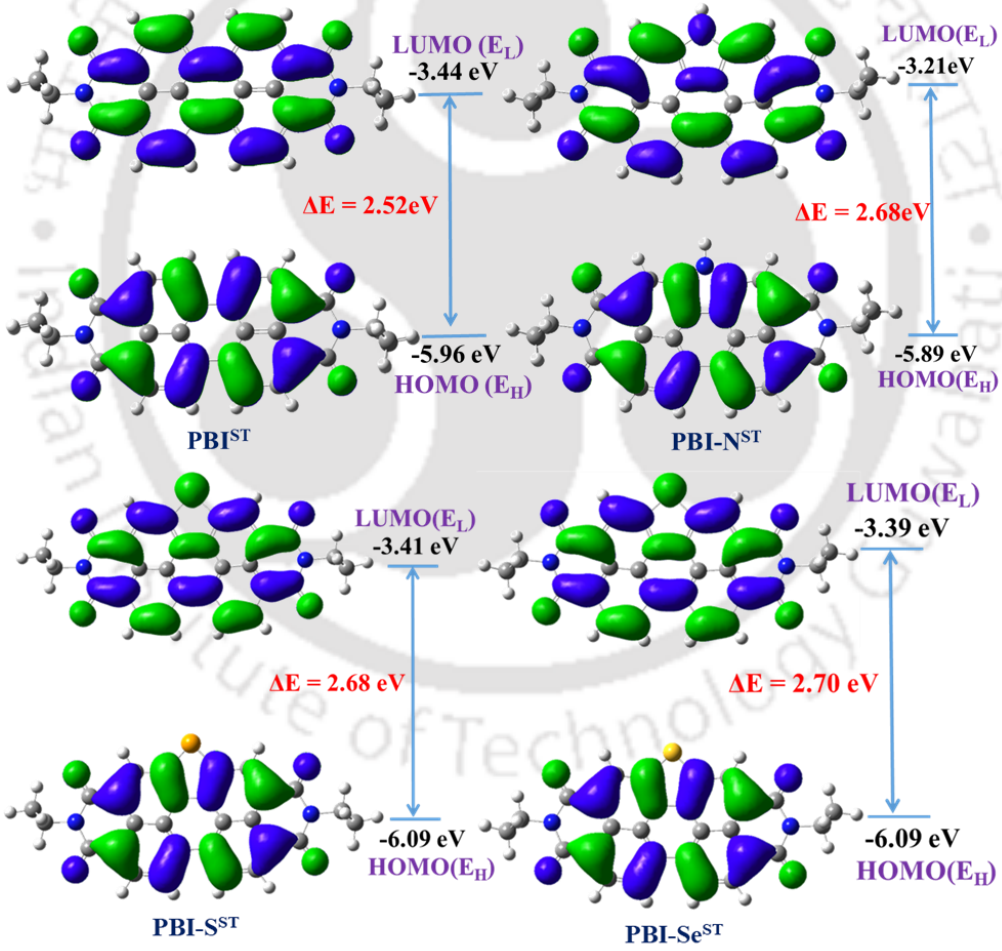

Figure 4.14. Frontier molecular orbitals of compounds **PBIST; PBI-NST; PBI-SST and PBI-SeST** obtained from DFT calculations at the B3LYP/6-31G(d,p) level. E_H and E_L denote energies of the highest occupied molecular orbital (HOMO) and the lowest unoccupied molecular orbital (LUMO), respectively.

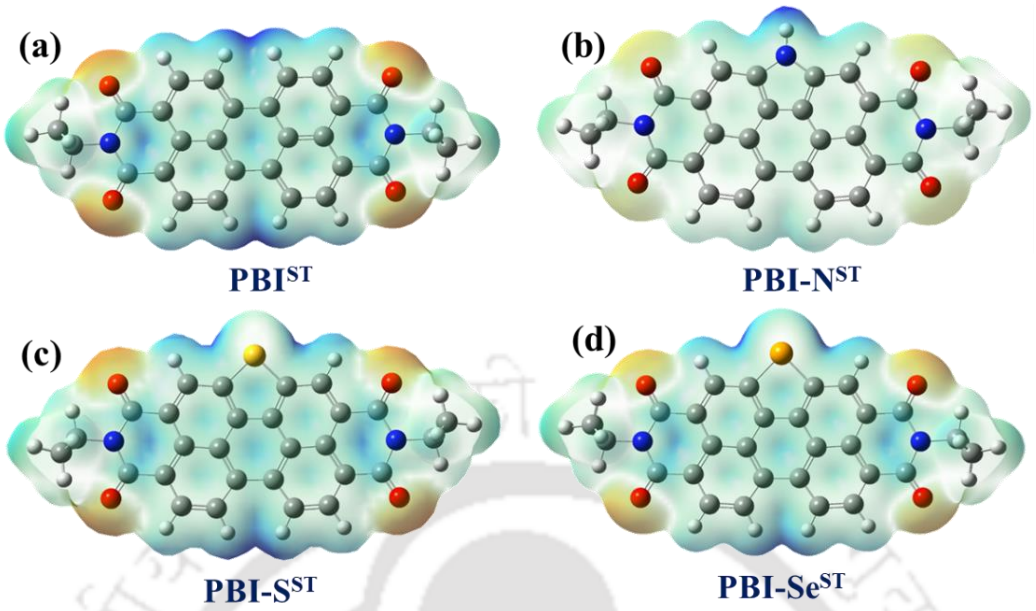

Figure 4.15. 3D molecular electrostatic potential contour map of optimized structure of PBIs derived from swallow-tail amines (In the mapped electro-static potential surface, the red and blue colors refer to the electron-rich and electron-poor regions, respectively, whereas the green color signifies the zero electrostatic potential, chain length is limited to isopropyl for clarity purpose).

The molecular electrostatic potential surfaces calculated for these PBIs indicated that the oxygen atoms had a higher electron density, whereas the central perylene core remained electron deficient (Fig. 4.15). The theoretical band gap of these PBIs were calculated to be in the range of 2.52-2.70 eV, slightly higher than the optical bandgap, as shown in Table 4.4. Furthermore, the HOMO and LUMO levels were determined to be -6.09 eV and -3.41 eV, respectively.

4.3. Charge Carrier Mobility Studies

The study of charge carrier mobility for **PBIST** and heteroatom annulated PBIST compounds was carried out using Space Charge Limited Current (SCLC) technique. In order to measure hole mobility, ITO/PEDOT:PSS/**PBIST**s/MoO_3/Ag device architecture was prepared whereas ITO/ZnO/**PBIST**s/Ag was used for electron-mobility calculations (Fig. 4.16c). In hole only devices ITO/PEDOT: PSS electrode combination was chosen for establishing Ohmic/near Ohmic contact for hole injection during SCLC measurements whereas ITO/ZnO electrode combination was chosen for electron injection.

To achieve SCLC regime, an Ohmic contact is a fundamental requirement with material under test in both hole (Injecting electrode-HOMO for hole mobility measurement) as well as electron

(Injecting electrode-LUMO, for electron mobility measurement) only devices. It is to be noted that solution-processed thin films having amorphous nature were being used for charge mobility extraction of both hole and electron of **PBIST**s derived from swallow tail amines (**PBIST, PBI-NST, PBI-SST** and **PBI-SeST**). Detailed experimental details is discussed in appendix 4.6.8.

In SCLC technique, during current-voltage measurement, at initial low voltages current follows ohmic regime with slope of one whereas at higher voltages, where injected charge carrier dominates over existing intrinsic charge carriers, SCLC regime with a slope two is observed. Considering contacts to be Ohmic/Near Ohmic and material to be trap free, charge mobility of the material can be extracted using Mott-Gurney law given by equation 1.

$$J = \frac{9}{8}\varepsilon_0\varepsilon_r\mu\frac{V^2}{d^3} \quad \text{..... 1}$$

Where ε_0 is the permittivity of free space (8.86×10^{-14} *F/cm*), ε_r represents the relative dielectric constant of the material (~ 2.29), *V* is the applied voltage, *d* is the thickness of the material and *J* is density. In thin films where applied electric field is much higher as compared to the bulk, modified Mott−Gurney equation is widely used where a field-dependent charge mobility correction is introduced for the charge mobility calculation shown in equation 2.

$$J = \frac{9}{8}\varepsilon_r\varepsilon_0\mu\frac{V^2}{d^3}\exp\left(0.891\gamma\sqrt{\frac{V}{d}}\right) \quad \text{..... 2}$$

where γ is the fitting parameter that represents the strength of the field dependence of mobility.

In this work modified Mott-Gurney equation was used for fitting the measured *J*−*V* curves for **PBIST**s (**PBIST, PBI-NST, PBI-SST** and **PBI-SeST**) to extract their hole / electron mobilities. The mobility values of **PBIST, PBI-NST, PBI-SST** and **PBI-SeST** is summarized in Table 4.5. Figure 4.16 represents the observed as well as SCLC fitted curves for all **PBIST**s. The reported mobility values for both electron and hole are an average of at least 5 best devices (Table A1).

From the comparison of charge carrier mobility values (Table 4.5 and Fig. 4.16), it can be concluded that overall, **PBIST**s derived from swallow tail amines (**PBIST, PBI-NST, PBI-SST** and **PBI-SeST**) exhibit comparable values for ambipolar conductivity with the PBIs derived from tri(*n*-alkyl) anilines and tri(*n*-alkoxy) anilines with a good μ_e/μ_h ratio (see chapter 3). In literature, there are ambipolar materials formed by the incorporation of electron rich moieties to electron deficient moieties,[26-28] or by mixing electron rich and deficient moieties in varying ratio.[29-32] However, here

it is shown that PBIs and their hetero-atom *bay*-annulated derivatives also may work as ambipolar organic semiconductors.

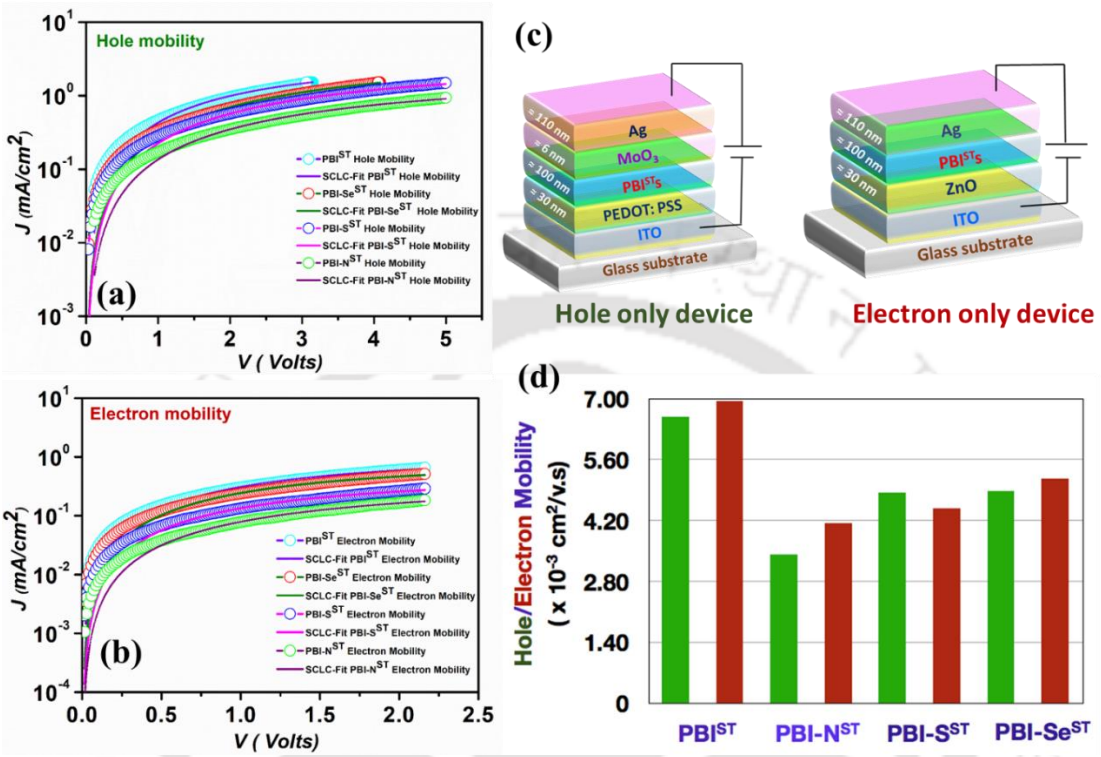

Figure 4.16. *J-V* curves along with SCLC fitting for *J-V* curves along with SCLC fitting for PBIs (**PBIST, PBI-NST, PBI-SST** and **PBI-SeST)** on semi log scale (a) for electron mobility; (b) for hole mobility; (c) Schematic diagram showing the device configuration; (d) Comparison of hole mobility values (green bars) and electron mobility values (red bars) of PBIs studied.

Table 4.5. Hole and electron mobility values for **PBIST**s derived from swallow tail amines (**PBIST, PBI-NST, PBI-SST** and **PBI-SeST**).

Entry	Hole mobility (μ_h) $\times 10^{-3}$ (cm^2/ V.s)	Electron mobility (μ_e) $\times 10^{-3}$ (cm^2/ V.s)	μ_e/ μ_h
PBIST	6.59±0.44	6.94±1.28	1.04
PBI-NST	3.41±0.21	4.14±0.99	1.21
PBI-SST	4.84±1.81	4.48±1.83	0.92
PBI-SeST	4.88±1.38	5.17±0.49	1.05

4.4. Conclusions

In conclusion, a series of well soluble, high fluorescent, and low melting perylene bisimides have been synthesized exhibiting room temperature columnar phases. These PBIs are appended with branched alkyl tails to provide low melting liquid crystallinity. Compounds **PBIST** and **PBI-NST** exhibited a columnar oblique phase, whereas the **PBI-SST** and **PBI-SeST** exhibited a columnar hexagonal phase, down to room temperature with a wide thermal range. Low clearing and melting point offered by the incorporation of swallow tail amines promises to be an ideal method for the synthesis of higher rylene imides and their hetero atom annulated analogues exhibiting ambient liquid crystallinity and solution processability. These compounds exhibited intense absorption spectra with high molar extinction coefficients. All the compounds except **PBI-SeST** were found to be highly fluorescent with good quantum yield. Considering the requirement of new n-type semiconductors capable of self-assembly, this class of compounds is exceptional and encouraging. The charge carrier mobility of these PBIs was examined using the space charge limited current (SCLC) method, which revealed that all of the swallow tail PBIs have a high potential in solution processable ambipolar organic semiconductors. According to the literature review, the majority of the reported PBIs exhibit n-type semiconducting behaviour, whilst the current collection of compounds exhibits ambipolar conductivity. The current molecular design for ambipolar conductivity can be improved further by modifying the mesophase clearance temperatures, mesophase type, and surface alignment. These compounds are currently being investigated further as non-fullerene acceptor for solar cells.

4.5. Experimental section

In this section the detailed synthesis procedure and the molecular structural characterization data have been presented for the intermediates and target compounds mentioned in the scheme.

Synthetic route of Tricosan-12-amine (2): [33]

A 250 mL round-bottom flask was charged with 12-tricosanone (**1**) (5 g, 14.76 mmol), NH_4OAc (11.35 g, 147.6 mmol), $NaBH_3CN$ (1.275 g, 1.38 mmol) and MeOH (100 mL) and stirred at room temperature (r.t.) for 72 h, until the starting material was consumed (monitored by TLC). The reaction was quenched by drop wise addition of conc. HCl (~12 mL) and the solvents removed by rotary evaporation. The resulting white solid was dissolved in H_2O (200 mL) and adjust to pH ~10 with KOH, then extracted with $CHCl_3$ (3× 150 mL) to give desired product as a white solid (4.8g, 95.6%). ^{1}H-NMR (600MHz, $CDCl_3$): δ =0.88 (t, 6H), 1.10-1.50 (m, 42H), 2.68 ppm (s, 1H).

Synthetic route of *N, N*-bis(Tricosan-12-amine)-perylene-3,4,9,10-tetracarboxylicbisimide, (PBIST) (3): [33]

A mixture of perylene-3,4,9,10-tetracarboxylic dianhydride (PTCDA) (2 g, 5.09 mmol), $Zn(OAc)_2$ (0.35 g, 1.61 mmol), imidazole (5 g) and tricosan-12-amine (3.548 g, 10.44 mmol) was vigorously stirred at 160 ^oC for 5h. After cooling to r.t. the mixture was dissolved in minimum amount of THF and precipitated in 1000 mL of 1N HCl/MeOH 2:1 v/v. The orange red precipitate was collected by filtration, washed with H_2O followed by MeOH, dried at 80 ^oC in vacuum and further purified by silica flash-column chromatography with $CHCl_3$. The final product was recrystallized by chloroform-methanol system and obtained as orange solid (4.86 g, 92.1%). R_f = 0.6 (10% $CHCl_3$-Hexane); IR: ν_{max} in cm^{-1}: 2952, 2919, 2849, 1694, 1651, 1592, 1576, 1507, 1467, 1434, 1404, 1366, 1336, 1274, 1252, 1194, 1100, 856, 813, 750, 722; ^{1}H NMR (600 MHz, $CDCl_3$, ppm): δ 8.67 (s, 2H), 8.63 (s, 2H), 8.60-8.59 (s, 4H), 5.20-5.15 (m, 2H), 2.27-2.17 (m, 4H), 1.87-1.86 (m, 4H), 1.31-1.19 (m, 72H), 0.83 (t, *J* = 6 Hz, 12H). ^{13}C NMR (150 MHz, $CDCl_3$, ppm): δ 164.4, 163.57, 134.49, 131.89, 131.12, 129.59, 126.43, 123.94, 123.20, 123.00, 54.77, 32.37, 31.91, 29.62, 29.61, 29.55, 29.33, 26.97, 22.67, 22.55, 14.10. MALDI-TOF exact mass calculated for $C_{70}H_{103}N_2O_4$ $(M+H)^+$: 1035.79, found: 1035.367.

Synthetic route of *N, N*-bis(Tricosan-12-amine)-1-nitroperylene-3,4,9,10-tetracarboxydianhydride (4): [34]

In a round bottom flask, compound **3** (2 g, 1.93 mmol) was dissolved in CH_2Cl_2 (150 mL) and $NaNO_2$ (0.13 g, 1.93 mmol) was added to it. Then conc. HNO_3 (2.62 mL, 62.4 mmol) was added dropwise to the reaction mixture was stirred at 0 ^oC for 20-25 min. Then it was allowed to stir at rt. TLC was used for indicating completion of reaction. The reaction was quenched by adding H_2O (90 mL). The layers were separated and the aqueous phase was extracted with CH_2Cl_2 (3 times). The organic phases were combined, washed with water (3 times), dried over anhydrous Na_2SO_4 and concentrated under reduced pressure. The residue was purified through silica gel column chromatography ($CHCl_3$/Petroleum Ether 1:1) to afford compound **4** as a dark red solid (1.95 g, 90.8%). ^{1}H NMR (600 MHz, $CDCl_3$, ppm): δ 8.80-8.71 (m, 5H), 8.61-8.58 (m, 1H), 8.26 (d, *J* = 6 Hz, 1H), 5.16 (m, 2H), 2.22 (t, *J* = 6 Hz, 4H), 1.85 (t, *J* = 6 Hz, 4H), 1.25-1.20 (m, 72H), 0.84 (t, *J* = 6 Hz, 12H).

Synthetic route of N, N-bis(Tricosan-12-amine)-NH-annulated perylene-3,4,9,10-tetracarboxydianhydride (PBI-NST): [34]

Nitro-PDI (**4**) (50 mg, 0.06 mmol) and NaN_3 (12 mg, 0.19 mmol) were suspended in a DMF/THF mixture (1:1) (6 mL). The reaction mixture was stirred at rt for 18 h. HCl (1N) was added and the mixture was extracted with $CHCl_3$ (5 times). The organic phases were combined, dried and concentrated under reduced pressure. The residue was purified through silica gel column chromatography by eluting with 20-30% $CHCl_3$-Hexane system followed by 50% $CHCl_3$-Hexane system ($CHCl_3$) to afford 6 as a red solid (36 mg, 76%). R_f = 0.5 (10% $CHCl_3$-Hexane); IR: ν_{max}

in cm^{-1}: 3049, 2953, 2920, 2851, 1701, 1655, 1592, 1596, 1540, 1465, 1427, 1406, 1348, 1331, 1249, 1200, 1117, 945, 863, 813, 745, 718;
^{1}H NMR (600 MHz, $CDCl_3$, ppm): δ 10.00 (s, 1H, -NH), 9.09 (s, 1H), 9.04 (s, 1H), 8.98 (d, *J* = 12 Hz, 2H), 8.89(d, *J* = 12 Hz, 1H), 8.84(d, *J* = 12 Hz, 1H), 5.33-5.30 (m, 2H), 2.36-2.31 (m, 4H), 1.96-1.91 (m, 4H), 1.41-1.16 (m, 72H), 0.82-0.80 (t, *J* = 6 Hz, 12H). ^{13}C NMR (150 MHz, $CDCl_3$, ppm): 166.48, 165.37, 164.98, 163.92, 133.58, 133.55, 132.30, 132.18, 128.11, 127.34, 125.05, 124.27, 123.23, 122.74, 122.03, 121.90, 121.27, 121.14, 120.42, 119.68, 119.59, 55.18, 32.76, 32.61, 31.84, 29.67, 29.61, 29.56, 29.27, 27.30, 22.61, 14.04. MALDI-TOF exact mass calculated for $C_{70}H_{102}N_3O_4$ $(M+H)^+$: 1048.79, found: 1048.385.

Synthetic route of N, N-bis(Tricosan-12-amine)-S-annulated perylene-3,4,9,10-tetracarboxydianhydride (PBI-S^{ST}): [19]

A mixture of compound (**4**) (1 g, 0.92 mmol) and Sulfur powder (.30 g, 9.2 mmol) was heated to dissolve in *N*-methylpyrrolidone (20 mL) at 70 °C for 30 min. and then refluxed at 180 °C under Ar atmosphere for overnight until the starting material could not be detected by TLC. After cooling to room temperature, 2M HCl was added, then the precipitate was filtered, washed with water and dried. The crude product was purified by column chromatography on neutral alumina. Elution with 5-10 % $CHCl_3$-Hexanes system followed by 20% $CHCl_3$-Hexane system yields the desired product in good yield. Further purification was done by addition of concentrate solution of compound in cold methanol gives the waxy product (0.730 g, 74%).
R_f = 0.6 (10% $CHCl_3$-Hexane); IR: ν_{max} in cm^{-1}: 2952, 2920, 2851, 1694, 1651, 1596, 1559, 1454, 1426, 1361, 1347, 1302, 1243, 1234, 1199, 1162, 1115, 911, 840, 808, 742, 721;
^{1}H NMR (600 MHz, $CDCl_3$, ppm): δ 9.24-9.19 (m, 2H), 8.85-8.80 (m, 4H), 5.30 (m, 2H), 2.36-2.30 (m, 4H), 1.94-1.93 (m, 4H), 1.24-1.17 (m, 72H), 0.82-0.80 (t, *J* = 6 Hz, 12H). ^{13}C NMR (150 MHz, $CDCl_3$, ppm): δ 165.15, 164.72, 163.97, 163.65, 138.08, 133.00, 132.24, 130.03, 129.28, 127.87, 127.09, 126.13, 123.37, 122.96, 122.66, 122.25, 55.07, 32.49, 31.89, 29.72, 27.63, 29.32, 27.10, 22.65, 14.09. MALDI-TOF exact mass calculated for $C_{70}H_{101}N_2O_4S$ $(M+H)^+$: 1065.75, found: 1065.689.

Synthetic route of *N*, *N*-bis(Tricosan-12-amine)-Se-annulated perylene-3,4,9,10-tetracarboxydianhydride (PBI-Se^{ST}): [19]

A mixture of compound (**4**) (1 g, 0.92 mmol) and Selenium powder (0.730 g, 9.2 mmol) was heated to dissolve in *N*-methylpyrrolidone (20 mL) at 70 °C for 30 min. and then refluxed at 180 °C under Ar atmosphere for overnight until the starting material could not be detected by TLC. After cooling to room temperature, 2M HCl was added, then the precipitate was filtered, washed with water and dried. The crude product was purified by column chromatography on neutral alumina. Elution with 10-20% $CHCl_3$-Hexanes system followed by 40% $CHCl_3$-Hexane system yields the desired product in good yield. Further purification was done by addition of concentrate solution of compound in cold methanol gives the waxy product (0.700 g, 68%).

R_f = 0.6 (10% $CHCl_3$-Hexane); IR: ν_{max} in cm^{-1}: 2952, 2920, 2851, 1693, 1648, 1593, 1557, 1455, 1420, 1361, 1347, 1303, 1243, 1231, 1199, 1164, 1113, 913, 847, 808, 742, 721;
^1H NMR (600 MHz, $CDCl_3$, ppm): δ 9.01 (m, 2H), 8.61-8.54 (m, 2H), 8.33 (s, 2H), 5.27-5.26 (m, 2H), 2.34 (m, 4H), 1.98 (s, 4H), 1.37-1.15 (m, 72H), 0.78 (t, J = 6 Hz, 12H). ^{13}C NMR (150 MHz, $CDCl_3$, ppm): δ 164.69, 163.54, 140.15, 139.18, 133.31, 132.37, 129.56, 128.81, 125.96, 123.51, 122.83, 122.33, 122.11, 121.65, 55.2, 55.05, 32.49, 31.93, 31.90, 29.71, 29.68, 29.64, 29.56, 29.52, 29.41, 29.34, 27.25, 22.70, 22.65 14.12, 14.07. MALDI-TOF exact mass calculated for $C_{70}H_{100}N_2O_4Se$ $(M)^+$: 1112.68, found: 1112.546.

4.6. Appendix

4.6.1. NMR Spectra

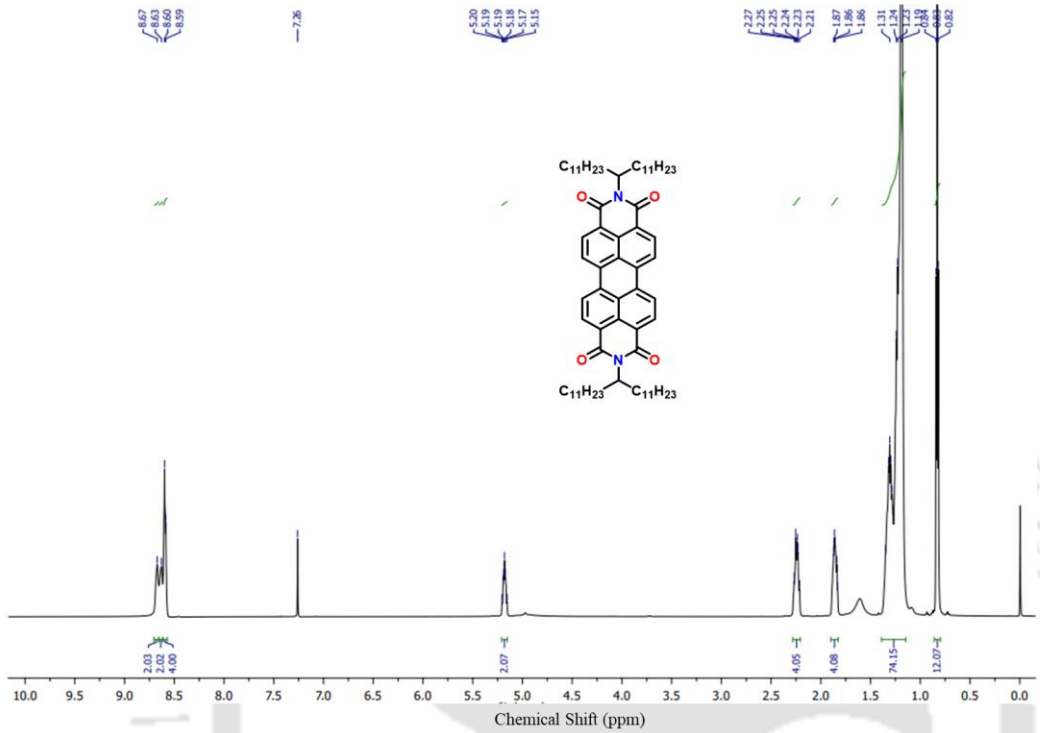

Figure A1. ^{1}H NMR (600 MHz) spectra of **PBIST** in $CDCl_3$.

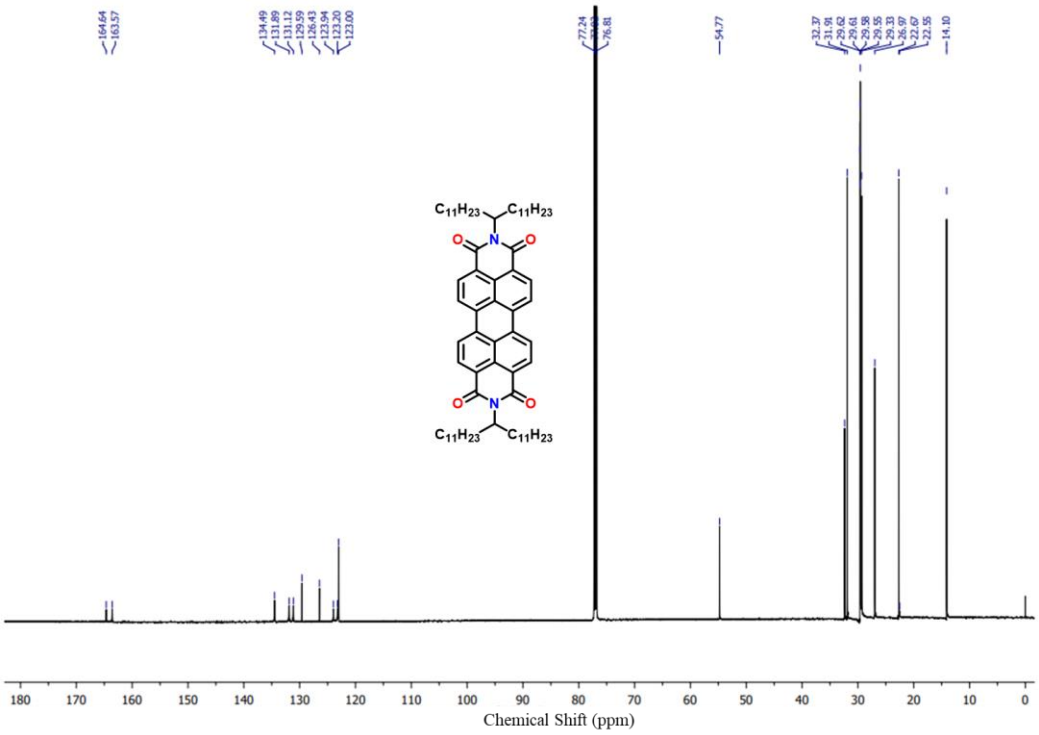

Figure A2. ^{13}C NMR (150 MHz) spectra of **PBIST** in $CDCl_3$.

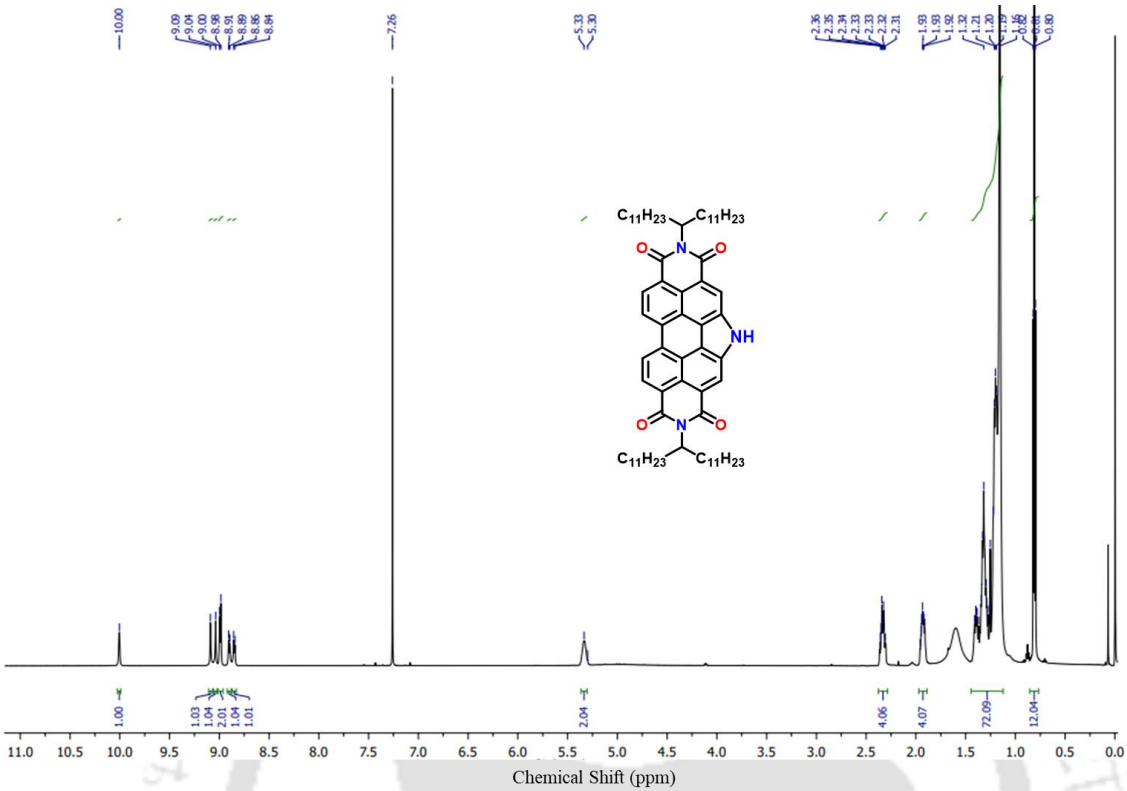

Figure A3. ^{1}H NMR (600 MHz) spectra of **PBI-NST** in $CDCl_3$.

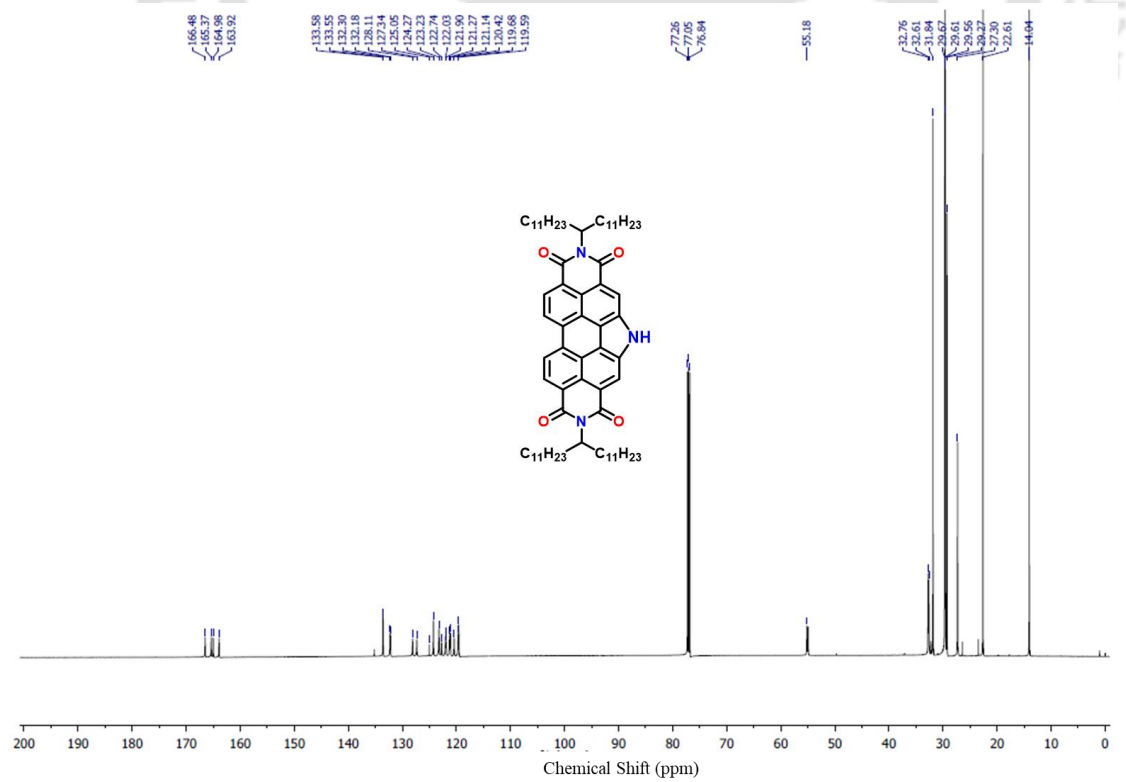

Figure A4. ^{13}C NMR (150 MHz) spectra of **PBI-NST** in $CDCl_3$.

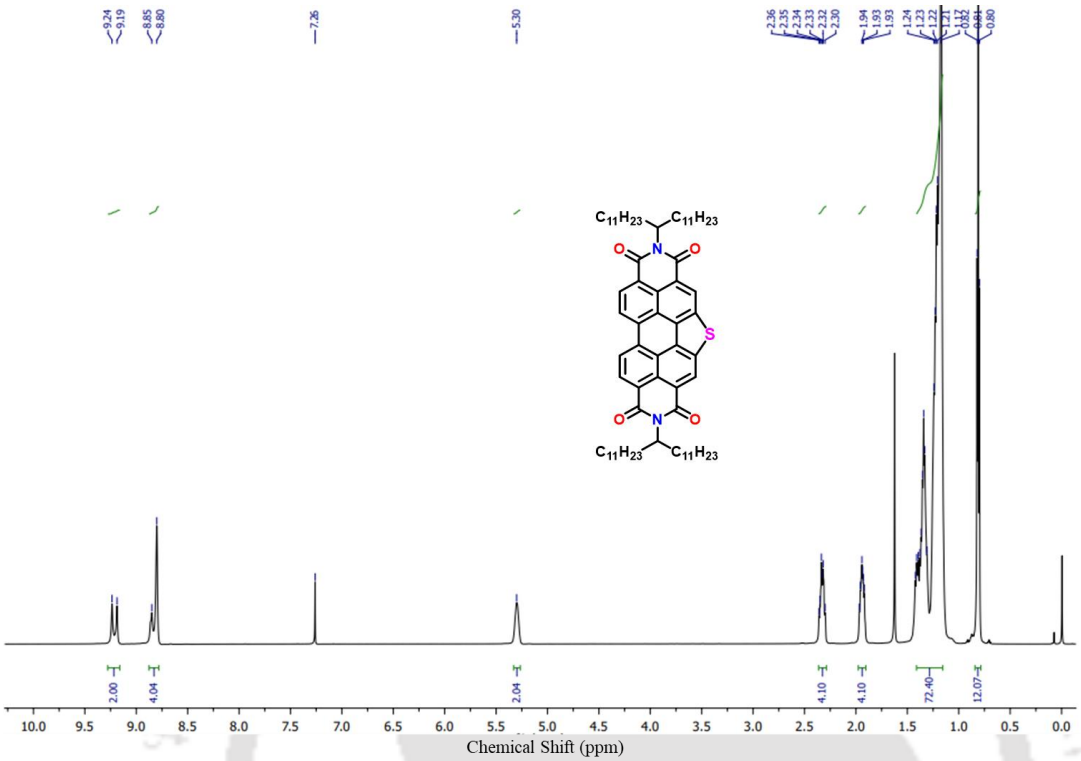

Figure A5. ^{1}H NMR (600 MHz) spectra of **PBI-SST** in $CDCl_3$.

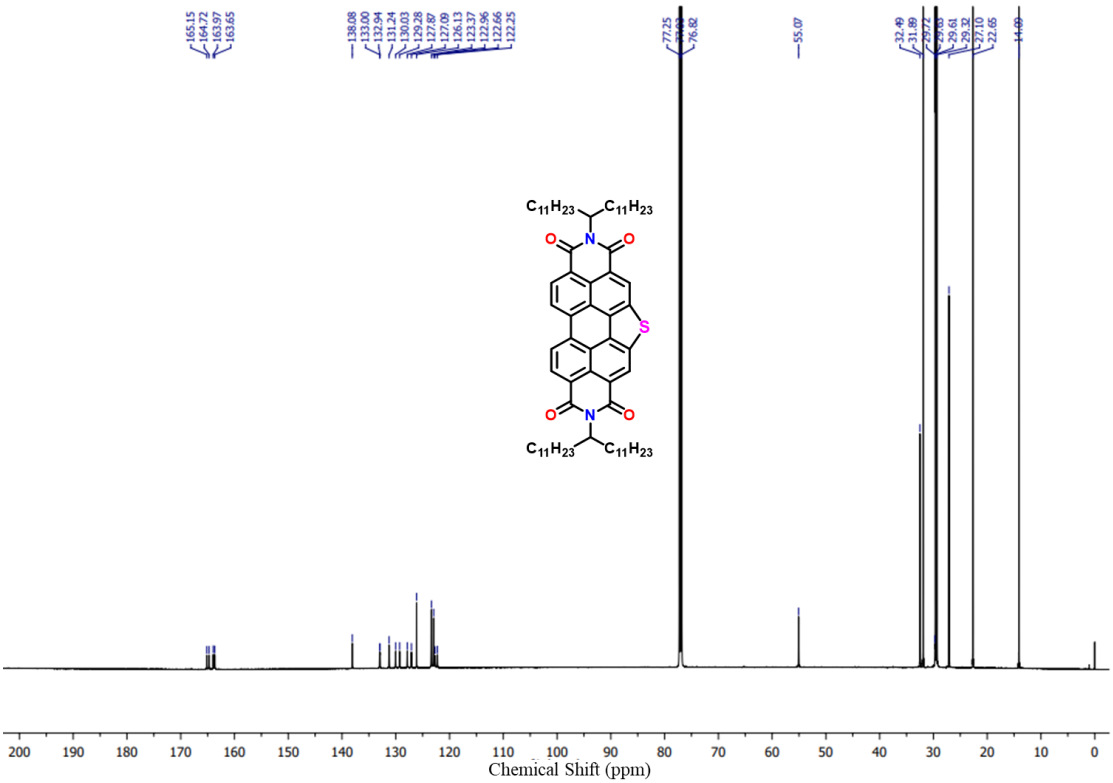

Figure A6. ^{13}C NMR (150 MHz) spectra of **PBI-SST** in $CDCl_3$.

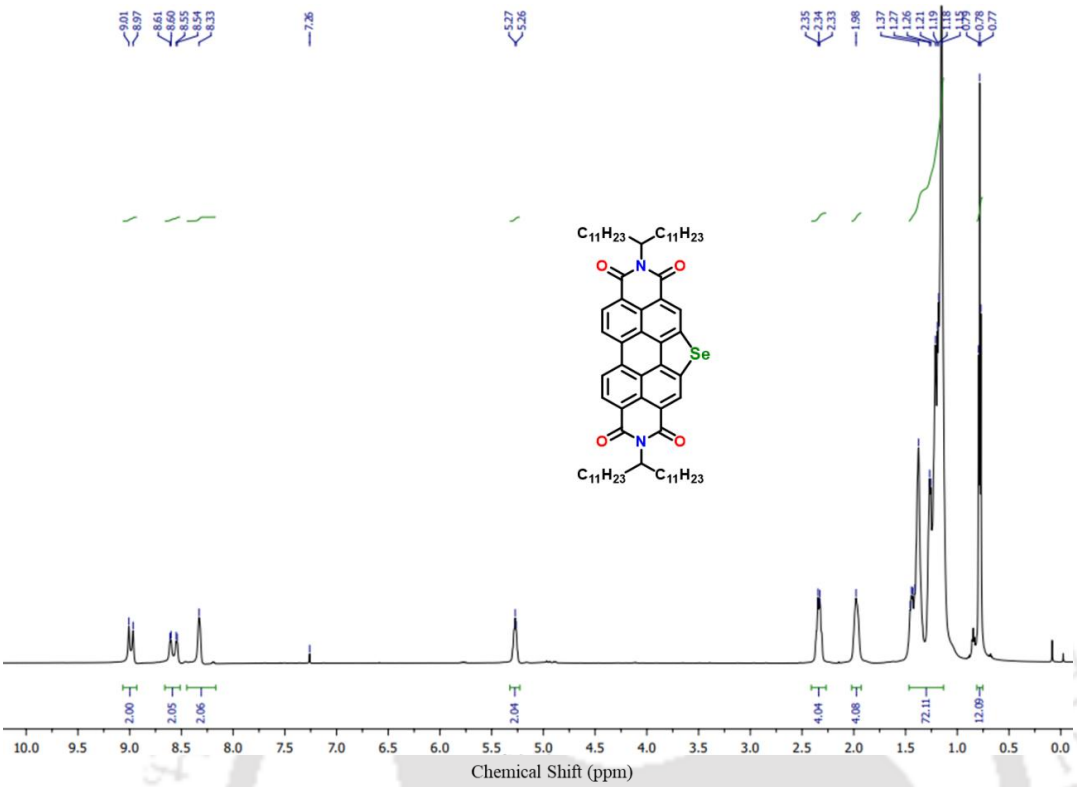

Figure A7. ^{1}H NMR (600 MHz) spectra of **PBI-SeST** in $CDCl_3$.

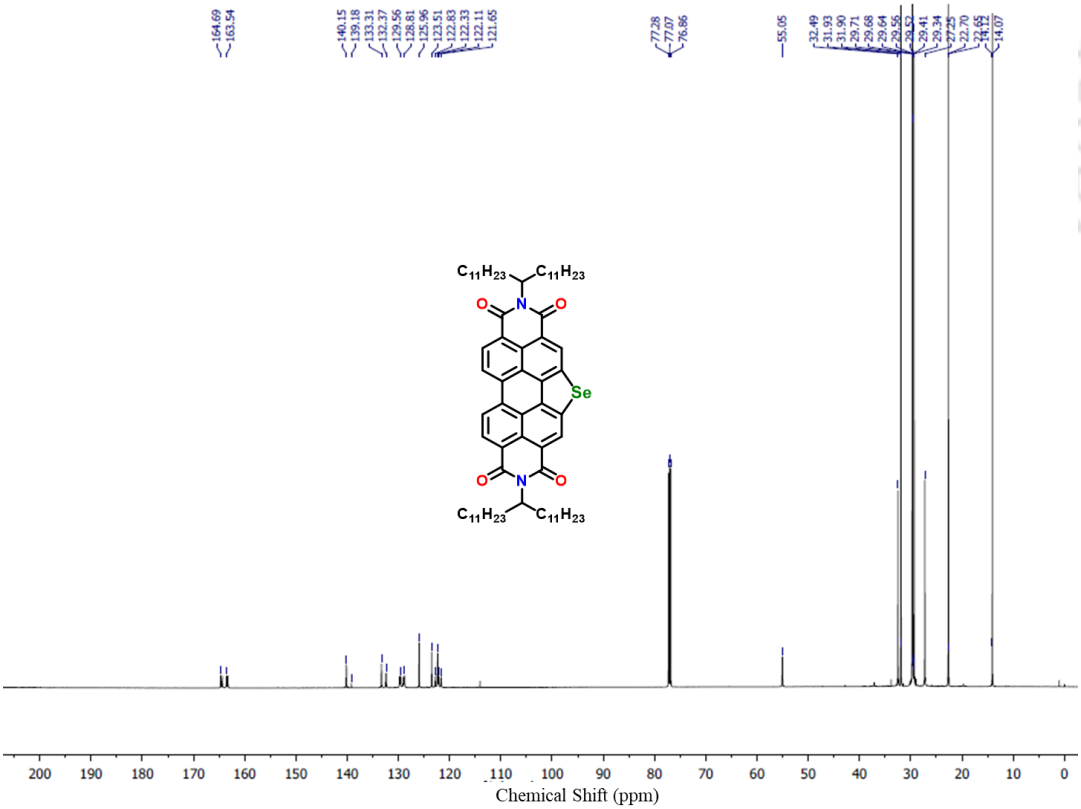

Figure A8. ^{13}C NMR (150 MHz) spectra of **PBI-SeST** in $CDCl_3$.

4.6.2. Polarizing optical microscopy (POM) images

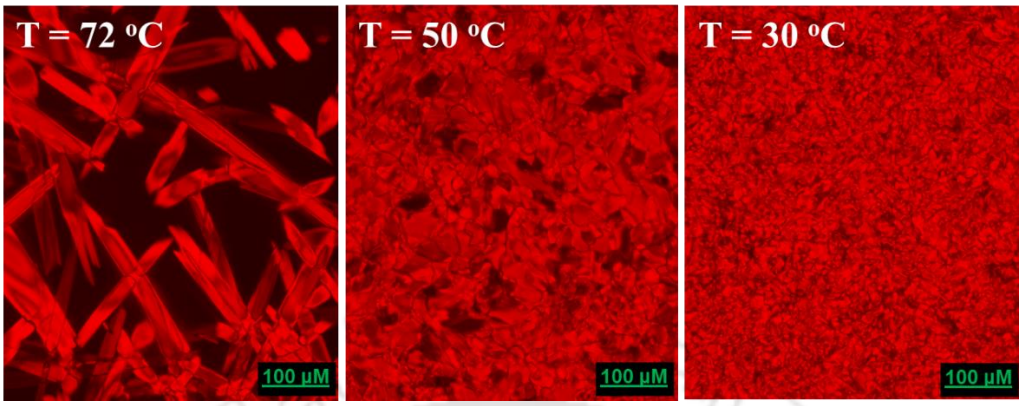

Figure A9. POM images of **PBIST** at different temperature intervals obtained on cooling the isotropic melt.

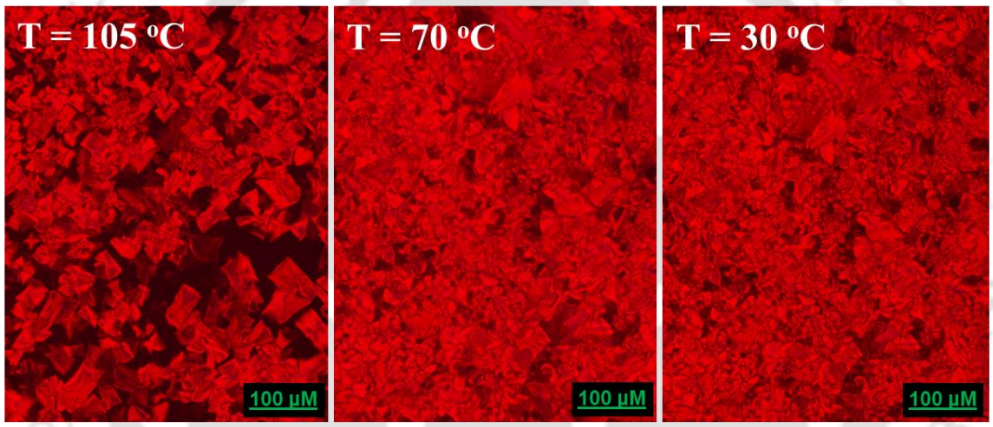

Figure A10. POM images of **PBI-N^{O10}** at different temperature intervals obtained on cooling the isotropic melt.

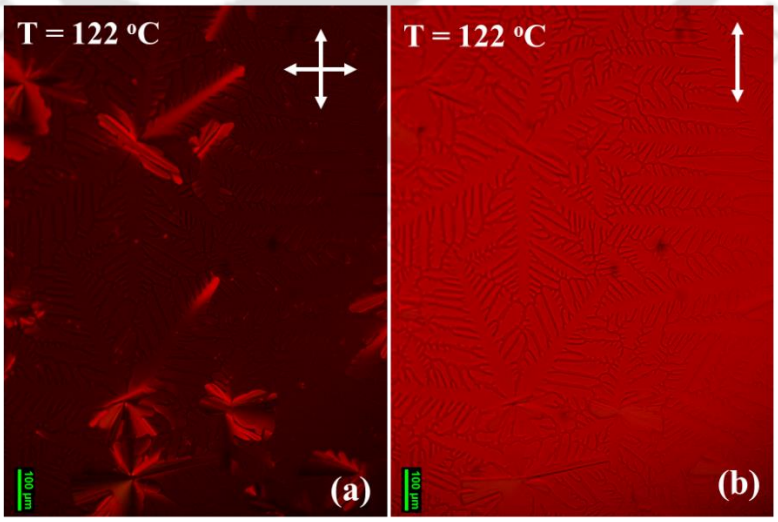

Figure A11. POM images obtained for **PBI-SST** at 122 °C in crossed polarizer (a) and parallel polarizer (b).

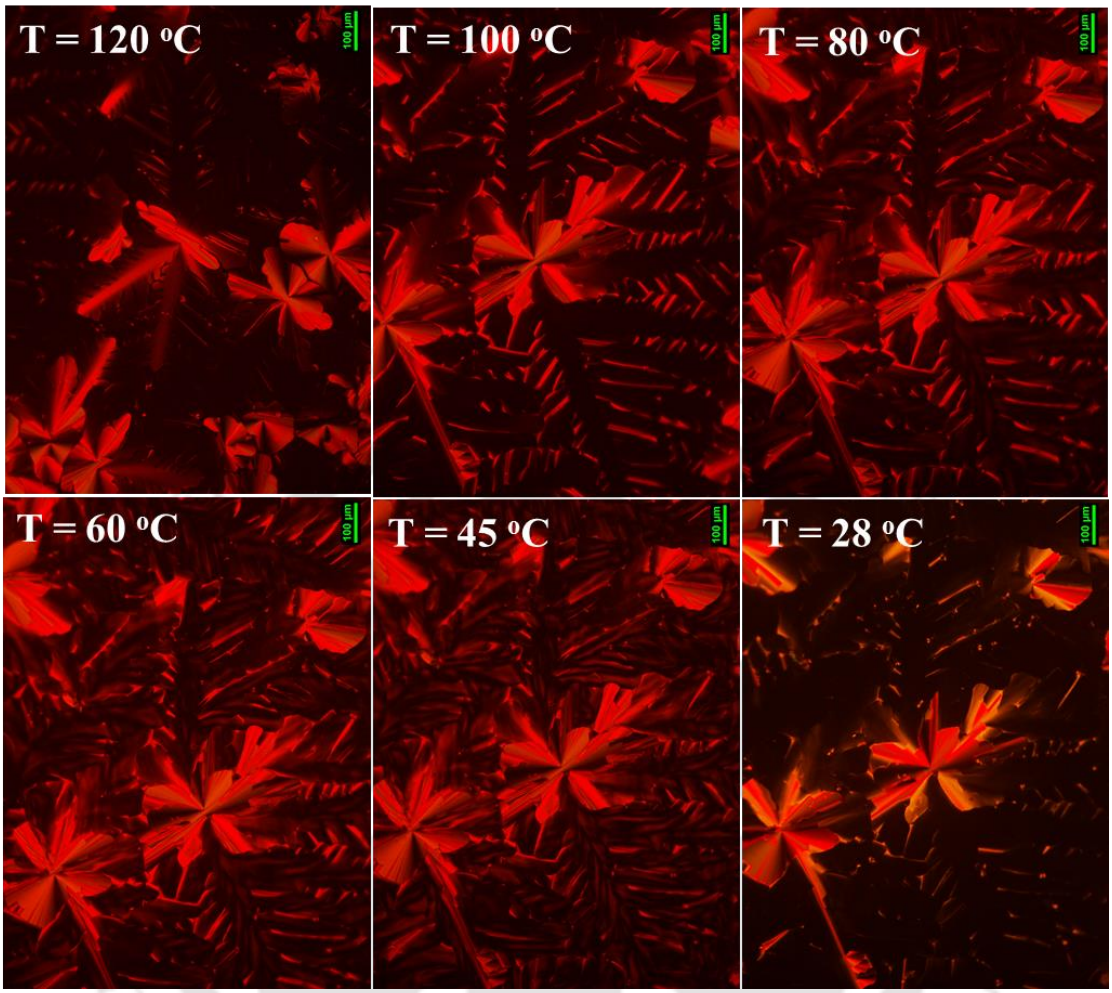

Figure A12. POM images of **PBI-SST** at different temperature intervals obtained on cooling the isotropic melt.

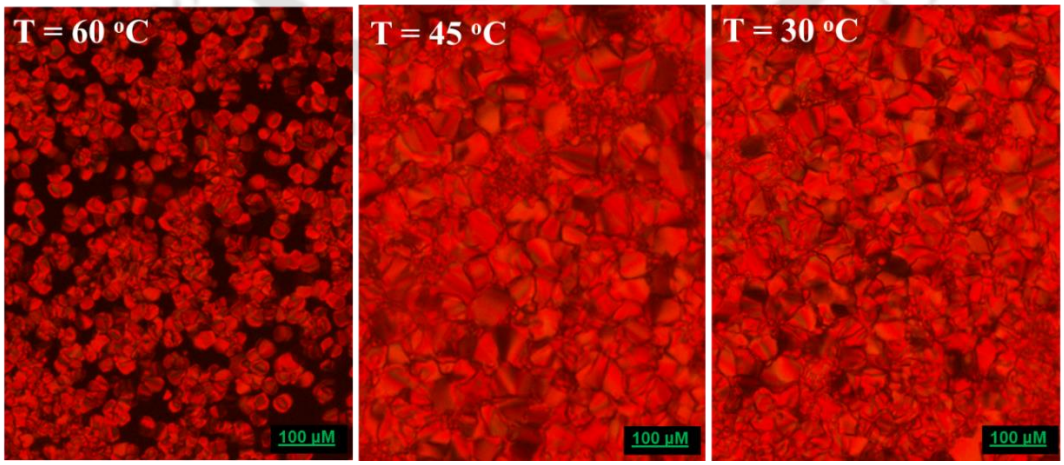

Figure A13. POM images of **PBI-SeST** at different temperature intervals obtained on cooling the isotropic melt.

4.6.3. XRD Studies

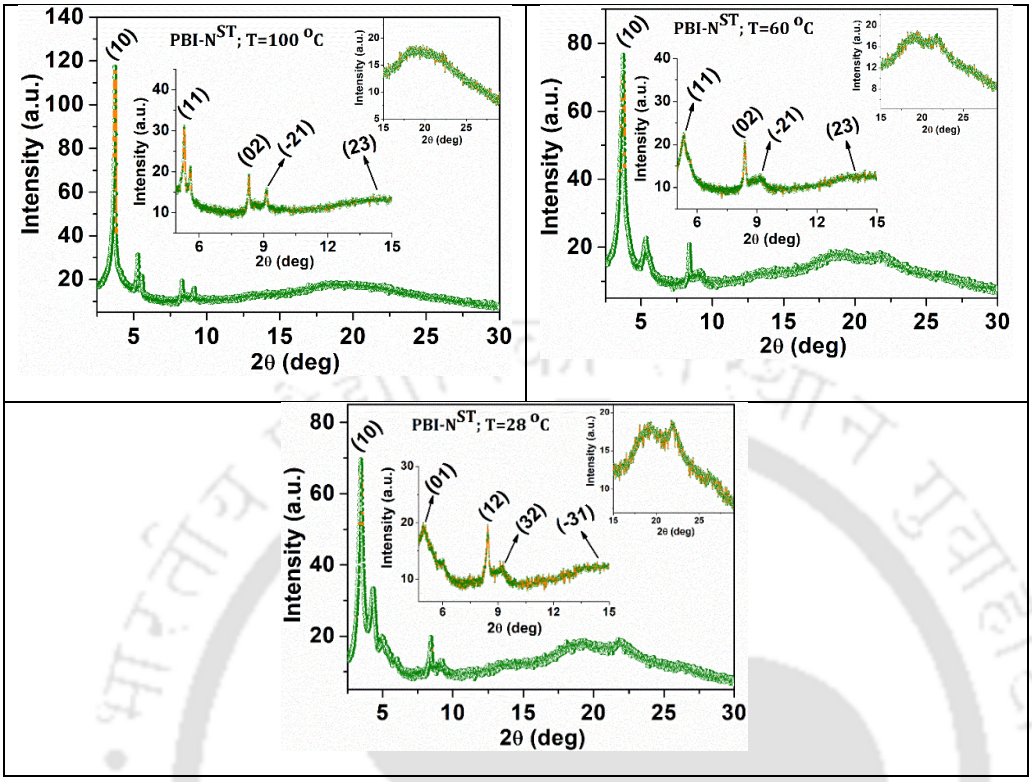

Figure A14. Plot of the intensity against 2θ obtained from the powder XRD pattern of the Col_{ob} phases **PBI-NST** at different temperature intervals.

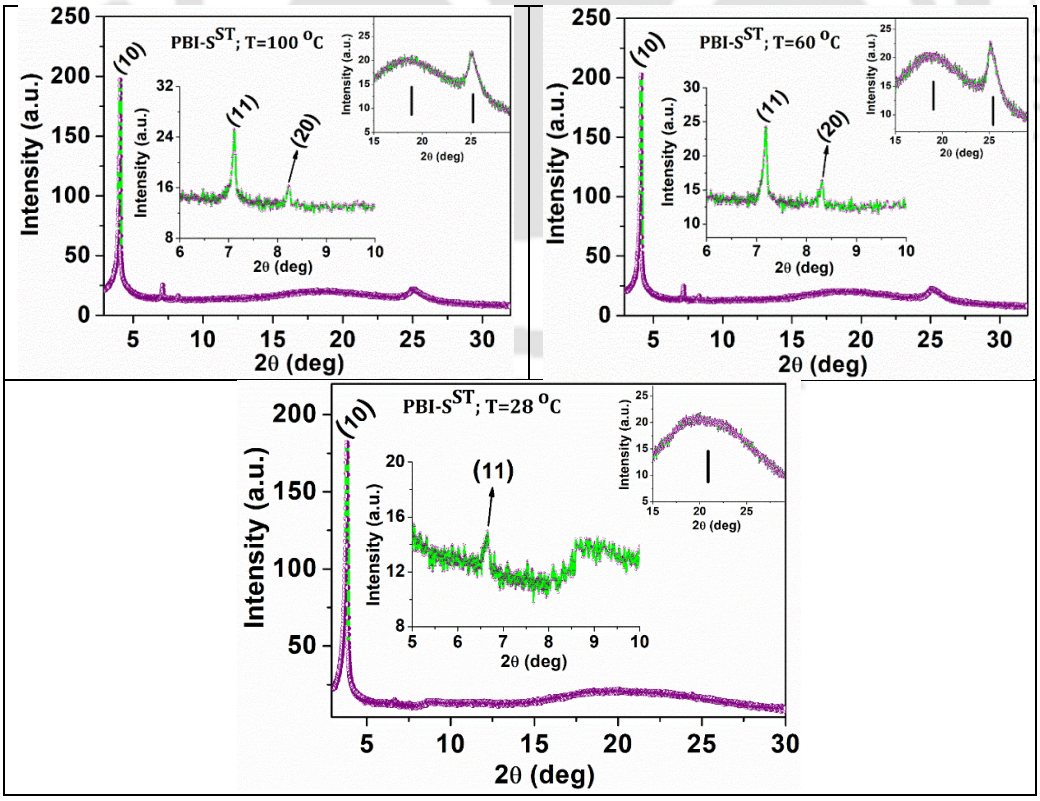

Figure A15. Plot of the intensity against 2θ obtained from the powder XRD pattern of the Col_h phases **PBI-SST** at different temperature intervals.

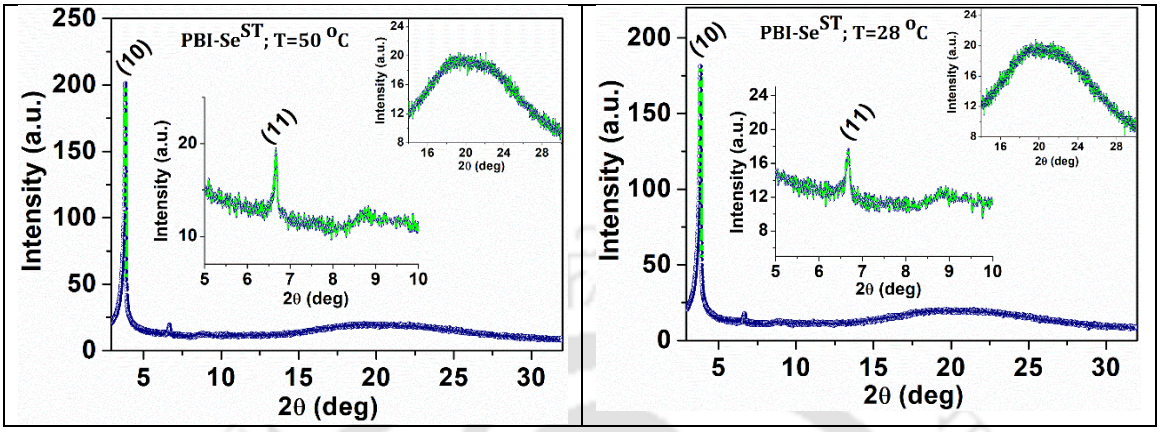

Figure A16. Plot of the intensity against 2θ obtained from the powder XRD pattern of the Col_h phases **PBI-SeST** at different temperature intervals.

3.6.4. Thermogravimetric analysis (TGA)

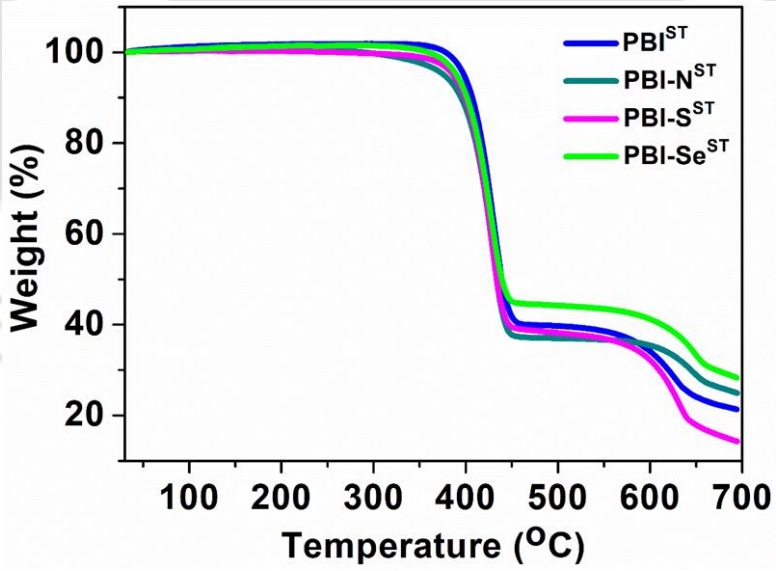

Figure A17. TGA plots of compound **PBIST, PBI-NST, PBI-SST** and **PBI-SeST**.
(heating rate of 10 °C/min, Nitrogen atmosphere).

4.6.5. Photophysical studies

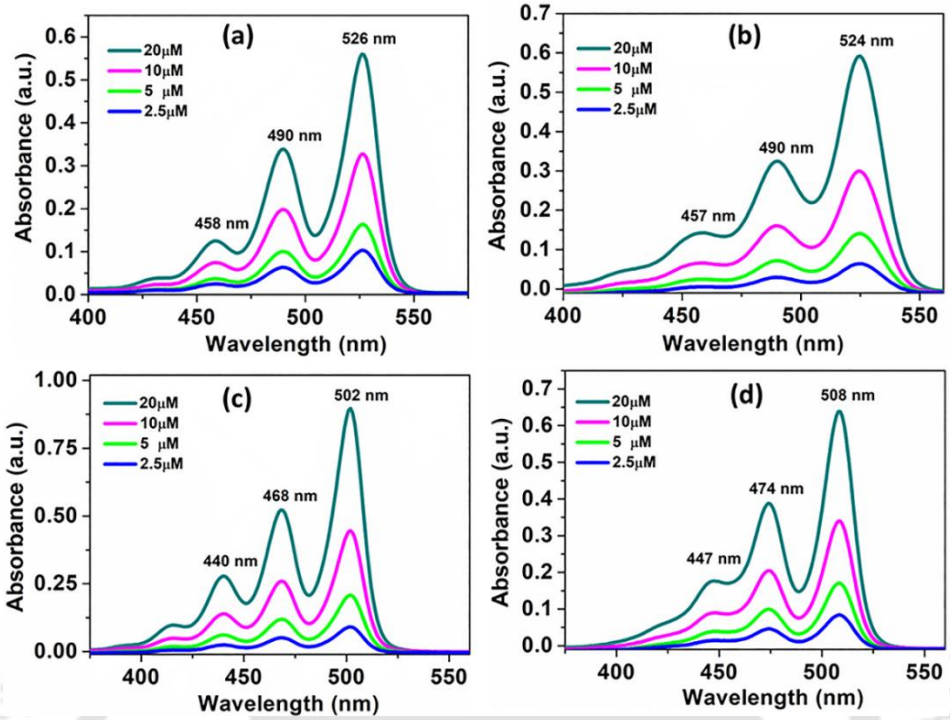

Figure A18. Absorption spectra of **PBI**ST (a), **PBI-N**ST (b), **PBI-S**ST (c), and **PBI-Se**ST (d) in chloroform solution as a function of concentration.

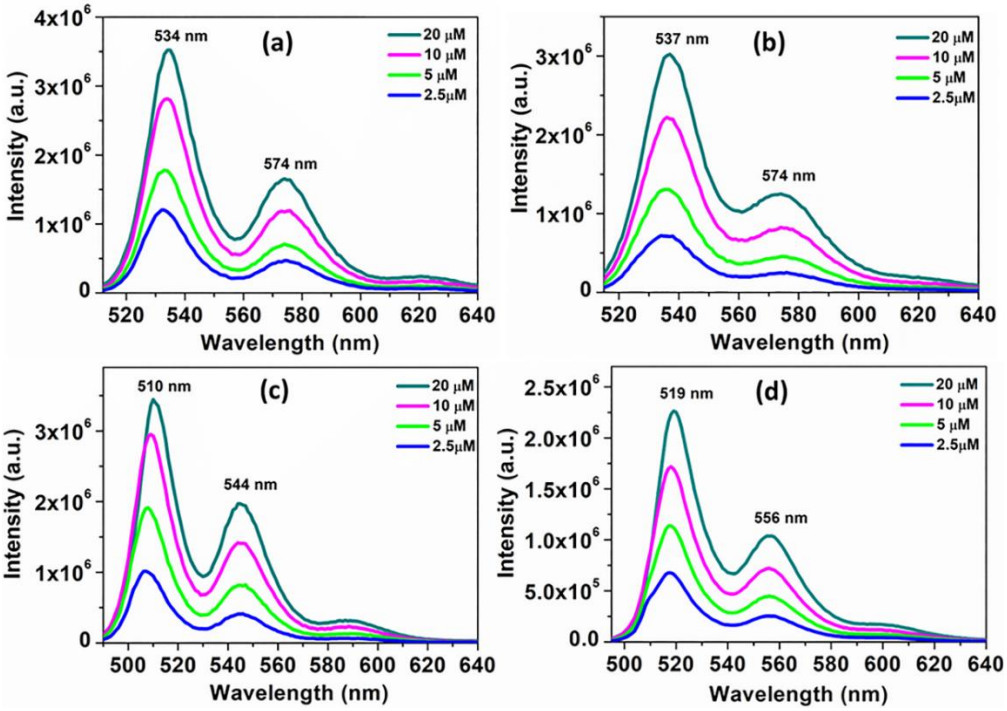

Figure A19. Emission Spectra of **PBI**ST (a), **PBI-N**ST (b), **PBI-S**ST (c), and **PBI-Se**ST (d) in chloroform solution as a function of concentration

4.6.6. Quantum yield measurement (Relative)

Quantum yield was measured according to established procedure by using rhodamine 6g in ethanol as the standard. Absolute values were calculated according to the following equation: $Q_S = Q_R \times (m_S / m_R) \times (n_S / n_R)^2$, Where, Q: Quantum yield, m: Slope of the plot of integrated fluorescence intensity vs absorbance (Calculated from Fig.A18), n: refractive index (1.361 for ethanol and 1.445 for chloroform). The subscript R refers to the reference fluorophore i.e. rhodamine 6G solution in EtOH and subscript S refers to the sample under investigation. In order to minimize re-absorption effects, absorbance was kept below 0.15 at the excitation wavelength of 526, 524, 502 and 508 nm respectively for compounds **PBIST**, **PBI-NST**, **PBI-SST** and **PBI-SeST**. Quantum Yield of rhodamine 6g in EtOH is 0.95. Simplified equation for the calculation after substituting the appropriate values is given below and values obtained are given in table below.

$$Q_S = 0.95 \times (m_S / m_R) \times (1.445/1.361)^2$$

Compounds	**m_S**	**m_R**	**Q_S ^{a,b,c}**
PBIST	6.93578×10^8	8.70249×10^9	0.88
PBI-NST	6.36608×10^8	7.58948×10^8	0.93
PBI-SST	6.37322×10^8	9.53557×10^8	0.74
PBI-SeST	4.82451×10^7	8.21323×10^8	0.06

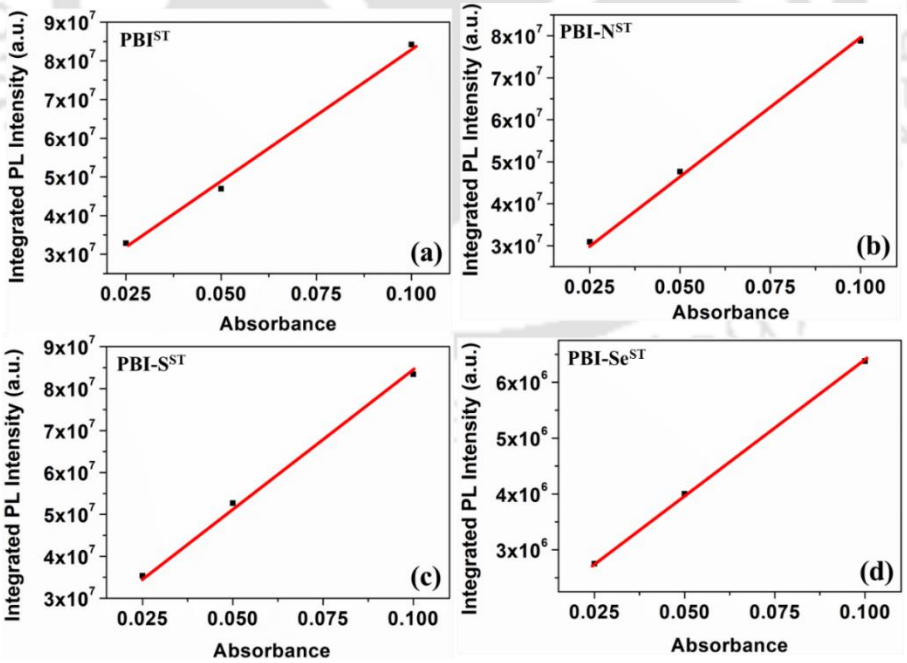

Figure A20. Plots of integrated photoluminescence intensity vs absorbance of reference compound **PBIST** (a), **PBI-NST** (b), **PBI-SST** (c) and **PBI-SeST** (d) respectively.

4.6.7. Device Fabrication and characterization:

The charge transport properties of PBISTs are studied by the SCLC technique in this work. The device configurations for hole-only are ITO/PEDOT: PSS /**PBISTs** /MoO_3-Ag and ITO/ **PBISTs** /Ag for electron-only devices were used.

Prepatterned ITO (Xinyan Technologies, Taiwan, 15 Ω/cm^2) substrates were first cleaned using a 3% soap solution in deionized water (Hellmanex III, Sigma-Aldrich), and rinsed in deionized water to remove traces of soap solution. Again substrates were sequentially cleaned with distilled water, acetone, and isopropyl alcohol (IPA) in an ultrasonicator for 20 min duration each. Cleaned substrates were then dried using a gentle blow of nitrogen gas, followed by 30 min of UV ozone (BioBEE Tech, India) treatment at 50 °C.

The electron-only devices were fabricated by the first depositing electron layer (ZnO) using spin coating technique from the prepared ZnO solution using sol−gel technique (100 mg of zinc acetate dihydrate, Zn $(CH_3COO)_2 \cdot 2H_2O$) + 28 mg of ethanolamine in 1 mL of 2-methoxy ethanol, stirred heavily overnight at room temperature. The ZnO solution was then filtered through a 0.45 μm PTFE filter followed by spin-coating at 4500 rpm for 60 s to achieve a thin layer of around 30 nm thickness. The substrates were then annealed at 180 °C in a hot place for 1 hr duration under ambient conditions. The active layer of PBISTs (**PBIST, PBI-NST, PBI-SST** and **PBI-SeST**) was deposited on the top ZnO layer followed by a 110-120 nm of Ag metal electrode obtained using thermal evaporator (Hind High Vacuum, India) at 1 ×10^{-6} m bar pressure connected with a glove box (H_2O <5 ppm, O_2 <5 ppm). Active layer solution of PBISTs were prepared (10 mg/ml) in anhydrous chloroform and spin-coated at 1500 rpm for 45 s, which constructs a layer of ~ 90−95 nm. The active areas of fabricated device are 0.066 cm^2, calculated from the overlap area of patterned ITO and top contact/electrode). For measuring the thickness of different layers Dektak surface profiler (Dektak XT, Bruker) was used.

Similarly, the hole-only devices were begun from the deposition of a poly (3,4-ethylene dioxythiophene)/polystyrene sulfonate (PEDOT: PSS) (Clevios PVP Al 4081-Heraeus) solution on the top of precleaned and UV-ozone treated patterned ITO Coated substrate and the solution filtration were also take place using 0.45 μm PVDF filters. The Filtered solution was deposited using spin-coating at 4000 rpm for 65s having a layer thickness of ~30-35 nm. Then PEDOT: PSS-coated substrates were annealed at 150 °C on a hot plate for 20 min. The active layer of **PBISTs** was then spin-coated at 1500 rpm for 45sec to obtain a layer thickness of 100 nm prepared from the same solution used for electron only devices. Finally, in order to complete device, 6 nm of MoO_3 layer and a 110-120 nm layer of Ag were sequentially thermally evaporated to establish top contact. The completed device was immediately used for the measurement of current−voltage ($J-V$) characteristics measurement using Keithley 2450 source-measure unit. The dielectric constant of **PBISTs** compounds were calculated from the capacitance−voltage characteristics (ϵ_r ~ 2.29) using a high-frequency LCR meter ZM2376 (NF Corporation, Japan) with an applied oscillation level voltage of 1 V and frequency sweep from 20 Hz to 1 MHz.

Table A1. Statistics of hole and electron mobility values for five best devices obtained from hole only (ITO/PEDOT: PSS / **PBISTs** /MoO_3/Ag) and electron only (ITO/ZnO/ **PBISTs**/Ag) devices of **PBISTs** derivatives.

Entry	Hole mobility (cm^2/ V.s)	Electron mobility (cm^2/ V.s)
PBIST	5.91E-03 7.30E-03 6.68E-03 6.47E-03 6.59E-03	7.96E-03 7.41E-03 4.41E-03 7.36E-03 7.57E-03
Avg. **Stdev**	**6.59E-03** **4.45E-04**	**6.94E-03** **1.28 E-03**
PBI-NST	3.24E-03 3.44E-03 3.51E-03 3.11E-03 3.74E-03	3.45E-03 3.19E-03 3.36E-03 5.39E-03 5.32E-03
Avg. **Stdev**	**3.41E-03** **2.18E-04**	**4.14E-03** **9.94E-04**
PBI-SST	4.60E-03 2.90E-03 2.87E-03 6.65E-03 7.16E-03	2.33E-03 5.42E-03 2.19E-03 6.32E-03 6.15E-03
Avg. **Stdev**	**4.84E-03** **1.81E-03**	**4.48E-03** **1.83E-03**
PBI-SeST	3.35E-03 3.43E-03 5.35E-03 5.20E-03 7.06E-03	5.19E-03 5.28E-03 5.57E-03 5.58E-03 4.22E-03
Avg. **Stdev**	**4.88E-03** **1.38E-03**	**5.17E-03** **4.98E-04**

3.7. References

1. Q. Li, Y. Zhang, Z. Xie, Y. Zhen, W. Hud and H. Dong, *J. Mater. Chem. C*, 2022, **10**, 2411—2430.
2. S. Sergeyev, W. Pisulab and Y. H. Geerts, *Chem. Soc. Rev.*, 2007, **36**, 1902-1929.
3. K. Zhou, H. Dong, H. l. Zhang and W. Hu, *Phys. Chem. Chem. Phys.*, 2014, **16**, 22448.
4. C. Huang, S. Barlow and S. R. Marder, *J. Org. Chem.* 2011, **76**, 8, 2386–2407.
5. F. Würthner, C. R. Saha-Möller, B. Fimmel, S. Ogi, P. Leowanawat and D. Schmidt, *Chem Rev*, 2016, **116**, 962–1052.
6. X. Zhan, A. Facchetti, S. Barlow, T. J. Marks, M. A. Ratner, M. R. Wasielewski, and S. R. Marder, *Adv. Mater.* 2011, **23**, 268–284.

7. T. Wöhrle, I. Wurzbach, J. Kirres, A. Kostidou, N. Kapernaum, J. Litterscheidt, J. C. Haenle, P. Staffeld, A. Baro, F. Giesselmann, and S. Laschat, *Chem. Rev.* 2016, **116**, 3, 1139–1241.
8. R. K. Gupta, A. A. Sudhakar, *Langmuir* 2019, **35**, 2455-2479.
9. Z. An, J. Yu, S. C. Jones, S. Barlow, S. Yoo, B. Domercq, P. Prins, L. D. Siebbeles, B. Kippelen, S. R. Marder, *Adv. Mater.* 2005, **17**, 2580−2583.
10. F. Würthner, C. Thalacker, S. Diele, C. Tschierske, *Chem. - Eur. J.* 2001, **7**, 2245−2253.
11. V. Dehm, Z. Chen, U. Baumeister, P. Prins, L. D. Siebbeles, F. Würthner, *Org. Lett.* 2007, **9**, 1085−1088.
12. A. Wicklein, A. Lang, M. Muth, M. Thelakkat, *J. Am. Chem. Soc.* 2009, **131**, 14442−14453.
13. M. Funahashi, A. Sonoda, *J. Mater. Chem.* 2012, **22**, 25190−25197.
14. D. Sahoo, M. Peterca, E. Aqad, B. E. Partridge, P. A. Heiney, R. Graf, H. W. Spiess, X. Zeng, V. Percec, *J. Am. Chem. Soc.* 2016, **138**, 14798−14807.
15. Y. Sun, L. Tan, S. Jiang, H. Qian, Z. Wang, D. Yan, C. Di, Y. Wang, W. Wu, G. Yu, S. Yan, C. Wang, W. Hu, Y. Liu and D. Zhu, *J. Am. Chem. Soc.*, 2007, **129**, 1882.
16. W. Jiang, H. Qian, Y. Li and Z. Wang, *J. Org. Chem.*, 2008, **73**, 7369.
17. W. Jiang, Y. Zhou, H. Geng, S. Jiang, S. Yan, W. Hu, Z. Wang, Z. Shuai and J. Pei, *J. Am. Chem. Soc.*, 2011, **133**, 1, 1-3.
18. H. Langhals and S. Kirner, *Eur. J. Org. Chem.* 2000, 365-380.
19. R. K. Gupta, D. S. S. Rao, S. K. Prasad, A. S. Achalkumar, *Chem. - Eur. J.* 2018, **24**, 3566−3575.
20. S. Ito, M. Ando, A. Nomura, N. Morita, C. Kabuto, H. Mukai, K. Ohta, J. Kawakami, A. Yoshizawa, A. Tajiri, *J. Org. Chem*. 2005, **70**, 3939 – 3949.
21. S. Laschat, A. Baro, N. Steinke, F. Giesselmann, C. Hägele, G. Scalia, R. Judele, E. Kapatsina, S. Sauer, A. Schreivogel, and M. Tosoni, *Angew. Chem. Int. Ed*. 2007, **46**, 4832–48.
22. J. Sivanarayanan, E. Sebastian, K. Vinod, F. Würthner, and M. Hariharan, *J. Phys. Chem. C* 2022, 126, **31**, 13319–13326.
23. J. Gierschner, L. Lu¨er, B. Milan-Medina, D. Oelkrug and H.-J. Egelhaaf, *J. Phys. Chem. Lett.*, 2013, **4**, 2686–2697.
24. S. K. Lee, Y. Zu, A. Herrmann, Y. Geerts, K. Müllen, A. J. Bard, *J. Am. Chem. Soc.* 1999, **121**, 3513 − 3520.
25. A. Pron, R. R. Reghu, R. Rybakiewicz, H. Cybulski, D. Djurado, J. V. Grazulevicius, M. Zagorska, I. Kulszewicz-Bajer, J. M. Verilhac, *J. Phys. Chem. C* 2011, **115**, 15008 −15017.
26. R. R. Reghu, H. K. Bisoyi, J. V. Grazulevicius, P. Anjukandi, V. Gaidelisc, V. Jankauskas, *J. Mater. Chem.* 2011, **21**, 7811–7819.
27. G. Balaji, T. S. Kale, A. Keerthi, A. M. Della Pelle, S. Thayumanavan, S. Valiyaveettil, *Org. Lett.* 2011, **13**(1), 18–21.
28. L. Zhang, I. Song, J. Ahn, M. Han, M. Linares, M. Surin, H. J. Zhang, J. H. Oh, J. Lin, *Nat. Commun.* 2021, **12**, 142.
29. R. Sato, D. Yoo, T. Mori, *CrystEngComm* 2019, **21**, 3218–3222.
30. P. Yu, Y. Li, H. Zhao, L. Zhu, Y. Wang, W. Xu, Y. Zhen, X. Wang, H. Dong, D. Zhu, W. Hu, *Small* 2021, **17**, 2006574.
31. Y. Su, Y. Li, J. Liu, R. Xing, Y. Han, *Nanoscale* 2015, **7**, 1944–1955.
32. B. Balambiga, R. Dheepika, P. Devibala, *Sci. Rep.* 2020, **10**, 22029.
33. A. Siddiqui, S. Thawarkar, S. P. Singh, *J. Solid State Chem.* 2022, **306**, 122687.
34. L. Rocard, D. Hatych, T. Chartier, T. Cauchy, and P. Hudhomme, *Eur. J. Org. Chem.*, 2019, 7635–7643.

Chapter 5

Highly Soluble *anti*-Perylene-3,4:9,10-bis(benzimidazole)s Stabilizing Room Temperature Columnar Hexagonal Phase With Ambipolar Conductivity

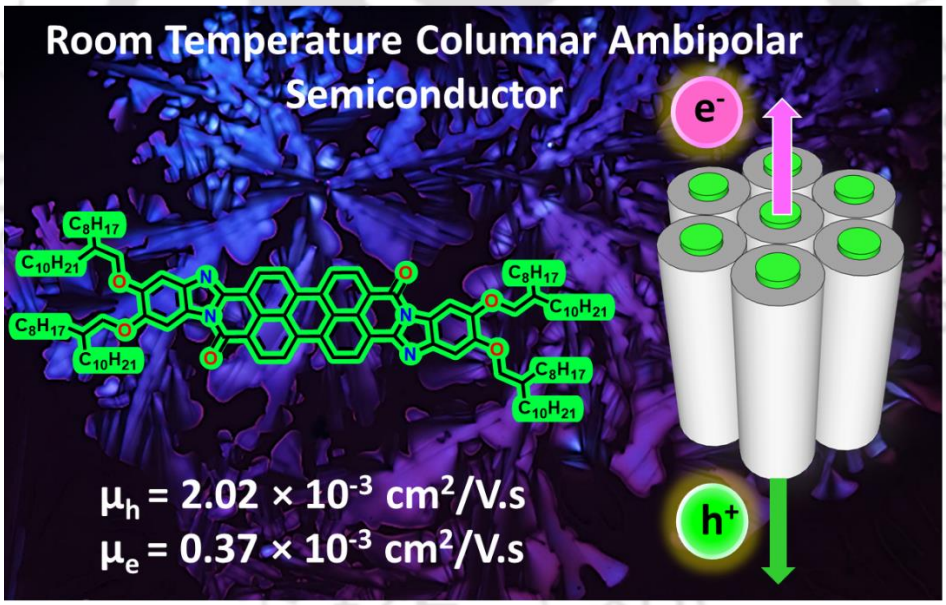

5.1. Introduction

Benzimidazoles prepared from perylene bisanhydride (PBA) and naphthalene dianhydride (NDA) form an important class of organic electronic materials with great potential due to their high photochemical and thermal stability.[1] Perylene bisbenzimidazoles (PBs) have been utilized in the first organic thin film solar cell reported by C.W. Tang as an n-type material. Though it was a major breakthrough with a power conversion efficiency (PCE) of 0.95%, the device fabrication required a vacuum evaporation of the materials.[2] Later, the solar cells based on PB with PCE of around 2.4% were achieved.[3] PBs were used as electron acceptors in three layer solar cells[4] and also served as electron transporters in *p-i-n* solar cells.[5] PBs also shown an electron mobility of 2.4×10^{-6} $cm^2V^{-1}s^{-1}$ as investigated by space charge limited current method.[6] High quality monolayers prepared from PBs showed an excellent n-type mobility of 0.05 $cm^2V^{-1}s^{-1}$.[7]

PBs are low band gap materials that can be prepared easily from commercially available 3,4,9,10-perylenetetracarboxylic bisanhydride (PTCDA) and 1,2-diamine compounds. They are known for a wide absorption band covering the entire UV-Vis to near IR region. PBs usually exist as a mixture of *syn*- and *anti*-isomers and when separated they crystallize in different unit cells, with the *syn*-PB stabilized in a monoclinic structure, while the *anti*-PB stabilized a triclinic structure.[8] From the literature it is evident that, PBs started their journey as promising materials much earlier than their cousins' perylene bisimides (PBIs),[9,10,11] but over the years the interest in PBs has been reduced. This could be ascribed to the following problems namely, difficulty in their solution processability, and structural modification of PB cores as well as the separation of isomers. The two isomers formed have different electronic properties, while no control on their ratio can be achieved during synthesis. Therefore, the material properties depend on the ratio of these isomers, which makes it difficult to achieve reproducibility. Qian *et.al* used trifluoromethylation at *bay*-position to separate three isomers of PBs, however in the process, the planarity of the aromatic core was lost.[12] Unsymmetric derivatives, with benzimidazole unit at one end and imide unit at another end of perylene core stabilizing columnar liquid crystallinity is reported by Thelakkat *et.al*.[13] An unsymmetric donor-acceptor PB was also reported as a nonlinear dielectric material for capacitors,[14] but it was used as a mixture of two isomers. Hudhomme *et.al.* noticed that introducing chlorines at *bay*-position or even the introduction of long alkyl chains on the diamines used for the coupling with PBA did not improve the solubility of PBs in common

organic solvents and the isomers were not separable.[15] Do *et.al*., reported soluble symmetric PBs and asymmetric imide benzimidazoles, where the LUMO levels can be altered by the incorporation of electron donating or withdrawing groups on the imidazole benzene unit.[16] The importance of the understanding required on PBs and the immense possibility of PBs in organic electronics motivated us to design PBs, where their *syn*- and *anti*- isomers can be isolated, can be made soluble, and capable of ordered self-assembly. Further, we envisaged that if such molecules could organize into columns of indefinite length by stacking one above the other, it could lead to the one-dimensional (1D) charge carrier mobility along the columns, and once again make them accessible for the utilization in organic photovoltaics (OPVs) and organic field effect transistors (OFETs).[17,18,19,20]

Herein, the synthesis of perylenetetracarboxylicacid *anti*-Bis(4,5-dialkoxybenzimidazole)s derived from PBA and 3,4-dialkoxy benzene diamines bearing branched alkoxy chains has been described. Branched alkoxy chains were introduced to increase the solubility and reduce the melting point of the compound on transition from crystal to mesophase. Interestingly these compounds exhibited high solubility, and room temperature columnar mesophases and an ambipolar conductivity.

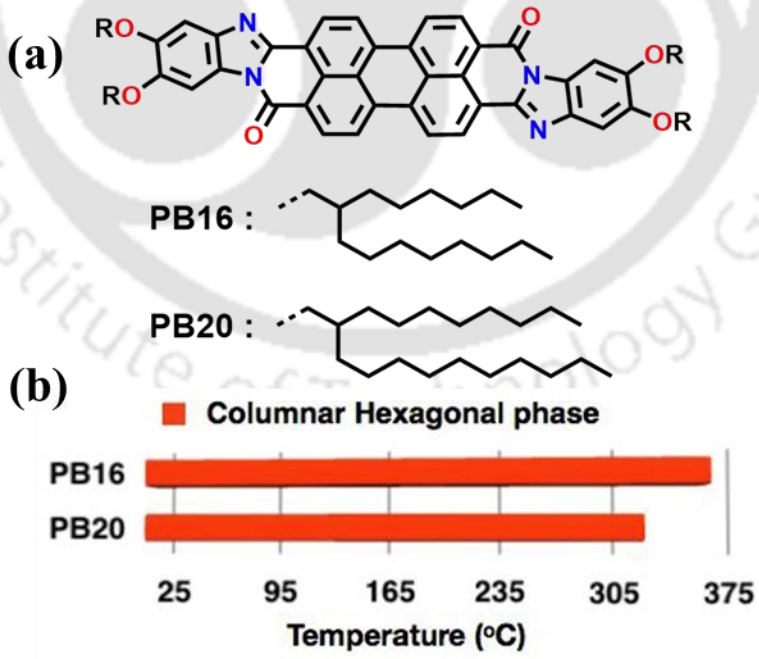

Figure 5.1. Structures of *anti*-perylene bisbenzimidazoles (**PB16** and **PB20**) studied in this work (a); Bargraph representing the mesomorphic behaviors (Considered the second heating of DSC) (b).

5.2. Results and discussion

5.2.1. Synthesis and molecular structural characterization

The synthesis of perylene bisbenzimidazoles (Scheme 5.1) was carried out by the condensation of PBA with 3,4-dialkoxy benzene diamines under microwave conditions in molten imidazole solvent and $Zn(OAc)_2$ as catalyst in good yields (Scheme 5.1). 2-Hexyldecyl and 2-octyl dodecyl flexible chains are utilized to enhance the solubility and to lower the melting as well as clearing temperatures of the resulting PBs. The key intermediate 4,5-dialkoxybenzene-1,2-diamines (**4a-b**) were prepared starting from catechol (Appendix 5.6). Initially, catechol was *O*-alkylated with 7-(bromomethyl)pentadecane or 9-(bromomethyl)nonadecane under Williamson's ether synthesis protocol to get corresponding 1,2-dialkoxybenzenes (**2a-b**). These dialkoxy benzenes were nitrated using nitric acid with sulphuric acid as a catalyst to get the corresponding dinitro derivatives (**3a-b**). Further reduction of these dinitro compounds was carried out using hydrazine hydrate in the presence of Pd/C to get corresponding diamines (**4a-b**).

Scheme 5.1

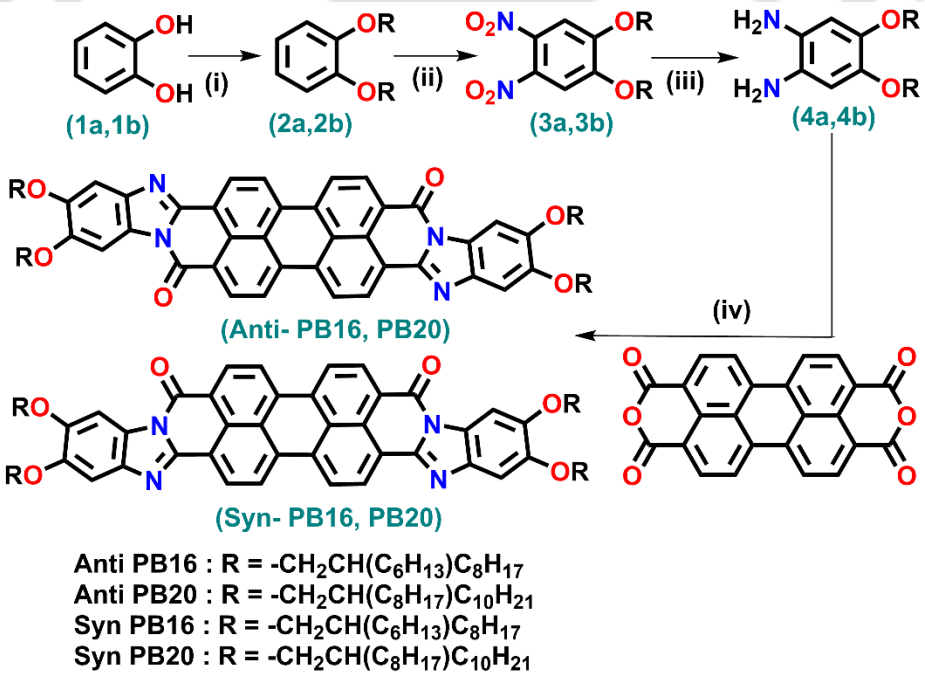

Reagents and conditions (i) 7-(bromomethyl)pentadecane/ 9-(bromomethyl)nonadecane, K_2CO_3, KI, anh. DMF, 90 ^oC, 48 h, (50%, 39%); (ii) H_2SO_4, HNO_3, DCM, 0 ^oC – rt, 24 h, (96%, 95%); (iii) $N_2H_4.H_2O$, Pd/C, CH_3OH, 80 ^oC, 12 h, (81%, 79%); (iv) **4**, imidazole, $Zn(OAc)_2$, MW, 35 W, 35 min., 100 Psi, 165 ^oC, (58%, 53%).

Microwave-assisted condensation of PBA with 3,4-dialkoxy benzene diamines yielded a mixture of *syn*- and *anti*-perylene bisbenzimidazoles, but it was found that the amount of *syn-isomer* was very less and could not be isolated in good amount for the characterization. Solution of *anti*-isomer was found to be blue in color (Fig. 5.3 inset). Column chromatography on neutral alumina was performed using a 50% chloroform-hexane eluent, where a mixture of *syn* and *anti*-isomer was eluted first, finally providing the *anti*-isomer alone at the end due to its higher affinity to stationary phase.

The ^{1}H NMR spectrum of the isolated compound **PB20** which was more polar compared to other fraction has shown very distinct NMR signals (Fig. 5.2b). Expanded region of the NMR from 7-9.5 ppm showed very distinct signals in the aromatic region, those could be ascribed to the *anti*-isomer as discussed in the following. The protons on the aryl ring connected to the imidazole unit H_c and H_c' appeared as a singlet and a partially resolved doublet at down field region in comparison to the protons in the perylene ring, with the H_c appearing at a higher chemical shift. Generally, for perylene bisimides the bay protons don't interact with each other because of the presence of symmetry axes. In the case of *syn*-**PB20**, the point group is C_{2V}. Thus, the symmetric molecular plane (σ_V) bisects the molecule at the bay region (see Fig 5.2a) due to which the bay protons would be in the same chemical environment and (H_b/H_b') and hence only show doublet splitting due to the neighboring *ortho* protons (H_a and H_a') only. However, in case of *anti*-**PB20,** one can observe an inversion center (C_i). In such scenario the *bay* protons (H_b/H_b') will not be identical, as a result of which they will split into a doublet of doublet by the *ortho* and the other *bay* proton, which has appeared as a triplet (as these doublets are close) at the chemical shifts of 8.2-8.3 ppm (each of these triplets correspond to 2H integral). The coupling between the two protons is further corroborated by the rotating-frame nuclear Overhauser effect correlation spectroscopy (2D-ROESY), which showed the interaction between *ortho* (H_a and H_a') and *bay* (H_b and H_b') protons (indicated by green circles, Fig. 5.2d). Two doublet peaks, each of 2H integral, observed at 8.44 and 8.35 ppm are assigned for the four *ortho* protons of perylene (H_a and H_a'). From the 2D-ROESY spectra, we noticed their interaction with their neighboring *bay* protons (H_b and H_b', Fig 5.2c, indicated by orange circle). It is important to note that usually, these molecules exist as an inseparable mixture of *syn*- and *anti*-perylene bisbenzimidazoles in various ratio managed by their positional and rotational disorder.[15,16] However, enhanced solubility with the introduction of the branched peripheral chains, enabled the isolation of *anti*- isomer in a qualitative

amount, though we could not isolate the *syn*-isomer, after repeated attempts to synthesize and separate by column chromatography. The formation of the two isomers typically occurs in the reaction mixture, with their ratios influenced by positional and rotational disorder.[15,16] Furthermore, the reaction conditions also may play a role in determining the isomeric composition. Comparatively, the *anti*-isomer is thermodynamically more favoured over the *syn*-isomer, which may explain its higher abundance in the mixture.

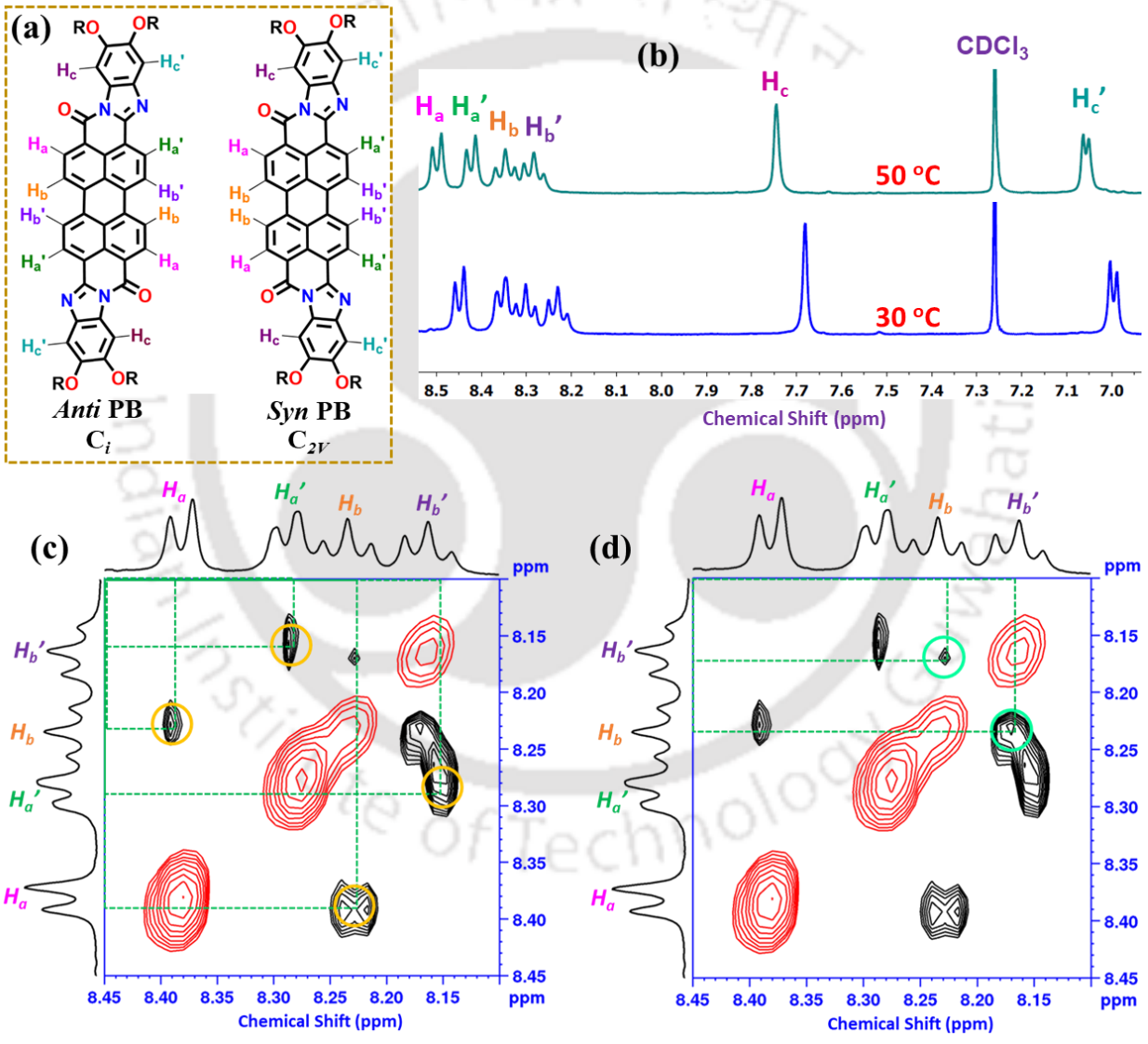

Figure 5.2. Molecular structures of ***syn*** and ***anti*-PB** (a); Overlay of the expanded portion of the ^{1}H NMR spectra of ***anti*-PB20** at 30 °C and 50 °C ($CDCl_3$, 600 MHz) (b); 2D-ROESY spectra of **PB20** showing interactions between *ortho* (H_a and H_a') and *bay* (H_b and H_b') protons (c); and interactions between *bay*-protons (H_b and H_b') (d).

5.2.2. Photophysical and Electrochemical properties

The UV visible spectra of these compounds, for example of *anti*-**PB20**, showed a broad absorption band with two absorption maxima centered at 515 nm and 650 nm (Fig. 5.3a, Fig. A17b). In comparison to PBIs, the expanded perylene bisbenzimidazole core shows strong bathochromically shifted absorption spectra covering the whole visible spectrum (400-800 nm). At 650 nm the molar extinction coefficient ε was found to be 7.3×10^4 L mol^{-1} cm^{-1}. This feature, almost an increase of 300 nm in comparison to PBIs is very important from the viewpoint of harvesting the light in visible region for organic solar cells. The increase in the concentration led to an increase in the intensities of absorption maximum in line with the Lambert-Beer's law. These compounds were not very fluorescent due to the intramolecular charge transfer that occurs due to the oxygen atoms in the peripheral alkoxy chains.

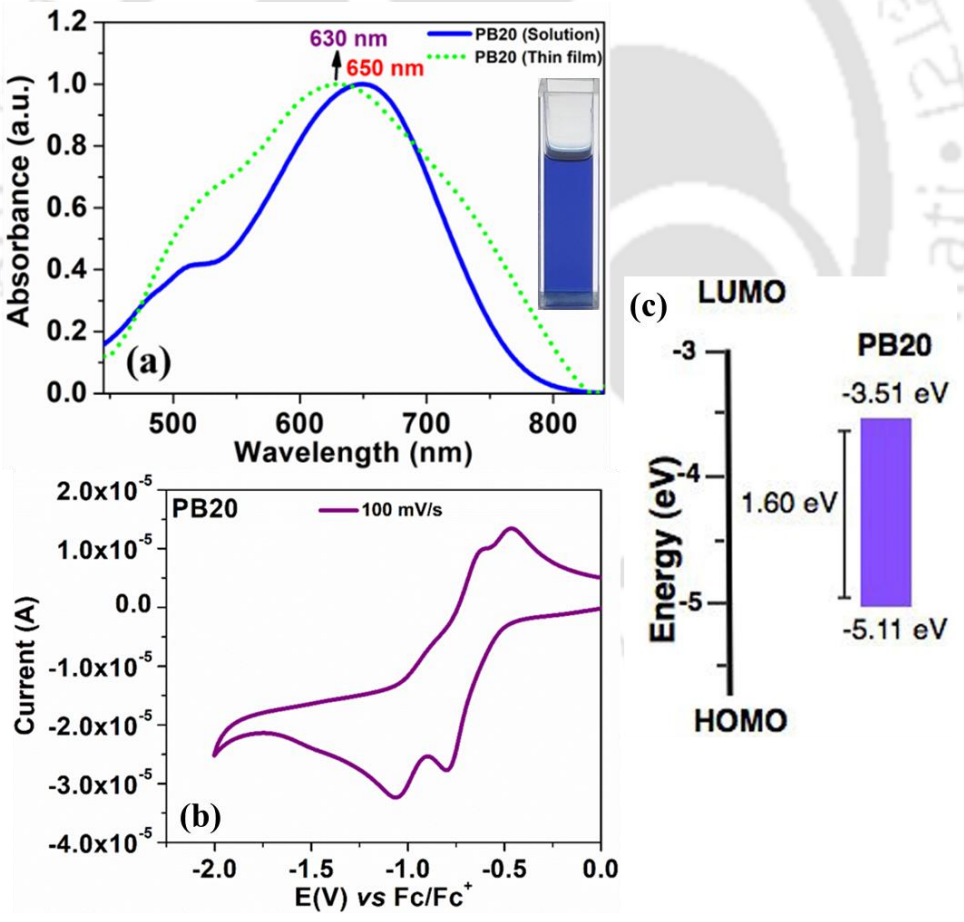

Figure 5.3. UV-Vis spectrum of *anti*-**PB20** in micromolar chloroform solution (solid line) and in thin film state (dotted line) (a) (Inset shows the image of the solution of *anti*-isomer in chloroform under daylight); Cyclic voltammogram of *anti*-**PB20** in micromolar dichloromethane solution (b); Energy level diagram for compound *anti*-**PB20** (c).

The thin film formed by the spin coating of the sample showed a blue shifted absorption maximum (λ_{max} = 630 nm) (Fig. 5.3a), which supports the formation of H-type or 'head to head' aggregates.[21] The estimation of FMOs and the reversibility of reduction-oxidation process was investigated with the help of cyclic voltammetry (CV). Compound **PB20** showed two quasi reversible reduction peaks, however oxidation peaks were not observed in the measurement window of upto +1 V *vs.* $Ag/AgNO_3$ (Fig. 5.3b, Table A2). From the first reduction potential (-0.79 V) LUMO level was estimated (-3.51 eV), while the HOMO level (-5.11 eV) was calculated from the optical bandgap derived from the red edge of the absorption spectrum (1.60 eV at 775 nm) measured in micromolar solution of **PB20** (Fig. 5.3c). In comparison to PBI derived from 3,4,5-tridodecyloxyaniline, **PB20** exhibited elevated LUMO and HOMO level and with a lower bandgap (Fig. 5.3).[27a] The extension of conjugation due to the fused benzimidazole units led to this elevation of LUMO and HOMO levels and a decrease in the bandgap. This is highly desirable from the view point of organic solar cells, where reducing the energy loss during the charge transfer from donor molecules to acceptor molecules (**PB20**) may contribute towards the enhanced open circuit voltages.

Density functional theory (DFT) calculations also suggested that the experimental values are in line with the predicted values, where the HOMO and LUMO were spread over all the aromatic rings (Fig. A26 and Table A2). Calculated molecular electrostatic potential surfaces of perylene *anti*-bis(4,5-dialkoxybenzimidazole) shows that the central perylene ring remains electron deficient, while the heteroatoms and imidazole rings show the concentration of electron density (Fig. A27). The compound **PB20** exhibited a very good film forming ability as seen in the scanning electron microscopy (SEM) image, which is very vital for the fabrication of organic electronic devices (Fig. A28).

5.2.3. Thermal behavior

PB16 and **PB20**, showed a thermal decomposition temperature of around 360 ^{o}C for the 5 weight % decomposition as evidenced from thermogravimetric analyses (TGA) (Fig. A23). The mesomorphic behaviour of the compounds were investigated with the help of polarising optical microscopy (POM) associated with a programmable hot stage, differential scanning calorimetry (DSC) and temperature dependant powder X-ray diffraction (XRD) studies. Compounds **PB16** and **PB20** were gummy and sticky mass, that can be sheared under mechanical stress and also

exhibited birefringence under microscope, which indicated the occurrence of mesophase at room temperature.

Both the compounds exhibited single transition in the DSC, *i.e*. from mesophase to isotropic liquid state. From the DSC scan of **PB16** it is seen that the compound shows mesophase to isotropic state at 354.8 ^{o}C (ΔH = 0.12 kJ/mol), which was also confirmed by POM studies (Fig. A22a). POM images displayed dendritic texture as well as mosaic texture with rectilinear defects; both are seen in the case of Col_h phase (Fig. 5.4a, and Fig. A19). From the XRD studies, it was confirmed that the mesophase was a columnar phase with hexagonal symmetry (Col_h phase). The high temperature XRD profiles (at 260 ^{o}C, 200 ^{o}C, and 100 ^{o}C) exhibited a single sharp reflection in the low angle region along with the two diffused peaks in the wide angle (Fig. A24a-c). The first diffused peak in the wide angle arises from the packing of alkyl chains, while the second is due to the packing of hard polyaromatic cores. Though the occurrence of a single reflection at low angles do not provide unambiguous structural confirmation; however, as often seen in the literature, corroborated by textural similarity,[22] such a pattern is assigned to the Col_h phase and this has been attributed to a minimum in the form factor (Fig. A24, Table A4). The XRD pattern obtained at RT showed additional peak at mid angle region, which can be indexed to hexagonal lattice along with the peak in low angle region (Fig. 5.4b). Further one more relatively sharp reflection corresponding to intracolumnar distance was also witnessed along with the diffused peak corresponding to the alkyl chain packing noticed at wide angle region. Such strong core-core correlation probably due to the increased π-π overlap, and the hetero atom integration in the core.

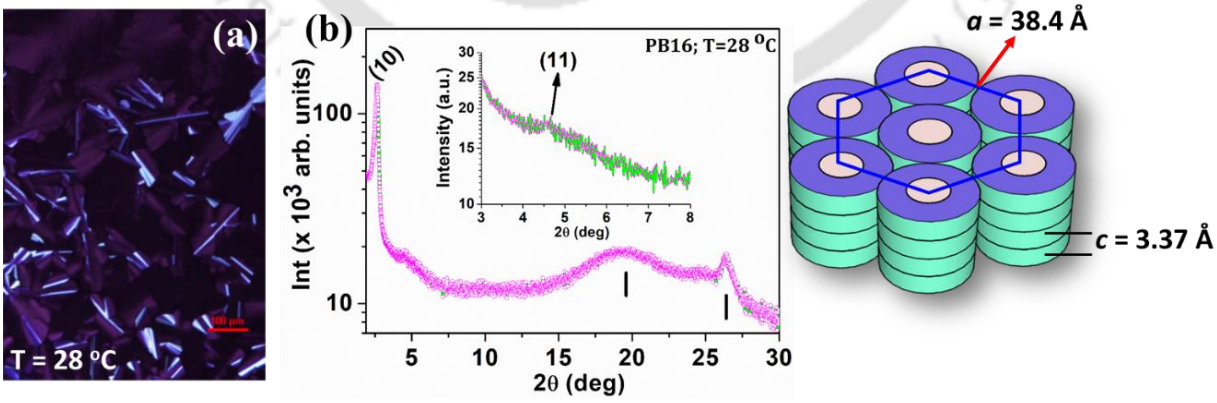

Figure 5.4. POM image of the Col_h phase exhibited by **PB16** at 28 ^{o}C (a) XRD profile depicting the intensity against 2θ obtained for the Col_h phase of compound **PB16** at 28 ^{o}C (b); (Schematic of the Col_h phases are given in the right hand side of XRD profile).

Compound **PB20** with longer chains also exhibited monomesomorphic behaviour and discussed in detail as below. **PB20** due to its increased flexibility owing to the longer branched alkoxy chains exhibited lower isotropic temperature (318 °C, ΔH = 0.5 kJ/mol, Fig. A22b), while cooling the isotropic liquid at a rate of 5 °C/min led to the growth of a birefringent leaf like pattern interspersed with dark background originating from the homeotropic orientation of the columnar phase (Fig. A20 and Fig. A21, Fig. 5.5a). Further cooling did not change the pattern, which was also confirmed by the DSC with no signatures of any phase transition (Fig. A22b).

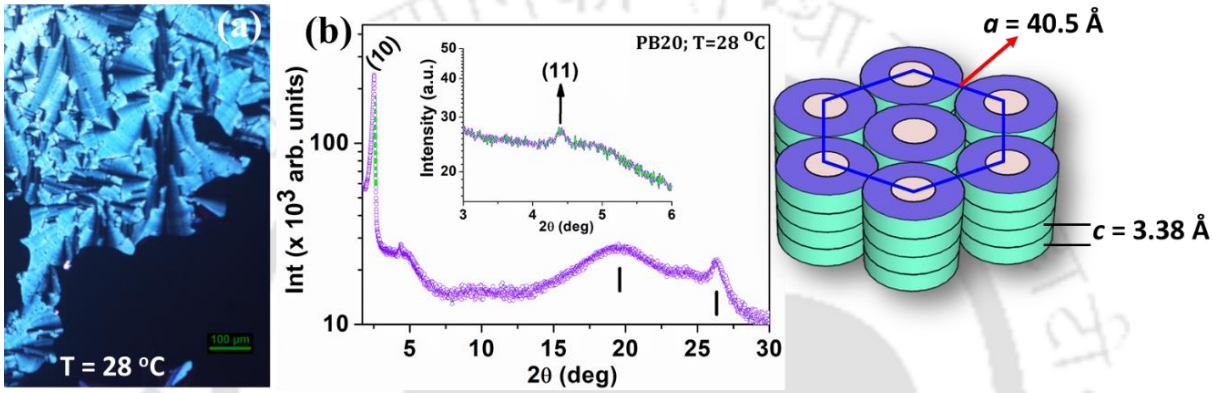

Figure 5.5. POM image of the Col_h phase exhibited by **PB20** at 28 °C (a); XRD profile depicting the intensity against 2θ obtained for the Col_h phase of compound **PB20** at 28 °C (b); (Schematic of the Col_h phase is given in the right hand side of XRD profile).

To understand the mesophase structures, XRD was carried out at different temperatures, for example, 260, 200, 100, and 28 °C. The plot of intensity *vs* 2θ values obtained from the XRD data obtained at 260 and 200 °C exhibited two peaks in the low-mid angle region along with the two diffused peaks in the wide-angle region. As explained earlier these peaks are corresponding to the packing of alkyl chains and the intracolumnar distance. In the case of XRD patterns obtained at 100 °C and 28 °C, one more reflection was observed in the mid-angle region. XRD profile depicting the intensity against 2θ obtained at 28 °C for example, showed the presence of a strong peak at a *d*-spacing of 35.03 Å followed by a weak peak with *d*-spacings of 20.06. Further, the wide-angle region showed the presence of two diffused peaks centered at 4.52 Å and 3.38 Å, which are corresponding to the packing of flexible chains and the packing of cores within the column. The reciprocal ratio of the *d*-spacings in the small and middle angle region was found to be 1: √3, which can be indexed to the Miller indices 10 and 11 of a hexagonal lattice. This confirms the mesophase to be a Col_h phase (Fig. 5.5b and Table A4). The hexagonal lattice constant '*a*' was found to be 40.5 Å, from which the lattice area and unit cell volume were calculated to be 1417.7

Å^2 and 4791.7 Å^3 respectively. Considering the intracolumnar distance or height of the unit hexagonal cell (h_c = 3.38 Å), the number of the molecules 'Z' in the unit cell was calculated and found to be approximately 2, where two **PB20** molecules can be arranged side by side to form a disc (see chapter 2). In comparison to the value of '*a*' at 260 ^{o}C, the value of '*a*' observed at 28 ^{o}C has increased approximately by 5%, with a concomitant decrease in the intracolumnar distance to 3.38 Å from 3.54 Å, which could be due to the stretching of alkyl chains at lowered temperatures.

5.3. Charge Carrier Mobility Studies

A good charge carrier mobility is one of the fundamental requirements of any organic electronic device to perform. With the potential for optoelectronic devices, charge carrier mobility of **PB20** was assessed for both holes as well as electrons using the space charge limited current technique (SCLC) in thin films. In this technique, a thin film of the material is sandwiched between two electrodes for current-voltage measurements. Depending on the work function alignment of the electrodes with HOMO/LUMO of the material, hole only and electron only devices can be fabricated. The benefits of having either hole only or electron only devices is, it ensures that measured mobility is mainly contributed by the hole and electrons in hole only and electron only devices respectively. However, having an ohmic contact for the charge injecting electrode (for holes, HOMO and for electrons, LUMO of the material) is a must have requirement for SCLC measurements.

In SCLC, at low applied voltage current varies linearly with applied voltage, mainly due to the dominance of the intrinsic charge carriers of the material whereas, at higher applied voltage due to the injection of charge carriers, a space charge builds up and current dependence does not follow linearly with the applied voltage and now becomes proportional to the square of the applied voltage. Considering material to be trap free, mobility of charge carriers can be extracted using Mott-Gurney equation given by equation1.[28]

$$J = \frac{9}{8}\varepsilon_0\varepsilon_r\mu\frac{V^2}{d^3} \qquad (1)$$

where J is the measured current density, ε_0 is the permittivity of free space (8.86×10^{-14} Fcm^{-1}), ε_r is the relative dielectric constant of the material (~ 4.65), V is the voltage applied, d is the thickness of the sample, and μ is the mobility.

When shallow traps are present in material then higher order dependence of voltage is observed and modelling of data can be done by using modified Mott-Gurney equation (2), where field dependent charge carrier mobility correction is mainly used for calculation of mobility, given by equation 2. [27]

$$J = \frac{9}{8}\varepsilon_r\varepsilon_0\mu\frac{V^2}{d^3}\exp\left(0.891\gamma\sqrt{\frac{V}{d}}\right) \qquad (2)$$

where γ is the fitting parameter representing the strength of the field dependence of mobility.

In this work, for hole mobility extraction of the reported *anti*-**PB20** compound, a combination of PEDOT: PSS (φ~ 5.0 - 5.1 eV) and MoO_3/Ag electrodes is used to fabricate hole only devices which ensure a good match with the HOMO (φ ~ -5.11 eV) value of **PB20** for effective hole injection. A thin layer of MoO_3 is known to increase the work function of metal by creating interfacial dipoles and is being used widely in creating hole only devices in organic electronics [23,24] was chosen as the injecting electrode to ensure efficient injection of holes (Fig. 5.6b). On contrary, for electron mobility measurements, three electron-only device configurations were fabricated using ZnO (φ ~ -3.8 - 4.10 eV), Al (φ~ 4.26 eV) and SnO_2 (φ ~ 3.70 - 4.10 eV), as injecting electrodes in order to achieve ohmic/near ohmic contact with the LUMO (φ ~ -3.51 eV) of **PB20** and Al as counter electrode (Fig. 5.6c). The semi log current–voltage characteristics obtained for *anti*-**PB20** in hole-only and electron only device is shown in which was used to perform fitting using equation 2 to extract hole and electron mobility (Fig. 5.6a). Table 5.1 summarises the average values of at least 5 best devices in extracting electron and hole mobility for *anti*-**PB20** compound.

Table 5.1. Hole and Electron mobility values of *anti*-**PB20**.

Entry	**Hole mobility (μ_h) × 10^{-3} ($cm^2V^{-1}.s^{-1}$)**	**Electron mobility (μ_e) × 10^{-3} ($cm^2V^{-1}.s^{-1}$)**	**μ_e/ μ_h**
***Anti*-PB20**	2.02 ± 0.81	0.37 ± 0.24	0.18

The electron mobility observed for the *anti*-**PB20** found to be several orders of magnitude higher than that observed for the mixture of *anti*- and *syn*-PBs[6] as well as the perylene diester benzimidazole side chain polymer.[25] However, the ambipolar nature of perylene bisbenzimidazole derivative with a well-balanced hole and electron mobility is reported for the first time here. As shown in the 3D molecular electrostatic potential contour map of optimized structure of PBs

(Fig.A27), it can be seen that the electron rich and electron poor regions are localized peripheral benzimidazole rings and central perylene core, which in turn act as the pathway for electrons and holes when the molecules stack one above the other to form columnar phases (Fig. 5.6d).

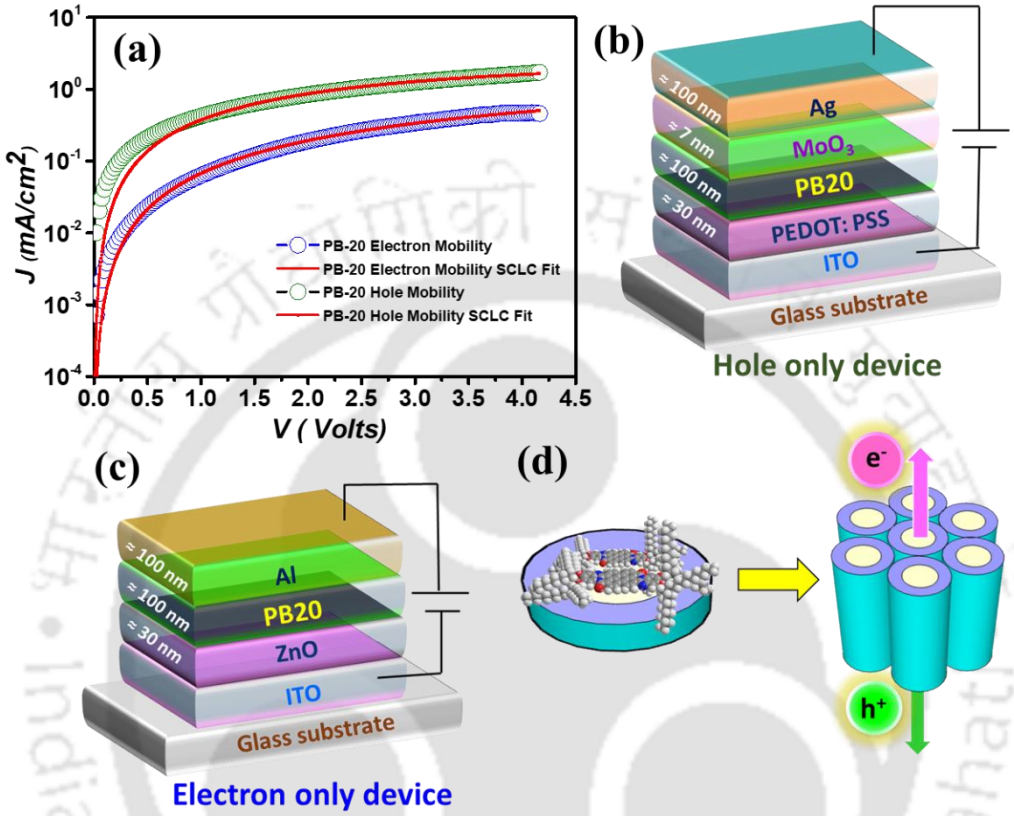

Figure 5.6. *J-V* curves of hole (Black) only and electron (Blue) only devices for *anti*-**PB20** along with SCLC fitting (a); schematic diagrams for hole only (b) and electron only (c) devices; Schematic showing the self-assembly of two **PB20** molecules to form a disc which self-organize to form a Col_h phase that acts as a molecular wire for the conduction of electrons and holes (d).

5.4. Conclusion

In conclusion *anti*-perylene-3,4:9,10-bis(benzimidazole) derivatives were successfully isolated and characterized after their synthesis starting from commercially available PBA. It was found that among the possible *syn*- and *anti*- isomers, only the *anti*-isomer was isolated and the *syn*- isomer was produced in a very less amount. The present set of compounds are unique as earlier reported perylene bis(benzimidazoles) were less soluble in common organic solvents, resulting in a coexistence of *syn* and *anti*-isomers. These compounds exhibited room temperature columnar hexagonal phase over a wide thermal range. Interestingly, these compounds exhibited a wide absorption band covering whole visible spectrum range (400-800 nm) along with high

extinction coefficient, which is due to the further expansion of the perylene core by benzimidazole rings. The hetero-atom incorporation and expanded aromatic skeleton led to an enhanced core-core interaction, that was corroborated with the high clearing temperatures and observation of core-core peak in the XRD studies. This also resulted in the elevated LUMO as well as HOMO levels and the bandgap reduction making them promising from the perspective of organic solar cells. These compounds, due to the presence of branched flexible chains exhibited high solution processability and stabilized the room temperature columnar hexagonal phase over a wide thermal range. In addition, this nitrogen enriched polyaromatic heterocyclic core forms a unique promising class of ambipolar organic semiconductors capable of self-organizing with a balanced hole and electron mobility.

5.5 Experimental section

In this section the detailed synthesis procedure and the molecular structural characterization data have been presented for the intermediates and target compounds mentioned in the scheme.

Procedure for the synthesis of 1,2-bis((2-hexyldecyl)oxy)benzene (2a) /1,2-bis((2-octyldodecyl)oxy)benzene (2b): [29,30]

A mixture of 1,2-dihydroxy benzene (**1**) (2 g, 18.16 mmol, 1 eq), anhydrous K_2CO_3 (11.04 g, 79.91 mmol, 4.4 eq), KI (0.26 g, 1.81 mmol, 0.1 eq) were dissolved in anhydrous *N*,*N*-dimethylformamide (40 mL) and stirred for 40 min at 50 ^oC. After that 7-(bromomethyl)pentadecane (11.64 g, 38.14 mmol, 2.1 eq) / 9-(bromomethyl)nonadecane (13.78 g, 38.14 mmol, 2.1 eq.) was added dropwise to it. The resultant reaction mixture was heated at 90 °C for 48 h. After completion, the reaction mixture was cooled to room temperature and filtered on a celite bed. Then the celite bed was washed with ethyl acetate (3 × 50 mL). The combined filtrates were washed with water three times (3 × 50 mL) followed by brine and dried over anhydrous Na_2SO_4 and the solvent was evaporated via rotary evaporation. The crude product was purified by column chromatography using hexane and ethyl acetate as eluent to obtain colourless liquid (hexane : ethyl acetate = 30 : 1).

2a: R_f = 0.5 (10% EtOAc-Hexane); Colourless liquid, yield: 50 % (5.28 g); IR ν_{max} in cm^{-1}: 2922, 2853, 1592, 1502, 1464, 1378, 1252, 1221, 1119, 1027, 771, 736; ^1H NMR (400 MHz, $CDCl_3$, ppm): δ 6.87 (s, 4H), 3.85 (d, *J* = 4 Hz, 4H), 1.81 (m, 2H), 1.55-1.27 (m, 48H), 0.88 (t, *J* = 8 Hz, 12H). ^{13}C NMR (100 MHz, $CDCl_3$, ppm): δ 149.63, 120.82, 113.85, 71.88, 38.22, 31.99, 31.98, 31.39, 29.73, 29.45, 22.77, 22.75, 14.17. MALDI-TOF exact mass calculated for $C_{38}H_{70}O_2Na$ $(M+Na)^+$: 581.5274, found : 581.218.

2b: R_f = 0.5 (10% EtOAc-Hexane); Colourless liquid, yield: 39 % (4.91 g); IR ν_{max} in cm^{-1}: 2922, 2853, 1592, 1501, 1464, 1379, 1252, 1222, 1119, 1029, 771, 733; ^1H NMR (400 MHz, $CDCl_3$,

ppm): δ 6.90 (s, 4H), 3.89 (d, *J* = 8 Hz, 4H), 1.85-1.81 (m, 2H), 1.54-1.30 (m, 64H), 0.92 (t, *J* = 4 Hz/8Hz, 12H). ^{13}C NMR (100 MHz, $CDCl_3$, ppm): δ 149.71, 120.85, 113.98, 71.97, 38.28, 31.99, 31.44, 30.18, 29.74, 29.73, 29.45, 29.44, 26.98, 22.74, 14.14. MALDI-TOF exact mass calculated for $C_{46}H_{86}O_2Na(M+Na)^+$: 693.6526, found : 694.572.

Procedure for the synthesis of 1,2-dinitro-4,5-bis((2-hexyldecyl)oxy)benzene (3a) / 1,2-dinitro-4,5-bis((2-octyldodecyl)oxy)benzene (3b):[28]

In a round bottom flask, compound (1,2-bis((2-hexyldecyl)oxy)benzene (**2a**) / 1,2-bis((2-octyldodecyl)oxy)benzene (**2b**)) (4 g, 7.16 mmol/ 5.95 mmol, 1 eq.) was dissolved in CH_2Cl_2 stirred at 0 ^oC for 30 mins. To this well stirred solution, 70% HNO_3 (4.7 mL/ 3.6 mL, 78.3 mmol/ 59.5 mmol, 10 eq.) followed by conc. H_2SO_4 (2.08 mL/ 1.59 mL, 39.1 mmol/ 29.7 mmol, 5 eq,) was added slowly dropwise manner. This mixture was stirred at room temperature for 24 h. Then it was poured into water and the aqueous layer was extracted with CH_2Cl_2. The organic layer was washed with H_2O, brine and dried over Na_2SO_4, then it was evaporated to dryness. The crude product was purified by column chromatography on silica gel (60-120 mesh) using hexane and CH_2Cl_2 as eluent to obtain slightly yellowish liquid (hexane: CH_2Cl_2 = 20: 1).

3a: R_f = 0.6 (10% EtOAc-Hexane); Yellow liquid, yield: 95% (5.11 g); IR ν_{max} in cm^{-1}: 2923, 2854, 1589, 1534, 1463, 1335, 1282, 1225, 1041, 864, 813, 753, 721; ^{1}H NMR (400 MHz, $CDCl_3$, ppm): δ 7.28 (s, 2H), 3.96 (d, *J* = 4 Hz, 4H), 1.85 (m, 2H), 1.46-1.27 (m, 48H), 0.87 (t, *J* = 4 Hz, 12H). ^{13}C NMR (100 MHz, $CDCl_3$, ppm): δ 152.07, 136.39, 107.46, 72.54, 37.83, 31.93, 31.85, 31.21, 30.02, 29.68, 29.62, 29.38, 26.81, 22.71, 14.13. MALDI-TOF exact mass calculated for $C_{38}H_{68}N_2O_6K(M+K)^+$: 687.4714, found : 687.65.
3b: R_f = 0.6 (10% EtOAc-Hexane); Yellow liquid, yield: 96% (4.56 g); IR ν_{max} in cm^{-1}: 2922, 2853, 1589, 1535, 1463, 1335, 1282, 1225, 1042, 864, 813, 771, 753, 720; ^{1}H NMR (400 MHz, $CDCl_3$, ppm): δ 7.28 (s, 2H), 3.96 (d, *J* = 4 Hz, 4H), 1.88-1.82 (m, 2H), 1.44-1.26 (m, 64H), 0.88 (t, *J* = 4 Hz /8 Hz, 12H). ^{13}C NMR (100 MHz, $CDCl_3$, ppm): δ 152.10, 136.42, 107.51, 72.59, 37.85, 31.94, 31.93, 31.22, 30.02, 29.38, 26.85, 22.70, 14.12. MALDI-TOF exact mass calculated for $C_{46}H_{84}N_2O_6K(M+K)^+$: 799.5966, found : 800.84.

Procedure for the synthesis of 4,5-bis((2-hexyldecyl)oxy)benzene-1,2-diamine (4a) / 4,5-bis((2-octyldodecyl)oxy)benzene-1,2-diamine (4b): [28]

To a suspension of nitro compound (**3a/3b)** (4g, 6.16 mmol/5.25 mmol, 1 eq.) and 10% Pd-C (10% weight of the nitro compound) in absolute ethanol, hydrazine monohydrate (13.98 mL/7.56 mL, 246 mmol/210 mmol, 40 eq.) was added and refluxed under N_2 atmosphere for 24 h. The reaction mixture was cooled to room temperature and CH_2Cl_2 was added and filtered through a celite bed. The filtrate was extracted with CH_2Cl_2 (3 × 50 mL). The combined extracts were washed with water, brine and dried over anhydrous Na_2SO_4 and the solvent was concentrated

via rotary evaporation and cooled methanol was added to get precipitate, then filtered to get the product.

4a: R_f = 0.2 (10% EtOAc-Hexane); Colourless liquid, yield: 78% (2.83 g); ^{1}H NMR (400 MHz, $CDCl_3$, ppm): δ 6.36 (s, 2H), 3.76 (d, *J* = 8 Hz, 4H), 2.49 (bs, 2 × -NH_2, 4H), 1.77-1.72 (m, 2H), 1.45-1.26 (m, 48H), 0.88 (t, *J* = 4 Hz/8 Hz, 12H). ^{13}C NMR (100 MHz, $CDCl_3$, ppm): δ 143.99, 128.40, 106.92, 73.73, 38.60, 32.16, 31.56, 30.37, 30.02, 29.91, 29.62, 22.93, 22.92, 14.34. MALDI-TOF exact mass calculated for $C_{38}H_{73}N_2O_2$ $(M+H)^+$: 589.5672, found : 589.90.
4b: R_f = 0.2 (10% EtOAc-Hexane); Colourless liquid, yield: 76% (2.79 g); ^{1}H NMR (400 MHz, $CDCl_3$, ppm): δ 6.35 (s, 2H), 3.74 (d, *J* = 4 Hz, 4H), 3.08(bs, 2 × -NH_2, 4H), 1.75-1.71 (m, 2H), 1.31-1.25 (m, 64H), 0.87 (t, *J* = 4 Hz, 12H). ^{13}C NMR (100 MHz, $CDCl_3$, ppm): δ 143.76, 128.19, 106.72, 73.52, 38.39, 31.94, 31.35, 30.15, 29.75, 29.73, 29.69, 29.38, 26.92, 22.69, 14.10. MALDI-TOF exact mass calculated for $C_{46}H_{89}N_2O_2$ $(M+H)^+$: 701.6924, found : 701.69.

Procedure for the synthesis of PB16 / PB20: [31]

PTCDA (1 eq.), 4,5-bis((2-hexyldecyl)oxy)benzene-1,2-diamine (**4a**) / 4,5-bis((2-octyldodecyl)oxy)benzene-1,2-diamine (**4b**) (2.2 eq.), zinc acetate (2 eq.) and imidazole (1 g) were taken in a microwave vessel, flushed with nitrogen and put in microwave reactor. The mixture was heated at 165 ^{o}C for 35 minutes at 35 W and 100 psi pressure. After cooling, reaction mixture was poured in 2(N) HCl (10 mL) and extracted with chloroform. Organic mixture was washed with water and saturated sodium chloride solution. The crude compound was purified by neutral alumina column chromatography using 50% chloroform-hexane system. Further purification was done by recrystallization from chloroform-methanol system.

PB16: R_f = 0.5 (10% $CHCl_3$-Hexane); Dark blue solid, yield: 81% (0.31 mg); IR ν_{max} in cm^{-1}: 2921, 2852, 1688, 1591, 1541, 1483, 1452, 1372, 1331, 1286, 1214, 1162, 1111, 1018, 987, 925, 882, 837, 803, 774, 742, 720; ^{1}H NMR (400 MHz, $CDCl_3$, ppm): δ 8.58 (d, *J* = 8 Hz, 2H), 8.51 (d, *J* = 8 Hz, 2H), 8.44 (t, *J* = 8 Hz, 2H), 8.38 (t, *J* = 8 Hz, 2H), 7.78 (s, 2H), 7.10 (d, *J* = 4 Hz, 2H), 3.92 (m, 4H), 3.83 (m, 4H), 1.87 (m, 4H), 1.31-1.25 (m, 96H), 0.89 (m, 24H). ^{13}C NMR (100 MHz, $CDCl_3$, ppm): δ 159.22, 149.53, 149.18, 146.24, 137.52, 135.36, 134.74, 131.34, 130.80, 127.16, 125.95, 125.46, 123.53, 122.71, 121.73, 120.87, 102.85, 99.11, 72.31, 38.25, 38.06, 32.23, 31.39, 30.48, 30.13, 30.02, 29.91, 29.73, 29.58, 27.13, 27.02, 23.04, 22.97, 14.38.

MALDI-TOF exact mass calculated for $C_{100}H_{145}N_4O_6$ $(M+H)^+$: 1498.1164, found : 1498.85.

PB20: R_f = 0.5 (10% $CHCl_3$-Hexane); Dark blue solid, yield: 79% (0.34 mg); IR ν_{max} in cm^{-1}: 2921, 2852, 1687, 1591, 1540, 1483, 1452, 1372, 1331, 1286, 1214, 1161, 1111, 1021, 987, 924, 882, 837, 803, 773, 743, 720; ^{1}H NMR (400 MHz, $CDCl_3$, ppm): δ 8.46 (d, *J* = 8 Hz, 2H), 8.37 (d, *J* = 8 Hz, 2H), 8.30 (t, *J* = 8 Hz, 2H), 8.23 (t, *J* = 8 Hz, 2H), 7.68 (s, 2H), 7.00 (d, *J* = 4 Hz, 2H), 3.88 (m, 4H), 3.77 (m, 4H), 1.85 (m, 4H), 1.44-1.26 (m, 128H), 0.89 (m, 24H). ^{13}C NMR (100 MHz, $CDCl_3$, ppm): δ 158.71, 149.32, 148.88, 145.77, 137.27, 134.77, 134.12, 130.77, 130.23,

126.69, 125.38, 125.15, 123.11, 122.32, 121.34, 120.48, 102.66, 98.87, 72.14, 38.06, 37.84, 32.06, 32.02, 31.15, 31.07, 30.32, 29.96, 29.93, 29.86, 29.84, 29.59, 29.56, 29.52, 26.96, 26.87, 22.78, 22.75, 14.14.

MALDI-TOF exact mass calculated for $C_{116}H_{177}N_4O_6$ $(M+H)^+$: 1722.3668, found : 1722.01.

5.6. Appendix

5.6.1. NMR Spectra

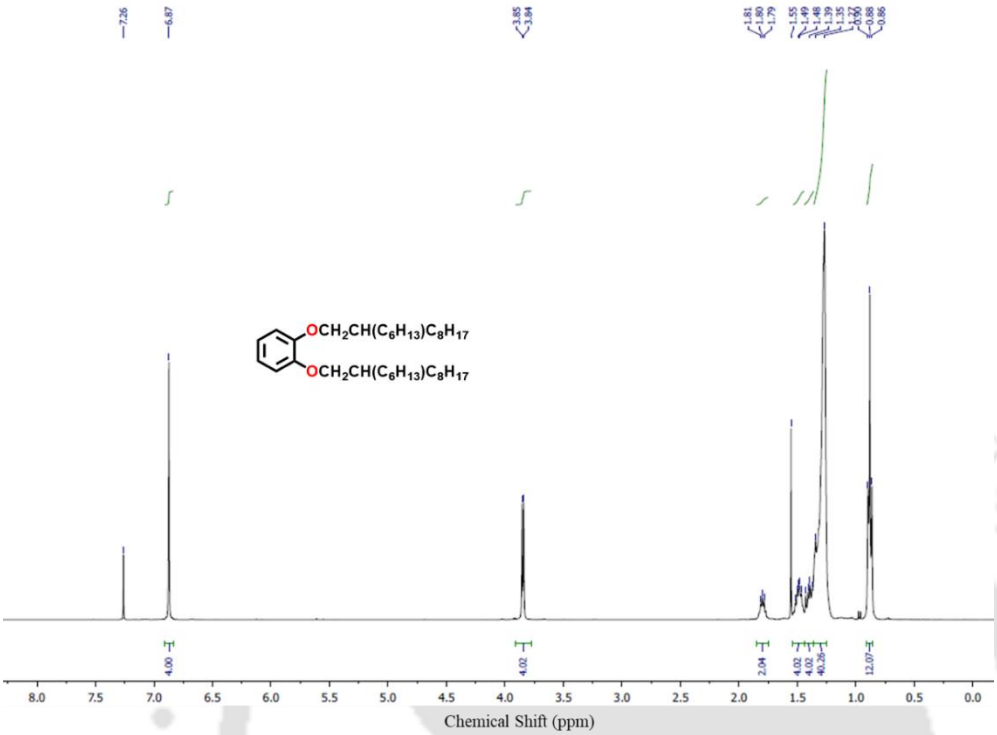

Figure A1. ^{1}H NMR (400 MHz) spectra of 1,2-bis((2-hexyldecyl)oxy)benzene **(2a)** in $CDCl_3$.

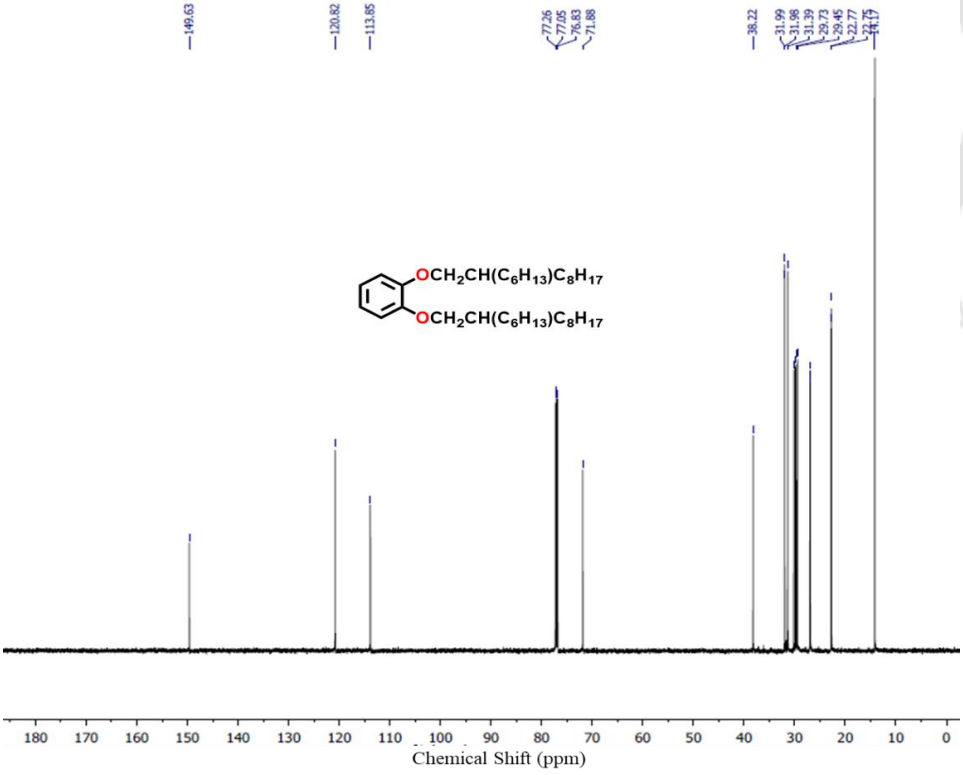

Figure A2. ^{13}C NMR (100 MHz) spectra of 1,2-bis((2-hexyldecyl)oxy)benzene **(2a)** in $CDCl_3$.

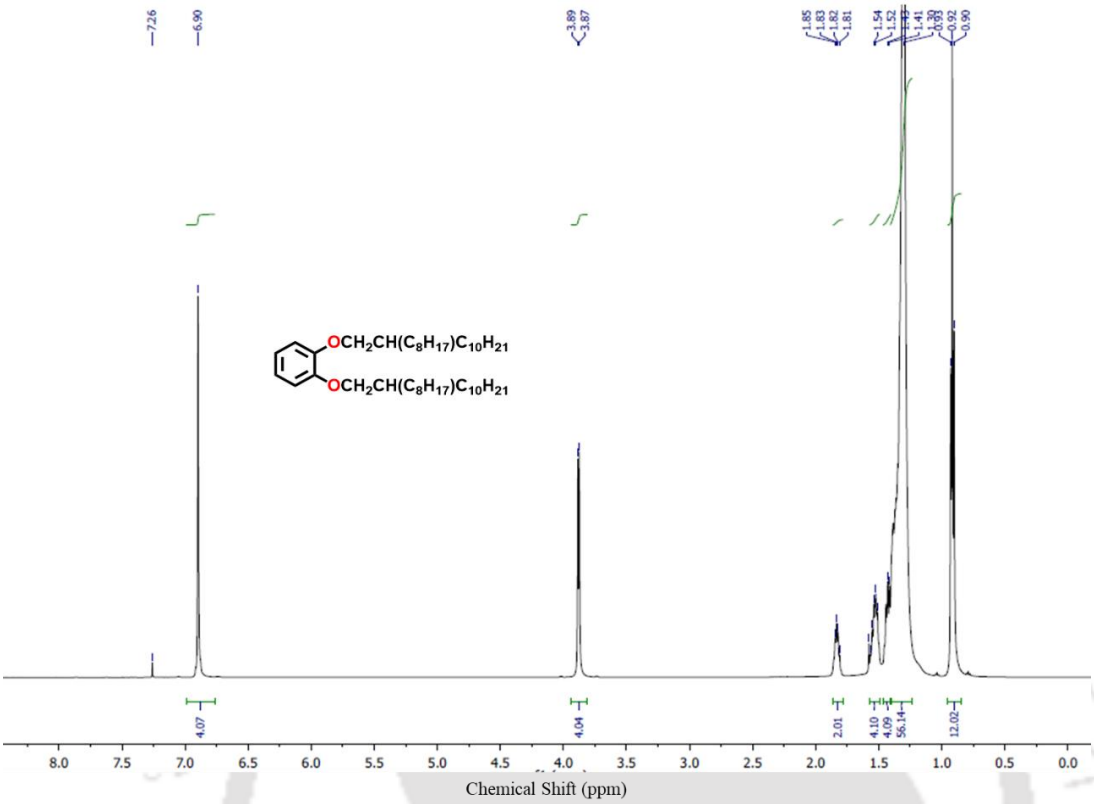

Figure A3. ^{1}H NMR (400 MHz) spectra of 1,2-bis((2-octyldodecyl)oxy)benzene **(2b)** in $CDCl_3$.

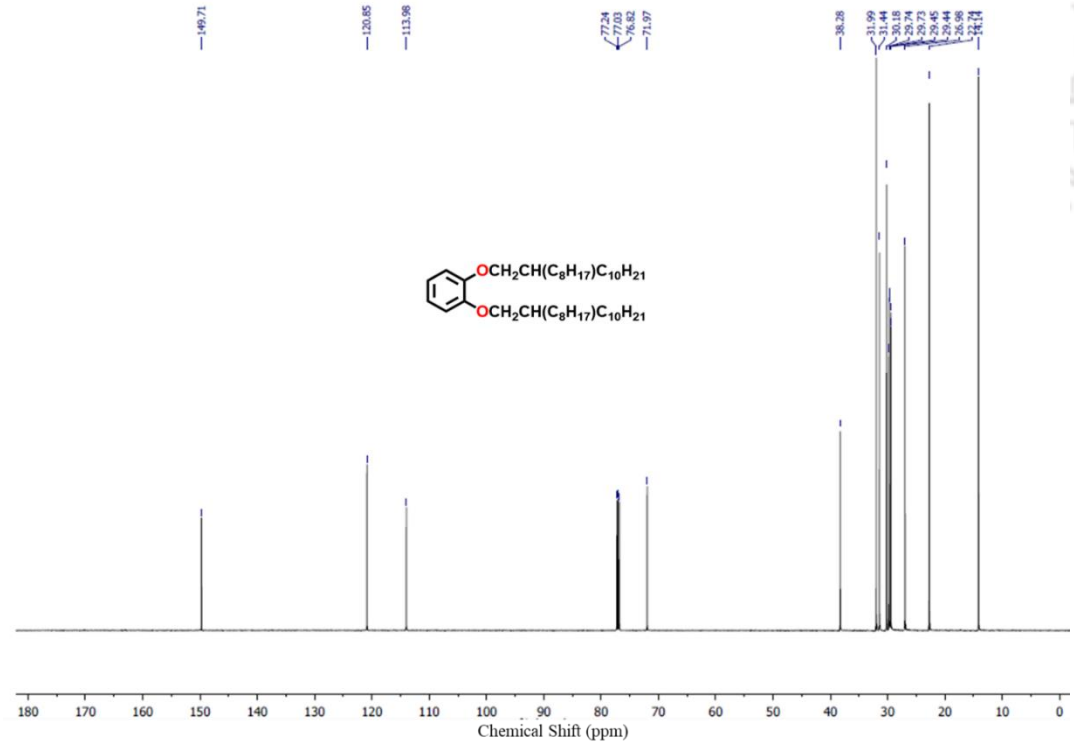

Figure A4. ^{13}C NMR (100 MHz) spectra of 1,2-bis((2-octyldodecyl)oxy)benzene **(2b)** in $CDCl_3$.

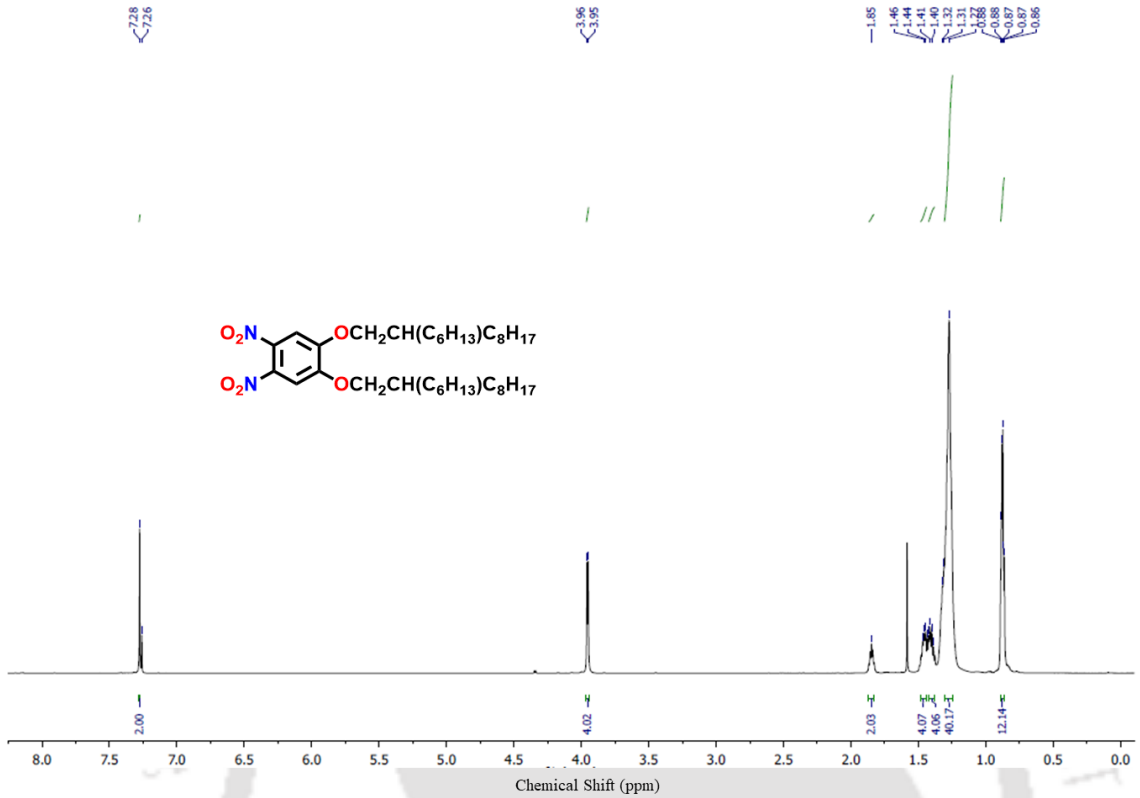

Figure A5. ^{1}H NMR (400 MHz) spectra of 1,2-dinitro-4,5-bis((2-hexyldecyl)oxy)benzene **(3a)** in $CDCl_3$.

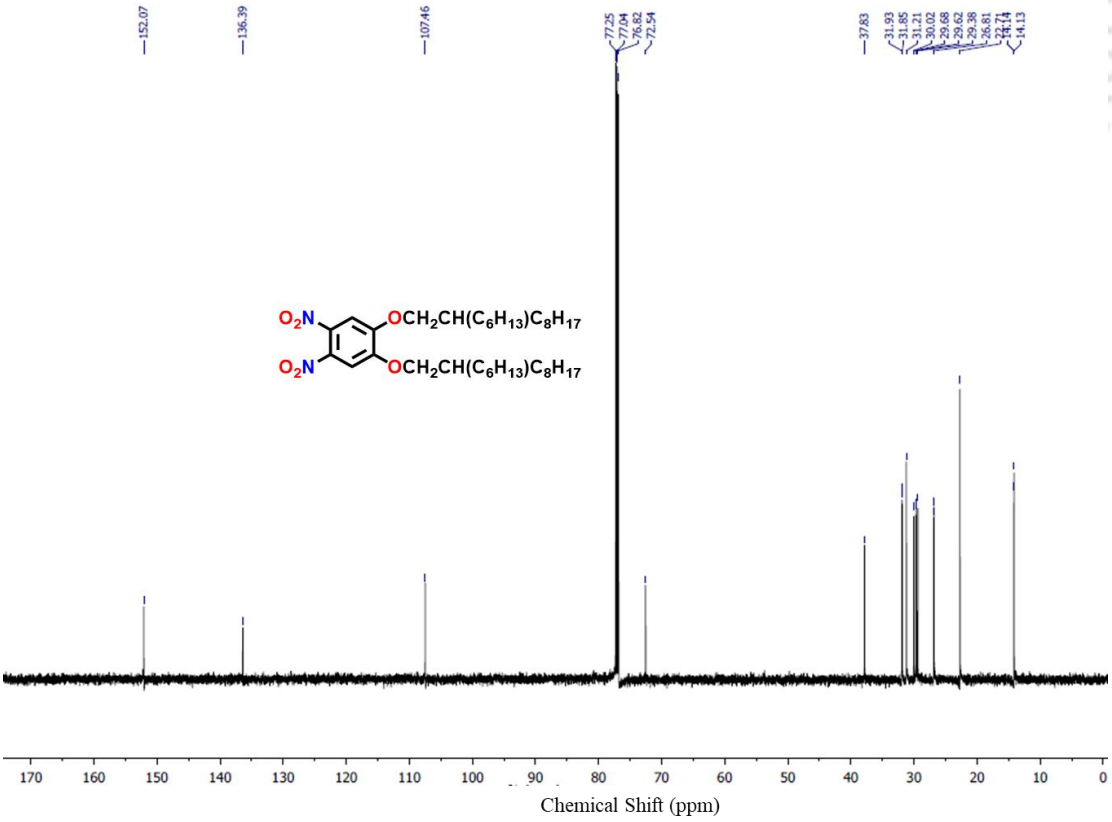

Figure A6. ^{13}C NMR (100 MHz) spectra of 1,2-dinitro-4,5-bis((2-hexyldecyl)oxy)benzene **(3a)** in $CDCl_3$.

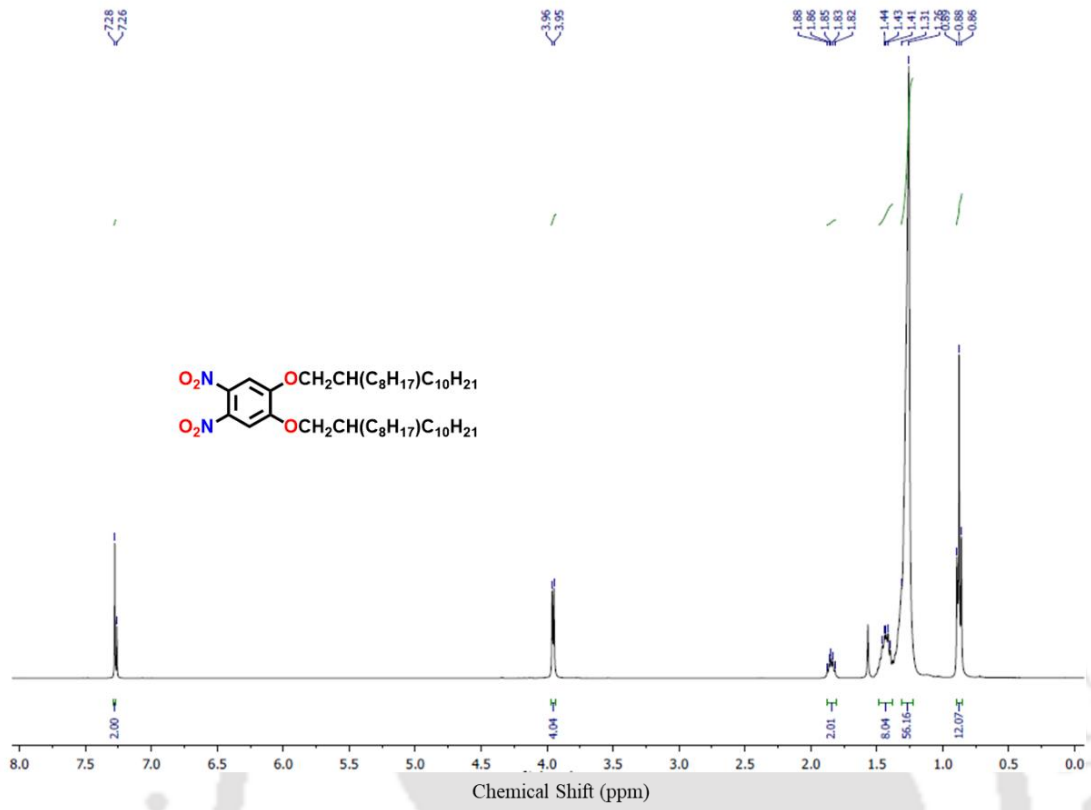

Figure A7. ^{1}H NMR (400 MHz) spectra of 1,2-dinitro-4,5-bis((2-octyldodecyl)oxy)benzene **(3b)** in $CDCl_3$.

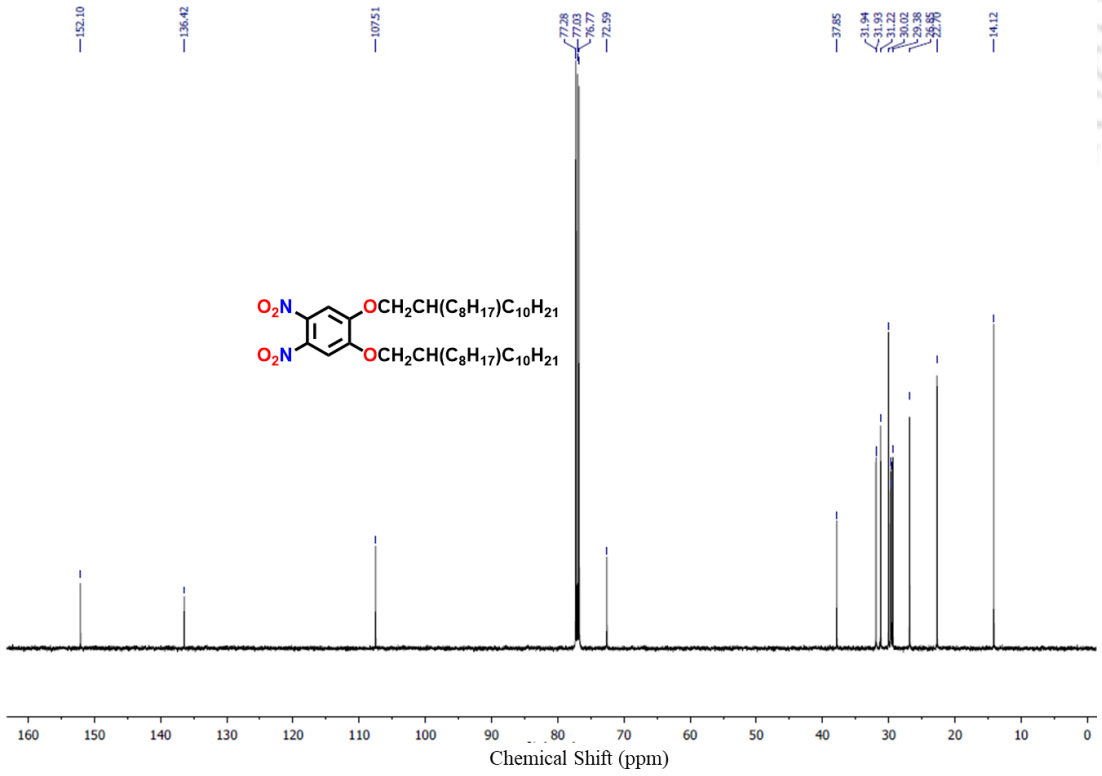

Figure A8. ^{13}C NMR (100 MHz) spectra of 1,2-dinitro-4,5-bis((2-octyldodecyl)oxy)benzene **(3b)** in $CDCl_3$.

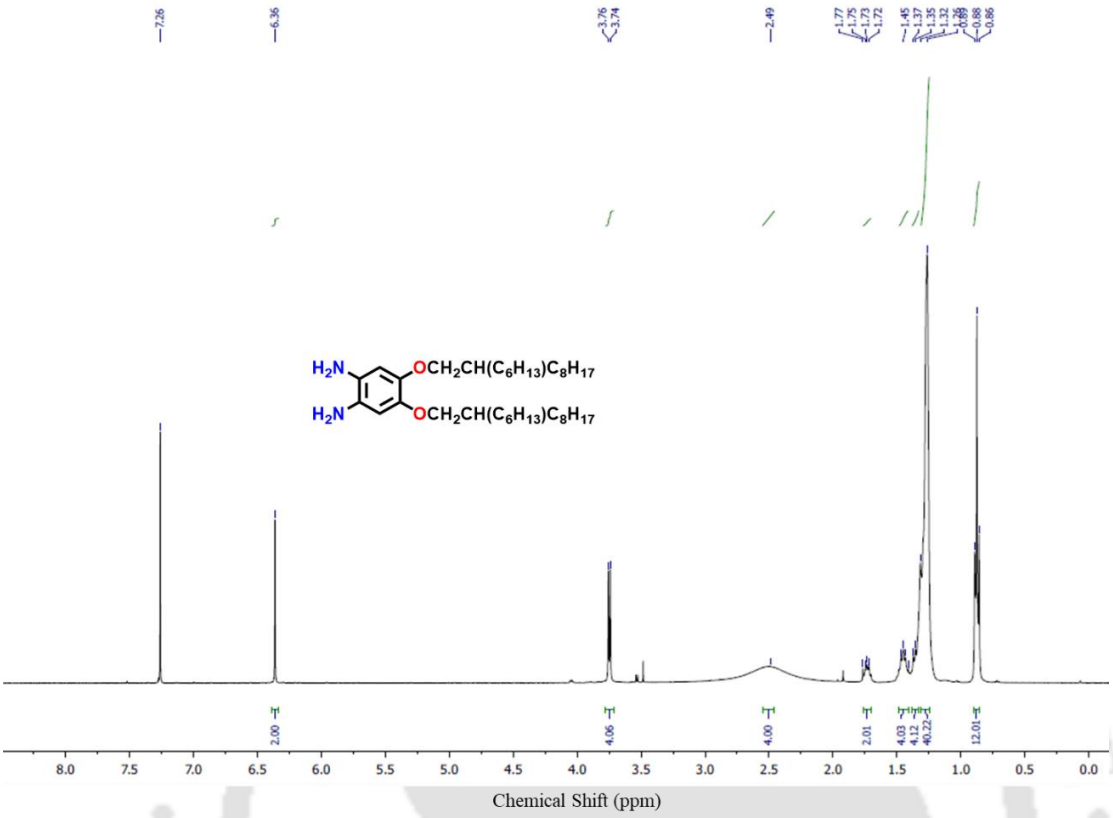

Figure A9. ^{1}H NMR (400 MHz) spectra of 4,5-bis((2-hexyldecyl)oxy)benzene-1,2-diamine **(4a)** in $CDCl_3$.

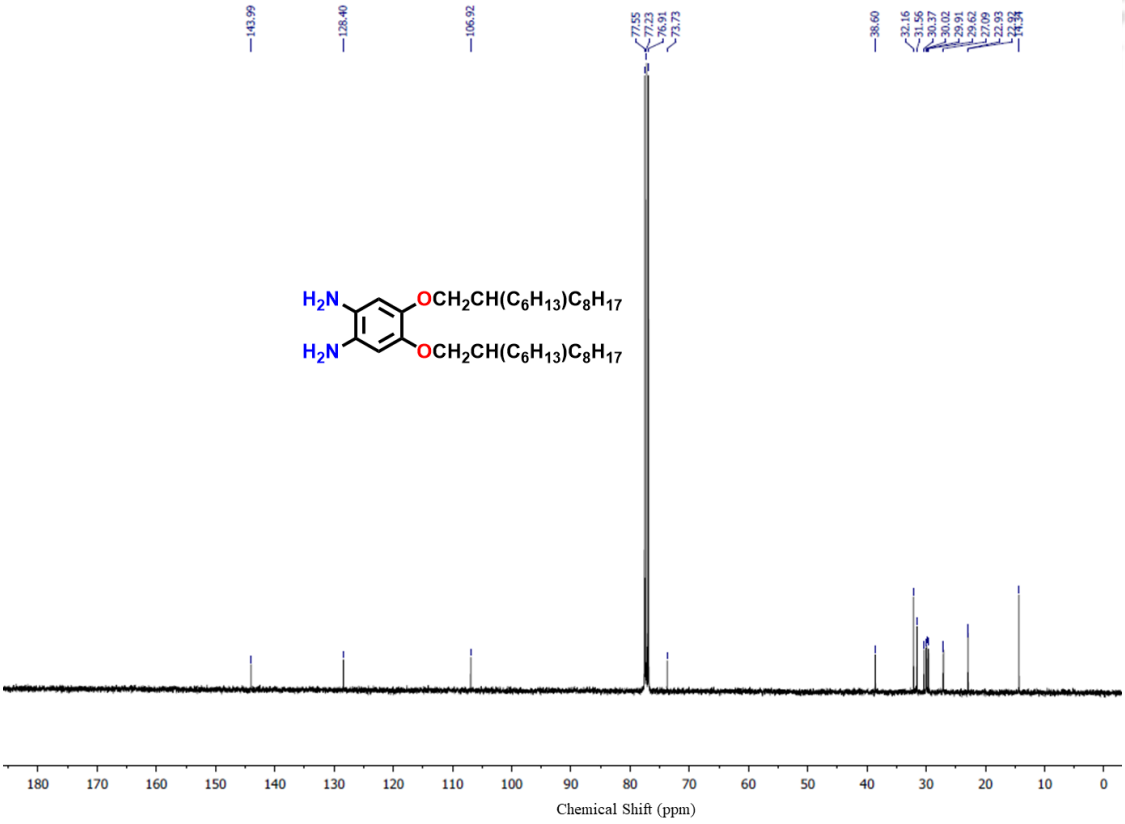

Figure A10. ^{13}C NMR (100 MHz) spectra of 4,5-bis((2-hexyldecyl)oxy)benzene-1,2-diamine **(4a)** in $CDCl_3$.

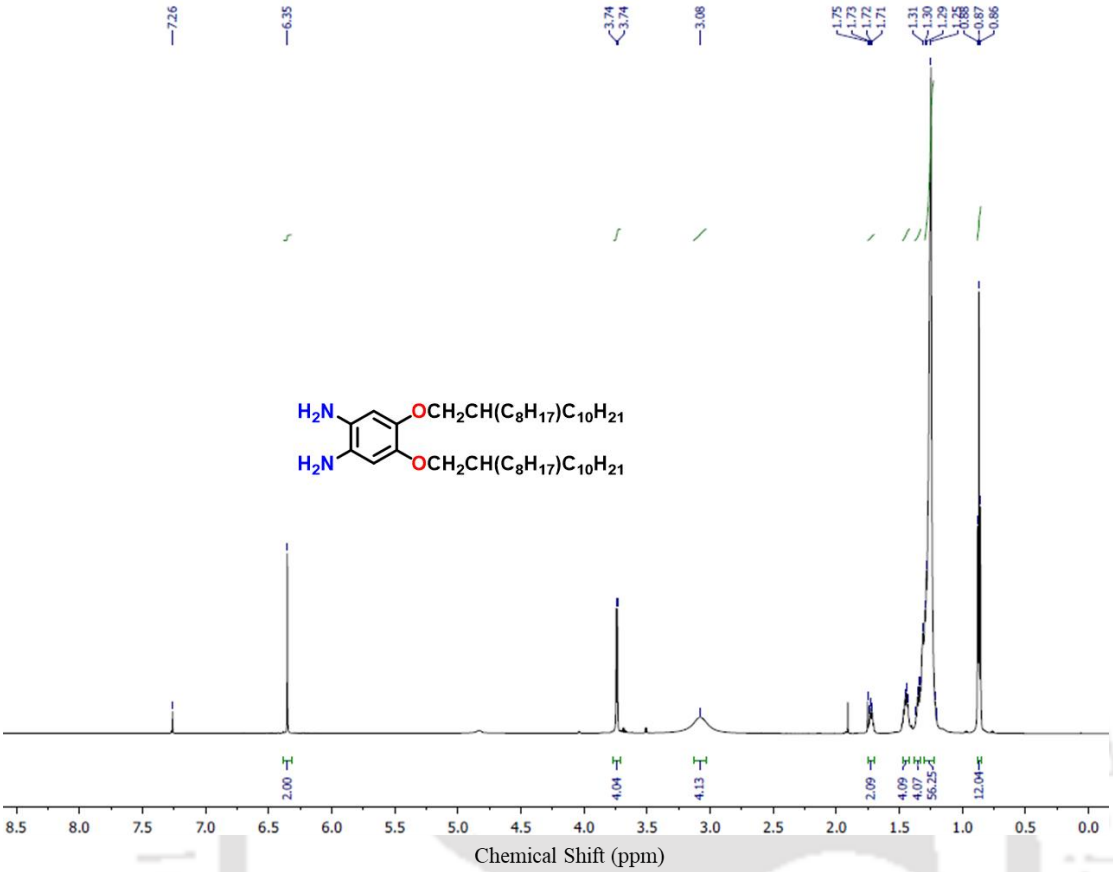

Figure A11. ^{1}H NMR (400 MHz) spectra of 4,5-bis((2-octyldodecyl)oxy)benzene-1,2-diamine **(4b)** in $CDCl_3$.

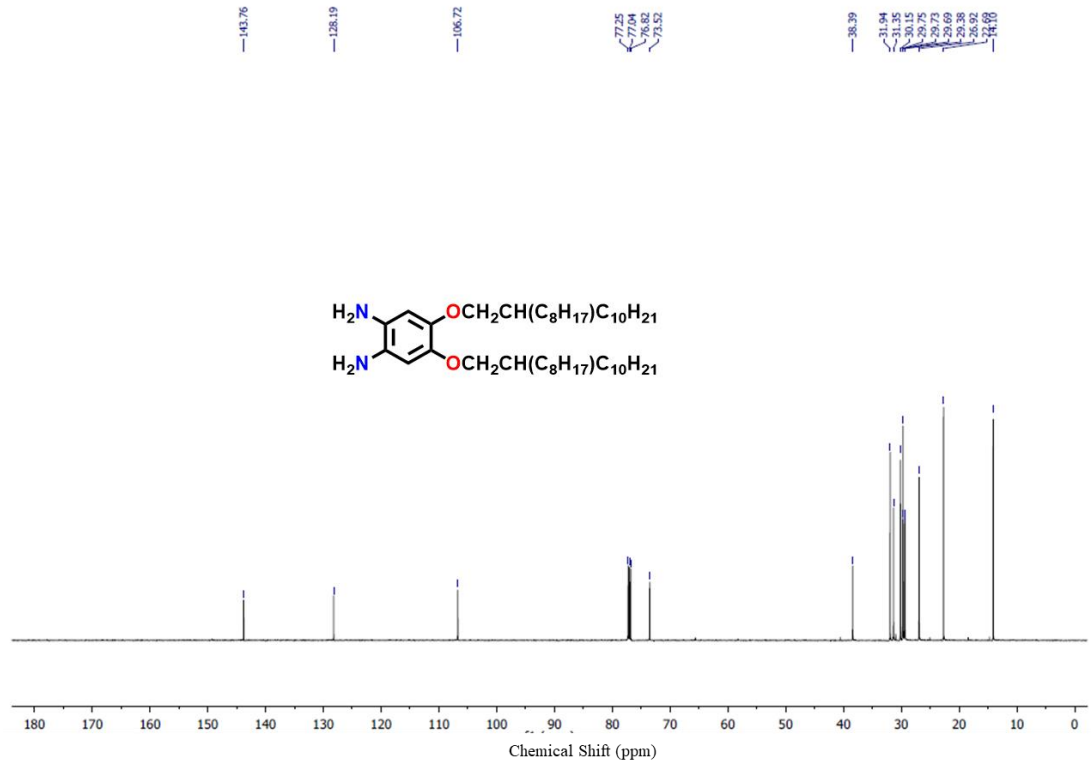

Figure A12. ^{13}C NMR (100 MHz) spectra of 4,5-bis((2-octyldodecyl)oxy)benzene-1,2-diamine **(4b)** in $CDCl_3$.

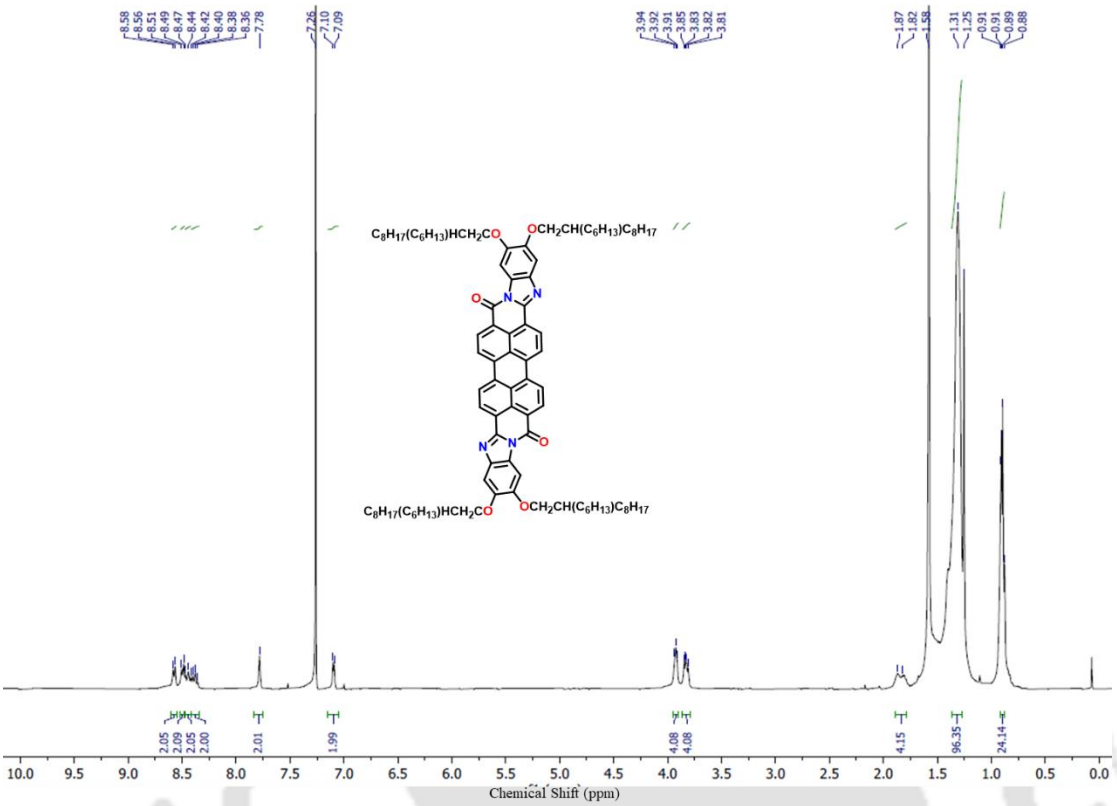

Figure A13. ^{1}H NMR (400 MHz) spectra of **PB16 (5a)** in $CDCl_3$.

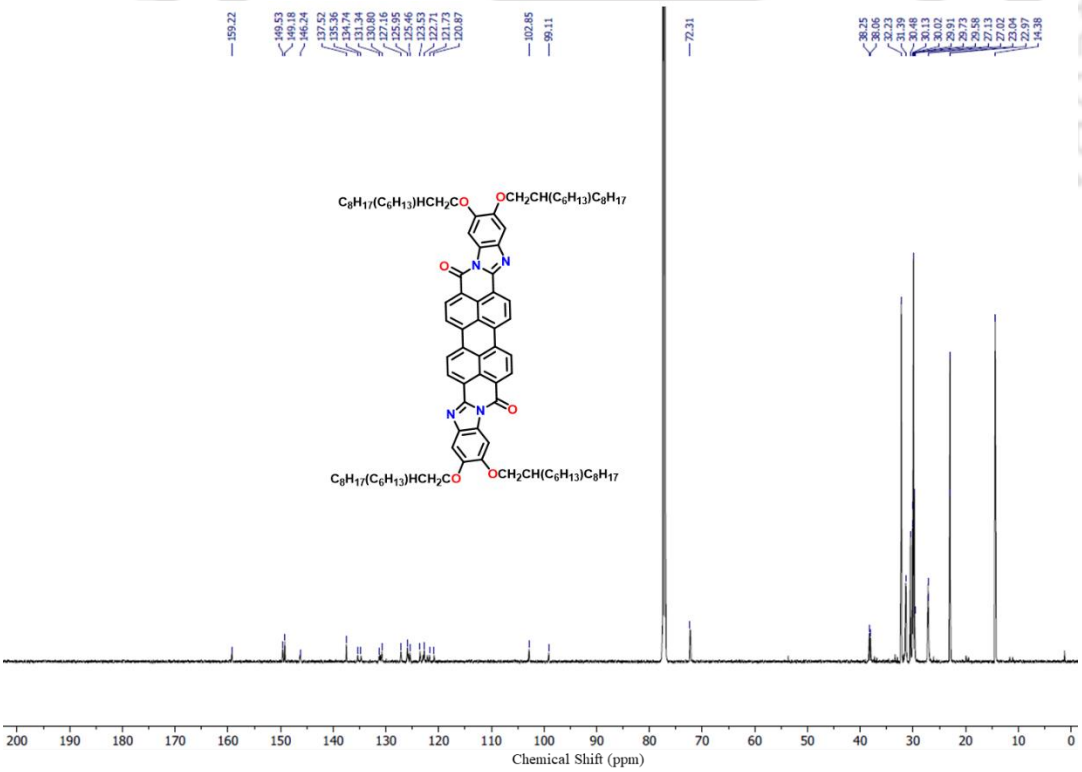

Figure A14. ^{13}C NMR (100 MHz) spectra of **PB16 (5a)** in $CDCl_3$.

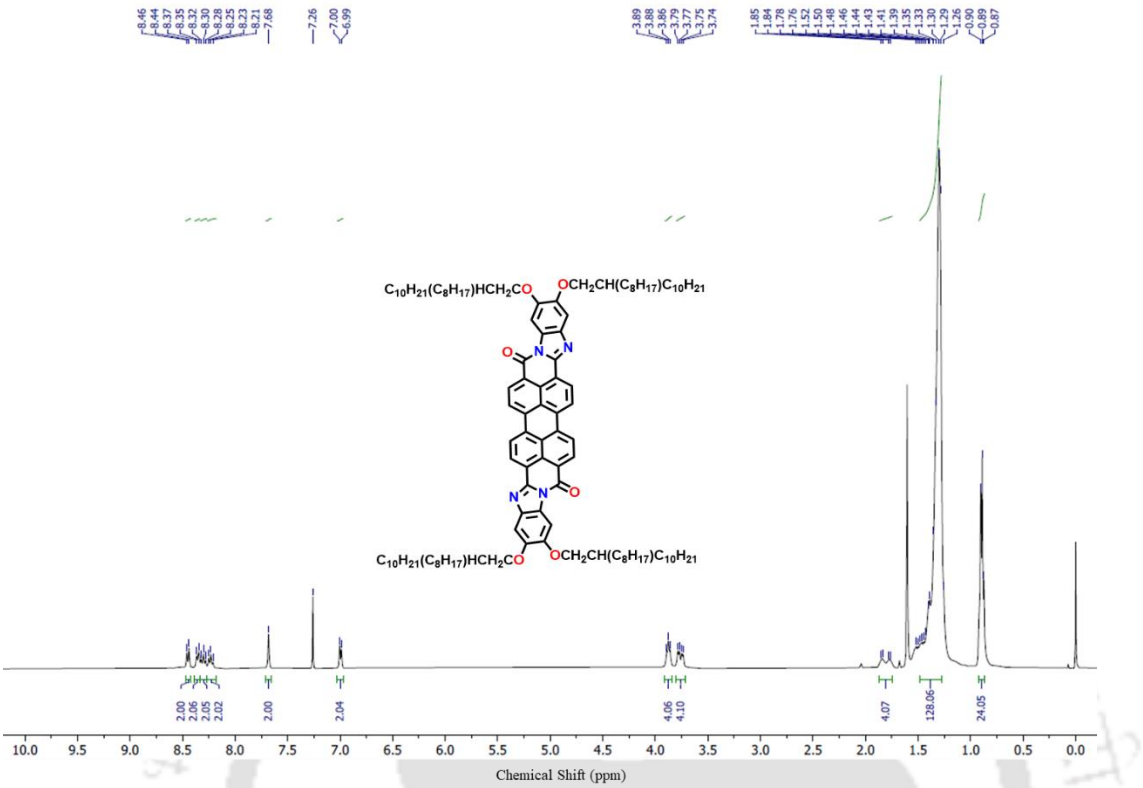

Figure A15. ^{1}H NMR (400 MHz) spectra of **PB20 (5b)** in $CDCl_3$.

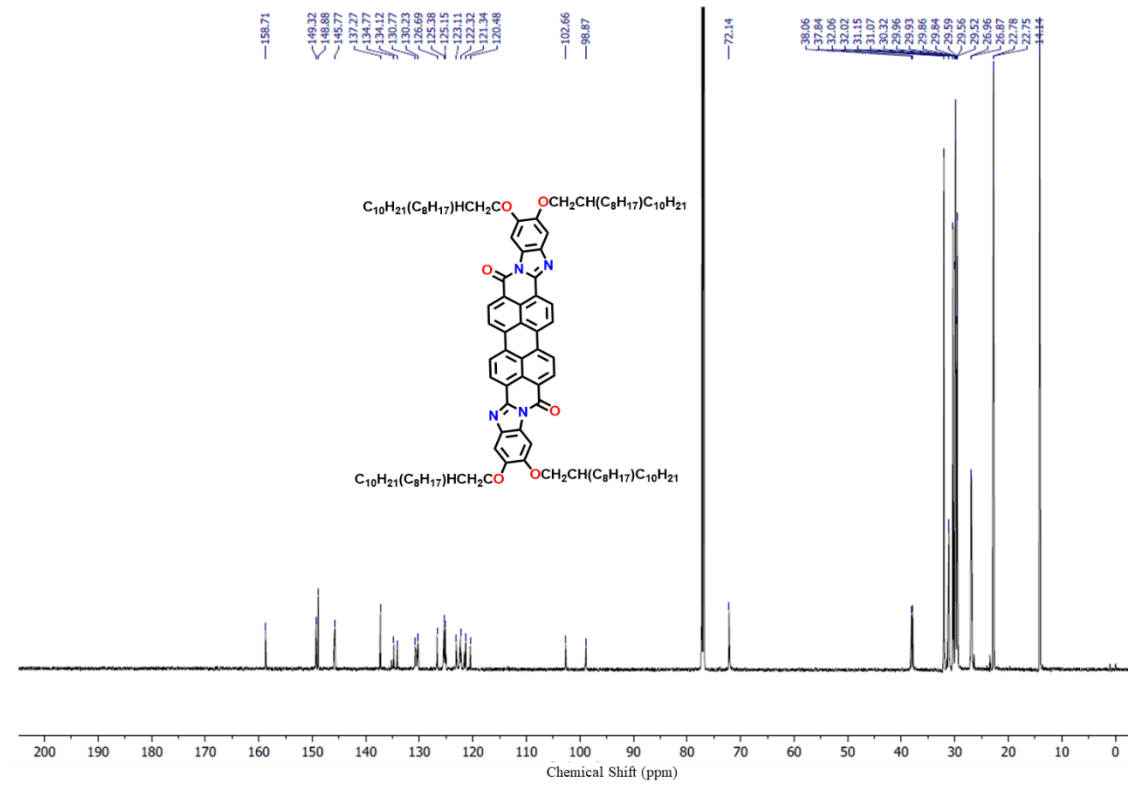

Figure A16. ^{13}C NMR (100 MHz) spectra of **PB20 (5b)** in $CDCl_3$.

7.6.2. UV-Visible (UV-Vis) Spectroscopy

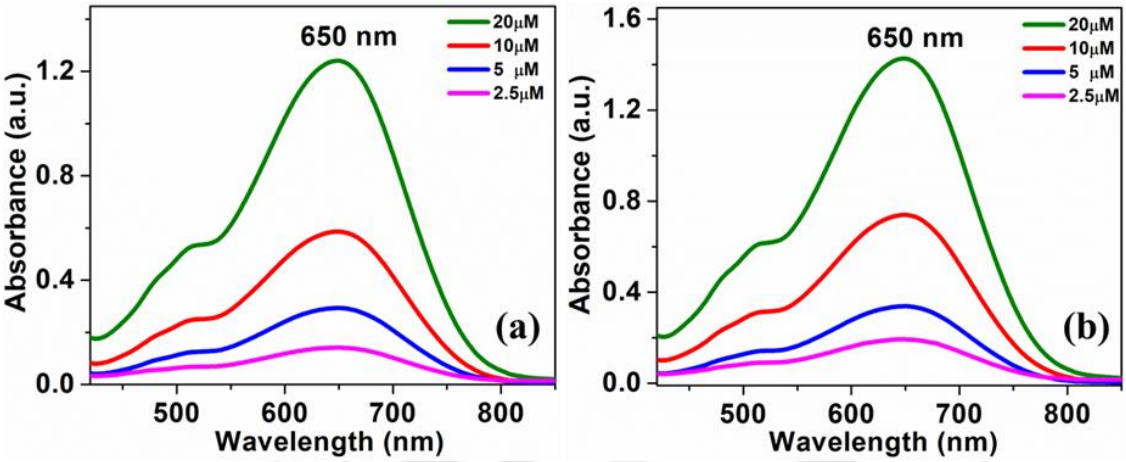

Figure A17. Concentration dependent absorption spectra of **PB16** (a) and **PB20** (b).

Table A1. Photophysical[a] properties of PBs in solution state and thin film state.

Compounds	[a]Absorption (nm)	$\Delta E_{g,\,opt}$ [eV]	[b]Absorption (nm)	Molar extinction coefficient ($Lmol^{-1}\,cm^{-1}$)
PB16	515, 650	1.60	630	5.8×10^4
PB20	515, 650	1.60	630	7.3×10^4
[a] Micromolar solutions in $CHCl_3$; [b]Prepared by spin coating of millimolar solution in $CHCl_3$.				

5.6.3. Cyclic Voltammetry (CV)

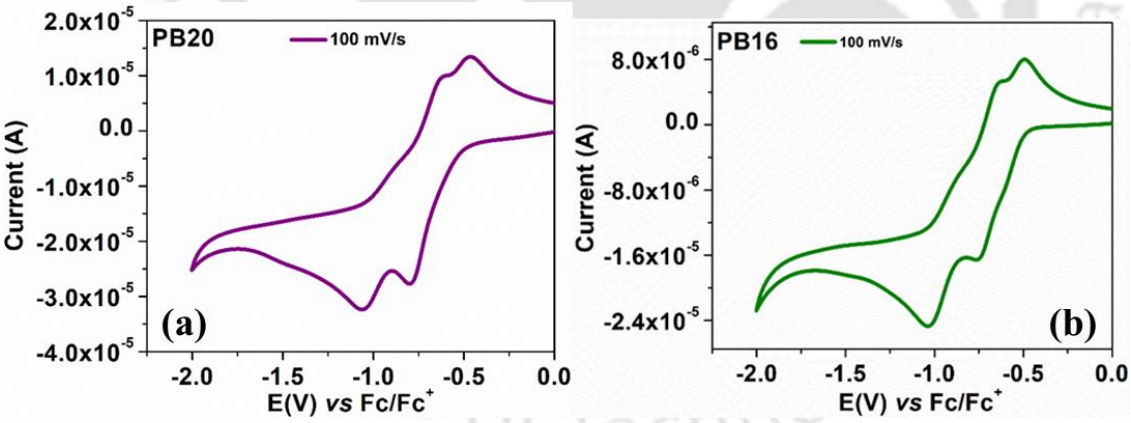

Figure A18. Cyclic voltammograms of **PB20** (a) and **PB16** (b).

Table A2. Electrochemical[a,b] data and data obtained from DFT[h] calculations for compounds **PB20**.

Electrochemical data					Data from DFT calculations		
Entry	$E_{1st\ red}$ (in V)	E_{LUMO}[c] (in eV)	E_{HOMO}[d] (in eV)	$\Delta E_{g,\,opt}$ [e] (in eV)	E_{LUMO}[f] (in eV)	E_{HOMO}[f] (in eV)	$\Delta E_{g,}$[f] (in eV)
PB20	-0.79	-3.51	-5.11	1.60	-3.35	-5.24	1.89
PB16	-0.76	-3.54	-5.14	1.60			

[a] 0.5 mM Dichloromethane solutions; [b]experimental conditions: $Ag/AgNO_3$ as reference electrode, glassy carbon working electrode, platinum wire counter electrode, TBAP (0.1M) as a supporting electrolyte, room temperature, scan rate 100 mV/s; [c] estimated from the formula by using $E_{LUMO} = -(4.8 - E_{1/2, Fc/Fc+} + E_{red, onset})$ eV; [d] estimated from the formula $E_{HOMO} = E_{LUMO} - E_{g,opt})$ eV; $E_{1/2, Fc/Fc+} = 0.50$ V.[e]calculated from the red edge of the absorption band of each compound. [f] Obtained from DFT calculations by employing the combination of Becke3-Lee-Yang-Parr (B3LYP) hybrid functional and 6-31G(d,p) basis set using the Gaussian 09 package, where the chain length is limited to methyl.

5.6.4. Polarizing Optical Microscopy (POM)

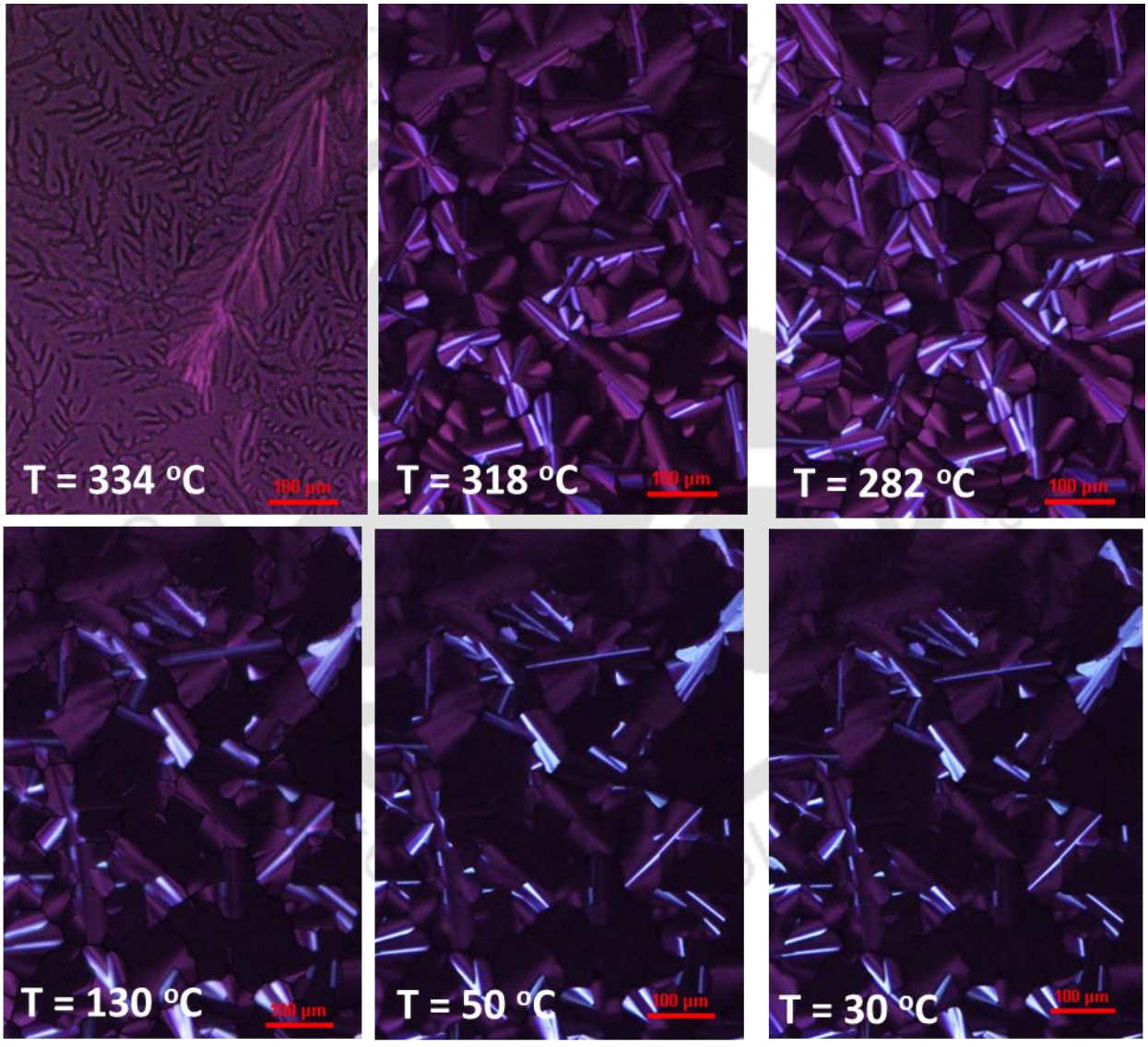

Figure A19. POM images of the Col_h phase exhibited by **PB16** at different temperatures (Dark regions in the images correspond to the homeotropically oriented columns).

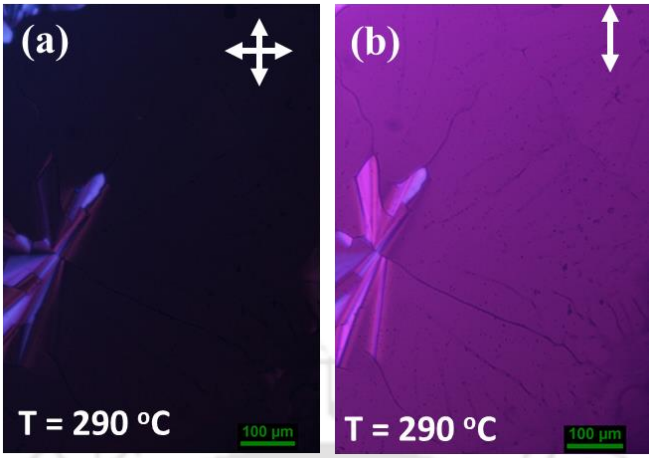

Figure A20. POM images of the Col_h phase exhibited by **PB20** at 290°C, under crossed polarizers (Dark regions in the image correspond to the homeotropically oriented columns) (a); under parallel polarizers (b).

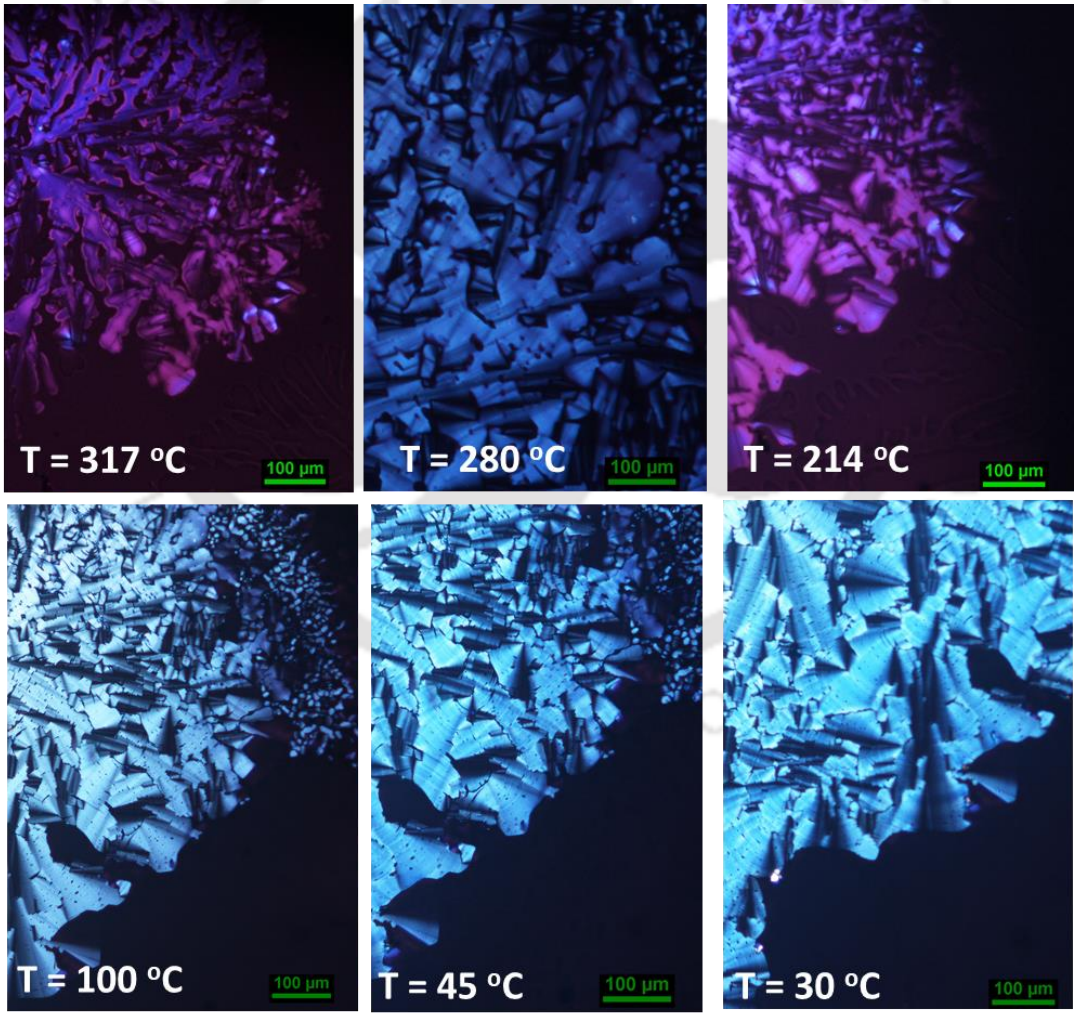

Figure A21. POM images of the Col_h phase exhibited by **PB20** at different temperatures (Dark regions in the images correspond to the homeotropically oriented columns).

5.6.5. Differential Scanning Calorimetry (DSC)

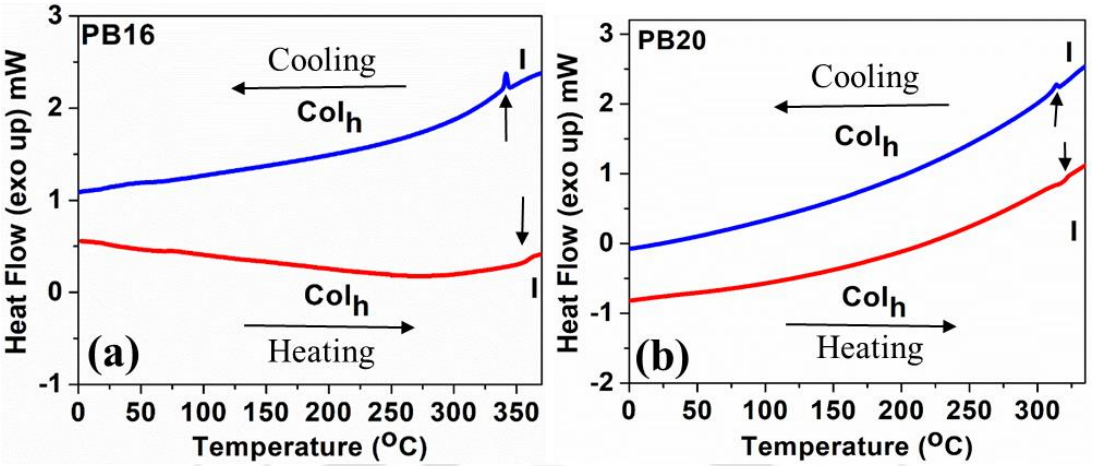

Figure A22. DSC thermograms of **PB16** (a) and **PB20** (b) carried out at a rate of 5^{o}C/min (red trace: second heating, blue trace: first cooling).

5.6.6. Thermogravimetric analysis (TGA)

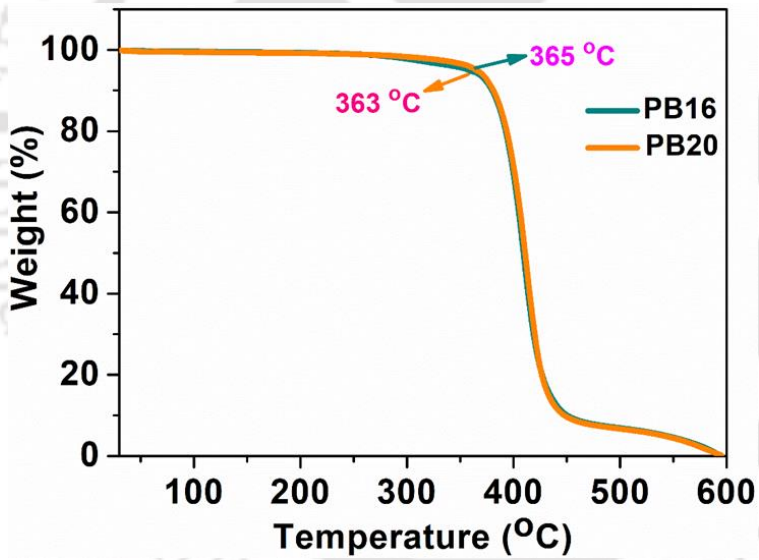

Figure A23. TGA plots of compound **PB16** and **PB20** (heating rate of 10 ^{o}C/min, Nitrogen atmosphere).

Table A3. Phase transition temperatures (^{o}C), corresponding enthalpies (kJmol^{-1})[a] and decomposition temperatures obtained by TGA.

Entry	Phase Sequence (kJ/mol)		T_5^b (^{o}C)
	Second heating	First Cooling	
PB16	Col$_h$ 354.79 (0.12) I	I 341.31 (0.56) Col$_h$	363
PB20	Col$_h$ 317.58 (0.51) I	I 313.93 (0.41) Col$_h$	365

[a] Peak temperatures in the DSC thermograms obtained during the second heating and first cooling cycles at 5 ^{o}C min^{-1}. Col$_h$ = Columnar hexagonal phase; I = Isotropic phase. [b] Temperature at which 5 wt% decomposition occurred obtained from TGA studies.

5.6.7. X-ray Diffraction Studies (XRD)

Table A4. Results of (*hkl*) indexation of XRD profiles of **PB16** and **PB20** at a given temperature (T) of mesophase[a].

Compounds (D/Å)	Phase (T/°C)	Space Group	d_{obs} (Å)	d_{cal} (Å)	Miller indices *hk*	Lattice parameters (Å), Lattice area S (Å^2), Molecular volume (Å^3)
PB16 (37.7) MW:1498.3	Col_h (260)	P6mm	32.60 4.91 3.53 (h_a)	32.60	10	a = 37.6 S = 1226.9 V = 4331 c = 3.53 $Z \approx 2$
	Col_h (200)		32.89 4.76 3.49 (h_a)	32.89	10	a = 37.9 S = 1249.2 V = 4359.7 c = 3.49 $Z \approx 2$
	Col_h (100)		33.31 4.68 3.42 (h_a)	33.31	10	a = 38.5 S = 1281.6 V = 4383.2 c = 3.42 $Z \approx 2$
	Col_h (28)		33.26 18.98 4.53 (h_a) 3.37 (h_c)	33.27 19.21	10 11	a = 38.4 S = 1278.3 V = 4307.9 c = 3.37 $Z \approx 2$
PB20 (42) MW:1722.7	Col_h (260)	P6mm	33.22 19.07 4.84 (h_a) 3.54 (h_c)	33.22 19.18	10 11	a = 38.4 S = 1274.3 V = 4521.4 c = 3.54 $Z \approx 2$
	Col_h (200)		33.70 19.42 4.81 (h_a) 3.50 (h_c)	33.70 19.46	10 11	a = 38.9 S = 1311.8 V = 4591.4 c = 3.5 $Z \approx 2$
	Col_h (100)		34.48 19.79 18.02 4.67 (h_a) 3.42 (h_c)	34.49 19.91	10 11	a = 39.82 S = 1373.15 V = 4696.19 c = 3.42 $Z \approx 2$
	Col_h (25)		35.03 20.06 17.87 4.52 (h_a) 3.38 (h_c)	35.04 20.23	10 11	a = 40.46 S = 1417.65 V = 4791.66 c = 3.38 $Z \approx 2$

[a]The diameter (D) of the disk (estimated from Chem 3D Pro 8.0 molecular model software from Cambridge Soft). d_{obs}: spacing observed; d_{cal}: spacing calculated (deduced from the lattice parameters; a for Col_h phase; c is height of the unit cell). The spacings marked h_a and h_c correspond to diffuse reflections in the wide-angle region arising from correlations between the alkyl chains and core regions, respectively. Z indicates the number of molecules per columnar slice of thickness h_c estimated from the lattice area S and the volume V.

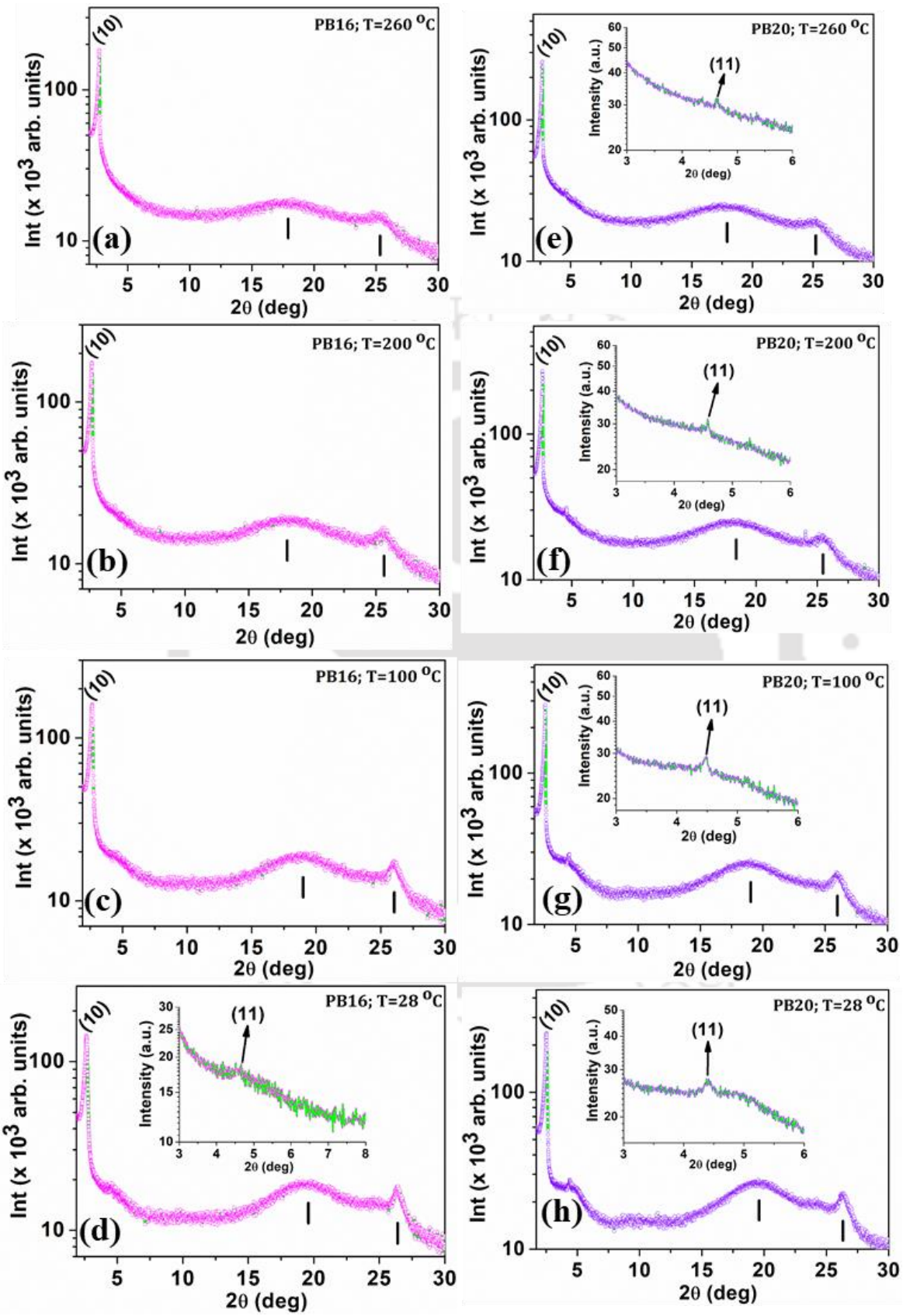

Figure A24. Plot of the intensity against 2θ obtained from the powder XRD pattern of the Col_h phases for compound **PB16** at 260 ºC (a); 200 ºC (b); 100 ºC (c); 28 ºC (d) **PB20** at 260 ºC (e); 200 ºC (f); 100 ºC (g); 28 ºC (h).

5.6.8. DFT Studies

To understand the electronic properties and frontier molecular orbital energy level of compounds **PB16** and **PB20**, computational studies was carried out in B3LYP/6-31g(d,p) method using Gaussian 09 program package. The absence of imaginary frequency ensured the energy minimized structure of all the compounds.

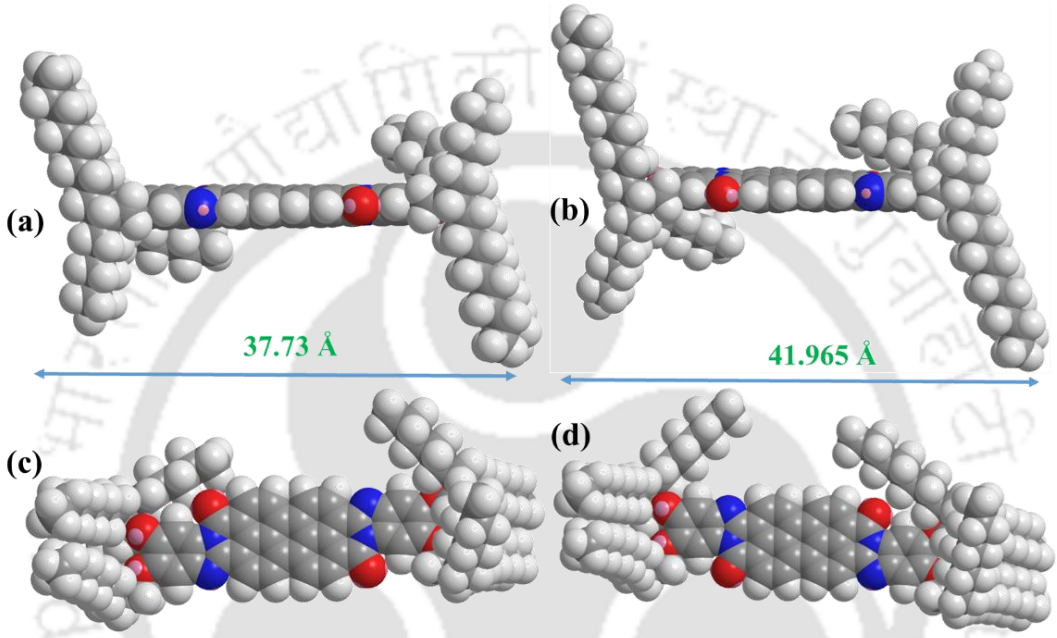

Figure A25. Optimized geometry of compounds **PB16** (a) (side view), **PB20** (b) (side view), **PB16** (c) (side view), **PB20** (d) (top view) (from Chem 3D 21.1.1).

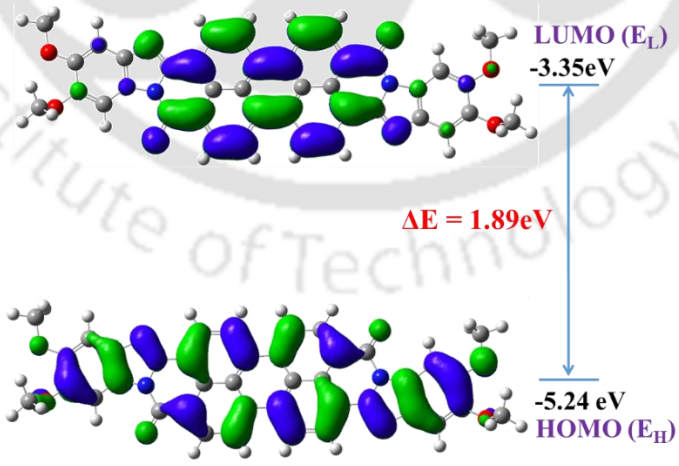

Figure A26. Frontier molecular orbitals of PBs derived from 4,5-bisalkoxybenzene-1,2-diamine. DFT calculations at the B3LYP/6-31G(dp) level. E_H and E_L denote energies of the highest occupied molecular orbital (HOMO) and the lowest unoccupied molecular orbital (LUMO), respectively (chain length on the phenyl group is limited to methyl for clarity purpose).

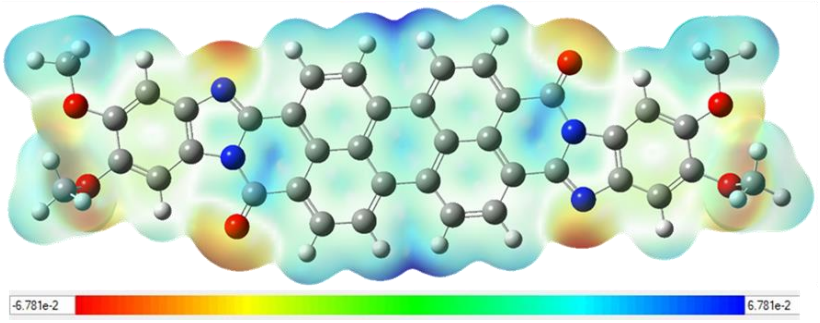

Figure A27. 3D molecular electrostatic potential contour map of optimized structure of PBs derived from 4,5-bisalkoxybenzene-1,2-diamine (In the mapped electro-static potential surface, the red and blue colors refer to the electron-rich and electron-poor regions, respectively, whereas the green color signifies the zero electrostatic potential, chain length on the phenyl group is limited to methyl for clarity purpose).

5.6.9. Scanning Electron Microscopy

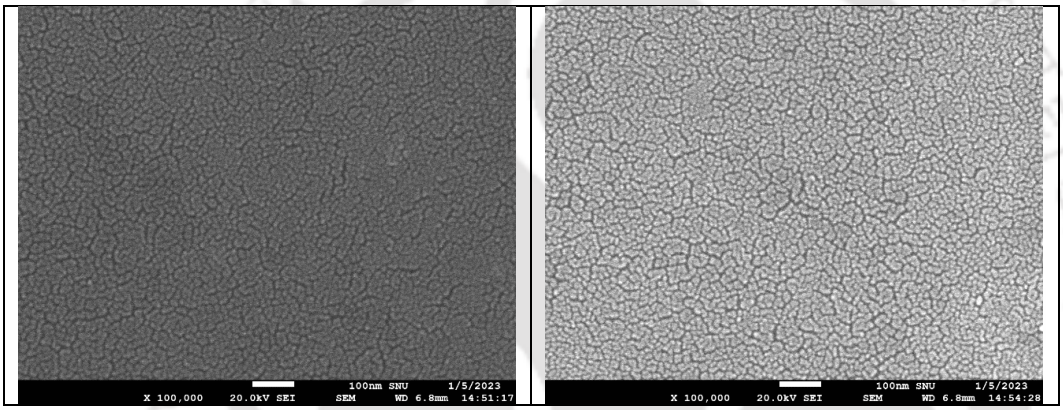

Figure A28. SEM images of spin coated sample of **PB20** in chloroform obtained after annealing 70 ºC (Scale bar is 100 nm).

5.6.10. Device Fabrication & characterization

To investigate the ambipolar charge transport property of **PB20** compound, different architectures were fabricated to have an electron and hole only devices. The hole only devices were fabricated in ITO/PEDOT:PSS/**PB20**/MoO_3/Ag architecture whereas electron only devices were fabricated with ITO/ZnO or SnO_2 or Al/ **PB20** /Al configuration respectively for hole and electron mobility measurements. Prepatterned indium tin oxide (ITO) substrates were cleaned in an ultrasonic bath via successive treatments with Soap solution, distilled water, acetone and isopropanol for 20 minute each followed by UV Ozone (BioBEE Tech, India) surface treatment at 50 °C for 30 min for removing any residues from the surface. In electron only (ITO/ZnO/**PB20**/Al) devices, ZnO layer was spin coated with speed of 4500 rpm for 45 sec on the pre-patterned cleaned ITO substrates to achieve a thickness of around 30 nm followed by film annealing at 180 °C for 1 hour. For ZnO solution preparation ,200 mg zinc acetate dihydrate (Zn $(CH_3COO)_2 2H_2O$) + 52 mg ethanolamine in 2 mL 2-methoxy ethanol, were stirred heavily overnight followed by filtration using 0.45 µm PTFE filter. For SnO_2 as electron injection electrode, SnO_2 (15% colloidal solution

in Water, Alfa Aesar) was prepared in DI water with the ratio of 1:6 (SnO_2: DI water) and stirred heavily for 2 hours followed the solution filtration using 0.45 μm PVDF Filter. SnO_2 layer was spin coated with speed of 5000 rpm for 65 secs on the pre-patterned cleaned ITO substrates to achieve a thickness of around 30 nm followed by film annealing at 180 °C for 30 minutes. MoO_3 (5-7 nm), Al (100 nm) and Ag (100 nm) were thermaly evaporated in thermal evaporation system (Hind High Vacuum, Bangalore, India) at high vacuum at 2.2 x 10^{-6} mbar base pressure. For active layer deposition 10 mg/ml in chloroform solution was spin coated at 1500 rpm for 45 secs to get a thickness of ~100 nm. For hole only (ITO/PEDOT: PSS/**PB20**/ MoO_3/Ag) devices, PEDOT: PSS (Sigma Aldrich) thin film was deposited on the cleaned ITO substrate at 4500 rpm for 45 sec followed by annealing at 150 ºC for 20 minutes. A 10 mg/ml in chloroform solution of active material (**PB20**) was spin coated at 1500 rpm for 45 secs for having thickness of 100 nm. A top contact of ~7 nm of MoO_3 and 100 nm of Ag layer was sequentially evaporated in thermal evaporation under high vacuum (2.2 x 10^{-6} mbar) for completion of device. The SCLC mobility for compound **PB20**, elucidated from the current/voltage curve Figure S31 is summarized in Table S5.

Table A5: Hole and electron mobility statistics table for **PB20** compound for best five devices.

Entry	**Hole mobility (cm^2/ V.s)** (ITO/PEDOT: PSS/PB20/ MoO_3/Ag)	**Electron mobility (cm^2/ V.s)** (ZnO/PB20/Al)	**Electron mobility (cm^2/ V.s)** (Al/PB20/Al)	**Electron mobility (cm^2/ V.s)** (SnO_2/PB20/Al)
PB20	1.41E-03	8.29E-04	4.53E-04	4.29E-05
	1.44E-03	3.25E-04	3.85E-04	3.56E-06
	3.01E-03	1.28E-04	5.19E-04	3.25E-04
	3.00E-03	3.46E-04	5.50E-04	7.86E-04
Avg.	1.22E-03	2.24E-04	1.19E-06	9.38E-04
Stdev	**2.02E-03**	**3.70E-04**	**3.82E-04**	**4.19E-04**
	8.11E-04	**2.42E-04**	**1.98E-04**	**3.81E-04**

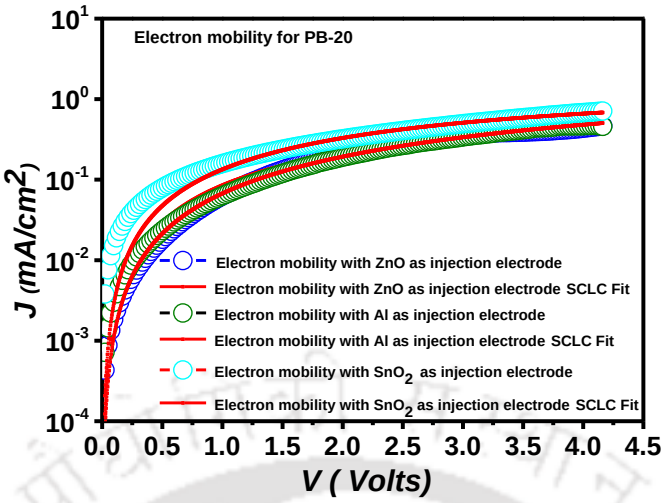

Figure A29. *J-V* Characteristics of electron only devices with different electron injection electrode (ZnO, Al and SnO_2) for **PB20** compound.

5.7 References

1. M. Mamada, C. Pérez-Bolívar, D. Kumaki, N. A. Esipenko, S. Tokito, and P. Anzenbacher, *Chem. Eur. J.* 2014, **20**, 11835 – 11846.
2. C. W. Tang, *Appl. Phys. Lett.* 1986, **48**, 183 – 185.
3. P. Peumans, V. Bulović, and S. R. Forrest, *Appl. Phys. Lett.* 2000, **76**, 2650.
4. K. Takahashi, N. Kuraya, T. Yamaguchi, T. Komura, and K. Murata, *Sol. Energy Mater. Sol. Cells* 2000, **61**, 403.
5. D. Gebeyehu, M. Pfeiffer, B. Maennig, J. Drechsel, A. Werner, and K. Leo, K., *Thin solid films*, 2004, **451**, 29-32.
6. J. Xue, B. P. Rand, S. Uchida, and S. R. Forrest, *Journal of Applied Physics*, **98**(12), p.124903.
7. P. Dhagat, H. M. Haverinen, R. J. Kline, Y. Jung, D. A. Fischer, D. M. DeLongchamp, and G. E. Jabbour, *Adv. Funct. Mater.* 2009, **19**, *2365–2372.*
8. J. Mizuguchi, and N. Shimo, *J. Imaging Sci. Tech* 2006, **50**, *115.*
9. F. Würthner, *Chem. Commun.* 2004, *1564–1579*.
10. C. Huang, S. Barlow, and S. R. Marder, *J. Org. Chem.* 2011, **76**, *2386–2407*.
11. R. K. Gupta, and A. A. Sudhakar, *Langmuir* 2019, **35**, *2455–2479*.
12. Z. Yuan, Y. Xiao, Z. Li, and X. Qian, *Org. Lett.*, 2009, **11**, *2808-2811*.
13. A. Wicklein, P. Kohn, L. Ghazaryan, T. Thurn-Albrecht, and M. Thelakkat, *Chem. Commun.* 2010, **46**, *2328–2330.*
14. S. J. Hein, C. Edder, M. Kowalczyk, A. Borzenko, L. Mourokh, and P. Lazarev, *RSC Adv.* 2019, **9**, *361–364.*
15. L. Perrin, and P. Hudhomme, *Eur. J. Org. Chem.* 2011, 5427–5440.
16. S. H. Oh, B. G. Kim, S. J. Yun, M. Maheswara, K. Kim, and J. Y. Do, *Dyes and Pigments* 2010, **85**, *37-42.*
17. S. Kumar, *Chemical Society Reviews*, 2006, **35**, 83-109.
18. M. Kumar, and S. Kumar, *Polymer Journal*, 2017, **49**, 85-111.
19. T. Wöhrle, I. Wurzbach, J. Kirres, A. Kostidou, N. Kapernaum, J. Litterscheidt, J. C. Haenle, P. Staffeld, A. Baro, F. Giesselmann, and S. Laschat, *Chemical reviews*, 2016, **116**, 3, 1139-1241.
20. S. Sergeyev, W. Pisula, and Y. H. Geerts, *Chemical Society Reviews*, 2007, **36**, 12, 1902-1929.
21. V. K. Vishwakarma, S. Nath, M. Gupta, D. K. Dubey, S. S. Swayamprabha, J. H. Jou, S. K. Pal, and A. A. Sudhakar, *ACS Appl. Electron. Mater.* 2019, **1***, 1959−1969.*
22. S. Nath, S. K. Pathak, J. De, S. K. Pal, and A. S. Achalkumar, *Mol. Syst. Des. Eng.*, 2017, **2**, *478–489.*
23. Y. Yi, P. E. Jeon, H. Lee, K. Han, H. S. Kim, K. Jeong, and S. W. Cho, *J. Chem. Phys.* 2009, **130**, 094704.
24. W. Yu, L. Huang, D. Yang, P. Fu, L. Zhou, J. Zhang, and C. Li, *J. Mater. Chem. A*, 2015, **3**(20), 10660-10665.
25. M. A. Muth, M. Carrasco-Orozco, M. and M. Thelakkat, *Adv. Func. Mater*, 2011, **21**(23), 4510-4518.

26. (a) S. A. Moiz, I. A. Khan, W. A. Younis and K. S. Karimov, *Conduct. Polym.*, 2016, **5**, 91.; (b) J. De, I. Bala, S. P. Gupta, U. K. Pandey, and S. K. Pal, *J. Am. Chem. Soc.*, 2019, **141** (47), 18799-18805.
27. (a) Z. An, J. Yu, S. C. Jones, A. Barlow, S. Yoo, B. Domercq, P. Prins, L. D. A. Siebbeles, B. Kip- pelean and S. R. Marder, *Adv. Mater.*, 2005, **17**, 2580—2583; (b) I. Bala, H. Kaur, M. Maity, R. A. K. Yadav, J. De, S. P. Gupta, J.-H. Jou, U. K. Pandey, and S. K. Pal, *ACS Applied Electronic Materials*, 2022, **4**, 3, 1163-1174.
28. A. Wicklein, M. Muth and M. Thelakkat, *J. Mater. Chem.*, 2010,**20**, 8646-8652.
29. M. C. Hwang, J. W. Jang, T. K. An, C. E. Park, Y. H. Kim, and S. K. Kwon, *Macromolecules* 2012, **45**, 4520−4528.
30. V. Percec, M. Peterca, T. Tadjiev, X. Zeng, G. Ungar, P. Leowanawat, E. Aqad, M. R. Imam, B. M. Rosen, U. Akbey, R. Graf, S. Sekharan, D. Sebastiani, H. W. Spiess, P. A. Heiney, and S D. Hudson, *J. Am. Chem. Soc.* 2011, **133**, 12197–12219.
31. R. K. Gupta, A. Dey, A. Singh, P. K. Iyer, and A. A. Sudhakar, *ACS Appl. Electron. Mater.*, 2019, **1**, 1378−1386.

Chapter 6

Conclusion

6.1. Summary

In conclusion, this thesis, titled 'Design and Synthesis of Liquid Crystalline Perylene Derivatives as Materials for Organic Electronics,' comprises five comprehensive chapters, each contributing to the understanding and exploration of novel liquid crystalline organic materials for various applications.

Chapter 1 serves as an introduction to liquid crystals and presents a thorough review of perylene-based discotic liquid crystals. It underscores the significance of perylene's unique properties, such as its strong π-π interactions and self-organizing capabilities, laying the foundation for our subsequent investigations. Additionally, it highlights the advantages of *bay*-annulated perylene derivatives in comparison to *bay*-substituted ones, setting the stage for research work discussed in the subsequent chapters.

Chapter 2 focuses on the synthesis and characterization of electron-deficient perylene derivatives, and their hetero-atom *bay*-annulated analogues bearing tri-*n*-decylphenyl moiety. These compounds exhibit room-temperature columnar liquid crystalline behavior and possess exceptional optical properties, making them promising candidates for organic electronics. Notably, they demonstrate significant potential in the realm of solution-processed host-guest OLEDs as deep red/NIR emitters.

Chapter 3 delves into the exploration of PBI and its bay-annulated analogs bearing tri-n-decyloxyphenyl moieties. These compounds exhibit remarkable room temperature columnar phases and high molar extinction coefficients, offering promising prospects for applications in organic solar cells and as non-fullerene acceptors. Their unique ambipolar conductivity behavior sets them apart from typical n-type semiconductors.

Chapter 4 introduces a swallowtail modification to lower the clearing point of perylene bisimide and its heteroatom annulated derivatives. These compounds exhibit stable liquid crystalline behavior up to room temperature with low melting points, strong fluorescence, and ambipolar conductivity. Their potential in organic electronics is further highlighted.

Chapter 5 addresses the challenge of solubility in the less explored class of perylene bis benzimidazole derivatives (PBs) with expanded aromatic cores. These compounds exhibit wide absorption spectra, elevated LUMO and HOMO levels, reduced band gap, enhanced solution

processability, stabilized columnar hexagonal phase up to room-temperature and ambipolar behavior, making them ideal candidates for organic solar cells and unique organic semiconductors.

Looking ahead to future prospects, ongoing research is focused on harnessing the potential of heteroatom *bay*-annulated PBIs. These compounds have shown excellent ambipolar charge carrier mobility and are being explored for their use in organic solar cells and sunlight-style OLEDs. Additionally, the introduction of asymmetry at the imide position, by preparing molecules like perylene diester monoimides with swallowtail substituents, is being considered as a means to further lower melting temperatures and enhance fluidity. In the case of perylene bisbenzimidazole derivatives, future work may involve incorporating additional conjugation at the *bay*-position alongside the imide position to reduce the band gap, potentially improving the efficiency of solar cells by capturing a broader range of the visible spectrum.

In summary, this thesis presents a comprehensive exploration of liquid crystalline perylene derivatives with diverse applications in organic electronics, showcasing their unique properties and potential contributions to the field. These research findings offer valuable insights into the design and synthesis of innovative materials for future advancements in the realm of organic electronics.